Lecture Notes in Nanoscale Science and Technology 11

Stefano Bellucci *Editor*

Physical Properties of Ceramic and Carbon Nanoscale Structures

The INFN Lectures, Vol. II

Springer

Physical Properties of Ceramic and Carbon Nanoscale Structures

Lecture Notes in Nanoscale Science and Technology

Volume 11

Volumes Published in This Series:
Volume 1: Self-Assembled Quantum Dots, Wang, Z.M., 2007
Volume 2: Nanoscale Phenomena: Basic Science to Device Applications, Tang, Z., and Sheng, P., 2007
Volume 3: One-Dimensional Nanostructures, Wang, Z.M., 2008
Volume 4: Nanoparticles and Nanodevices in Biological Applications: The INFN Lectures - Vol I, Bellucci, S., 2009
Volume 5: Toward Functional Nanomaterials, Wang, Z.M., 2009
Volume 6: B-C-N Nanotubes and Related Nanostructures, Yap, Y.K., 2009
Volume 9: Nanoscale Photonics and Optoelectronics, Wang, Z.M.; Neogi, A., 2010
Volume 11: Physical Properties of Ceramic and Carbon Nanoscale Structures: The INFN Lectures - Vol II, Bellucci, S., 2011

Forthcoming Titles:
Crystallization and Growth of Colloidal Nanocrystals. Leite, E.R., 2011
Epitaxial Semiconductor Nanostructures, Wang, Z.M., and Salamo, G., 2011

Stefano Bellucci (Ed.)

Physical Properties of Ceramic and Carbon Nanoscale Structures

The INFN Lectures, Vol. II

Springer

Editor
Stefano Bellucci
Istituto Nazionale di Fisica Nucleare
Laboratori Nazionali di Frascati
via E. Fermi 40
00044 Frascati RM
Italy
stefano.bellucci@lnf.infn.it

ISBN 978-3-642-15777-6 e-ISBN 978-3-642-15778-3
DOI 10.1007/978-3-642-15778-3
Springer Heidelberg Dordrecht London New York

Cover design: eStudio Calamar S.L., Heidelberg

Printed on acid-free paper

Springer is part of Springer Science+Business Media (www.springer.com)

In Memory of the Late Giorgio Bellucci
(1931–2009)

Preface

This is the second volume in a series of books on selected topics in Nanoscale Science and Technology based on lectures given at the well-known INFN schools of the same name. The aim of this collection is to provide a reference corpus of suitable, introductory material to relevant subfields, as they mature over time, by gathering the significantly expanded and edited versions of tutorial lectures, given over the years by internationally known experts.

The Nanotechnology group at INFN – LNF organizes since 2000 a series of international meetings in the area of nanotechnology. The conferences in 2006 and 2008 were devoted to recent developments in nanoscience and its manifold technological applications. They included of a number of tutorial/keynote lectures, which are reflected in this volume, besides research talks presenting frontier nanoscience research developments and innovative nanotechnologies in the areas of biology, medicine, aerospace, optoelectronics, energy, materials and characterizations, low-dimensional nanostructures and devices. Selected papers, based on conference talks and related discussions, were published on dedicated issues of international journals.

Special poster and equipment session were devoted to the exhibit by various firms of their institutional activities in selected areas of application where nanoscience can have a deep impact. There was also the possibility for sample testing by the participants. *Tutorial lectures were delivered at the School, addressing general and basic questions about nanotechnology, such as what they are, how does one go about them, what purposes can they serve.* In tutorial sessions the nature of nanotechnology, the instruments of current use in its characterizations and the possible applicative uses were *described at an introductory level*.

The Conferences covered a large range of topics of current interest in nanoscience and nanotechnology, including aerospace, defence, national security, biology, medicine, electronics. This broad focus is reflected in the decision to publish different areas of application of these technologies in different volumes. The present set of notes results in particular from the participation and dedication of prestigious lecturers, such as Andrzej Huczko, Nicola Pugno Alexander Malesevic, Stefano Bellucci. All lectures were subsequently carefully edited and reworked, taking into account the extensive follow-up discussions at the Conferences.

A tutorial lecture by *Andrzej Huczko* and collaborators (Warsaw University, Poland) shows how different carbon and ceramic nanostructures (nanotubes,

nanowires, nanofibres, nanorods, and nanoencapsulates) have a great potential for improving our understanding of the fundamental concepts of the roles of both dimensionality and size on physical properties, as well as for many potential applications. *Stefano Bellucci* and *Pasquale Onorato* (INFN-LNF, Italy) engaged in an extensive review of the transport properties in carbon nanotubes, encompassing a description of the electronic structure from graphene to single-wall nanotubes, the quantum transport in such systems, as well as the description of experimental evidence of superconductivity in carbon nanotubes and the corresponding theoretical interpretation. *Nicola Pugno* (Turin Polytechnic University, Italy), in the first of his contributions, goes about new laws to design futuristic self-cleaning, super-adhesive and releasable hierarchical smart materials, as well as large invisible cables, based on carbon nanotube technology. He also reviewed the mechanical strength of nanotubes and megacables, with an eye to the challenging project of the carbon nanotube-based space elevator megacable. In this second contribution, he outlined the role on the fracture strength of thermodynamically unavoidable atomistic defects with different size and shape, both numerically (with *ad hoc* hierarchical simulations) and theoretically (with quantized fracture theories), for nanotubes and nanotube bundles. Focusing on graphitic allotropes, the chapter by *Stefano Bellucci* and *Alexander Malesevic* tries to give a taste of the widespread implications carbon nanostructures have on research and applications, starting from an historical overview, followed by a discussion of the structure of carbon nanotubes and graphene, over viewing several different synthesis techniques and illustrating the physical properties of these innovative materials, before summarizing their broad range of applications.

In concluding this effort, I wish to thank all lecturers, and especially those who contributed to the present second volume in this series, as well as speakers and participants to the n&n 2006 and n&n 2008 Conferences, for having contributed to create a pleasant and productive atmosphere, fostering the settling of pervasive collaborative spirit and pedagogical drive. I am confident that this first set of lectures, in turn, will provide an opportunity for those who are just now beginning to get involved with nanoscience and nanotechnology, allowing them to get contacts and prime, up-to-date information from the experts. I also wish to acknowledge the enduring dedication and caring support of my wife Gloria and our great daughters Costanza, Eleonora, Annalisa, Erica and Maristella, which allowed me to put this volume together.

Frascati, Italy Stefano Bellucci
May 2010

References

1. S. Bellucci (ed.), in Proceedings of the School and Workshop on Nanotubes & Nanostructures 2000, Santa Margherita di Pula (Cagliari), Italy, Italian Physical Society, Bologna, Italy, 2001, ISBN 88-7794-291-6, 24 Sept – 4 Oct 2000

2. M. De Crescenzi, S. Bellucci (eds.), *J. Phys. Condens. Matter* **15**(34), (3 Sept 2003)
3. S. Bellucci (ed.), *J. Phys. Condens. Matter* **18**(33), S1967–S2238 (23 Aug 2006)
4. S. Bellucci (ed.), *J. Phys. Condens. Matter* **19**(39), 390301–395024 (3 Oct 2007)
5. S. Bellucci (ed.), *J. Phys. Condens. Matter* **20**(47), 470301, 474201–474214 (26 Nov 2008)
6. S. Bellucci (ed.), *Nanoparticles and Nanodevices in Biological Applications. The INFN Lectures- Vol I*, vol 4, (Springer, Berlin Heidelberg) pp. 1–198, ISBN: 978-3-540-70943-5
7. S. Bellucci (ed.), Guest Editorial: Selected Papers from the INFN-LNF Conference on Nanoscience and Nanotechnology, Special section of *J. Nanophoton.*, **3**, 031999 (2009); doi:10.1117/1.3266501

Contents

Contributors

Piotr Baranowski Laboratory of Nanomaterials Physics and Chemistry, Department of Chemistry, Warsaw University, 1 Pasteur, 02-093 Warsaw, Poland, piobar@chem.uw.edu.pl

Stefano Bellucci INFN, Laboratori Nazionali di Frascati, P.O. Box 13, 00044 Frascati, Italy, stefano.bellucci@lnf.infn.it

Michał Bystrzejewski Laboratory of Nanomaterials Physics and Chemistry, Department of Chemistry, Warsaw University, 1 Pasteur, 02-093 Warsaw, Poland, mibys@chem.uw.edu.pl

Andrzej Huczko Laboratory of Nanomaterials Physics and Chemistry, Department of Chemistry, Warsaw University, 1 Pasteur, 02-093 Warsaw, Poland, ahuczko@chem.uw.edu.pl

Hubert Lange Laboratory of Nanomaterials Physics and Chemistry, Department of Chemistry, Warsaw University, 1 Pasteur, 02-093 Warsaw, Poland, lanhub@chem.uw.edu.pl

Alexander Malesevic VITO Materials, Flemish Institute for Technological Research, Boeretang 200, BE-2400 Mol, Belgium; Laboratory of Solid-State Physics and Magnetism, Katholieke Universiteit Leuven, Celestijnenlaan 200 D, BE-3001 Leuven, Belgium, malesevic@mac.com
Present address: BrainLAB AG, Kapellenstrasse 12, Feldkirchen, D-85622, Germany

Pasquale Onorato INFN, Laboratori Nazionali di Frascati, P.O. Box 13, 00044 Frascati, Italy; Dipartimento di Fisica Alessandro Volta, Università degli Studi di Pavia, Pavia, Italy, onorato@fisicavolta.unipv.it

Nicola M. Pugno Department of Structural Engineering and Geotechnics, Politecnico di Torino, Corso Duca degli Abruzzi 24, 10129 Torino, Italy, nicola.pugno@polito.it

Formation and Characterization of Carbon and Ceramic Nanostructures

Andrzej Huczko, Michał Bystrzejewski, Hubert Lange, and Piotr Baranowski

Abstract Different carbon and ceramic nanostructures (nanotubes, nanowires, nanofibres, nanorods, and nanoencapsulates) have great potential for improving our understanding of the fundamental concepts of the roles of both dimensionality and size on physical properties, as well as for many potential applications. Carbon nanotubes (CNTs) were produced in carbon arc plasma using different starting carbons, as the anode material. Low-graphitized carbons (including carbon black) proved to be much more efficient comparing to the regular graphite material. The optical emission and absorption spectroscopy was used for spectral diagnostics of the carbon arc. Carbon arc was also used to produce carbon onions containing magnetic nanocrystallites (Fe and magnetic alloys) in the core. The process was optimized and the procedure to isolate encapsulates was elaborated. Carbon nanocapsules containing Fe were also obtained via combustion synthesis from mixtures NaN_3-C_6Cl_6-Ferrocene. This technique also proved to be very efficient to produce silicon carbide nanowires from Teflon (PTFE) and different reductants ($CaSi_2$, Si). The protocol to isolate and efficiently purify the final product (up to 98 wt%) was proposed.

Synthesis of Carbon Nanotubes in Carbon Arc

We have studied the CNTs synthesis by using the arc discharge technique as well non-equilibrium plasmas, e.g., [1–12]. The aim of those studies was also the plasma diagnostics based mainly on optical emission spectroscopy (OES), e.g. [13–18].

In this work we summarize our recent research in which the influence of carbon electrode structure on effectiveness of single-walled carbon nanotubes (SWCNTs) formation in the carbon arc discharge under the presence of catalysts

A. Huczko (✉)
Laboratory of Nanomaterials Physics and Chemistry, Department of Chemistry, Warsaw University, 1 Pasteur, 02-093 Warsaw, Poland
e-mail: ahuczko@chem.uw.edu.pl

S. Bellucci (ed.), *Physical Properties of Ceramic and Carbon Nanoscale Structures*, Lecture Notes in Nanoscale Science and Technology 11,
DOI 10.1007/978-3-642-15778-3_1,

was investigated. This study was undertaken after Zhao et al. [19] had shown that using the arc discharge with Fe-doped graphite anode generated in Ar-H_2 atmosphere one can obtain macroscopically oriented web-like product which appeared to be very rich in high quality SWCNTs. The authors showed also that the as–obtained bulk product can be easily purified from catalyst by a liquid-phase process on a macroscale [20]. In fact, Fe and other transition metals, e.g. Co, has already been used for SWCNTs synthesis via arc discharge method for a long time [21, 22]. However, we did not succeed while trying to reproduce this process. Since all the experimental conditions were nearly the same, including the origin of the electrodes (Toyo Tanso Comp.), the only reasonable explanation of the high process yield seemed to be related to different properties of the electrode materials. Indeed, it was established that the electrodes were of different batches and different preparation receipts. Thus, the diversity could be related to the electrodes structure in a nanometric scale. To elucidate the mentioned mysterious effect a number of tests were performed with different anode materials and gas atmospheres. The experiments and results are discussed below.

Along with CNTs synthesis, we extended our research by using optical emission (OES) and absorption (OAS) spectroscopy for the diagnostics of carbon arc.

Experimental

The experimental system has been described in details elsewhere [23]. The most important feature of our arc reactor is a possibility of automatic control of the arc gap within 1 and 2 mm and its position on the optical axis of a system for plasma spectroscopy measurements. The pressure was also controlled in the reactor chamber during the synthesis. Different types of Fe-doped (ca. 1 at.% Fe) electrodes were tested in the process of SWCNTs synthesis which was carried out in Ar, Kr, Xe, Ne and N_2-H_2 (40 vol%) gas mixtures. First, all the starting electrodes differed with degree of graphitization, namely with the size of primary particles. The XRD patterns of the electrode materials are shown in Fig. 1. Well- and medium-graphitized

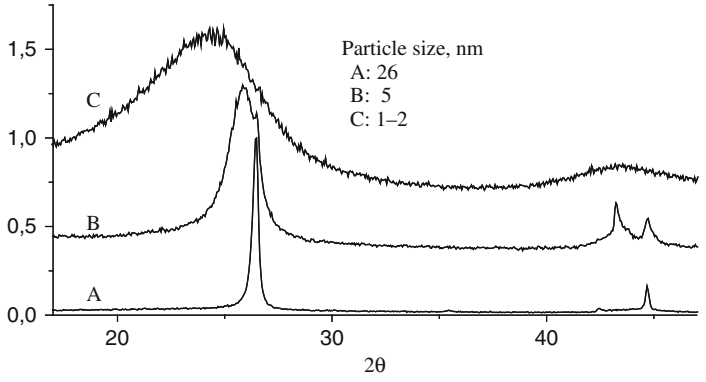

Fig. 1 XRD patterns of starting carbon electrodes

and amorphous electrodes, A, B and C, respectively, doped with Fe, Ni or Co catalysts were sublimated in the arc. The electrodes C were home made from industrial carbon black (IRB) mixed with a tar pitch and catalysts. The electrodes were baked at 1,300 K.

Both A and B electrodes were Toyo Tanso Comp. (Japan) products. The profile of XRD curve B in Fig. 1 points to a fact that this electrodes is composed of a mixture of low as well highly graphitized carbon. The arc discharge current varied between 10 and 50 A and pressure in the reactor chamber was kept constant at about 300 mb.

The morphology and characteristics of the carbon products were investigated using SEM, TEM and Raman spectroscopy techniques.

The plasma diagnostics was performed by a combined optical emission and absorption spectroscopy. Both techniques were applied to 0–0 bands of d $^3\Pi_g$–a $^3\Pi_u$ and B $^2\Sigma^+$–X $^2\Sigma^+$ spectra of C_2 and CN radicals, respectively. The absorption spectroscopy was also used for the detection of iron atoms.

Since our OES method has been frequently used and described in details elsewhere [15–17, 24], here we highlight only the most important points of the OAS method, which we began to use recently. The aim of OAS was to detect CN, C_2 radicals and Fe atoms in the arc plasma periphery, i.e. in the so-called dark plasma zone. To the best of our knowledge such measurements related to carbon arc plasma under condition of carbon nanostructures formation have never been performed so far. Shortly, the method is based on a calculation of respective absorption spectra assuming different temperatures and optical depths. The latter ones were expressed by column densities.

The spectral absorption is define as $A_\nu = 1 - \exp(-\kappa_\nu l)$, where $\kappa_\nu = \sum \kappa_\nu^J$ is the spectral absorption coefficient at a given frequency ν, which is a function of temperature and column density of the absorbing species. The summation obviously covers contribution from all the rotational line of components situated in the vicinity of a given frequency ν. The calculations were performed taking into account collision and Doppler broadening by the use of the Voigt profile. The as-calculated absorption spectra were convoluted with the Gaussian apparatus function of 0.023 nm in width at the half-maximum. An examples of a simulated CN absorption spectrum, assuming temperature equal to 3,500 K and column density 10^{15} cm^{-2}, along with an experimental spectrum are shown in Fig. 2, *left* and *right*, respectively.

The absorption was recorded on the background of a continuum spectrum emitted by a Xe arc lamp. Because of a light modulation caused by interference at the protected window located in front of a CCD detector, both experimental and calculated spectra had to be smoothed within the 0.052 nm spectral window. The as-filtered spectra are represented by thick lines in Fig. 2. The absorption at maximum 0–0 band served as a measure of CN column density. Examples of absorption growth curves, including 1–1 band head, for two temperatures 2,000 and 4,000 K are shown in Fig. 3.

Let us note that the absorption at the 0–0 band head does not vary much with temperature and therefore can be used for CN(v = 0) column density determination

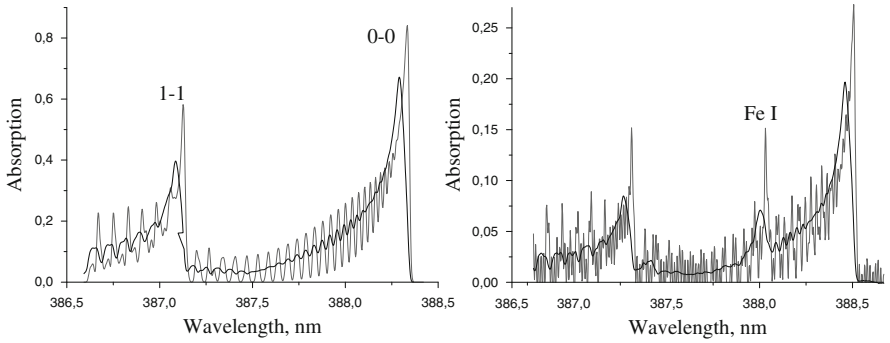

Fig. 2 Calculated (T = 3,500 K, nl = 10^{15} cm^{-2}) and experimental spectra of CN(B $^2\Sigma^+$ X $^2\Sigma^+$)

with a high precision. On the other hand a significant variation of the absorption at 1–1 band head can be used for temperature determination through the ratio of the absorption at 1–1 to 0–0 band heads. This ratio, however, changes also with the column density. Therefore temperature can be derived on the basis of the ratio only in the case of a sufficiently weak absorption. The same procedure for detection of C_2 by OAS was applied in [25].

In Fig. 2 (*right*) one can also find an absorption line at 387.8 nm which corresponds to absorption by Fe I atoms in the a $^5D_2$ state. There are also some other iron absorption lines and one of them, namely at 388.62 nm, which appears not to be overlapped by any neighboring lines, was chosen for quantitative Fe I (a $^5D_3$) measurements. For such a purpose a similar absorption growth curves were constructed.

It is worth to mention here that all such calculations can be quite easy performed by using the Matlab software.

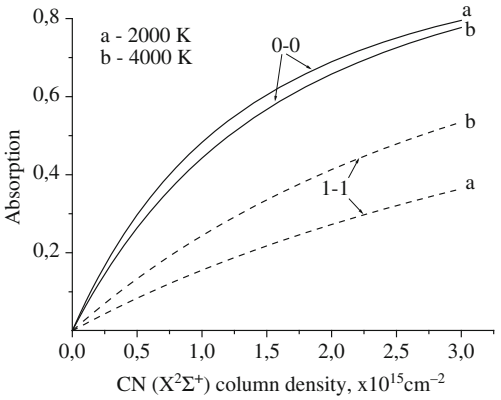

Fig. 3 Absorption growth curves at 0–0 and 1–1 CN(X $^2\Sigma^+ \rightarrow$ B $^2\Sigma^+$) band heads

Results and Discussion

Carbon Nanotubes

As it was already mentioned, the SWNTs were produced with a high yield when the electrodes with the smallest primary particles, i.e. the electrode B and C (Fig. 1) were arc sublimated [12]. Then the product was almost entirely in a web-form. Such a web was obtained in Ar-H_2 and in N_2-H_2 gas mixtures when electrodes B and C contained Fe catalyst. The photos of the web are shown in Fig. 4.

Let us note that the very fine web starts growing just at the electrode tip. It can be on the cathode as well on the anode, *left* and *right* photos in Fig. 1, respectively. The arcing in Ar-H_2 gas mixture of the electrode A, i.e. well graphitized one, and therefore having the largest primary particle, resulted only in a rubber-like soot. Examples of TEM images of the web and soot are shown in Fig. 5. Evidently the product obtained from the well-graphitized electrode A contains mostly soot and graphite nanoparticles with embedded catalyst, while the web-like product from the electrode B is rich into CNTs. Comparative SEM and TEM images of products in Fig. 4 are shown in Fig. 6. The bulk product formed from more amorphous carbon, i.e. using carbon black (C), seems to be slightly more fine and pure.

Other catalysts from the transition metal group (Co and Ni) were also tested for SWCNTs formation by Ar-H_2 arc discharge using electrodes prepared of carbon material C. It follows from the work by Zhao et al. [19] that such catalysts or their binary mixtures are not suitable for SWCNTs production by Ar-H_2 arc plasma. However, it is very likely that the authors used well graphitized electrodes. We found that although a macroscopic web was not formed, the final product appeared in a form of a fine membrane which could be peeled off from the reactor lid and contained SWCNTs shown in Fig. 7.

Fig. 4 Photograph of web-like products from two tests performed with electrode B (N_2-H_2 atmosphere) and C (Ar-H_2 atmosphere), respectively. Catalyst: Fe

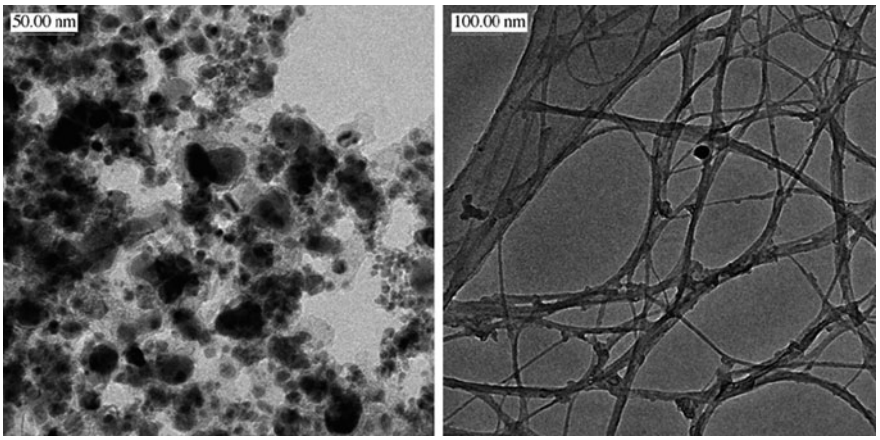

Fig. 5 TEM images of products obtained from electrode A (*left*) and B (*right*) during arc discharge in Ar–H_2 gas mixture. Arc current: 50 A and pressure: 260 kPa. Catalyst: Fe

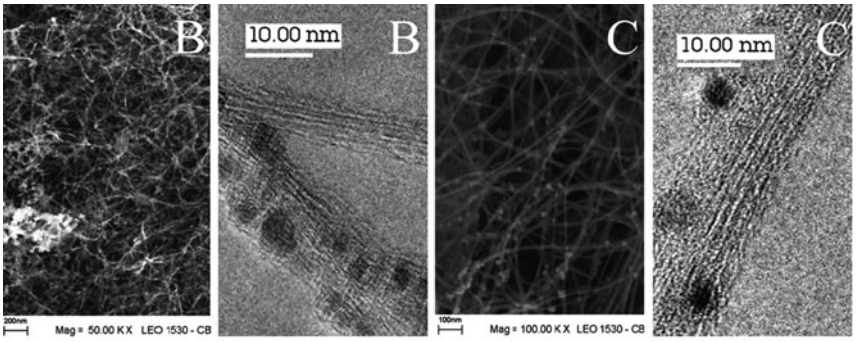

Fig. 6 SEM and TEM images of products obtained from electrodes B and C during arc discharge in Ar–H_2 gas mixture. Arc current: 50 A and pressure: 260 kPa. Catalyst: Fe

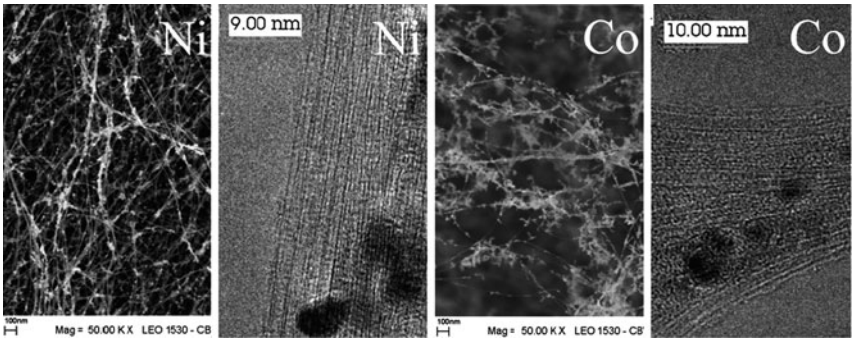

Fig. 7 SEM and TEM images of products obtained from electrode material C prepared (IRB) and Co- and Ni- catalysts

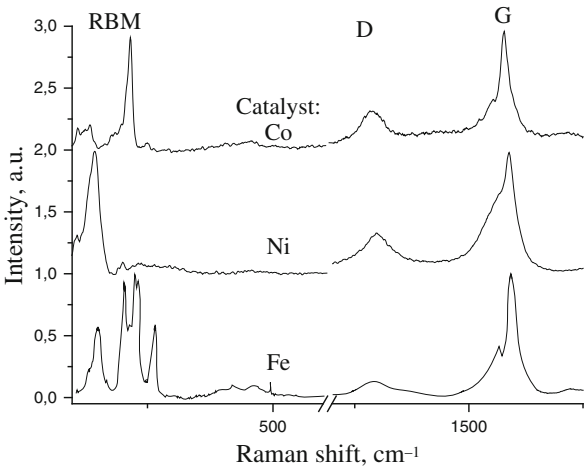

Fig. 8 Raman spectra (laser 780 nm) of carbon products obtained using electrode C doped with various catalysts and arced in Ar-H_2 gas atmosphere

The presence of RBM bands as well as the shape of G bands in Raman spectra (Fig. 8) clearly point to SWCNTs [24]. In this and following Raman spectra the RBM bands were normalized as for high frequency D and G bands. It is worth to note that using different catalysts one can influence the diversity in diameters of SWCNTs. Under the presence of Co and Ni one breathing band for a particular catalyst is in the resonance with the laser light (780 nm) while in the case of Fe-catalyst there are at least four RBM bands resulting from the resonance with SWCNTs of different diameters [24].

The only explanation of the effect of products diversity resulting from the electrode materials under consideration seems to be connected with the effect of sublimation. One can suspect that along with the simple carbon species, e.g., $C_{n=1,2,3,..}$ also bigger, e.g. graphene fragments including primary particles are leaving the anode surface and undergo further thermal break-up just to a desire size and form. If so, the bigger graphite particles, i.e. arc ablated from the electrode A, leave the plasma zone before their fractionation to CNT precursor occurs. Assuming such a hypothesis, a number of tests were performed under different gas atmospheres e.g., Kr- and Xe-H_2 using the electrode A. Thus, in the environment of heavier buffering noble gases the diffusion of carbon particles should be, to some extend, retarded. Also, inelastic collisions between carbon agglomerates and heavier noble gas species are more effective. As expected, by replacing Ar by Kr (or Xe) we were able to obtain products which contained SWCNTs. The Raman spectra in Fig. 9 show drastic changes in the observed bands when Kr and Xe was used instead of Ar. In this and others Raman spectra the RBM bands were magnified.

Another way to overcome the problem of SWCNTs synthesis staring from the well-graphitized electrode seemed to be the use of an active gas instead of the noble gas. The most suitable seems to be nitrogen. It has already been shown by Zho et al. [20].

TEM images and Raman spectra of products obtained from the electrode A and B containing Fe-catalyst and using arc discharge in N_2-H_2 gas mixture are shown in

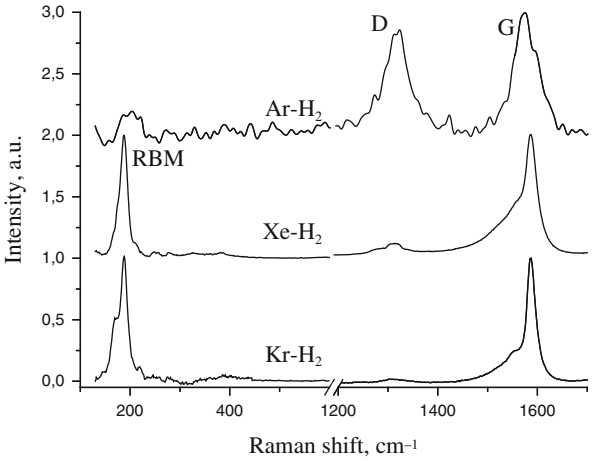

Fig. 9 Raman spectra of carbon products obtained during arc discharge in different 8gas atmospheres and using electrode A

Figs. 10 and 11, respectively. TEM images clearly show bundles of SWCNTs. The Raman spectra also confirm that the bulk product from the well graphitized material (A) contains SWCNTs. However, it follows from the ratio of G/D bands that there are still more amorphous phase that in the case of the electrodes B subjected to the arc discharge in N_2-H_2

On the basis of RBM bands one can draw a conclusion that SWCNTs of different diameter distributions result from both electrodes in N_2-H_2 arc plasma.

Non-conventional tests were performed to show that indeed the graphitization degree of the electrode material plays a crucial role in SWCNTs synthesis by arc

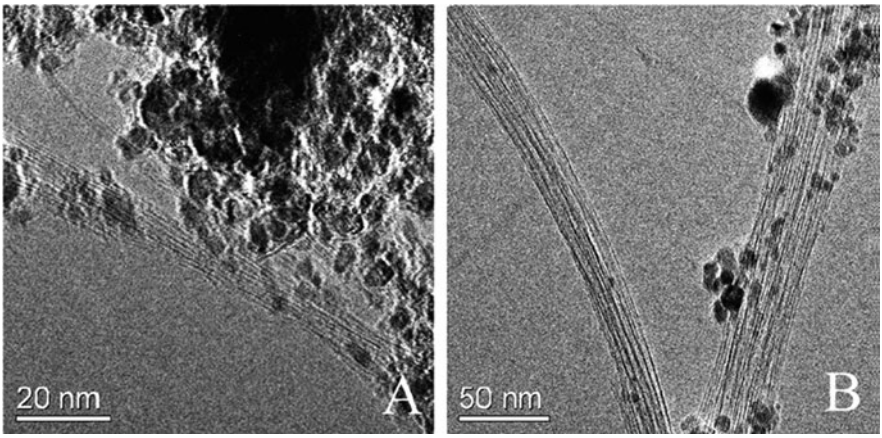

Fig. 10 TEM images of products obtained from electrodes A (*left*) and B (*right*) (Fe-catalyst) in N_2-H_2(90/5) at arc current 40 A and pressure 300 mb

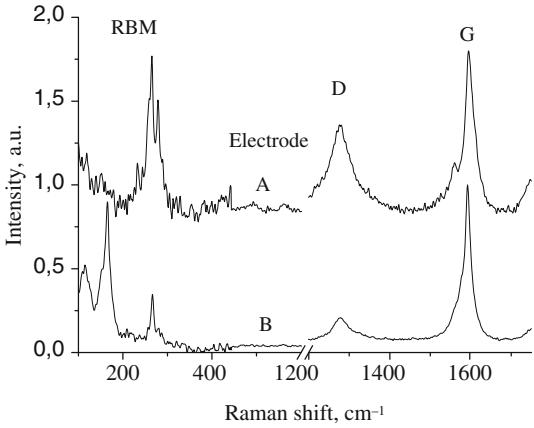

Fig. 11 Raman spectra of products after arcing electrodes A and B (Fe-catalyst) in N_2-H_2 arc discharge

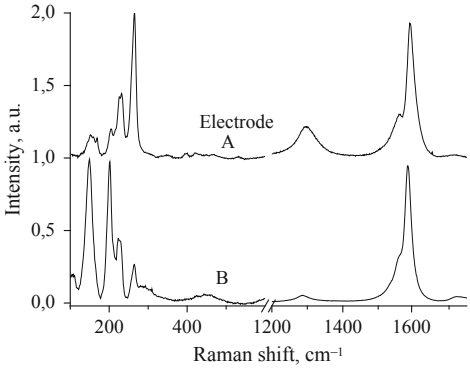

Fig. 12 Raman spectra of products obtained from electrode A and B (Fe-catalyst) with reverse polarity of the electrodes in Ar – H_2 arc discharge

discharge technique. The electrodes A and B were used as the cathode in the Ar – H_2 arc discharge. The anode was made of pure graphite with 1 cm in diameter to prevent its sublimation. It turned out that one could collect a web-like products originated from both, A and B-type electrodes. The carbon web was rich in SWCNTs. The respective Raman spectra confirming it are shown in Fig. 12.

An explanation of the observed effect becomes obvious taking into account that carbon species leave the cathode surface mostly as a result of the so-called cathode sputtering process which is triggered by ionized argon species. During such interaction a fractionation of bigger primary carbon particles can take place. However, recently it was found that the decisive role in SWCNT formation plays not only the size of primary particles but also the electrode density [25].

Carbon Arc Plasma Diagnostics

The OES was used to estimate the temperature and C_2 radical contents across the arc discharge [11]. The aim was a comparison of the arc behavior when two electrodes

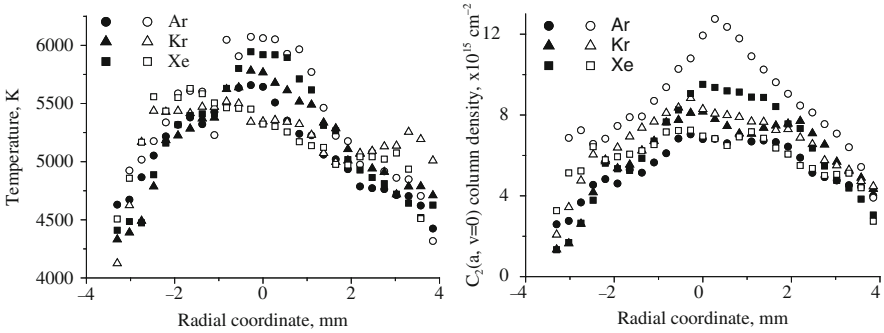

Fig. 13 Average temperature and column density distributions of C_2(a, v=0) radicals across arc discharge generated in Ar-, Kr- and Xe – H_2 gas mixtures using electrodes A and B (solid and open markers, respectively) doped with 1 at.% Fe. I = 50 A

A and B were arced under different gas mixture atmospheres. It follows from the results of the OES measurements shown in Fig. 13 that the average plasma temperature along the arc radius is about 5,500 ±250 K and drops to about 4,000 K at the plasma periphery. The C_2 content does not differ very much regardless of the gas atmospheres and anode material, especially at the plasma edge, where CNTs are starting to grow. Therefore one can expect that the content of other 'small' carbon species resulting from the equilibrium composition (LTE) of carbon gas is also similar. Since there is no evident correlation between C_2 radical concentration in the arc plasma zone and SWCNT yield one can assume that there must be also some bigger carbon particles influencing the CNTs formation in the vicinity of the arc zone.

Probably the semi-amorphous graphite (B) or soot-like material (C) are more efficient sources of such small carbon blocks. The primary graphite particles leaving the well-graphitized electrode during the arc ablation process can also become enough small for SWCNTs formation under conditions of longer residence times in the plasma zone. Such a situation takes place when Ar is replaced by heavier noble gas as, e.g. Kr or Xe. It can also be accomplished using more active gas like nitrogen. Then, due to surface etching by active nitrogen species the carbon particles will change their size.

Between numerous possible intermediate carbon/nitrogen/hydrogen species, the C_2 and CN radicals are the ones that can be quantitatively measured by using conventional OES and OAS. The average temperature distributions across the arc gap for two arc currents 20 and 40 A are shown in Fig. 14 (*left*). The temperature profiles were evaluated using the C_2 emission band.

The respective C_2 column density distributions are shown also in Fig. 14 (*right*). Let us note only that there is a strong influence of arc current on C_2 radical content. At current 20 A C_2 column density was almost on a verge of its detection by the self-absorption method. Similar temperatures and C_2 column densities were obtained when electrode B was arced under the same conditions.

Examples of the experimental intensity distributions within the CN($B\,^2\Sigma^+ X\,^2\Sigma$, 0–0) emission band are shown in Fig. 15 (*left*). The spectra where normalized

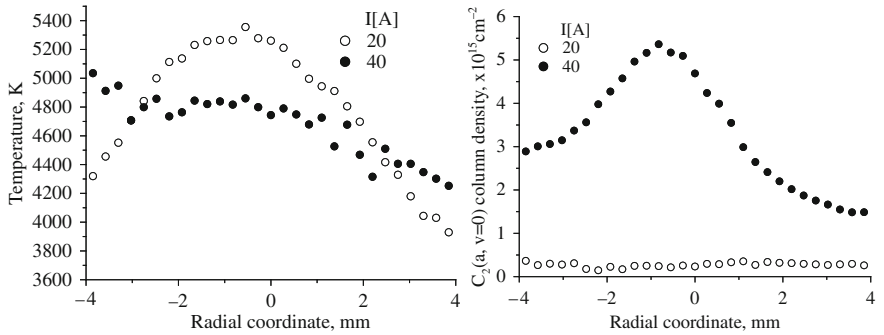

Fig. 14 Average temperature and column density distributions of C_2(a, v=0) radicals in arc plasma generated in N_2– H_2 gas mixture at arc current 20 and 40 A and using electrodes A

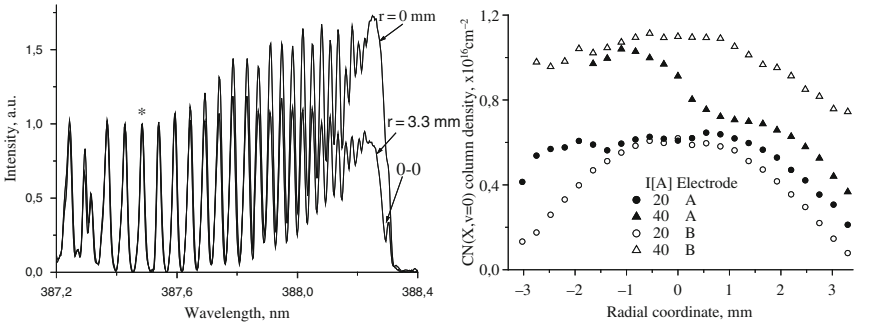

Fig. 15 Emission CN(B-X, 0–0) spectra at different radial position (I = 20 A, electrode B) and average column density distributions of CN(X, v=0) radicals across arc discharge generated in N_2-H_2 (95/5) gas mixtures using carbon electrodes A and B (solid and open markers, respectively)

against the rotational line marked with an asterisk. A very strong self-absorption effect appears in the position of the P(0–0) band head, where many rotational components lines overlap and cause disappearance of the band head, especially in the case of the emission along the plasma radius (r = 0). This has already been observed when influence of nitrogen on formation of fullerenes was investigated [26]. In order to find the CN(X, v = 0) column density across the arc a very similar procedure as for C_2 radicals was applied [27]. The column density distributions of CN(X, v = 0) across the arc plasma are shown in Fig. 15 (*right*). In contrast to C_2, the CN species are much more spread beyond the arc and are abundant at the plasma edge.

A transition from the column density to the average local concentrations can be simply made by dividing column densities by the radial coordinates of the radicals, which for CN are much greater. In order to find the spatial range for both radicals OAS was applied. The absorption measurements covered radial coordinate from 8 mm to 17 mm, i.e. the space where most of species are already in their ground electronic states. Nevertheless, a very weak emissions by C_2 and CN radicals were still detectable. The C_2 emission band was free of self-absorption, while CN band

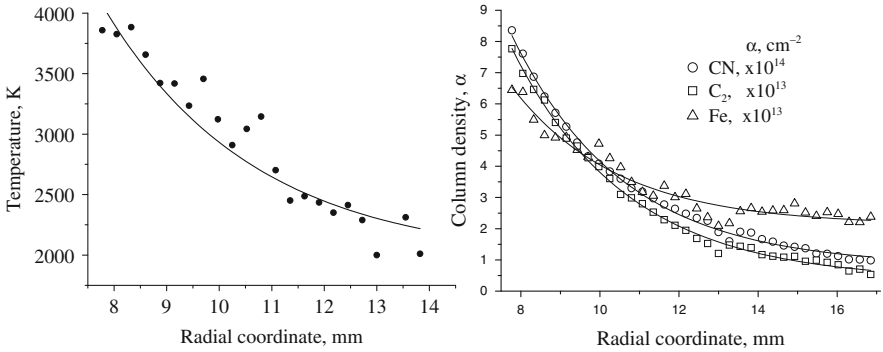

Fig. 16 Radial distributions of temperature and column density of CN(X, v=0), C_2(a,v=0) and Fe I(a $^5D_3$) in 'dark' zone of arc discharge in N_2-H_2 (166-106, mb). Arc current: 40 A, Anode: electrode A

was still affected by this phenomenon. The OAS measurements confirmed much stronger absorption by CN than C_2 in this dark zone. Radial average temperature distributions and column density of C_2 and CN in this zone of the arc plasma for the electrode A are shown in Fig. 16. The temperature was determined from the intensity distribution in the rotational structure of the 0–0 Swan absorption band. The temperature decreases exponentially from about 4,000 to 2,000 K. The value at 8 mm is in quite good agreement with that obtained from the emission band at the arc plasma edge shown in Fig. 14. The column densities of C_2 as well CN also match the values resulted from the self-absorption consideration. The contents of these species decreases exponentially with the radial coordinate with different, however, rate. Generally lower contents of C_2 follow also from the thermodynamic considerations. At wide range of temperatures, whenever nitrogen is in a much excess relatively to the carbon vapor pressure, the equilibrium concentration of CN radicals will be at least one order higher than C_2.

In Fig. 16 the column densities of iron atoms are also shown. It is worth to notice that the spreading range of iron atoms is much higher than the radicals under consideration. Therefore, one can assume that also some nanometric iron clusters necessary for catalytic growth of CNTs exist far away from the arc.

In the light of these data it would appear that there are suitable conditions for catalytic CNTs formation. The study is under way, however, to explain much lower yield, specially in Ar-H_2 atmosphere.

Synthesis of Carbon Encapsulated Magnetic Nanoparticles in Carbon Arc and by SHS Route

The discovery of fullerenes and carbon nanotubes accelerated a worldwide research into nanocarbon materials. Recently, the synthesis of novel and interesting structures was reported, e.g., endohedral fullerenes [28], filled nanotubes [29], onions

[30], pea-pods [31], nanohorns [32], and carbon-encapsulated magnetic nanoparticles (CEMNPs) [33]. A considerable attention has been paid to CEMNPs due to their fascinating properties. Magnetic nanoparticles exhibit unique properties (e.g., higher coercive force and retentivity than bulk materials) but their practical applications are still strongly limited [34]. Magnetic nanoparticles are very sensitive to oxidation and agglomeration because of their large specific surface area and high chemical activity. Under ambient conditions, rapid oxidation of the nanoparticle surface occurs, leading to the creation of thin oxide layer that dramatically changes the particle properties. Spontaneous agglomeration of nanoparticles into larger clusters is another problem that hinders the processing of such nanomaterials. In order to preserve their specific magnetic properties and to protect nanoparticles from both oxidation and agglomeration, the application of the encapsulation procedure has been proposed. The encapsulation of nanoparticles has been successfully employed by using carbon [35, 36], BN [37], silica [38], and organic polymers [39]. Carbon and BN are the most stable coatings which can perfectly isolate the encapsulated magnetic nanoparticles from the external environment.

CEMNPs are composite nanomaterials with a core-shell structure. The core is a metal nanocrystallite (5–50 nm in the diameter) and the shell consists of several to tens graphene layers. Carbon-encapsulated magnetic nanoparticles are stable in a strong acid and in high temperature oxygen-free environment [40]. Unique properties of CEMNPs were also reflected in their prospective applications: (1) magnetic data storage [34], (2) catalysis [41], (3) xerography [42], (4) magnetic resonance imaging [43], and (5) biomedical applications (drug and gene delivery systems, disease detection, cancer therapy, rapid toxic cleaning) [44].

Recently, we have shown [45–47] that CEMNPs have a great potential for the use in environmental protection. Carbon encapsulates containing Fe nanoparticles are capable to adsorb various toxic heavy metals (e.g., Cd, Cu, Co). Their sorption performance is better in comparison to activated carbons. Importantly, the presence of magnetic core in CEMNPs makes them fully mobile and facilitate their separation from the cleansed solution.

The synthesis of CEMNPs is one of our major current research activities. So far, the synthesis has been successfully accomplished by using carbon arc plasma [48–54], low energy gaseous lasers [55] and combustion synthesis [56–61]. We have also adapted a RF plasma technique for the large scale fabrication of CEMNPs [62, 63]. In this approach we reached the production level, which exceeded 500 g/h. Our recent findings show that oxygen added to the reactants in RF plasma synthesis of CEMNPs exclusively etches by-products (e.g., amorphous carbon). This results in more pure product formation with better magnetic characteristics [64].

The self-propagating high-temperature synthesis (SHS) is a combustion process of any chemical character that results in the formation of valuable condensed products for practical purposes [65]. The research on SHS was pioneered in the 1960s of twentieth century by Merzhanov et al. in the Soviet Union [66, 67] who studied i.e., the combustion of cylindrical ceramic compacts, which consisted of e.g. a Ti-B mixture. Several years later the group from University of California in Davis led by Munir used SHS technique e.g., to produce Ni-Al alloys [68], TiB_2 [69] and other

refractory compounds [70]. The combustion synthesis utilizes the heat released by the highly exothermic reactions between the precursor components. In the majority of SHS processes, the combustion front, forming a smooth surface between reactants propagates layer-to-layer with a constant velocity. This is a unique technology for preparing advanced ceramic materials including the most valuable various refractory compounds (borides, carbides, nitrides, silicides, and the like) which, in fact are not easily produced by conventional production methods.

Carbon Arc Formation of CEMNPs

The goal of our recent studies was to synthesize CEMNPs filled with a hard magnetic phase with a stoichiometry of $Fe_{14}Nd_2B$ [48–54]. Fe-Nd-B permanent magnets, which were developed in 1984, have become a major hard magnetic material used in electrical devices. Theoretical considerations predict that their magnetic performance will be higher if the grain size will be below 100 nm (single-domain material) [71]. Thus, the encapsulation in carbon shells seems to be an excellent rout to decrease the grain size, and to avoid the agglomeration and oxidation of the as-formed magnetic nanoparticles.

Experimental

Experiments were carried out using the same arc reactor system as for CNTs synthesis [23]. The arc discharge was generated in helium under different pressures (Table 1). The drilled anode was filled with a mixtures of $Fe_{14}Nd_2B$ and graphite powder (Table 1). The electrodes were arc-sublimated and the products were collected in the form of a cathode deposit and soot. Boiling in 2 M HCl and washing with distilled water and ethanol with subsequent drying in open air resulted in the removal of non-encapsulated metals and carbides from the products. The as purified final products were analyzed by electron microscopy (SEM, TEM), phase analysis (XRD), thermogravimetry (TG), Raman spectroscopy and magnetic measurements.

Results and Discussion

It follows from SEM images (Fig. 17) that soot and cathode deposit are mostly composed of uniform spherical nanoparticles with the diameter well below 100 nm.

Table 1 Experimental parameters and anode composition [52]

Test	Voltage [V]	Current [A]	Pressure [mbar]	Erosion rate [mg s^{-1}]	$Fe_{14}Nd_2B$ [wt%]
1	17	83	133	7.5	27
2	19	61		2.5	42
3	27	79	600	9.8	27
4	28	65		9.6	42

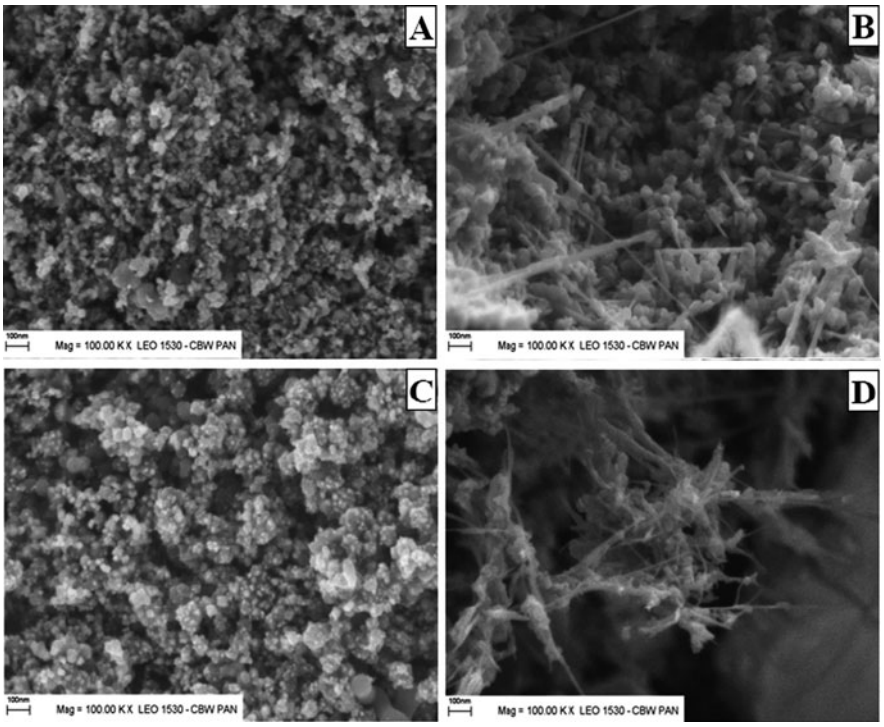

Fig. 17 SEM images of purified products: (**a**, **c**) soot from test 2 and 4, respectively; (**b**, **d**) cathode deposit from test 2 and 4, respectively [52]

The products deposited on the cathode occasionally contained multi-walled carbon nanotubes (as confirmed by TEM). Detailed morphology has been investigated by TEM microscopy (representative images are shown in Fig. 18). The nanoparticles in the soot have generally an oval shape while those in the cathode deposit are polyhedral. Size of the metallic cores is between 20 and 50 nm independently on pressure and anode composition (local EDX analysis proved that the cores are composed of Fe, Nd and B). Thickness of the carbon coating was found to be between 1 and 20 nm (the coating includes up to 58 graphene layers). The interlayer spacing between carbon layers surrounding the metallic nanoparticles is between 0.36 and 0.37 nm, these values being higher of that of a well crystallized bulk graphite (0.3354 nm). This increase is related to the presence of defects in the carbon coatings (penta- and heptagonal rings), which are necessary to introduce the curvature into the graphene layer. The crystallinity of carbon coating of the cathode nanoparticles is higher in comparison to those in the soot. This is due to the fact that the latter ones are formed during much more rapid quenching conditions. The temperature of the cathode deposit remains very high during the arcing (ca. 3,000 K). Therefore heating of CEMNPs in a cathode deposit will favour the graphitization of the carbon coatings.

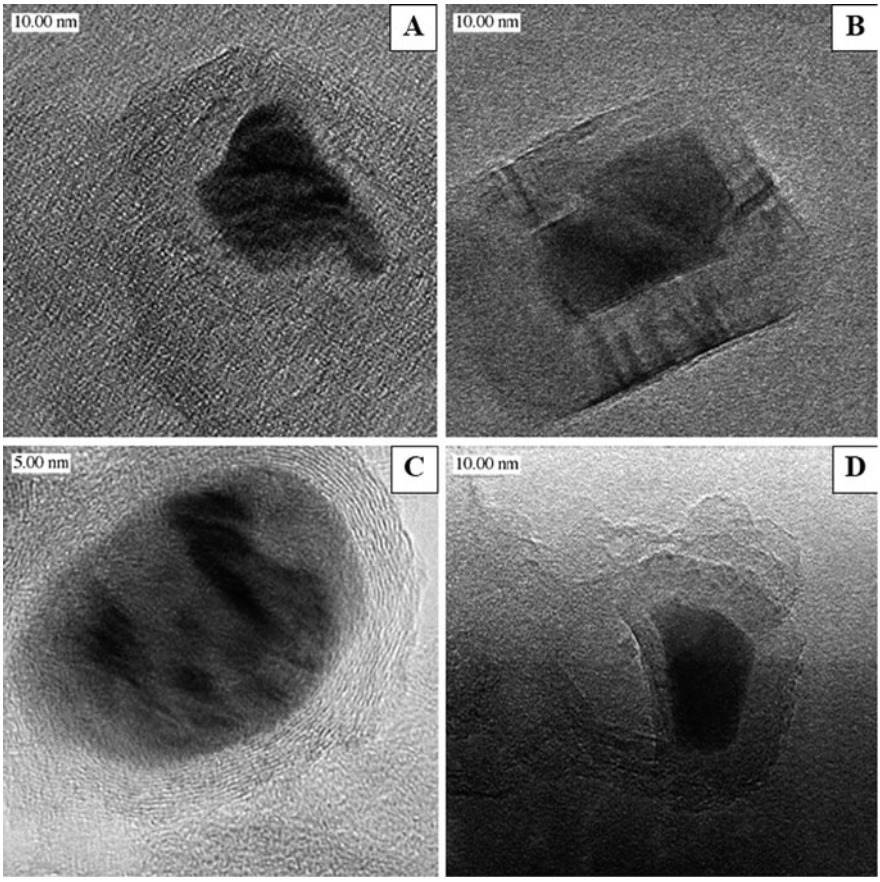

Fig. 18 TEM images of purified products: (**a**, **c**) soot from test 1 and 3, respectively, (**b**, **d**) cathode deposit from test 1 and 3, respectively [52]

X-ray diffraction spectra were recorded to study the phase composition of the encapsulated nanoparticles. XRD diffractograms showed turbostratic carbon only and occasionally weak signals coming from Fe crystallites. The lack of any signals from Nd and B is probably due to the small crystallite size, stacking faults, and low crystallization degree. In order to evaluate the core composition the samples were burned in oxygen atmosphere and XRD analysis of the residues was performed. The burning process has been monitored by thermogravimetric analysis (Fig. 19). During the first step the oxidization of amorphous carbon particles and CEMNPs carbon coating occurs. Next, the core is burned yielding appropriate oxides. The residue is composed of various oxides (XRD in Fig. 20) and its composition provides the information on the encapsulated metallic cores. For example, Fe_2O_3 and Fe_3O_4 indicate that the encapsulate core is composed of iron, while $FeNdO_3$ oxide shows that the core was composed of Fe and Nd.

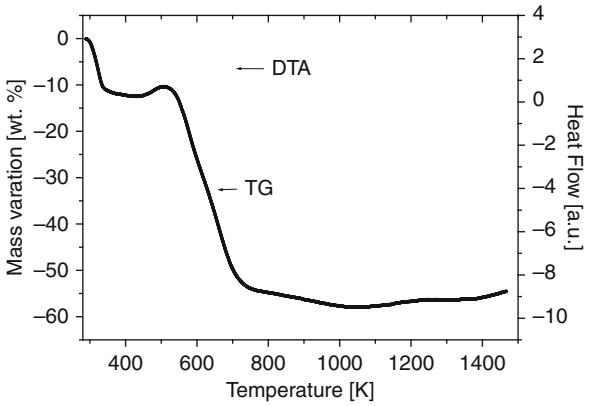

Fig. 19 TG and DTA curves of purified soot obtained in test 2 [40]

Raman spectroscopy is a very useful and non-destructive technique which can provide many structural information about the carbon coating of CEMNPs. A representative Raman spectrum of CEMNPs is showed in Fig. 21. There are two main bands at ca. 1,350 cm^{-1} (D band) and 1,595 cm^{-1} (G band). The G band is associated with the E_{2g} mode (stretching vibrations) in the basal plane of graphite [72]. Disorder, imperfections, and finite particle size effects mainly contribute to the so called D band. The G band in all samples was upshifted comparing to the position of G peak (1,582 cm^{-1}) for highly oriented pyrolytic graphite. It is related to the decrease of the L_a size (L_a is the diameter of the graphite basal plane) [73]. The G to D intensity ratio is a useful indicator of the graphitization degree [72], and

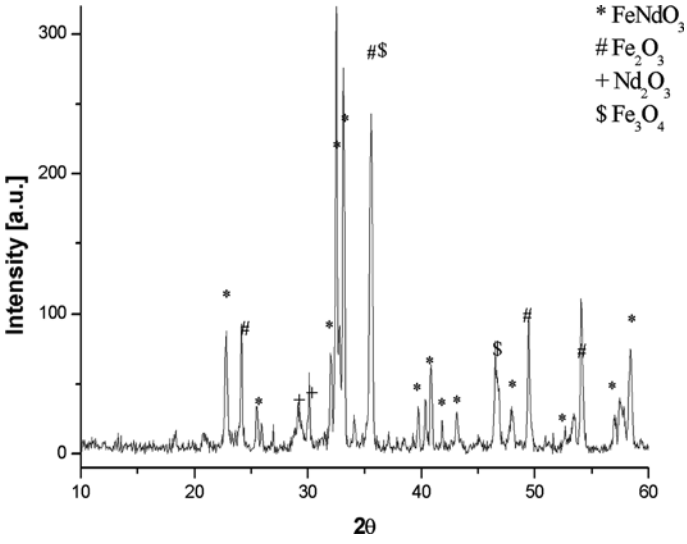

Fig. 20 XRD diffraction patterns of the residue formed after burning soot obtained in test 2

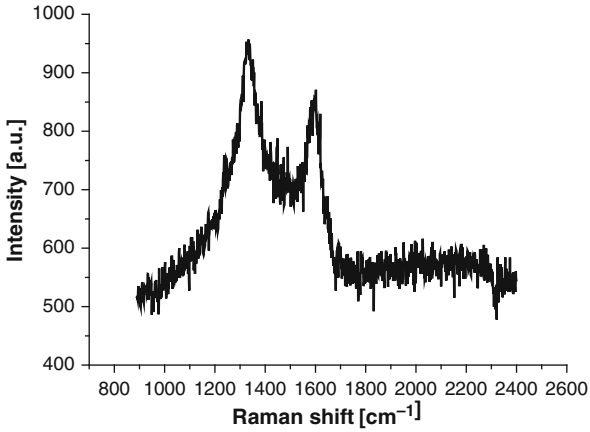

Fig. 21 Raman spectrum of soot obtained in test 2

in our case it can be considered as a carbon coating crystallinity. The G/D ratio for the investigated samples varied between 0.6 and 0.8 and was in an agreement with TEM (images show defects and imperfections). The G/D ratio was found to be higher for cathode deposit samples. It undoubtedly points to the higher crystallinity of the cathode deposit products.

All purified products show superparamagnetic behaviour (a typical hysteresis loop is presented in Fig. 22). The samples exhibit substantially different coercivity (H_c), saturation (M_s) and remanence (M_r) magnetization depending on the experimental conditions (Table 2). The differences in saturation magnetization are obviously caused by the presence of the paramagnetic carbon coatings and amorphous carbon nanoparticles (their magnetic susceptibility is a few orders of

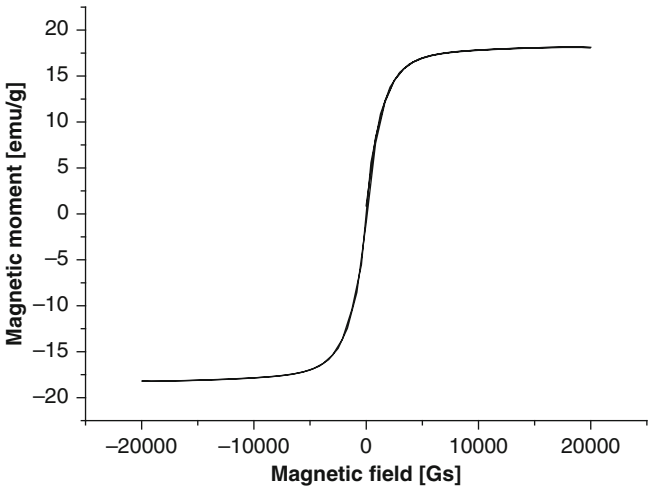

Fig. 22 Hysteresis loop of soot obtained in test 2

Table 2 Magnetic characteristics of products [52]

	Soot			Cathode deposit		
Test	H_c [Oe]	M_s [emu/g]	M_r [emu/g]	H_c [Oe]	M_s [emu/g]	M_r [emu/g]
1	26	8	0.2	26	14	0.2
2	51	30	1.3	64	5	0.2
3	413	2	0.2	98	5	0.3
4	144	32	3.4	44	18	0.5

magnitude lower than that of the encapsulated particles). The results show that soot from tests 2 and 4 have the highest saturation magnetization values, what points also to the high content of CEMNPs in these samples. It is worth to notice, that the M_s in cathode deposits (test 2 and 4) is much lower than in a respective soot. The cathode deposit during arc discharge grows at very a high temperature, what can favour the evaporation of CEMNPs and therefore decreasing the overall magnetic moment.

Emitted light from the discharge zone contains information regarding the plasma composition and the temperature distributions. Two examples of the spectra recorded along the arc radius within 512.5 and 519.5 nm spectral ranges under low and high pressures (tests 1 and 3) are shown in Fig. 23. There are the C_2 (d–a, 0–0) band and some of FeI, FeII and NdII lines. The presence of atomic lines of Fe and Nd proves that the heterogeneous anodes vaporize congruently. There is a significant difference in the intensity distributions within the molecular band for both pressures. At higher pressure (spectrum B) the band head completely disappears, what is caused by the very strong self-absorption. The intensity distribution in the rotational structure of the band can be used for the gas temperature evaluation [15]. The temperature distributions are very similar for low and high pressures. The average temperature along the arc radius is 5,250 ± 250 K and drops to about 3,500 K at the plasma edge.

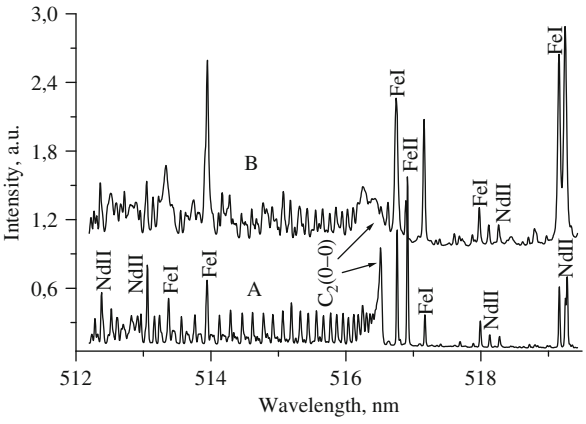

Fig. 23 Spectrum emitted along arc radius under He pressures 13.3 and 60.0 kPa, **a** (test 1) and **b** (test 3), respectively [52]

To conclude, carbon arc is a suitable method to synthesize carbon encapsulated magnetic nanoparticles. The formation of CEMNPs in this method is based on vaporization of graphite and magnetic powders and further quenching and condensation to the solid nanocrystalline phases. The high temperature processing of $Fe_{14}Nd_2B$ (starting material) led to its total vaporization and decomposition. Electron microscopy studies showed that the obtained structures have core-shell structure, with the core diameter between 20 and 50 nm. The CEMNPs cores consisted of Fe, Nd and B crystallites. Magnetic measurements revealed that all products exhibit superparamagnetic properties at room temperature.

SHS Formation of CEMNPs

SHS technique was used in our study to generate the carbon gas which coalesced in the presence of encapsulated matter thus capturing the latter one in the core of nanometric carbon onions [56–61, 74, 75]. The method is based on the deep transformation of the starting materials using the heat released during the combustion synthesis. High temperature and pressure gradients lead to the fast quenching of the carbon-metal gas to the nanocrystalline particles.

Experimental

Combustion synthesis was carried out in a closed stainless steel reactor (a modified calorimetric bomb) of ca. 400 ml in volume. The reactants (Table 3) were prepared in the form of a mixture made from fine powders (particle size below 100 μm). The combustion process was initiated by an electrically heated reaction promoter immersed in quartz crucible containing the reacting mixture. The combustion reaction resulted in an abrupt pressure increase which was monitored by using quartz pressure transducer. At least two runs were performed for each mixture. After the combustion was completed, the gaseous products were vented. The products, very puffy soot-like black solids, were collected for further purification and characterization (the same procedure as presented in Part 3.1).

Results and Discussion

SEM images of purified products (Fig. 24) show that the samples exhibit a similar morphology regardless the composition of the starting mixtures. The morphology

Table 3 Details of reactant composition and reaction heat [56]

Test No.	Starting stoichiometric mixture [wt%]	Heat of reaction [kJ/kg]
1	NaN_3(62.2)/HCE(37.8)	2,320
2	NaN_3(49.8)/HCE(30.2)/Ferrocene(20.0)	2,810
3	NaN_3(57.8)/HCB(42.2)	2,630
4	NaN_3(46.2)/HCB(33.8)/Ferrocene(20.0)	2,780

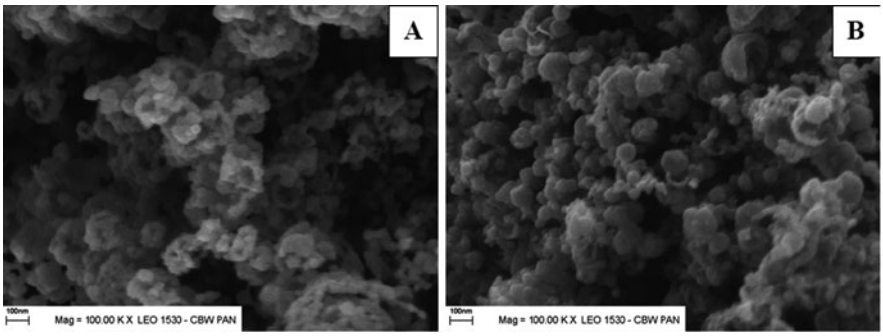

Fig. 24 SEM images of purified products: (**a**) and (**b**) test 1 and 2, respectively [56]

of the products from runs 3 and 4 was much the same. TEM studies revealed (Fig. 25) the morphological diversity. Along with empty carbon nano-onions of ca. 20–40 nm, CEMNPs have been also found. Carbon encapsulates have a diameter between 30 and 60 nm. The carbon coatings consist of 10–15 graphene layers and exhibit different crystallinity. with the interlayer distance of ca. 0.35–0.37 nm (Fig. 25c).

Figure 26 shows XRD diffraction patterns of the purified products from tests 3 and 4. In both cases the strongest signals can be ascribed to the turbostratic carbon and *bcc* Fe (a small fraction of iron carbide is present). Since NaCl is water soluble, its XRD signal indicates that such crystallites are also encapsulated in the protective graphene shells. In the case of test 4 $Fe_4[Fe(CN)_6]_3$ was additionally detected pointing to a very complex combustion synthesis mechanism.

Purified products exhibit similar magnetic performance (Fig. 27). The samples from test 2 and 4 exhibit superparamagnetic behavior with the coercive force between 60 and 70 Oe.

The saturation magnetization for both samples was between 21 and 22 emu/g. Such a value equals ca. 11% of saturation magnetization of pure iron. It indicates that the CEMNPs content in the samples does not exceed 15 wt% (a rough estimation with an assumption that the thickness of the carbon coating is 5 nm).

During the course of combustion synthesis there is fast temperature and pressure increase. Both halocarbons are thermodynamically unstable against reductive chlorination. We believe that the combustion synthesis occurs following to the scheme

$$6\ NaN_3 + C_6Cl_6 \rightarrow 9\ N_2 + 6\ C + 6\ NaCl.$$

Calorimetric measurements show that the released heat during the combustion synthesis (Table 3) can decompose the ferrocene into elements. The simultaneous condensation of carbon-metal gas results in carbon-encapsulated magnetic nanoparticles. Similar quenching and condensation processes take a part in a carbon arc route.

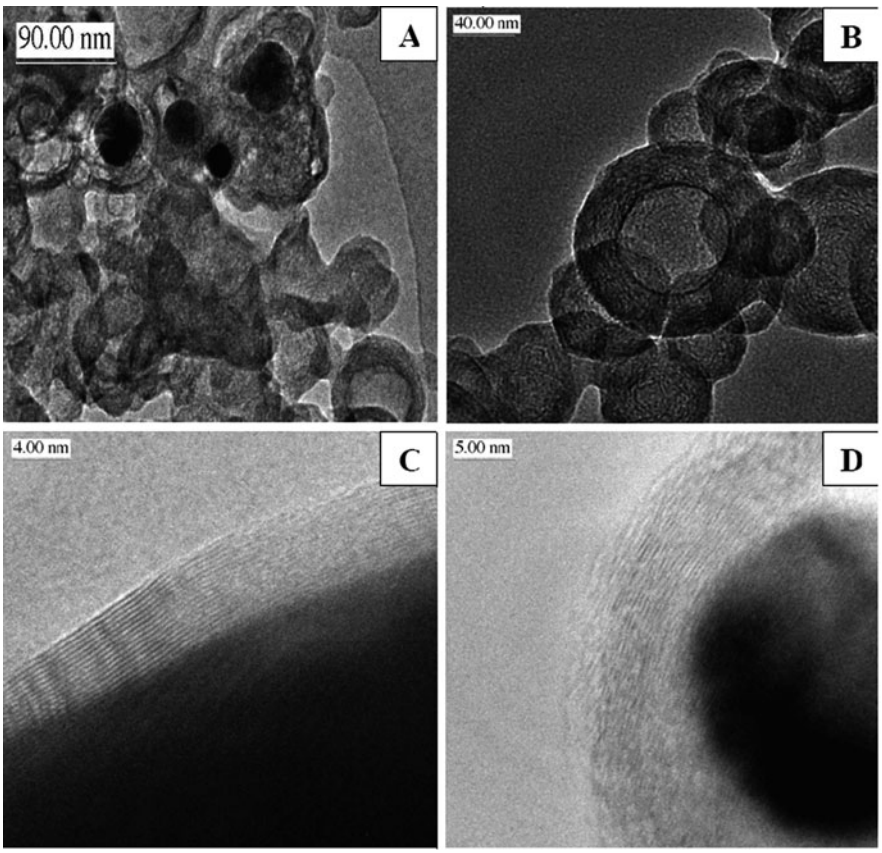

Fig. 25 TEM images of purified product (test 2) [56]

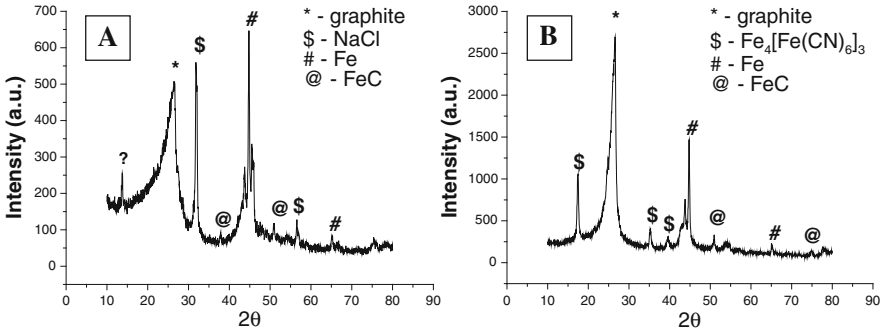

Fig. 26 XRD spectra of products resulting from test 2 (**a**) and 4 (**b**) [56]

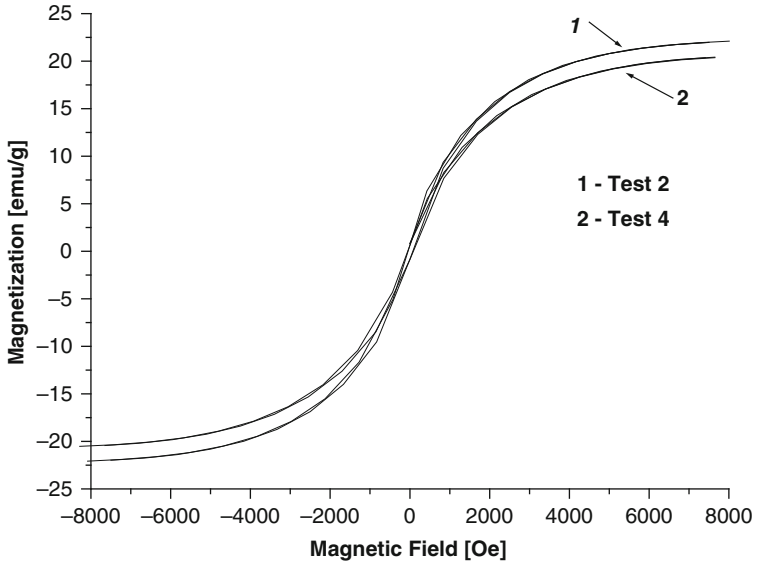

Fig. 27 Hysteresis loops of products from tests 2 and 4 [56]

Synthesis of Silicon Carbide Nanofibers by SHS Route

SHS technique, as explained above, makes use of the heat generated by exothermic reactions and can be applied to synthesize e.g. different nanomaterials [76]. In fact, this process was shown to produce a submicron SiC [77] and a host of other materials: oxides, borides, cermets, nitrides, and silicides [78–81]. While unsuccessfully exploring the possibility of production of carbon nanotubes using the combustion synthesis Huczko et al. [82], in collaboration with S. Cudziło from Warsaw Military University of Technology, serendipitously found that nanometric silicon carbon nanofibers can be efficiently formed when polytetrafluoroethylene (PTFE) is decomposed via SHS route in the presence of silicon atoms. Indeed, the powdered mixture of PTFE and silicon-bearing species (Fe-Si, different silicides, Si elemental) reacted abruptly in a calorimetric bomb upon the ignition (by ohmic heating) of reactants. This self-assembling technique of SiC nanofibres formation was later investigated more in detail [49, 64, 83–85] since silicon carbide, as an outstanding large-gap semiconductor, exhibits a set of unique physical and chemical properties, which makes it a promising candidate for many high-temperature and harsh-environment applications [86–89]. If fabricated in the form of 1-D nanostructures, SiC would have, obviously, new properties resulting from both its marked shape-specific and quantum-confinement effects. The existing methods of preparing 1-D SiC nanostructures [90–95] are, in fact, quite involved and require high temperature and long processing times. We found earlier that a complex set of parallel gas phase reactions with participating silicon-fluorine radicals yielded gaseous SiF_4 and solid SiC as the main reactions products during the combustion of $CaSi_2$-PTFE

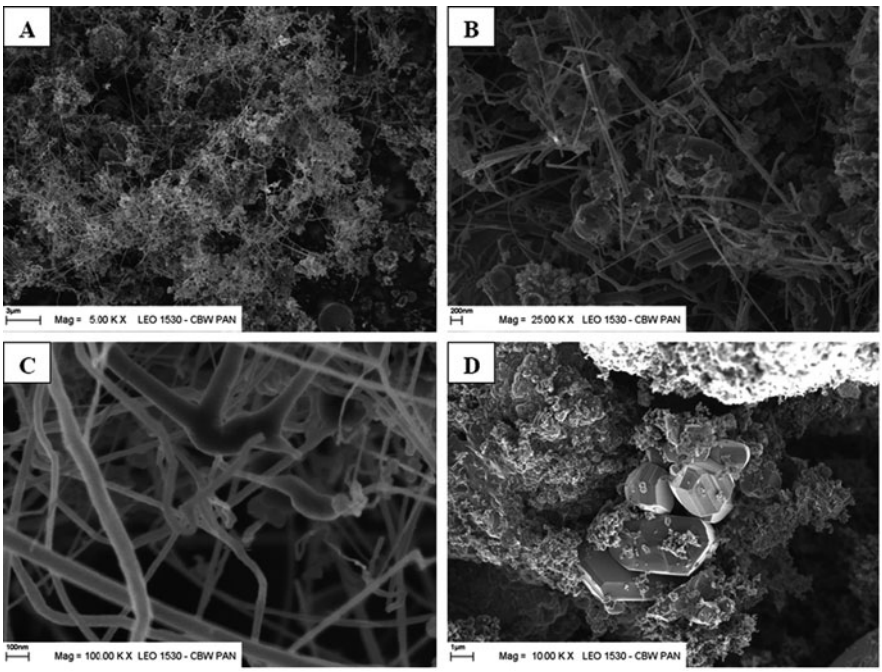

Fig. 28 SEM images of the solid product formed from $CaSi_2$/PTFE (57.8/42.2) mixture

mixture. Electron microscope observation of condensed products revealed its complex morphology (Fig. 28) and fibrous nanostructure (images a, b and c). Some 3-dimensional SiC nanocrystallites (Fig. 28d) were also found in products.

The isolation and purification of SiC nanofibers, and, above all, the removal of side products (e.g., CaF_2) proved, however, to be an arduous task. A four-step protocol (by wet chemistry) to separate the fibers was elaborated [96] but the final yield of the process was limited. Thus, the process involving pure silicon powder as starting reductant (reacting with PTFE) was implemented and optimized, with the results presented below, since for these reactants the solid product is composed of carbon, unreacted silicon and silicon carbide only. In this paper we describe the spontaneous SHS formation of 1-D SiC nanostructures by reductive defluorination of PTFE (as carbon precursor) with Si elemental. Comparing to our forementioned research the distinct improvement of the proposed present route is related to the higher reaction yield and simplified protocol for purification of the sought product.

Experimental

All tests were performed in a modified calorimetric bomb using the experimental procedure as described in Part 3.2. During the combustion the accompanying pressure increase, resulting from the evolution of gaseous products and reaction heat

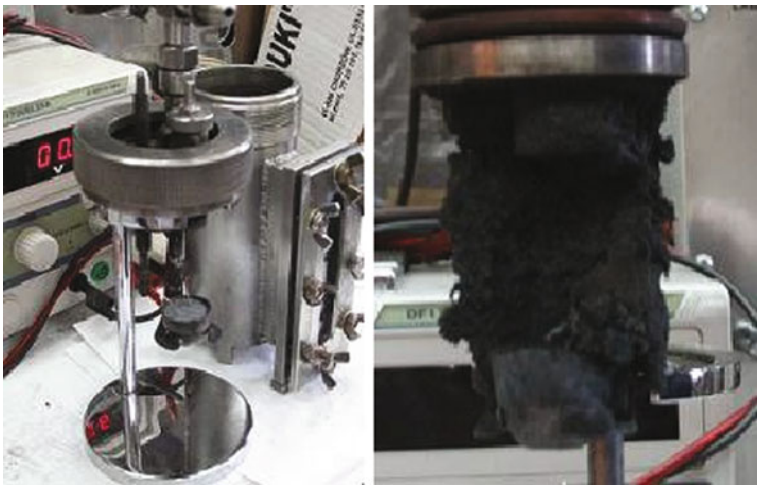

Fig. 29 Calorimetric bomb before (*left*) and after (*right*) the combustion synthesis in Si/PTFE system

(calorimetrically measured), was monitored. Also, for the selected runs the emission spectroscopy was applied to evaluate the process averaged temperatures which proved to be well above 2,000 K [85]. Figure 29 shows the calorimetric bomb before and after a typical run.

The powdered mixture of starting reactants (ca. 3–4 g) with the immersed resistance (kanthal) wire was contained in a quartz crucible. After a combustion (lasting usually a fraction of a second only) yielding SiC nanofibres the bomb was filled with a sponge-like greyish solids with a fibrous morphology. The solid products were collected after process termination and its structure, composition, and morphology were investigated by using SEM and TEM electron microscopy, Raman spectroscopy, elemental analysis (C and H content), and X-ray diffraction as described in Part 2. The solid samples of products were later dissolved in concentrated KOH_{aq} and the measured volume of evolved hydrogen gas gave a way to the evaluation of unreacted silicon content and total Si conversion during the synthesis. In the selected runs the produced gases were qualitatively analyzed by UV and IR spectroscopy. The content of fluorine compounds was also electrochemically measured after gas absorption in KOH solution.

Results and Discussion

A set of combustion synthesis of SiC nanofibres in Si-PTFE system was performed in which the following operating parameters were altered:

- grain size of reactants: Si (Fluka) between 1 and 150 μm, PTFE (Alfa Aesar) between 1 and 100 μm,

- combustion atmosphere and initial pressure
- positioning of quartz crucible containing reactants
- mass of starting reactants
- diameter and positioning of the combustion promoter within the starting reactants.

All other variables were kept constant. From the results of the preceding exploratory runs the following reaction scheme was assumed:

$$2\,Si + 2\,CF_2 \Rightarrow SiC + C + SiF_4$$

Thus, all experiments were carried out for Si/PTFE = 36.0/64.0 mixture (as the preceding testing had proven to be the most favourable composition for 1-D SiC formation) if not stated otherwise. For each run the following data were gathered: initial mass of starting reactants, pressure variation, and the mass of the product collected after the combustion in the reactor.

The heat release accompanying the combustion was measured calorimetrically for the selected runs. The heat of reaction in argon atmosphere for the starting composition (Si/PTFE = 26.0/74.0) under consideration is relatively high (5,650 kJ/kg). Thus, once started the exothermal process is usually terminated within a fraction of a second. The combustion synthesis is accompanied by the abrupt evolution of heat resulting in high temperature (well above 2,000°C as mentioned above) and pressure in the system. The latter one is additionally augmented by the generation of gaseous radical and molecular (SiF_4) species. As an example, the high heating rate and pressure increase equal to ca. 3.2×10^4 K s^{-1} and 7.9×10^6 Pa s^{-1}, respectively, were obtained earlier for $CaSi_2$/PTFE combustion synthesis in air [64]. Not only the peak pressure, but also the final pressure in the bomb was measured, after thermal relaxation of the system.

The fluorine content in the evolving gases was measured for the selected runs by using an electrochemical technique (after absorption of the gas in concentrated KOH_{aq}). It follows from both measurements that, as expected, SiF_4 is the main component of gaseous products, along with some elemental fluorine and C–F compounds (as confirmed by UV and IR spectroscopy).

The results show that the yield of Si→1-D SiC (the main component of the sponge-like product, see below) reaction is strongly dependent on some of the combustion parameters. There is an optimal initial mass of reactants for the volume of the reactor used (ca. 4 g) and initial pressure (ca. 1 MPa as shown below), which yields the highest mass of the desired product and the highest conversion rate.

The performed experiments showed that neither the initial mass and positioning of reactants (within the reactor) nor the diameter and location of the reaction promoter within the starting mixture seem to distinctly influence the combustion course. Thus, once initiated the combustion wave instantly propagates through the solid reactants and the evolved gaseous intermediates freely diffuse to the colder zone where coalescence and condensation of solid products occur.

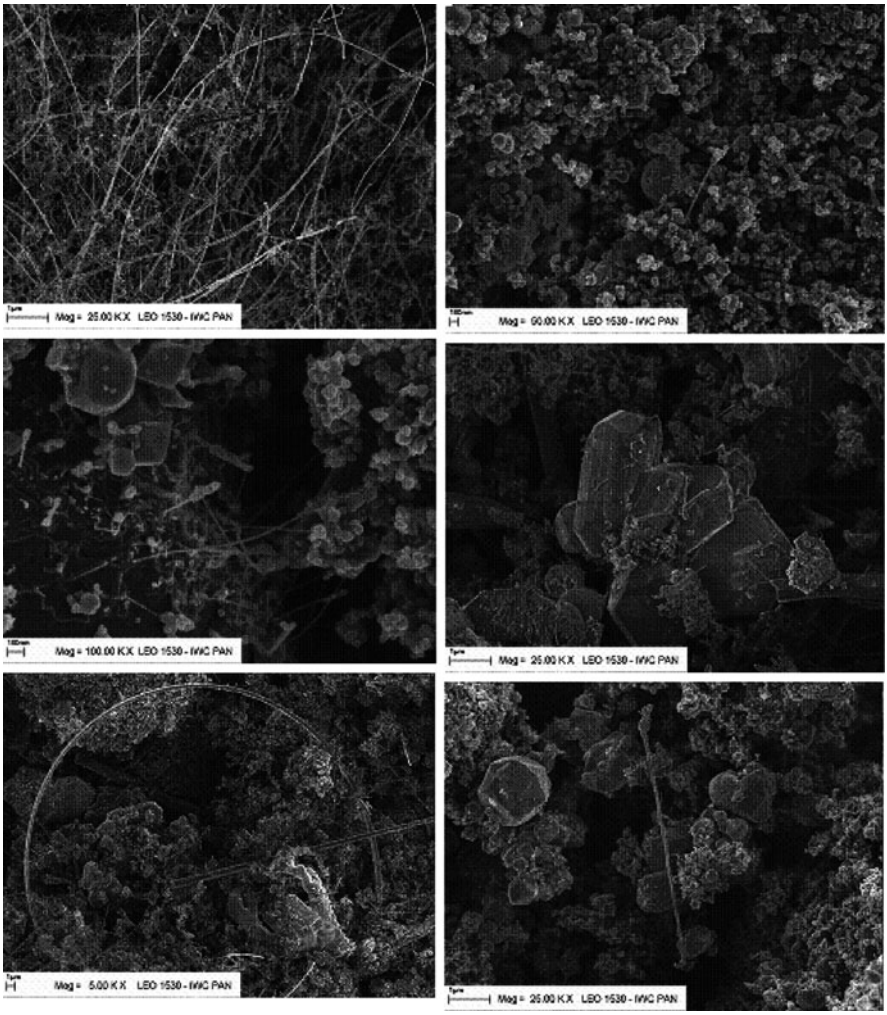

Fig. 30 SEM images of solid products showing its highly diversified morphology

The morphology of combustion products has been studied by SEM and TEM techniques. We detected various types of novel nanostructures in collected solids, i.e. nanofibres, nanocrystallites and soot (see Fig. 30 as an example).

Table 4 shows the operating parameters and the results of runs (initial pressure 1 MPa, air) in which granulation of starting reactants was changed. SEM images of products are presented in Fig. 31.

The results show that PTFE particle size does not seem to influence the combustion course. In fact, the initial temperature of the process (ohmic heating) is high enough to promote the thermolysis of PTFE and to generate gaseous fluorine-bearing species. PTFE has covalent C-F bonds that, when dissociated, will

Table 4 Influence of Si/PTFE granulation on combustion synthesis in air

Si below (μ)	PTFE below (μ)	Initial mass of reactants (g)	Peak pressure (MPa)	Combustion duration	Mass of products (g)	Products morphology	Unreacted silicon (wt%)	Silicon conversion (%)
43	1	2.55	3.6	Very short	0.88	Sponge-like	9	≥ 90
43	100	5.90	3.8	Relatively long	1.96	Sponge-like	15	80
150	1	3.83	3.0	Relatively long	0.93	Sponge- and soot-like	17	78
150	100	4.39	2.4	Very long	1.60	Sponge- and soot-like	21	69

produce more reactive lower carbon-fluorine (molecular and radical) species. The highest total Si conversion (above 90%) was obtained for the fine starting silicon. The process was also easily initiated and the combustion was very fast. In the case of coarse-grained silicon the process could even not be started at a slightly lower pressure. At pressure equal to 1 MPa the combustion duration is long thus pointing out to the lower rate of phase transformation of coarse silicon grains and a mass-diffusion barrier. These conclusions are confirmed by the presented SEM images. While all products contain fibrous nanostructures, their content is higher for product collected in runs with fine silicon. Also the average diameter of those nanofibres is definitely smaller comparing to those obtained in runs with coarse silicon.

The initial pressure of air was also varied and the results of the runs with fine and coarse reactants are presented in Table 5. It is evident that this parameter strongly influence the combustion course. With the increasing pressure the reaction is more vigorous and much shorter, Si conversion increases and the products contain more nanofibres. This observation is even more pronounced for coarse-grained reactants: at lower pressures (0.1 and 0.3 MPa) the process can not be initiated at all.

Those results clearly confirm the involvement of gaseous intermediates in the reaction course since at low pressure their diffusion and expansion (and accompanying quench) is too fast to provide for the coalescence of resulting solids. Only at pressure high enough (1.0 MPa) there is enough time for gaseous reactants to form products. Also, the outlined above influence of reactants granulation on process yield is again reaffirmed.

Figure 32 shows, as an example, SEM images of products obtained from fine-grained reactants at different pressures. At the lowest pressure (0.1 MPa) only very few short SiC nanofibers can be spotted and their growth seems to be not terminated yet. The pressure increase allows for the prolonged growth of many 1-D nanostructures and the sponge-like morphology of the products points to high concentration of nanofibres.

The reaction atmosphere also strongly influences the process performance with the best results obtained (Table 6) in runs carried out in oxygen-containing gases

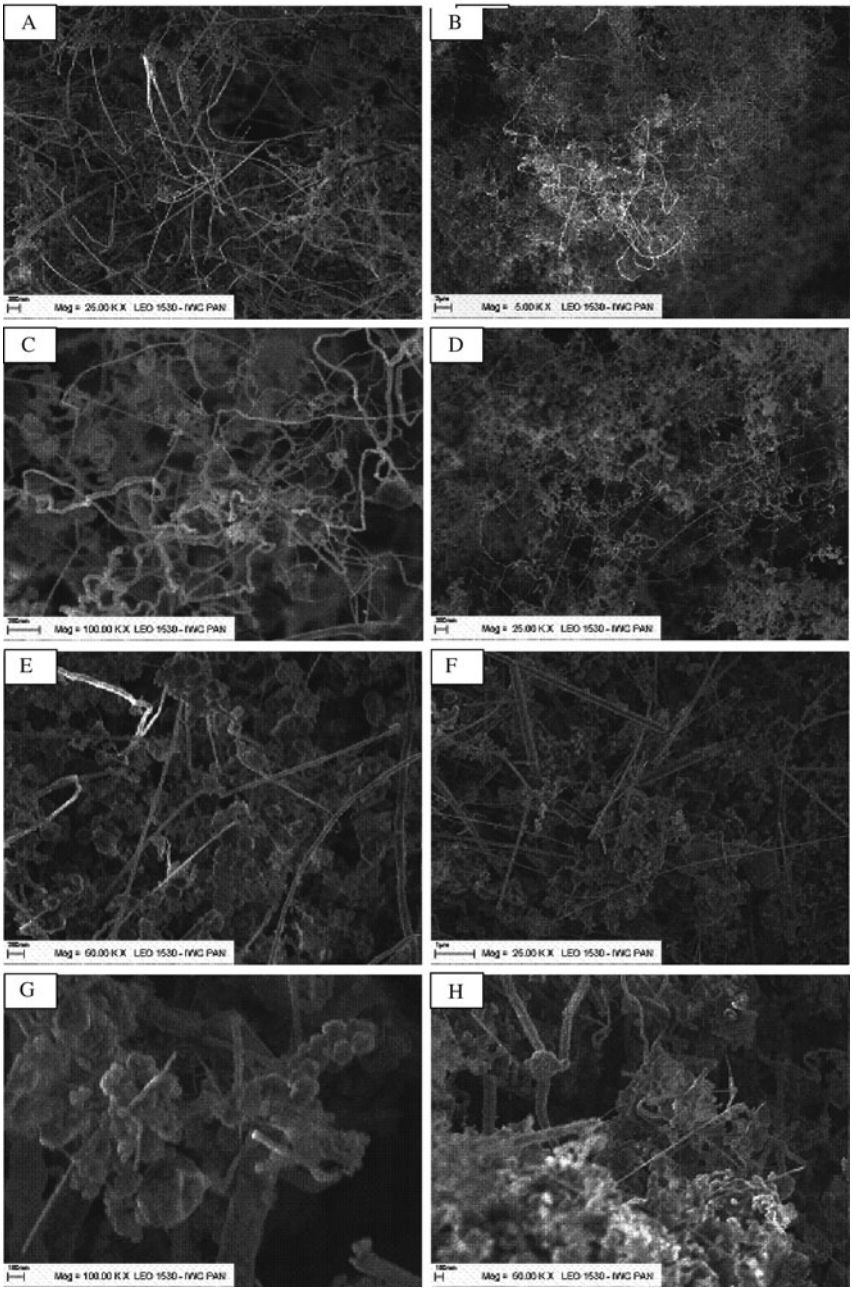

Fig. 31 SEM images of products: (**a**, **b**) Si 43 μm/PTFE 1 μm; (**c**, **d**) Si 43 μm/PTFE 100 μm; (**e**, **f**) Si 150 μm/PTFE 1 μm; (**g**, **h**) – Si 150 μm/PTFE 100 μm

Table 5 Influence of initial pressure on combustion synthesis in Si/PTFE system in air

Si below (μ)	PTFE below (μ)	Initial mass of reactants (g)	Initial pressure (MPa)	Peak Pressure (MPa)	Combustion duration	Mass of products (g)	Products morphology	Unreacted silicon (wt%)	Silicon conversion (%)
43	1	3.89	0.1	1.0	Relatively long	1.22	Soot-like	26	53
43	1	2.77	0.3	2.0	Relatively long	1.91	Sponge-like and soot-like	14	84
43	1	2.52	1.0	3.6	Very short and strong	1.10	Sponge-like	9	90
150	100	4.80	0.1	no reaction	–	–	–	–	–
150	100	4.97	0.3	no reaction	–	–	–	–	–
150	100	4.40	1.0	2.4	Very long	1.60	Sponge-like and soot-like	21	69

(air, carbon dioxide, oxygen) at 1 MPa, this probably due to their higher heat capacity and better transport and quenching properties. Also, the involvement in combustion of oxygen-bearing intermediates (SiO?) can not be ruled out. It is worth to mention here that the involvement of oxygen – as an intermediate – was earlier proposed by Rümmeli [97, 98] in the formation mechanism of carbon nanotubes. As mentioned earlier, the process could not be initiated at a soft vacuum this probably due to the very fast expansion of gaseous intermediates. Also, there was no combustion in helium. In the case of pure oxygen the reaction duration is much longer (at least few seconds comparing to a fraction of a second for other reaction environment). Thus, the direct high temperature partial oxidation of reactants can not be ruled out. The morphology of the 1-D product does not depend heavily on the process environment (excluding pure oxygen). The results of these parametric studies confirm again that the nucleation mechanism involving radical gaseous intermediates is responsible for the product formation.

Figure 33 presents SEM images of the corresponding products which are in line with the data from Table 6. The specimens from runs carried out in argon and nitrogen atmosphere (A,B and C,D, respectively) contains very few nanofibres; some 3-D SiC nanocrystallites can also be spotted. The fibrous structure of the product is evident for combustion in oxygen-containing atmosphere (E,F – carbon dioxide, G,H – air, I,J – oxygen); in the case of pure oxygen the product also contains ball-shaped silica particles with diameters within a fraction of a micron.

1-D SiC nanostructures produced from present route typically have diameters ranging from ~ 20 to several tens of nanometers and with lengths up to several tens of microns (Figs. 28, 30, 31, 32, and 33). They were present in almost all samples. The electron images revealed the presence of thread-like features, as if 1-D nanostructures were linked together in a spaghetti-like manner. The thread-like microstructures corresponded to varied diameters in a relatively wide range with the aspect ratio well above 10^3.

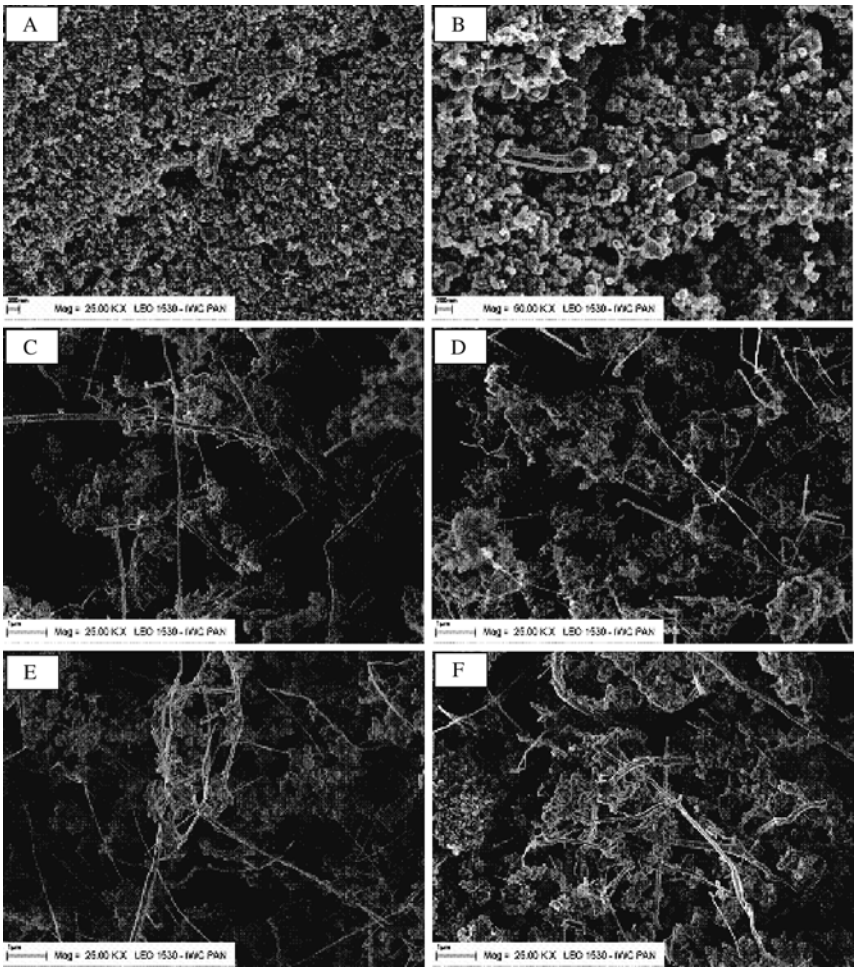

Fig. 32 SEM images of products: (**a**, **b**) Si 43 μm/PTFE 1 μm, 0.1 MPa; (**c**, **d**) Si 43 μm/PTFE 1 μm, 0.3 MPa; (**e**, **f**) Si 43 μm/PTFE 1 μm, 1.0 MPa

To further confirm the composition of the products from those runs XRD analyses of selected samples were carried out (Fig. 34).

The products (argon and air atmosphere) contain crystalline phases of unreacted silicon and β-SiC (with stacking faults) [99] with some $C_{20}F_{42}$ and graphite C (002). Product from the run carried out in pure oxygen is dominated by the presence of semi-amorphous silica with relatively low content of Si and SiC.

Depending on the starting reactants, the carbon content of the solid products varied between 8 wt% and 80 wt%. The higher content of carbon can be, obviously, related to the lower content of the other products (e.g., volatile metal fluoride), which, in the case of Si-containing mixtures is gaseous SiF_4. Calcination of the

Table 6 Influence of reaction atmosphere on combustion synthesis in Si/PTFE system at initial pressure 1 MPa

Si below (μ)	PTFE below (μ)	Initial mass of reactants (g)	Reaction atmo-sphere	Peak pressure (MPa)	Combustion duration	Mass of products (g)	Products morphology	Unreacted silicon (wt%)	Silicon conversion (%)
43	1	4.15	Argon	4.0	Short	1.24	Soot-like	31	33
43	1	4.32	Nitrogen	4.0	Relatively long	2.58	Sponge-like and soot-like	32	26
43	1	3.42	Carbon dioxide	4.0	Short	1.23	Sponge-like	11	88
43	1	2.52	Air	3.6	Very short and strong	1.10	Sponge-like	9	90
43	1	3.23	Oxygen	5.0	Very long	0.83	White powder	3	>90

product in air resulted in a distinct decrease of free carbon content due to its oxidation. The residual carbon can be only related to carbide phases resistant against oxidation at the heating temperature.

Raman spectroscopy was also used to determine the formation of ß-SiC, α-SiC, and any residual Si and C in the specimen. Bulk scale studies showed the product to be comprised of mostly cubic polytype of ß-SiC and that finite size effects are present. The ß-SiC is characterized by sharp peaks at 795 and 970 cm^{-1} arising from transverse optical (TO) and longitudinal optical (LO) phonons, respectively. However, a mixture of different SiC polytypes along with disorder in the structure and stacking faults (shown in HRTEM image below) is also visible.

TEM observations (Fig. 35) showed that the resulting nanofibres have primarily smooth and straight whisker-like morphology with some of them possessing bends and kinks, and appeared to be rigid, displaying dimensions similar to those observed by SEM.

Figures. 35a, b reveal the overview of the produced bulk sample, which consisted of SiC nanofibres and other products, with very few carbon particles attached to the fibres surface walls. HRTEM and EDX were performed in order to obtain information about the structure and composition of the products. Fig. 35c, d demonstrate the variety (diameters from below 10 nm up to several tens of nm) of Si- and C-containing (EDX analysis) fibrous products, with a relative high density of stacking faults and striations on the image. The spacing of the crystallographic planes measured from the HRTEM image (Fig. 35e, f) is ca. 0.25 nm which is consistent with the reported value (JCPDS card, No. 29–1129) to the (111) lattice planes of the crystalline SiC. The HRTEM images of the SiC nanofibres showed no evidence of axial screw dislocations, suggesting that these nanostructures were not grown by the screw dislocation mechanism [100]. Instead, the liquid globules found e.g., on the tip of some nanofibres could suggest the VLS mechanism [101]. However, much more work remains to be done to fully confirm such growth of these nanofibers. The chemical composition analysis by EDX spectroscopy in both SEM and TEM confirmed that the atomic ratio of Si atoms to carbon atoms in the nanofibres was

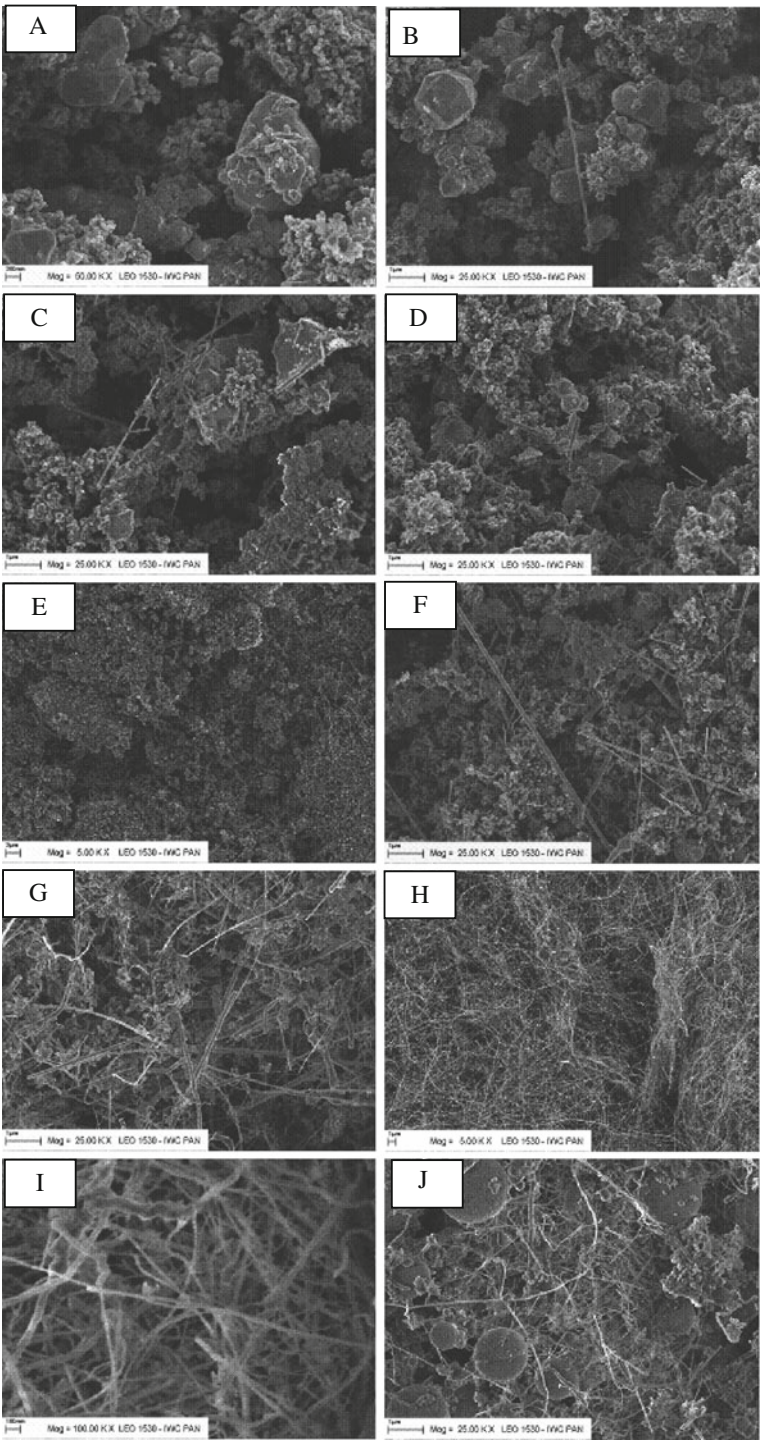

Fig. 33 SEM images of products, Si 43 μm/PTFE 1 μm, 1 MPa: (**a**, **b**) argon; (**c**, **d**) nitrogen; (**e**, **f**) carbon dioxide; (**g**, **h**) air, (**i**, **j**) – oxygen

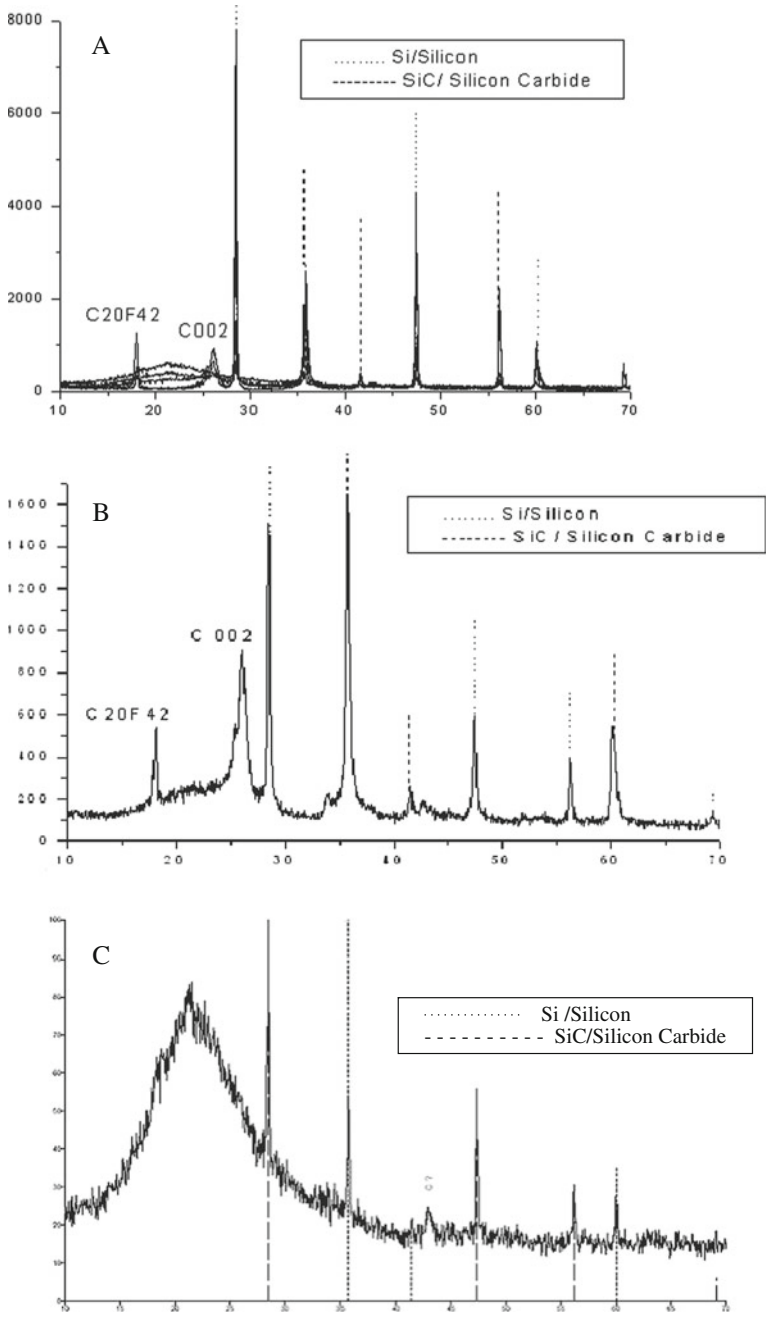

Fig. 34 XRD spectra of products, Si 43 μm/PTFE 1 μm, 1 MPa: (**a**) argon; (**b**) air; (**c**) – oxygen

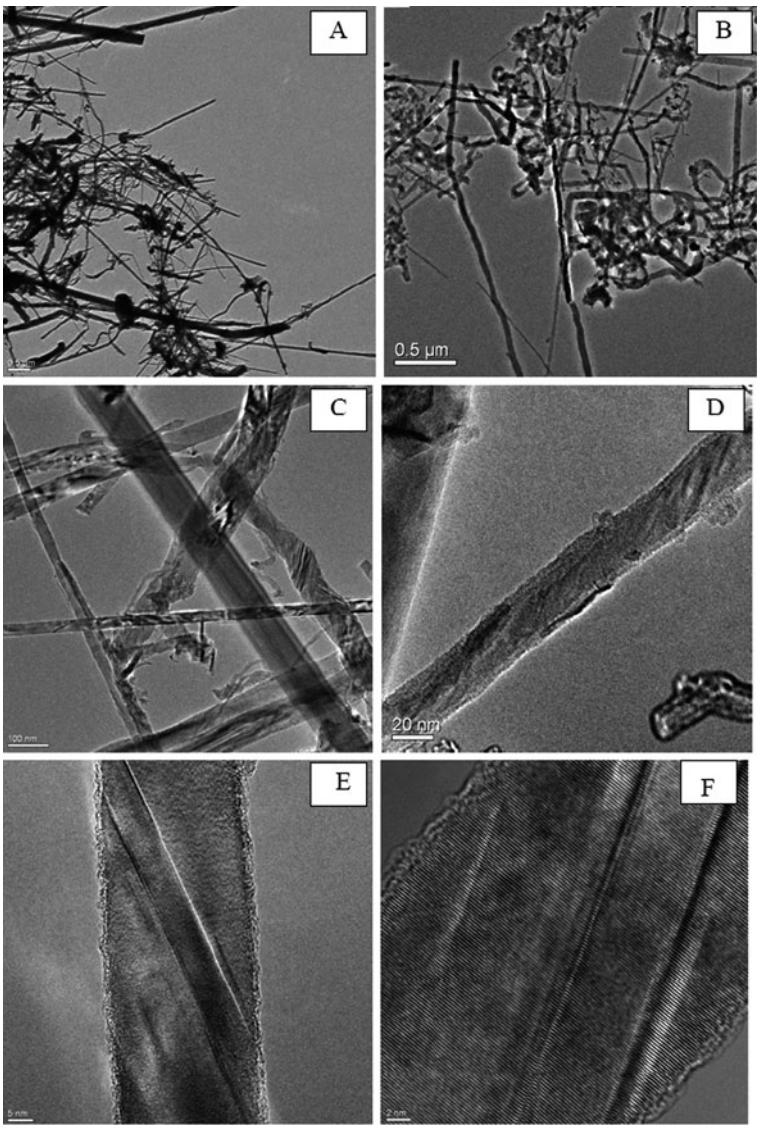

Fig. 35 TEM/HRTEM images of products, Si 43 μm/PTFE 1 μm, air, 1 MPa

approximately the same as that of a reference SiC crystal. Further insight into the structure of the nanofibres shows (EDX) that the centre nanofibre is wrapped in a uniform thin (ca. 2 nm) outer layer of SiO_2 (Fig. 35e, f). It is apparent that these fibres, with their close-packed atomic planes, should possess high tensile strengths and Young's modulus.

Thus, the elemental, XRD, Raman analyses, and microscopic observations have shown that the as-obtained products of Si/PTFE combustion contain, along with

dominating SiC 1-D crystallites, turbostratic graphite, some un-reacted silicon, and also silicon dioxide (for runs in oxygen atmosphere).

Following the synthesis of a bulk product the protocol to chemically isolate and finally purify the SiC nanofibres was elaborated as follows. The silicon and silicon dioxide were removed by boiling the product suspension in KOH solution (30 wt%) under reflux for 8 h. The solid product was washed with plenty of water and calcinated in air at 700°C for 2 h in order to remove the elemental carbon. Finally, to remove the residual silicon-bearing compounds the product was again boiled in KOH solution (30 wt%) under reflux for 8 h. The final product was filtered and the deposit was washed with plenty of water. Figure 36 shows SEM images of the SiC 1-D material before and after purification (for Si/PTFE compositions).

The carbon content (elemental analysis) in the purified product varied between 28.55 wt% and 28.76 wt% (with hydrogen between 0.34 wt% and 0.36 wt%, and nitrogen between 1.05 wt% and 1.20 wt%). Thus, the chemical purity of the isolated 1-D SiC could be estimated to be at least 98.2 wt%.

The formation mechanism of SiC 1-D nanostructures formation could be proposed as a set of parallel radical reactions. However, the exact formation mechanism, specially regarding 1-D morphology of the product, is not completely understood. The thermal initiation of the combustion promotes PTFE decomposition yielding low molecular weight gaseous fragments/radicals with a dominating proportion of the monomers. These gaseous species form in the hot core of the combustion zone. They expand rapidly from the central zone towards the colder area (e.g., water-cooled inner reactor wall). The expansion of reactive radicals gives a way to following quenching and coalescence processes the course of which depends heavily e.g., on the partial pressure of condensing species and quench environment. The rearrangements of several different atoms and radicals within milliseconds yield new nanosized morphologies, e.g., nanofibres. Hence the distinct influence of process variables on reaction yield. The freshly formed carbon atoms assemble either into hexagonal carbon clusters (which may grow further into soot particles) or form other compounds. Meanwhile, oxygen (which unavoidably exists in the reactor) may also react with Si to form thin SiO_2 amorphous layer, partly sheathing the SiC. As a result, this cover may hinder the stacking of further atomic planes on top of this

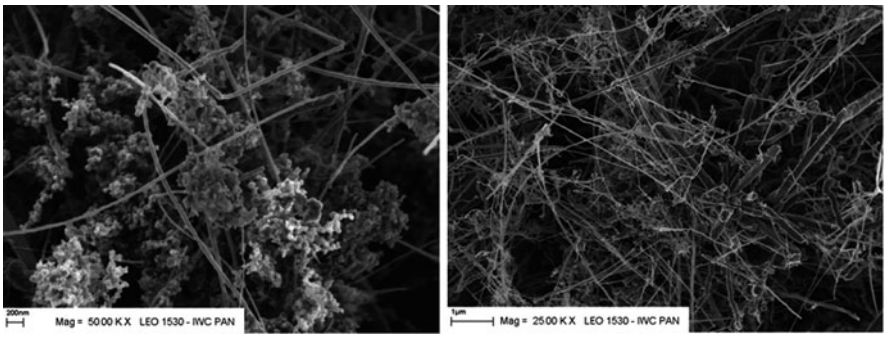

Fig. 36 SEM images of as-obtained (*left*) and purified (*right*) SiC nanofibres

nucleus, thus preventing an increase in fibre diameter. Further growth can only proceed continuously in the close-packed atomic direction, i.e., the fibre axis direction. Thus, the resulting SiC fibres are relatively thin, and exhibit a unique crystal plane-axis relationship. In the case of air atmosphere a very reactive SiO is probably the main gaseous intermediate responsible for the mass transfer as proposed elsewhere [102]. In a pure oxygen atmosphere the chemical process is by no means dominated by direct high temperature oxidation of silicon and amorphous silica nanospheres dominate the reaction products.

Thus, the SiC clusters are produced by the gas phase reactions of different radicals which can be represented by

$$\mathrm{Si_{(s)} + (CF_2)_{n(s)} + O_2 \rightarrow SiF_{n(g)}^{\cdot} + CF_{m(g)}^{\cdot} + SiO_{(g)}^{\cdot} \rightarrow SiC_{(s)} + SiF_{4(g)} + CO_{(g)} + CO_{2(g)} + C_{(s)}}$$

All products are in a nanometer size. This can be again explained as the condensing reactants do not have enough time to grow into larger 3-D microcrystals due to the inherent short duration of the combustion reaction and the fast quench during product expansion.

It follows from some of the SEM images (see Fig. 37) that the catalytic growth via the vapor-liquid-solid (VLS) mode should also be taken into account while discussing the formation of 1-D SiC nanofibers.

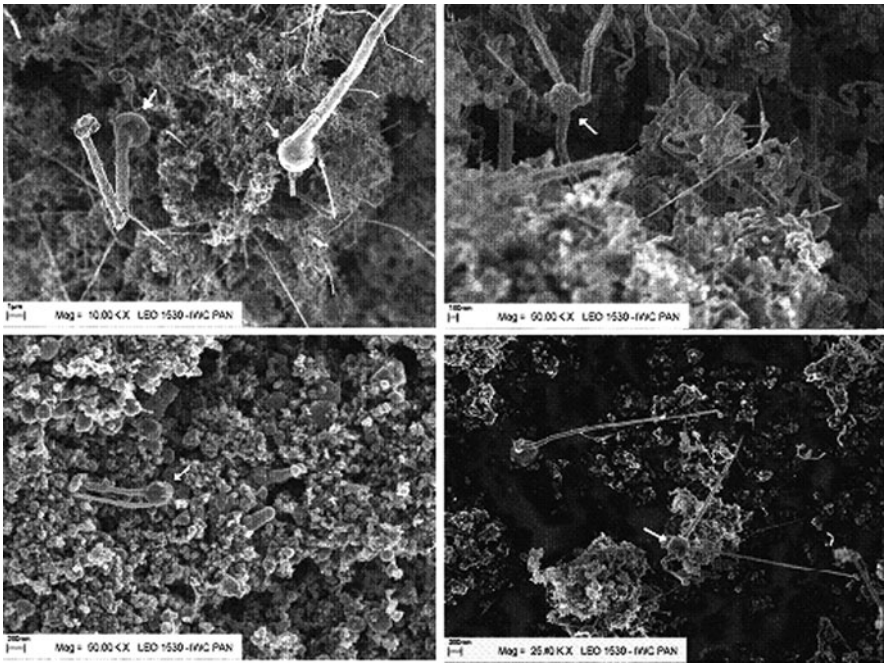

Fig. 37 SEM images of solid products showing the morphologies of 1-D SiC nanostructures grown evidently via VLS mechanism

The VLS crystal growth mechanism was discovered by Wagner and Ellis [101] and thoroughly investigated later by Baker et al. [103] to explain carbon filament growth. The principles of VLS mechanism were studied by Wagner et al. mainly on silicon crystals, but the information obtained from experiments with the growth of other elements or chemical compounds is equally valuable from the vantage point of the knowledge of VLS mechanism. The morphologies shown in Fig. 37 seem definitely to grow from a nanosphere of a catalyst (Si?).

Finally, one should mention here that not only the efficient SHS formation of SiC nanofibers has been experimentally studied, but also its possible applications are being currently sought those including e.g. (1) novel adsorbents [104–106], (2) nanomass sensing [107], and (3) optical limiting [108]. The electrochemical measurements also showed that the electrical double layer performance of SiC nanofibres-derived amorphous carbon is better than most of the common pyrolytically made carbons [106]. The parametric optimization studies led to the conversion of starting Si into products exceeding 90% [109]. The measurements of the thermal conductivity of the purified nanofibres were also carried out [110]. Obtained results suggest that the apparent thermal conductivity (over 100 $Wm^{-1}K^{-1}$) is much greater than the data of SiC thin films. Rümmeli et al. [111] proposed recently the annealing route to chemically transform SiC nanofibres into tubular SiC nanostructures while coaxial silica/SiC reverse their sheath/core structure. The process could be exploited as a viable route to manipulate a variety of nanostructures and films for doping and etching and structural manipulation. Cathodoluminescence spectra from SiC nanofibres within the temperature range of 77 ... 300 K were also measured [112], showing obvious differences with respect to the bulk material. Using for the first time the scanning tunneling spectroscopy (STS), scanning tunneling microscopy (STM) topography and current imaging tunneling spectroscopy (CITS) Busiakiewicz et al. carried out extensive studies on the electronic structure of SiC nanofibres [113–117]. N-type observed doping was attributed to nitrogen presence in the sample. The measurements also revealed fluctuations of the local density of electronic states (LDOS) in the vicinity of structural defects. Epoxy resin/SiC nanofibres were also prepared [118] and their mechanical properties were measured. Even a low content of fibres (0.25 wt%) distinctly improved the flexural modulus and strength, and ultimate elongation of the produced nanocomposites.

In summary, the advantages of the combustion synthesis method for easily realizing scale-up of 1-D SiC nanocrystallites production include that it is a simple, fast and unique one-pot process without the need for a catalyst or template, is low cost, has high yield, and the starting reactants are readily available. We believe that the nucleation mechanism involving radical gaseous species is responsible for 1-D nanoSiC growth. Thus, the present study has enlarged the family of nanofibres and nanotubes available and offers a possible, new general route to 1-D single-crystalline materials. It appears, however, that much more work remains to be done to fully understand the growth mechanism of SiC nanofibres and nanotubes.

Acknowledgments This work was supported by the Ministry of Science and Education through the Department of Chemistry, Warsaw University, under Grants No. N204 096 31/2160 (Sect. 2),

N N204 132137 (Sect. 3). This research was also (Sect. 4) co-financed by the European Regional Development Fund within the Innovative Economy Operational Programme 2007–2013 (title of the project 'Development of technology for a new generation of the hydrogen and hydrogen compounds sensor for applications in above normative conditions' No UDA-POIG.01.03.01-14-071/08-00). We also acknowledge technical assistance and helpful discussion with M.H. Rümmeli, T. Gemming, J. Szepvolgyi, Z. Karoly, A. Grabias, W. Kaszuwara, S. Cudziło and M. Osica.

References

1. P. Byszewski et al., Fullerene and nanotube synthesis. Plasma spectroscopy studiem. J. Phys. Chem. Solids. **58**, 1679 (1997)
2. H. Lange et al., Influence of boron on carbon arc plasma and formation of fullerenes and nanotubes. Chem. Phys. Lett. **289**, 174 (1998)
3. A. Huczko et al., Influence of Fe and Co/Ni on carbon arc plasma and formation of fullerenes and nanotubes. J. Phys. Chem. A **104**, 10708 (2000)
4. H. Lange et al., Carbon plasma as a source of fullerenes and nanotubes: Optical emission studies. New Diam. Front. Carbon Technol. **11**(6), 399 (2001)
5. H. Lange et al., Influence of gadolinium on carbon arc plasma and formation of fullerenes and nanotubes. Plasma Chem. Plasma Process. **22**(4), 523 (2002)
6. A. Huczko et al., Hollow cathode plasma synthesis of carbon nanofiber arrays at low temperature. J. Phys. Chem. B **106**, 1534 (2002)
7. H. Lange et al., Nanocarbon production by arc discharge in water. Carbon **41**, 8, 1613 (2003)
8. H. Lange et al., Carbon arc plasma as a source of nanotubes: Emission spectroscopy and formation mechanism. J. Nanosc. Nanotech. **3**, 51 (2003)
9. A. Sioda et al., Role of diamond on carbon nanostructure formation in the arc discharge. Acta Physica Slovaca **55**(4), 405 (2005)
10. M. Bystrzejewski et al., Synthesis of heterogenous multi-walled carbon nanotubes in a carbon arc in water. Fullerenes, Nanotubes, Carbon Nanostruct **14**, 207 (2006)
11. A. Huczko et al., Formation of SWCNTs in arc plasma: Effect of graphitization of Fe-doped anode and optical emission studies. J. Nanosc. Nanotech. **6**, 1319 (2006)
12. H. Lange et al., Influence of carbon structure on carbon nanotube formation and carbon arc plasma. Diam. Relat. Mater. **15**, 1113 (2006)
13. H. Lange et al., Spectroscopic study of C_2 in carbon arc discharge. Specrosc. Lett. **29**, 1215 (1996)
14. H. Lange, Spectral diagnostics of helium-carbon arc plasma during carbon nanostructure formation. Fullerene Sci. Technol. **5**, 1177 (1997)
15. H. Lange et al., Temperatures and column densities in carbon arc plasma. J. Phys. D: Appl. Phys. **32**, 1024 (1999)
16. H. Lange et al., Optical emission studies of arc plasma with C, C/Fe and C/Co/Ni electrodes, in *Progress in Plasma Processing of Materials*, ed. by P. Fauchais (Begell House, New York, 2001), pp. 23–28
17. K. Saidane et al., Characteristics of a carbon arc discharge. High Temp. Material Processes. Int. J. **5**, 243 (2001)
18. H. Lange et al., Thermal plasma processing of domestic waste incneration ashes, in *Progress in Plasma Processing of Materials 2003*, ed. by P. Fauchais (Begell House, New York, 2003), p. 99
19. X. Zhao et al., Macroscopic oriented web of single-wall carbon nanotubes. Chem. Phys. Lett. **373**, 3, 266 (2003)
20. X. Zhao et al., Large-scale purification of single-wall carbon nanotubes prepared by electric arc discharge. Diam. Relat. Mater. **15**, 1098 (2006)
21. S. Iijima et al., Single-shell carbon nanotubules of 1-nm diameter. Nature **363**, 603 (1993)
22. D.S. Bethune et al., Cobalt-catalysed growth of carbon nanotubes with single-atomic-layer walls. Nature **363**, 605 (1993)

23. H. Lange et al., An opto-electronic control of arc gap during the formation of fullerenes and carbon nanotubes. Rev. Sci. Instrum. **68**, 3723 (1997)
24. A. Jorio et al., Characterizing carbon nanotube samples with resonance Raman scattering. New J. Phys. **5**, 139.1 (2003)
25. O. Łabędź et al., Influence of carbon structure of the anode on the synthesis of single-wall carbon nanotubes in a carbon arc plasma. Carbon **47**, 2847 (2009)
26. H. Lange et al., Influence of nitrogen on carbon arc plasma and formation of fullerenes. Chem. Phys. Lett. **34**, 1 (2001)
27. H. Lange, Optical emission studies of C_2 and CN radicals in carbon arc plasma. Symp. Proc. I, 221 (1999)
28. A. Huczko, Heterohedral fullerenes and nanotubes: Formation and characteristics. Full. Sci. Technol. **5**, 1091 (1997)
29. D. Jain, R. Wilhelm, An easy way to produce α-iron filled multiwalled carbon nanotubes. Carbon **45**, 602 (2007)
30. T. Gorelik et al., Carbon onions produced by laser irradiation of amorphous silicon carbide. Chem. Phys. Lett. **373**, 642 (2003)
31. S. Bandow et al., Raman scattering study on fullerene derived intermediates formed within single-wall carbon nanotube: From peapod to double-wall carbon nanotube. Chem. Phys. Lett. **384**, 320 (2004)
32. T. Yamagachi et al., Synthesis of carbon nanohorn particles by simple pulsed arc discharge ignited between pre-heated carbon rods. Chem. Phys. Lett. **389**, 181 (2004)
33. H. Song, X. Chen, Large-scale synthesis of carbon-encapsulated iron carbide nanoparticles by co-carbonization of durene with ferrocene. Chem. Phys. Lett. **374**, 400 (2003)
34. R.H. Kodama, Magnetic nanoparticles. J. Magn. Magn. Mater. **200**, 359 (1999)
35. Z.H. Wang et al., Microstructure and magnetic property of Fe–Co nanoparticles prepared by chemical vapor condensation process. J. Alloys Compd. **351**, 319 (2003)
36. Y. Saito, Nanoparticles and filled nanocapsules. Carbon **33**, 979 (1995)
37. H. Tokoro et al., Iron fine particles coated with boron nitride nanolayers synthesized by a solid phase reaction. Diam. Relat. Mater. **13**, 1139 (2004)
38. R. Fernández-Pacheco et al., Highly magnetic silica-coated iron nanoparticles prepared by the arc-discharge method. Nanotechnology **17**, 1188 (2006)
39. M. Mikhaylova et al., The effect of biocompatible coating layers on magnetic properties of superparamagnetic iron oxide nanoparticles. Hyperfine Interact. **156–157**, 257 (2004)
40. M. Bystrzejewski et al., Thermal stability of carbon-encapsulated Fe–Nd–B nanoparticles. J. Alloys Compd. **423**, 74 (2006)
41. T. Oku et al., Formation of carbon nanostructures with Ge and SiC nanoparticles prepared by direct current and radio frequency hybrid arc discharge. J. Mater. Res. **15**, 2182 (2000)
42. W. Wu et al., Preparation of carbon-encapsulated iron carbide nanoparticles by an explosion method. Carbon **41**, 317 (2003)
43. H. Song, X. Chen, Large-scale synthesis of carbon-encapsulated iron carbide nanoparticles by co-carbonization of durene with ferrocene. Chem. Phys. Lett. **374**, 400 (2003)
44. P. Gould, Nanoparticles probe biosystems. Mater. Today **2**, 36 (2004)
45. M. Bystrzejewski et al., Carbon-encapsulated magnetic nanoparticles as separable and mobile sorbents of heavy metal ions from aqueous solutions. Carbon **47**, 1201 (2009)
46. K. Pyrzyńska, M. Bystrzejewski, Comparative study of heavy metal ions sorption onto activated carbon, carbon nanotubes, and carbon-encapsulated magnetic nanoparticles. Colloids Surf. A **362**, 102 (2010)
47. K. Pyrzyńska, Sorption of Cd(II) onto carbon-based materiale-a comparative study. Microchim. Acta **169**, 7 (2010)
48. M. Bystrzejewski et al., Arc plasma synthesis of (Fe-Nd-B) – containing carbon encapsulates. Solid State. Phenom. **99–100**, 273 (2004)
49. M. Bystrzejewski, A. Huczko, Heterogenne nanoklastry węglowe: otrzymywanie, charakterystyka i perspektywy aplikacyjne. Przem. Chem. **84**, 92 (2005)

50. M. Bystrzejewski et al., Arc plasma synthesis of carbon encapsulates containing Fe-Nd-B. J. High Temp. Mater. Proc. **9**, 237 (2005)
51. M. Bystrzejewski et al., Arc plasma route to carbon-encapsulated magnetic nanoparticles for biomedical applications. Sens. Actuators B **109**, 81 (2005)
52. M. Bystrzejewski et al., Carbon encapsulation of magnetic nanoparticles, Fullerenes, Nanotubes. Carbon Nanostruct. **15**, 167 (2007)
53. M. Bystrzejewski et al., Mössbauer spectroscopy studies of carbon-encapsulated magnetic nanoparticles obtained by different routes. J. Appl. Phys. **104**, 54307 (2008)
54. J. Borysiuk et al., Structure and magnetic properties of carbon encapsulated Fe nanoparticles obtained by arc plasma and combustion synthesis. Carbon **46**, 1693 (2008)
55. M. Bystrzejewski et al., Bulk synthesis of carbon nanocapsules and nanotubes containing magnetic nanoparticles via low energy laser pyrolysis of ferrocene. Mater. Lett. **63**, 1767 (2009)
56. S. Cudziło et al., Spontaneous formation of carbon-based nanostructures by thermolysis-induced carbonization of halocarbons. Carbon **43**, 1778 (2005)
57. M. Bystrzejewski et al., Combustion synthesis route to carbon-encapsulated iron nanoparticles. Diam. Relat. Mater. **16**, 225 (2007)
58. M. Bystrzejewski, M.H. Rumelli, Novel nanomaterials for prospective biomedical applications: Synthesis, structure and toxicity. Pol. J. Chem. **81**, 1219 (2007)
59. M. Bystrzejewski et al., Carbon-encapsulated magnetic nanoparticles spontaneously formed by thermolysis route. Fullerenes, Nanotubes, Carbon Nanostruct. **16**, 217 (2008)
60. M. Bystrzejewski et al., An easy one – step route to carbon – encapsulated magnetic nanopartials. Fullerenes, Nanotubes, Carbon Nanostruct. **17**, 600 (2009)
61. M. Bystrzejewski et al., Self-sustaining high-temperature synthesis of carbon-encapsulated magnetic nanoparticles from organic and inorganic metal precursors. New Carbon Mater. **25**, 81 (2010)
62. M. Bystrzejewski et al., RF Plasma synthesis of carbon encapsulates. Pol. J. Appl. Chem. **49**, 23 (2005)
63. M. Bystrzejewski et al., Large scale continuous synthesis of carbon-encapsulated magnetic nanoparticles. Nanotechnology **18**, 145608 (2007)
64. M. Bystrzejewski et al., Continuous synthesis of carbon-encapsulated magnetic nanoparticles with a minimum production of amorphous carbon. Carbon **47**, 2040 (2009)
65. A.G. Merzhanov, Twenty years of search and findings, in *Combustion and Plasma Synthesis of High-Temperature Materials*, ed. by Z.A. Munir, J.B. Holt. (VCH Publishers, New York, 1990), pp. 1–53
66. A.G. Merzhanov, A.K. Filonenko, O roli plamenii v mekhanizmie gorenija porokhov, Izv. Akad. Nauk, Otd. Khim. Nauk nr 3, 560 (1963)
67. A.G. Merzhanov, I.P. Borovinskaya, Selfpropagating high-temperature synthesis of high-melting inorganic compounds. Dokl. Akad. Nauk SSSR **204**, 366 (1972)
68. K.A. Philpot et al., An investigation of the synthesis of nickel aluminides through gasless combustion. J. Mater. Sci. **22**, 159 (1987)
69. M. Ouabdesselam, Z.A. Munir, The sintering of combustion-synthesized titanium diboride. J. Mater. Sci. **22**, 1799 (1987)
70. Z.A. Munir, Synthesis of high temperature materials by self-propagating combustion methods. Am. Ceram. Soc. Bull. **67**, 342 (1988)
71. D. Brawn et al., Developments in the processing and properties of NdFeb-type permanent magnets. J. Magn. Magn. Mater. **248**, 432 (2002)
72. F. Tuinistra, J.L. Koenig, Raman spectrum of graphite. J. Chem. Phys. **53**, 1126 (1970)
73. Y. Wang, Raman spectroscopy of carbon materials: Structural basis of observed spectra. Chem. Mater. **2**, 557 (1990)
74. S. Cudziło et al., Characterization of carbonaceons materials produced by reduction of halocarbons with sodium azide. Pol. J. Appl. Chem. **49**, 205 (2005)

75. A. Huczko et al., Combustion synthesis as a novel method for production of 1-D SiC nanostructures. J. Phys. Chem. B **109**, 16244 (2005)
76. K.C. Patil, Advanced ceramics: Combustion synthesis and properties. Bull. Mater. Sci. **16**, 533 (1993)
77. J. Narayan et al., Mechanism of combustion synthesis of silicon carbide. J. Appl. Phys. **75**, 7252 (1994)
78. Z.A. Munir, Synthesis of high temperature materials by self-propagating combustion methods. Am. Ceram. Bull. **67**, 342 (1988)
79. K.C. Patil, Advanced ceramics: Combustion synthesis and properties. Bull. Mater. Sci. **16**, 533 (1993)
80. J.C. Toniolo et al., Synthesis of alumina powders by the glycine–nitrate combustion process. Mater. Res. Bull. **40**, 561 (2005)
81. J. Jiang et al., Self-propagating high-temperature synthesis of α-SiAlON doped by RE (RE=Eu,Pr,Ce) and codoped by RE and Yttrium. J. Am. Ceram. Soc. **87**, 703 (2004)
82. A. Huczko et al., Synthesis of novel nanostructures by metal-polytetrafluoroethene thermolysis. J. Phys. Chem. B **107**, 2519 (2003)
83. A. Huczko et al., Studies on spontaneous formation of 1D nanocrystals of silicon carbide. Crystal Res. Tech. **40**, 334 (2005)
84. M. Rümmeli et al., Modification of SiC based nanorods via a hydrogenated annealing process. Synthetic. Met. **153**, 349 (2005)
85. A. Huczko et al., Quasi one-dimensional ceramic nanostructures spontaneously formed by combustion synthesis. Phys. Stat. Sol. (b) **243**, 3297 (2006)
86. E.J. Conolly et al., A porous SiC ammonia sensor. Sens. Actuators B **109**, 44 (2005)
87. E.W. Wong et al., Nanobeam mechanics: Elasticity, strength, and toughness of nanorods and nonotubes. Science **277**, 1971 (1997)
88. J.J. Niu, J.N. Wang, Synthesis of macroscopic SiC nanowires at the gram level and their electrochemical activity with Pt loading. Acta Materialia. **57**, 3084 (2009)
89. R. Madar, Materials science: Silicon carbide in contention. Nature **430**, 974 (2004)
90. H. Dai et al., Synthesis and characterization of carbide nanorods. Nature **375**, 769 (1995)
91. D.H. Feng et al., Catalytic synthesis and photoluminescence of needle-shaped 3C–SiC nanowires. Solid State Comm. **128**, 295 (2003)
92. K.-W. Chang, J.-J. Wu, Temperature-controlled catalytic growth of one-dimensional gallium nitride nanostructures using a gallium organometallic precursor. Appl. Phys. A **77**, 769 (2003)
93. N. Keller et al., Synthesis and characterisation of medium surface area silicon carbide nanotubes. Carbon **41**, 2131 (2003)
94. K.W. Wong et al., Field-emission characteristics of SiC nanowires prepared by chemical-vapor deposition. Appl. Phys. Lett. **75**, 2918 (1999)
95. Y. Zhang et al., Synthesis of SiC nanorods using floating catalyst. Solid State Comm. **118**, 595 (2001)
96. A. Huczko et al., A self-assembly SHS approach to form silicon carbide nanofibres. J. Phys. Condens. Matter **19**, 395022 (2007)
97. M.H. Rümmeli et al., Novel catalysts, room temperature, and the importance of oxygen for the synthesis of single-walled carbon nanotubes. Nanoletters **5**, 1209 (2005)
98. M.H. Rümmeli et al., Novel catalysts for low temperature synthesis of single wall carbon nanotubes. Phys. Stat. Sol. (b) **243**, 3101 (2006)
99. G. Shen et al., Silicon carbide hollow nanospheres, nanowires and coaxial nanowires. Chem. Phys. Lett. **375**, 177 (2003)
100. G.W. Sears, Mercury Whiskers. Acta Metall. **1**, 457 (1953)
101. R.S. Wagner, W.C. Ellis, Vapor-liquid-solid mechanism of single crystal growth. Appl. Phys. Lett. **4**, 89 (1964)
102. V.M. Kevorkijan et al., Low-temperature synthesis of sinterable SiC powders by carbothermic reduction of colloidal SiO_2. J. Mater. Sci. **27**, 2705 (1992)

103. R.T.K. Baker et al., Effect of the surface state of iron on filamentous carbon formation. J. Catal. **77**, 74 (1982)
104. S. Cudziło et al., Characterization of carbonaceons materials produced by reduction of halocarbons with sodium azide. Pol. J. Appl. Chem. **49**, 205 (2005)
105. S. Cudziło et al., Surface properties of carbons obtained from hexachlorobenzene and hexachloroethane by combustion synthesis. Carbon **45**, 103 (2007)
106. A. Huczko et al., Characterization of 1-D nanoSiC-derived nanoporous carbon. Phys. Stat. Sol. (b) **244**, 3969 (2007)
107. A. Huczko et al., One – dimensional nanostructures spontaneously formed by combustion synthesis, XXth IWEP NM 2006, 4–11 March 2006, Kirchberg, Austria, Abstract Book, p. 56
108. A. Huczko et al., Quasi one-dimensional ceramic nanostructures spontaneously formed by combustion synthesis. Phys. Stat. Sol. (b) **243**, 3297 (2006)
109. A. Huczko et al., A self-assembly SHS approach to form silicon carbide nanofibres. J. Phys. Condens. Matter. **19**, 395022 (2007)
110. K. Takahashi et al., Thermal conductivity of SiC nanowire formed by combustion synthesis. High Temp.-High Pressures **37**, 119 (2008)
111. M.H. Rümmeli et al., Hydrogen activated axial inter-conversion in SiC nanowires. J. Solid State Chem. **182**, 602 (2009)
112. A. Huczko et al., Silicon carbide nanowires: Synthesis and cathodoluminescence. Physica Status Solidi, Phys. Status Solidi B **246**, 2806 (2009)
113. A. Busiakiewicz et al., Silicon carbide nanowires: Chemical characterization and morphology investigations. Phys. Status Solidi B **245**, 2094 (2008)
114. A. Busiakiewicz et al., Scanning tunneling microscopy investigations of silicon carbide nanowires. Appl. Surf. Sci. **254**, 4268 (2008)
115. A. Busiakiewicz et al., Silicon carbide nanowires studied by scanning tunneling spectroscopy. Surf. Sci. **602**, 316 (2008)
116. A. Busiakiewicz et al., Characterization of SiC nanowires obtained via combustion synthesis. Acta Phys. Superficierum **XI**, 73 (2009)
117. A. Busiakiewicz et al., Defects of SiC nanowires studied by STM and STS. Appl. Surf. Sci. **256**, 4771 (2010)
118. V. Poornima et al., Epoxy/SiC nanocomposites: synthesis and characterization. Composites **10**, 11 (2010)

Transport Properties in Carbon Nanotubes

Stefano Bellucci and Pasquale Onorato

Abstract This chapter focuses on the general theory of the electron transport properties of carbon nanotubes, yielding an overview of theoretical models. It is organized in five sections describing the results of the research activity performed in electronic/electrical properties modelling. The first section, in addition to describing the scope of the review and providing an introduction to its content, yields as well a general introduction on carbon nanotubes. Sect. 'Electronic Structure of Single-Wall Nanotubes' describes the general theory of the electron transport in carbon nanotubes, starting from the band structure of graphene. Sect. 'Quantum Transport in Carbon Nanotubes' focuses on the quantum transport in carbon nanotubes, including ballistic transport, Coulomb-blockade regime, Luttinger Liquid theory. Sect. 'Results and Experiments' reports results and experimental evidence of the models decribed. Finally, Sect. 'Superconducting transition' addresses the issue of superconductivity transitions in carbon nanotubes.

Introduction

In the last 20 years progresses in technology allowed for the *construction* of several new devices in the range of nanometric dimensions. The well known Moore prediction states that the silicon-data density on a chip doubles every 18 months. So we are going toward a new age when the devices in a computer will live on the nanometer scale and will be ruled by the Quantum Mechanics laws.

Recently several scientists proposed a new carbon based technology against the usual silicon one. The allotropes of carbon, carbon nanotubes, single atomic layers of graphite (graphene), fullerene molecules and diamond have emerged recently as new electronic materials with unique properties. In this sense the discovery of

S. Bellucci (✉)
INFN, Laboratori Nazionali di Frascati, P.O. Box 13, 00044 Frascati, Italy
e-mail: stefano.bellucci@lnf.infn.it

S. Bellucci (ed.), *Physical Properties of Ceramic and Carbon Nanoscale Structures*,
Lecture Notes in Nanoscale Science and Technology 11,
DOI 10.1007/978-3-642-15778-3_2,

carbon nanotubes in 1991 [1] opened a new field of research in the physics at nanoscales [2]. Thus carbon nanotubes have become very promising in the field of molecular electronics, in which atoms and molecules are envisaged as the building blocks in the fabrication of electronic devices.

Hystory and Structure

The existence of single-walled carbon tubes was pointed out in 1976 [3] but the subject seems to have become prominent after the discovery of fullerene in 1985 [4] and the identification of nanotubes by Iijima in 1991 [1].

Carbon nanotubes (CNs) are basically rolled up sheets of graphite (hexagonal networks of carbon atoms) forming tubes that are only nanometers in diameter and have length up to some microns (see Fig. 1. *top*). Several experiments in the last 15 years have shown their interesting properties [5–7]. The nanometric size of CNs, together with the unique electronic structure of a graphene sheet, make the electronic prop erties of these one-dimensional (1D) structures highly unusual.

CNs may also display different behaviors depending on whether they are single-walled carbon nanotubes (SWNTs) or multi-walled carbon nanotubes (MWNTs) that are typically made of several (typically 10) concentrically arranged graphene sheets (see Fig. 1. *left bottom*). Thus SWNT can be thought of as the fundamental cylindrical structure, and these form the building blocks of both multi-wall nanotubes and the arrays of single-wall nanotubes, also bundles. Bundles typically contain many tens of nanotubes and can be considerably longer and wider than the nanotubes from which they are formed. This could have important toxicological

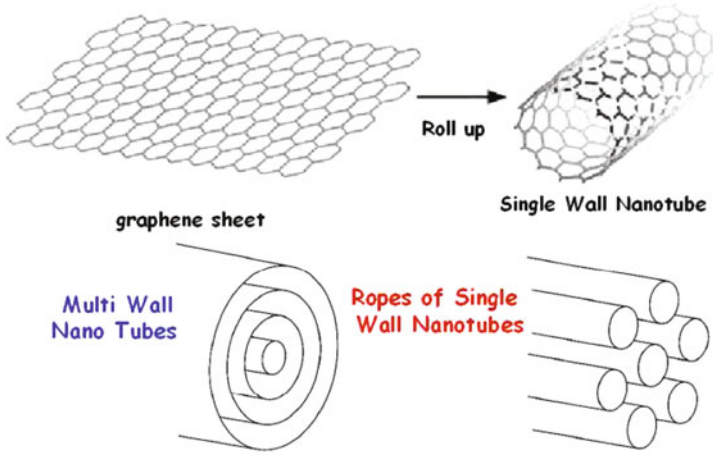

Fig. 1 The structure of a SWNT can be conceptualized by wrapping a one-atom-thick layer of graphite called graphene into a seamless cylinder. The way the graphene sheet is wrapped is represented by a pair of indices (n,m) called the chiral vector. The integers n and m denote the number of unit vectors along two directions in the honeycomb crystal lattice of graphene. (*Bottom left*) Multi Wall Nano Tubes : several (typically 10) concentrically arranged graphene sheets (Russian doll) (*Bottom right*) Ropes of SWCNTs Triangular lattice of 5–100 SWCNT

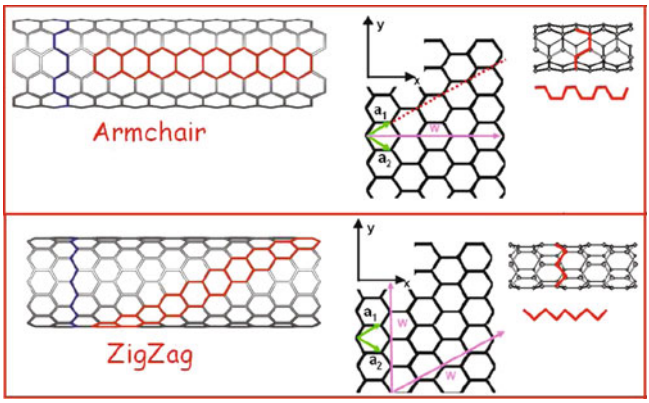

Fig. 2 Armchair and ZigZag nanotubes. The CN is made by coiling a graphene sheet about two points connected by the vector $\vec{w}$. (*Top*) In the case of armchair the vector $\vec{w}$ is known as $\vec{w} = (n \cdot a_1) + (n \cdot a_2)$, or $\vec{w} = (n, n)$. (*Bottom*) The second nanotube, the ZigZag one, is made by coiling a graphene sheet with a vector $(n \cdot a_1) + (0 \cdot a_2)$, or $(n, 0)$. Notice that analogous ZigZag CN is obtained with a wrapping vector $(n, -n)$

consequences. The strong tendency of both SWCNT or MWCNT to bundle together in ropes is a consequence of attractive van der Waals forces analogous to forces that bind sheets of graphite [8]. In Ref. [8] the authors found that the individual SWNTs are packed into a close-packed triangular lattice with a lattice constant of about 17 Å the density, lattice parameter, and interlayer spacing of the ropes was dependent on the chirality of the tubes in the mat [9] (see Fig. 2).

Synthesis and Characterization

CNs vary significantly in length and diameter depending on the synthetic procedure. Lengths are generally dependent on synthesis time but are typically tens of microns, although significantly shorter and longer nanotubes have been made [10, 11]. An individual SWNT has typical dimensions $L : 1\,\mu\text{m}$ and $R : 1\,\text{nm}$ while MWCNT generally range from 10 nm to 200 nm in diameter [12].

Structure of a Single Wall CN

A few key studies have explored the structure of carbon nanotubes using high-resolution microscopy techniques. These experiments have confirmed that nanotubes are cylindrical structures based on the hexagonal lattice of carbon atoms that forms crystalline graphite.

Three types of nanotubes are possible, called armchair, zigzag and chiral nanotubes, depending on how the two-dimensional graphene sheet is 'rolled up' (see

Fig. 1). The different types are most easily explained in terms of the unit cell of a carbon nanotube, the smallest group of atoms that defines its structure [13].

There are many ways of choosing the lattice vectors, but some are more comfortable to work with than others. In Fig. 1 we have chosen a_1 and a_2 to be two upright secants of a isosceles triangle within two hexagons. In Cartesian coordinates the lattice vectors can be written as,

$$a_1 = \frac{a_0}{2}(3, \sqrt{3}) = \frac{a}{2}(\sqrt{3}, 1), \quad a_2 = \frac{a_0}{2}(3, -\sqrt{3}) = \frac{a}{2}(\sqrt{3}, -1)$$

where $a_0 \approx 1.42$Å is the carbon-carbon distance and $a = \sqrt{3}a_0$. The so-called chiral (or wrapping) vector of the nanotube, $\vec{w}$, is defined by

$$\vec{w} = m_w a_1 + n_w a_2,$$

where n_w and m_w are integers. The roll up vector, $\vec{w}$, (also called the Chiral vector $\vec{C}_h$) determines the circumference of the carbon nanotube. In fact the radius, R, is simply the length of the chiral vector divided by 2π, and we find that

$$R = \frac{|(m_w \cdot a_1) + (n_w \cdot a_2)|}{2\pi}.$$

Another important parameter is the chiral angle, which is the angle between $\vec{w}$ and a_1. When the graphene sheet is rolled up to form the cylindrical part of the nanotube, the ends of the chiral vector meet each other. The chiral vector thus forms the circumference of the nanotube's circular cross-section, and different values of n and m lead to different nanotube structures. Armchair nanotubes are formed when $n_w = m_w$ and the chiral angle is 30° (see *top* figure). Zigzag nanotubes are formed when either n or m are zero and the chiral angle is 0°. All other nanotubes, with chiral angles intermediate between 0° and 30°, are known as chiral nanotubes. The properties of nanotubes are determined by their diameter and chiral angle, both of which depend on $\vec{w}$.

Thus values of n_w and m_w determine the chirality, or 'twist' of the nanotube. The chirality in turn affects the conductance of the nanotube, its density, its lattice structure, and other properties. As we demonstrate below SWNT is considered metallic if the value $n_w - m_w$ is divisible by three. Otherwise, the nanotube is semiconducting. Consequently, when tubes are formed with random values of n_w and m_w, we would expect that two-thirds of nanotubes would be semi-conducting, while the other one-third would be metallic, which happens to be the case.

Electronic Structure of Single-Wall Nanotubes

As we discussed above the electronic properties of CNs depend on their diameter, chiral angle (helicity) parameterized by the roll-up vector $\vec{w}$ and an applied magnetic field. Hence it follows that some nanotubes are metallic with high electrical conductivity, while others are semiconducting with relatively low band gaps.

Band Structure of Graphene

We describe here the band structure of carbon nanotubes by the technique of projecting the band dispersion of a 2D graphite layer into the 1D longitudinal dimension of the nanotube. The 2D band dispersion of graphene can be found in [14]. It consists of an upper and a lower branch that only touch at the corners of the hexagonal Brillouin zone. Thus, when the system is at half-filling, the metallic properties derive from a pair of inequivalent Fermi points, around which there is conical dispersion for the modes of the graphene sheet.

The 2D layer in graphite, known as *graphene* was largely studied in recent years [15] also because of the isolation of single layer graphene by Novoselov et al. [16]. One of the most interesting aspects of the graphene problem is that its low energy excitations are massless, chiral, Dirac fermions. In neutral graphene the chemical potential crosses exactly the Dirac point. This particular dispersion, that is only valid at low energies, mimics the physics of quantum electrodynamics (QED) for massless fermions except by the fact that in graphene the Dirac fermions move with a speed v_F which is 300 times smaller than the speed of light, c. Hence, many of the unusual properties of QED can show up in graphene but at much smaller speeds [17–19]. Dirac fermions behave in very unusual ways when compared to ordinary electrons if subjected to magnetic fields, leading to new physical phenomena [20, 21] such as the anomalous integer quantum Hall effect (IQHE) measured experimentally [22, 23].

Graphene has a honeycomb structure as shown in Fig. 3. The structure is not a Bravais lattice but it can be seen as a triangular lattice with a basis of two atoms per unit cell. Of particular importance for the physics of graphene are the two points

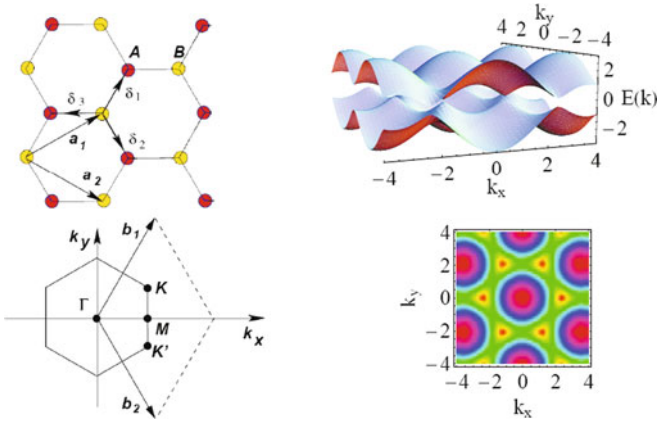

Fig. 3 (*Top.Left*) Lattice structure of graphene, made out of two interpenetrating triangular lattices ($\mathbf{a}_1$ and $\mathbf{a}_2$ are the lattice unit vectors, and $\boldsymbol{\delta}_i, i = 1, 2, 3$ are the nearest neighbor vectors) (*Bottom.Left*) corresponding Brillouin zone. The Dirac cones sit at the K and K′ points. (*Top.Right*) Energy bands for finite v t =2.7 eV and $t' = 0$, the cusps appear at the six corners of the first Brillouin zone as enphasized in panel (*Bottom.Right*) where the density plot of the energy levels in a graphite sheet is reported

K and K' at the corners of the graphene's Brillouin zone (BZ). These are named Dirac points. Their positions in momentum space are given by:

$$K = \left(\frac{2\pi}{3a}, \frac{2\pi}{3\sqrt{3}a}\right), \quad K' = \left(\frac{2\pi}{3a}, -\frac{2\pi}{3\sqrt{3}a}\right). \tag{1}$$

The three nearest neighbors vectors are given by, $\delta_1 = \frac{a}{2}(1, \sqrt{3})$, $\delta_2 = \frac{a}{2}(1, -\sqrt{3})$ and $\delta_3 = -a(1, 0)$, while the six second-nearest neighbors are located at: $\delta_1^{'} = \pm a_1, \delta_2^{'} = \pm a_2, \delta_3^{'} = \pm(a_2 - a_1)$.

The Tight-Binding Approach

The tight-binding Hamiltonian for electrons in graphene considering that electrons can hop both to nearest and next nearest neighbor atoms has the form,

$$H = -t \sum_{\langle i,j\rangle,\sigma} \left(a^{\dagger}_{\sigma,i} b_{\sigma,j} + \text{h.}c.\right) - t' \sum_{\langle\langle i,j\rangle\rangle,\sigma} \left(a^{\dagger}_{\sigma,i} a_{\sigma,j} + b^{\dagger}_{\sigma,i} b_{\sigma,j} + \text{h.}c.\right), \tag{2}$$

where $a_{i,\sigma}$ ($a^{\dagger}_{i,\sigma}$) annihilates (creates) an electron with spin σ ($\sigma = \uparrow, \downarrow$) on site R_i on sub-lattice A (an equivalent definition is used for sub-lattice B, see Fig. 2), t ($\approx$ 2.8 eV) is the nearest neighbor hopping energy (hopping between different sub-lattices). Next we neglect t' ($\approx$ 0.1 eV) i.e. the next nearest neighbor hopping energy (hopping in the same sub-lattice) [24]. The energy bands derived from this Hamiltonian have the form [25]:

$$E(k) = \pm t \sqrt{1 + 4\cos^2\left(\frac{\sqrt{3}}{2} k_y a_0\right) + 4\cos\left(\frac{\sqrt{3}}{2} k_y a_0\right)\cos\left(\frac{3}{2} k_x a_0\right)} \tag{3}$$

where the plus sign applies to the upper (π) and the minus sign the lower (π^*) band. It is clear from Eq. 3 that the spectrum is symmetric around zero energy. In Fig. 3. *Top.Right* we show the full band structure of graphene.

The band structure close to one of the Dirac points shows clearly a conical dispersion

$$E_{\pm}(\mathbf{q}) \approx \pm v_F |\mathbf{q}| \tag{4}$$

where $q = k - K$ is the momentum measured relatively to the Dirac points and v_F represents the Fermi velocity, given by $v_F = 3ta/2$, with a value v_F; 1×10^6 m/s [25].

The most striking difference between this result and the usual case, $\varepsilon(q) = q^2/(2m)$ where m is the electron mass, is that the Fermi velocity in Eq. 4 does not depend on the energy or momentum: in the usual case we have $v = k/m = \sqrt{2E/m}$ and hence the velocity changes substantially with energy.

Since the basis of the honeycomb lattice contains two atoms, there are two sub-lattices and two degenerate Bloch states at each Fermi point. If we choose the Bloch

functions separately on each sublattice such that they vanish on the other, then we can expand the electron operator in terms of the Bloch waves

$$\Psi_\sigma(x,y) : \sum_{p\alpha} \exp(-i\alpha K \cdot r) F_{p\alpha\sigma}(x,y) \tag{5}$$

where $\alpha = \pm$ labels the Fermi point, $r = (x,y)$ lives on the sublattice $p = \pm$ under consideration and $F_{p\alpha\sigma}(x,y)$ denote slowly varying operators. Thus, we can conclude that the low-energy excitations of the honeycomb lattice at half-filling are described by an effective theory of two 2D Dirac spinors [14].

Band Structure of Carbon Nanotubes

Starting from the graphene band structure Eq. 3, after introducing periodic boundary conditions due to the cylindrical geometry of the tube (i.e. the wrapping vector $\overleftarrow{w}$), we can obtain the energy bands of a carbon nanotube.

From Graphene to Carbon Nanotubes

In this section we start from Eq. 3 and discuss first the general case of Chiral CNs then the highly symmetric nanotubes, namely (1) the armchair (n,n) and (2) the zig-zag $(n,0)$.

For the case of a chiral nanotube we can write the general condition

$$\vec{w} \cdot \vec{k} = 2\pi m; \quad m \in Z.$$

It follows that we can define a quantization rule,

$$\frac{\sqrt{3}a}{2}(m_w + n_w)k_x + \frac{a}{2}(m_w - n_w)k_y = 2\pi m,$$

then

$$k_x = \frac{4\pi m}{\sqrt{3}a(m_w + n_w)} + \frac{(n_w - m_w)}{\sqrt{3}(m_w + n_w)}k_y = \frac{4\pi m}{\sqrt{3}an_+} + \frac{n_-}{\sqrt{3}n_+}k_y.$$

Substitution of the discrete allowed values for k_x into Eq. 3 yields the energy dispersion relations for the generic chiral tube,

$$E_m(k) = \pm t\sqrt{1 + 4\cos\left(\frac{2m\pi}{n_+} + \frac{n_-}{2n_+}k_y\right)\cos\left(\frac{\sqrt{3}k_y}{2}a_0\right) + 4\cos^2\left(\frac{\sqrt{3}k_y}{2}a_0\right)}. \tag{6}$$

In the case (1) $|2\pi R| = n|(a_1 + a_2)| = n\sqrt{3}a$. Thus due to the periodic boundary condition along the x direction, the wavevector component k_x is quantized,

$$k_x = m\frac{2\pi}{n\sqrt{3}a};\ \ m \in Z$$

Substitution of the discrete allowed values for k_x into Eq. 3 yields the energy dispersion relations for the armchair tube

$$E_m(k) = \pm t\sqrt{1 \pm 4\cos\left(\frac{m\pi}{n}\right)\cos\left(\frac{\sqrt{3}\,k}{2}a_0\right) + 4\cos^2\left(\frac{\sqrt{3}\,k}{2}a_0\right)} \tag{7}$$

where $-\pi < ka < \pi$.

The case (2), i.e. a zigzag nanotube, is characterized by a wrapping vector in the form $(n, 0)$ or $(n, -n)$, the latter case gives a simple quantization rule in the form

$$k_y = m\frac{2\pi}{na};\ \ m \in Z$$

so that

$$E_m(k) = \pm t\sqrt{1 + 4\cos^2\left(m\frac{2\pi}{n}\right) \pm 4\cos\left(\frac{2\pi}{n}\right)\cos\left(\frac{3}{2}k_x a_0\right)}, \tag{8}$$

where $-\pi/3 < k_x a_0 < \pi/3$.

Thus we obtain that just $1/3$ of the possible nanotubes are metallic when the condition $m_w - n_w = 3q$, with q integer, is fulfilled. At half-filling, metallic nanotubes have two Fermi points (see Fig. 3 *Left*) corresponding to large momenta

$$\pm K_s = \pm(2\pi)/(3a_0)$$

Here we choose a nanotube oriented as in Fig. 4. *left*, thus the low-energy expansion Eq. 5 transforms correspondingly and the electron operator reads [26]

$$\Psi_\sigma(\varphi, y) = \sum_{p\alpha} (2\pi R)^{-1/2} \exp(-i\alpha K \cdot r)\,\psi_{p\alpha\sigma}(y) \tag{9}$$

which introduces 1D fermion operators $\psi_{p\alpha\sigma}(y)$ depending only on the longitudinal coordinate y. The fact of having four low-energy linear branches at the Fermi level introduces a number of different scattering channels, depending on the location of the electron modes near the Fermi points.

In general, we can define an approximate one-dimensional bandstructure for momenta near $\pm K_s$

$$\varepsilon_0(m, \overleftarrow{w}, k) \approx \pm\frac{v_F\hbar}{R}\sqrt{\left(\frac{m_w - n_w + 3m}{3}\right)^2 + R^2(k \pm K_s)^2} \tag{10}$$

where R is the tube radius.

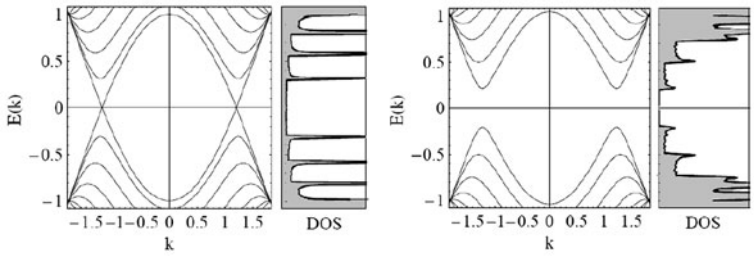

Fig. 4 Band structure and density of states for a (10, 10) armchair nanotube within the zone-folding model. The 1D energy dispersion relations are presented in the $(-1; 1)$ energy interval in units $t : 2.9$ eV. The Fermi level is located at zero energy. Band structure and density of states for a (20, 0) zigzag nanotube within the zone-folding model. The Fermi level is located at zero energy

For a metallic CN (e.g. the armchair one with $m_w = n_w$) we obtain that the energy vanishes for two different values of the longitudinal momentum $\varepsilon_0(\pm K_s) = 0$. As we discussed for graphene, the dispersion law $\varepsilon_0(m, k)$ in the case of undoped metallic nanotubes is quite linear near the crossing values $\pm K_s$. The linear dispersion relation holds for energy scales $E < D$, with the bandwidth cutoff scale

$$D : v_F \hbar / R \approx 0.7\, eV/R(\mathrm{nm}^{-1}),$$

which is a relevant quantity also to define a low-energy regime ($k_B T < D$). The latter regime is often met even at room temperature for usually small radius CNs.

Dirac Fermions Approach

Starting from Eq. 10 we can develop a Dirac-like theory for CNs obtained by taking a continuum limit in which the momenta are much smaller than the inverse of the $C - C$ distance a_0 [27] (the continuum limit also requires $\ell_\omega^2 >> aR$ so that lattice effects can be disregarded). Thus we write the Hamiltonian, near a Fermi point, as

$$H_D = v_F \left[\hat{\alpha}(\hat{\pi}_\varphi) + \hat{\beta}\, \hat{\pi}_y \right], \tag{11}$$

where $\hat{\pi}_\varphi = \frac{L_y}{R} = -i \frac{\hbar}{R} \frac{\partial}{\partial \varphi}$ corresponds to the momentum along the circumference of the nanotube while $\hat{\pi}_y = \hat{p}_y \pm \hbar K_s$ is the momentum along the axis. The Hamiltonian above gives a Dirac like equation which has a solution in the spinorial form $\hat{\psi}$ where

$$\hat{\alpha} = \alpha \begin{pmatrix} 0 & i \\ -i & 0 \end{pmatrix} \quad \hat{\beta} = \begin{pmatrix} 0 & 1 \\ 1 & 0 \end{pmatrix} \quad \hat{\Psi} = \begin{pmatrix} \psi_\uparrow \\ \psi_\downarrow \end{pmatrix}. \tag{12}$$

Eq. 11 can be compared with the one obtained in [28]. For the metallic CN, such as the armchair one, the problem in Eq. 11 has periodic boundary conditions

i.e. $\Psi(\varphi + 2\pi, y) = \Psi(\varphi)$, it follows that a factor $e^{im\varphi}$ appears in the wavefunction while for semiconducting CNs ($m_w \neq n_w$) we have to define *quasiperiodic boundary conditions i.e.* $\Psi(\varphi + 2\pi, y) = \omega\Psi(\varphi)$ [28] corresponding to a phase factor in the wavefunction $e^{i\left(m+\frac{m_w-n_w}{3}\right)\varphi}$ (next we use $m_0 = m_w - n_w$).

Thus we can trivially obtain the spinorial eigenfunctions as

$$\hat{\Psi}_+ = \begin{pmatrix} \cos(\gamma) \\ \sin(\gamma) \end{pmatrix} e^{i\left(m+\frac{m_w-n_w}{3}\right)\varphi} e^{iky}; \qquad \hat{\Psi}_- = \begin{pmatrix} -\sin(\gamma) \\ \cos(\gamma) \end{pmatrix} e^{i\left(m+\frac{m_w-n_w}{3}\right)\varphi} e^{iky}, \tag{13}$$

by choosing appropriately γ. The eigenenergies are given by Eq. 10.

Thus, in relation to the study of transport properties, often an important quantity linked to the dispersion relation is the so-called effective mass of the charge carriers. In semiconducting nanotubes, this quantity can be derived from the Eq. 10 as $m_{eff} = m + m_0$ and vanishes (massless Dirac Fermions) for the electrons belonging to the lowest subband of a metallic CN. This concept has been used [29] to estimate the charge mobility properties in semiconducting nanotubes.

The Density of States

The density of states (DOS) $\Delta N/\Delta E$ represents the number of available states for a given energy interval ΔE. This DOS is a quantity that can be measured experimentally under some approximations. The shape of the density of states is known to depend dramatically on dimensionality. In 1D, as shown below, the density of states diverges as the inverse of the square root of the energy close to band extrema. These spikes in the DOS are known as Van Hove singularities and manifest the confinement properties in directions perpendicular to the tube axis. As carbon nanotubes are one dimensional, their corresponding DOS exhibits a spiky behavior at energies close to band edges as shown in Fig. 3. The position of these Van Hove singularities can be analytically derived from the dispersion relations.

Magnetic Field and Landau Energy Bands of Carbon Nanotubes

The application of a uniform external magnetic field has profound consequences on the electronic band structure of carbon nanotubes. There exist two cases of high symmetry for the direction of the magnetic field with respect to the nanotube axis (see Fig. 4).

When the magnetic field is applied parallel to the tube axis, electrons within the nanotube are influenced by the electromagnetic potential, whose dominating effect is to add a new phase factor, the Aharonov-Bohm quantum phase, to the quantum wave function with subsequent modification of the associated momentum.

When a transverse magnetic field is present, in metallic tubes were found a suppression of the Fermi velocity at half-filling and an enhancement of the density of states while in semiconducting tubes the energy gap is suppressed.

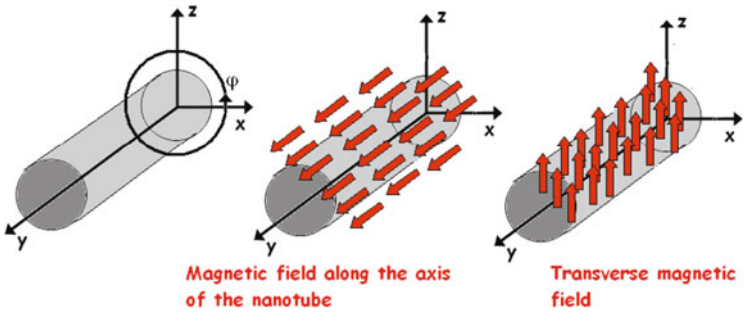

Fig. 5 (*Left*) Schematic draw of an isolated CN with the longitudinal axis along the y direction. The two cases of high symmetry for the direction of the magnetic field with respect to the nanotube axis: (Middle) the magnetic field is applied parallel to the tube axis, (*Right*) the magnetic field is applied perpendicular to the tube axis

Here the electron properties of carbon nanotubes are studied using a model of a massless Dirac particle on a cylinder [30]. As it was discussed by Lee and Novikov [28] the problem possesses supersymmetry which protects low-energy states and ensures stability of the metallic behavior in arbitrarily large fields. These features qualitatively persist (although to a smaller degree) in the presence of electron interactions. Here we propose a simplified version of the theory proposed in [28] also if several works on the standard tight binding approach were presented in the last years.

Transverse Magnetic Field

A cylindrical carbon nanotube with the axis along the y direction and B along z, corresponds to

$$H_D = v_F \left[\hat{\alpha}(\hat{\pi}_y) + \hat{\beta} \left(\hat{\pi}_y - \frac{e}{c} A \right) \right], \tag{14}$$

The minimal form of the coupling to external fields follows from the gauge invariance while we choose the gauge so that the system has a symmetry along the $\hat{y}$ direction,

$$A = (0, Bx, 0) = (0, BR\cos(\varphi), 0)$$

and we introduce the cyclotron frequency $\omega_c = \dfrac{eB}{m_e c}$ and the magnetic length $\ell_\omega = \sqrt{\hbar/(m\omega_c)}$.
It is customary to discuss the results in terms of two parameters, one for the scale of the energy following from Eq. 10

$$\Delta_0 = \hbar v_F R\,, \tag{15}$$

the second one being the scale of the magnetic field

$$\nu \equiv \pi R^2 2\pi \ell_\omega^2 = \pi R^2 B \Phi_0 \quad \text{where} \quad \Phi_0 = hce. \tag{16}$$

Here we can calculate the effects of the magnetic field by diagonalizing Eq. 14, after introducing the trial functions

$$\bar{\psi}_{s,m,k}(\varphi, y) = N e^{i(ky+(m+m_0)\varphi)}\big(\alpha_s + \beta_s \sin(\varphi) + \gamma_s \cos(\varphi)\big). \tag{17}$$

Results are reported in Fig. 6 for different CNs and values of the magnetic field.

From the expression of $|\Psi_{m,\pm k}(\varphi, y)|^2$ we deduce a kind of 'edge localization' of the opposite current, analogous to the one obtained for the QW [32] also for CNs.

Following the calculations reported in [28] for a metallic CN we can easily calculate the linear dispersion relation changes near the band center $\varepsilon = 0$. Thus, the magnetic dependent energy can be written, near the Fermi points $k : K_s$, in terms of ν as

$$\varepsilon(|k - K_s|) = \pm\hbar|k - K_s|\,(v_F I_0(4\nu)) \ . \tag{18}$$

This describes a reduction of the Fermi velocity $\hbar^{-1} d\varepsilon/dk$ near $\varepsilon = 0$ by a factor $I_0(4\nu)$.

Hence, the magnetic dependent Fermi wavevector follows

$$k_F(\varepsilon_F, \nu, 0) \approx K_s + \left(\frac{\varepsilon_F}{\hbar v_F}\right) I_0(4\nu),$$

where the second term in the r.h.s. depends on B as

$$k_F = K_s \pm k_0 + k(B) \approx K_s \pm k_0(1 + 4\nu^2 + ...) \rightarrow k(B) : 4k_0\nu^2,$$

where $k_0 = \left(\frac{\varepsilon_F}{\hbar v_F}\right)$.

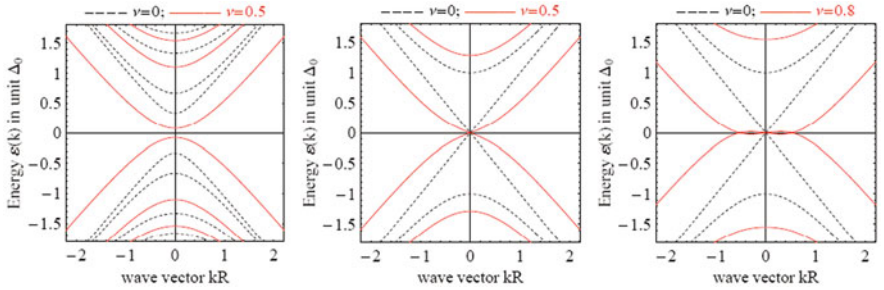

Fig. 6 In the x-axis the wavevector in unit $(k_y - K_s)R$ $(\pi_y R/\hbar)$. (*left*) Bandstructure of a non-metallic CN with (*red lines*) and without (*black dashed lines*) the transverse magnetic field ($\nu = 0.5$). The main consequence of B is the reduction of the semiconducting gap. (*Middle* and *right*) Bandstructure of a metallic CN with (*red lines*) and without (*black dashed lines*) the transverse magnetic field. The main consequence of B at intermediate fields is the rescaling of the Fermi velocity, while for quite strong fields a flat zone appears near $\pi_y = 0$. We know that the magnetic parameter $\nu \approx 0.2$ for $B : 5\,T$ and $R \approx 50\,nm$ [31]

In Fig. 6 we show how the bandstructure can be modified by the presence of a transverse magnetic field. On the left we show that for a semiconducting CN the main consequence of B is the reduction of the semiconducting gap. On the right we note that for metallic CNs that the gap vanishes and we get massless subbands crossing each other at zero energy. The flat region near K_s correspond to the insurgence of Localized Landau levels.

The closure of the gap at a magnetic field $B < 5$ T is consistent with the results for semiconducting carbon nanotubes in [33]. From there we can infer that the magnetic field needed to close the gap of a nanotube with radius $R = 10$ nm must be of the order of 10 T. This field strength would be reduced by a factor of 4 after doubling the nanotube radius, keeping the same ratio of R/ℓ_ω.

The evolution of the band structure of the thick nanotubes considered here is quite different from that of carbon nanotubes with typical radius (≈ 1 nm) in strong magnetic fields. The latter have been investigated in [34], where typical oscillations have been reported in the low-energy levels of carbon nanotubes with $R \approx 1$ nm as the magnetic field is increased to ratios of $R/\ell_\omega = 3$. The reason why the low-energy levels do not stabilize at increasing magnetic field can be traced back to the fact that, for such thin carbon nanotubes, there is no regime where the continuum limit with $aR/\ell_\omega^2 = 1$ can be realized.

Edge States, Landau Levels and Hall Effect

In the section above we discussed the effects of an external magnetic field on the bandstructure of a CN. Here, following Refs. [35, 36] we discuss how, for thick carbon nanotubes in a transverse magnetic field, the transport properties can be governed by the states localized at the flanks of the nanotube, which carry quantized currents in the longitudinal direction.

The effects of a transverse magnetic field on the transport properties of the carbon nanotubes were investigated making use of the description of the electronic states in terms of Dirac fermion fields [35, 36] i.e. the discussed continuum limit. It follows that the results reported in Fig. 6.*right* are valid for thick CNs while in the cases of thin CNs where the low-energy levels do not get stabilized at increasing magnetic field, by the time that we have $R \geq \ell_\omega$, the magnetic length cannot be much larger than the $C - C$ distance, so that a quantum Hall regime cannot exist in thin carbon nanotubes. This can be also appreciated in the results of cuni [37], where the density of states of several carbon nanotubes is represented at very large magnetic fields, with a marked difference between the cases of thin and thick nanotubes. It has been shown for instance that the density of states for nanotube radius $R \approx 14$ nm already resembles that of the parent graphene system, with clear signatures of Landau subbands in the low-energy part of the spectrum.

Thus we conclude that for nanotubes with a radius $R \approx 20$ nm, in a magnetic field of ≈ 20 T, the band structure shows a clear pattern of Landau levels. This opens the possibility of observing the quantization of the Hall conductivity in multi-walled nanotubes, σ_{xy}.

In the case of graphene, it has been shown that σ_{xy} has plateaus at odd multiples of $2e^2/h$, as a consequence of the peculiar Dirac spectrum [20, 21]. In Refs. [35, 36]

was obtained that the different topology of the carbon nanotubes leads instead to a quantization in even multiples of the quantity $2e^2/h$, with steps in σ_{xy} which are doubled with respect to those in graphene.

Regarding the spatial distribution, there is also a clear correspondence between the localization of the states in the angular variable φ and the value of the current. This can be appreciated from the analysis of the eigenstates of the Hamiltonian (see Eq. 17, Fig. 6 of [35], where the angular distribution of states from the lowest Landau subband for $B = 20$ T or the schematic plot in Fig. 7).

Thus the role of the magnetic field is to separate left-moving and right-moving currents at opposite sides of the tube. The localization of the current in the states of the dispersive branches opens the possibility to observe the quantization of the Hall conductivity in thick carbon nanotubes.

Therefore the Hall conductivity, defined by $\sigma_{xy} = I/V_H$, must have a first plateau as a function of the filling level, with a quantized value given by the spin degeneracy and the doubling of the subbands

$$\sigma_{xy} = 4\frac{e^2}{h} \tag{19}$$

As the filling level is increased, the situation changes when the Fermi level starts crossing the bumps with parabolic dispersion

The contribution of each inner dispersive branch to the Hall conductivity turns out to be then smaller than the quantized value from the outermost edge states. Consequently, an approximate quantization of σ_{xy} is observed above the first plateau, as shown in Fig. 6.*right*, with steps according to the degeneracy of the subbands:

$$\sigma_{xy} \approx (2 + 4n)2\frac{e^2}{h}. \tag{20}$$

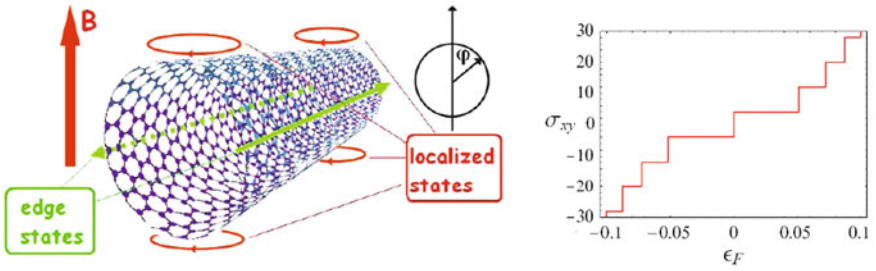

Fig. 7 Each eigenfunction is in general localized around a certain value of the angular variable φ. We observe, for instance, that the states at $k = 0$ have wave functions localized at $\varphi = 0$ or $\varphi = \pi$, with the contribution to the current from the left component compensating exactly that from the right component. For positive (negative) longitudinal momentum, the states in the flat zero-energy level are localized at angles between 0 and $\pi/2$ ($3\pi/2$), or between π and $\pi/2$ ($3\pi/2$), depending on the subband chosen. For the states in the dispersive branches, the eigenfunctions are centered around $\pi/2$ (for a *right* branch) or $3\pi/2$ (for a left branch). (*Right*) Plot of the Hall conductivity (in units of e^2/h) as a function of the position of the Fermi level ε_F in the band structure for a sharp voltage drop in the bulk of the nanotube (adapted from [35])

Magnetic Field along the Axis of the SWCNT

As we discussed above a magnetic field along the axis of the SWCNT also modifies the band structure. One way to see this is to add an Aharonov-Bohm flux term to the quantization condition

The cylindrical carbon nanotube with the axis along the y direction and B along y, corresponds to

$$H_D = v_F \left[\hat{\alpha}(\hat{\pi}_\varphi - \frac{\hbar}{R}\frac{\Phi(B)}{\Phi_0}) + \hat{\beta}\left(\hat{\pi}_y - \frac{e}{c}A\right)\right], \tag{21}$$

As we discussed above the boundary conditions in the φ direction are periodic for the metallic case and quasiperiodic for the dielectric case. In the presence of a parallel magnetic field the problem remains separable and thus the wave function can be factorized in just the same way as in the case of vanishing magnetic field. One again finds 1D subbands with the spectrum of Eq. 10, with an additive mass term,

$$\varepsilon_0(m,w,k) \approx \pm\frac{v_F\hbar}{R}\sqrt{\left(\frac{m_w - n_w + 3m}{3} + \frac{\Phi(B)}{\Phi_0}\right)^2 + R^2(k \pm K_s)^2} \tag{22}$$

Thus in the presence of a parallel field the gapless $m = 0$ branch of the metallic nanotube spectrum acquires a gap [40, 41]. Interestingly, there is no threshold for this effect, since the gap forms at arbitrarily weak field. The gap size is $2\Delta = 2|\frac{\Phi(B)}{\Phi_0}|\frac{\hbar v_F}{R}$. One notes that the field-induced gap appears not at the Fermi level but at the center of the electron band. Thus it affects the metallic NT properties only for electron density sufficiently close to half-filling.

The magnetic field basically shifts the quantization lines perpendicular to their direction. Because of the small diameter of the nanotubes the period to shift one quantization line to the next by the field is several thousands Tesla. However, effects due to the modification (small shifts) of the band structure with common laboratory accessible fields as $B < 10\,\mathrm{T}$ can easily be observed in low temperature experiments.

As we show in Fig. 8 a metallic armchair SWCNT can thus be made semiconducting by applying a magnetic field while for semiconducting SWCNT, the two lowest subbands are shifted in opposite directions by the field. Such a field, by inducing backscattering between right and left electron modes, opens a minigap at the band center. This gap, linear in the field (see Fig. 8.*right*), is given by the magnetic flux scaled by the flux quantum, $(\pi R^2 B/\Phi_0)$, times the semiconducting gap size. Effects of parallel field on multi-walled NT have been reported in [42]. Electronic properties are also sensitive to mechanical distortion, such as twisting, bending, or squashing, [43–47] as well as to external electric fields [48, 49].

Aharonov-Bohm Effect

In addition to the periodic band-gap oscillations, discussed above, the Aharonov-Bohm effect more generally affects the whole subband structure, as evidenced by

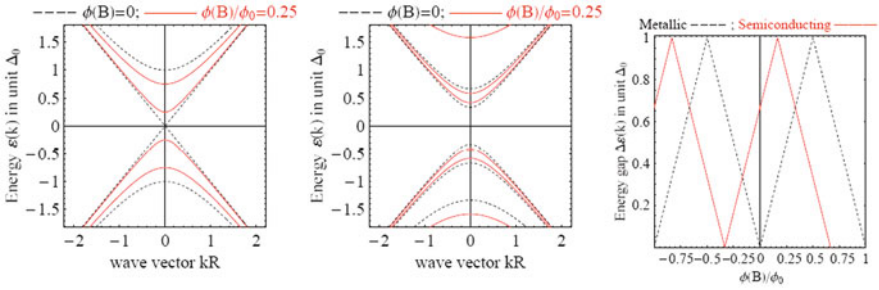

Fig. 8 In the x-axis the wavevector in unit $(k_y - K_s)R$ $(\pi_y R/\hbar)$. (*left*) Bandstructure of a metallic CN with (*red lines*) and without (*black dashed lines*) the magnetic field (in unit ϕ/ϕ_0). This is a metallic tube at zero magnetic flux but a gap opens up once a finite flux is applied and increases with the flux. (Middle) Bandstructure of a semiconducting CN with (*red lines*) and without (*black dashed lines*) the parallel magnetic field. (*Right*) The energy gap modified by applying a finite magnetic flux threading the tube: for a metallic CN the band gap opens and increases linearly with B, to reach a maximum value at half the quantum flux $\phi/\phi_0 = 1/2$. Further, the band gap, ΔE is linearly reduced until it finally closes back when the field reaches one quantum flux. The behaviour of a semiconducting CN is analogous and is represented by a shifted curve in the plain $\phi - \Delta E$ [33, 38, 39]

Van Hove singularity splitting and shifts [50–52]. In the Aharonov-Bohm effect [53, 54] a beam of quantum particles, such as electrons, is split into two partial beams that pass on either side of a region containing a magnetic field, and these partial beams are then recombined to form an interference pattern. The interference pattern can be altered by changing the magnetic field – even though the electrons do not come into contact with the magnetic field see Fig. 9.

Thus the large diameter of MWNTs enables one to investigate quantum-interference phenomena in a magnetic field and especially the AB effect that not only reveals that electrons are waves, but also demonstrates that the vector potential not the magnetic field plays a basic role. For the study of this phenomenon, a magnetic field of several Tesla was applied along the nanotube axis. The electrical resistance measurements showed pronounced oscillations with a period of $h/2e$, as in Fig. [9]. The oscillations are associated with the 'weak localization', a quantum-mechanical manifestation of coherent backscattering of electrons, which arises from interference contributions adding up constructively in zero field. Backscattering is thereby enhanced, leading to a resistance larger than the classical Drude resistance. This observation has given compelling evidence that the phase coherence length, can exceed the circumference of the tube.

In Ref. [55] magnetoresistance measurements on individual multi-walled nanotubes, which display pronounced resistance oscillations as a function of magnetic flux were reported (see Fig. 9.*right*). It was found that the oscillations were in good agreement with theoretical predictions for the Aharonov-Bohm effect in a hollow conductor with a diameter equal to that of the outermost shell of the nanotubes.

More recently experiments on magnetoconductance in ballistic multiwalled carbon nanotubes threaded by magnetic fields as large as 55 T. In the high temperature

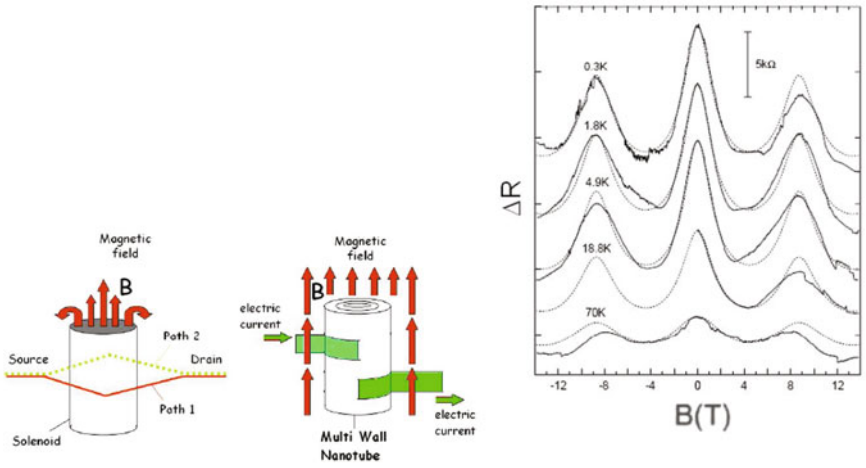

Fig. 9 In the standard Aharonov-Bohm effect the magnetic flux through the solenoid changes the relative phase of the electron waves in paths 1 and 2, leading to the formation of an interference pattern on the screen. When the flux is changed, the interference pattern shifts on the screen. (middle) Imagine a carbon nanotube placed in a magnetic field with its axis parallel to the field. Since nanotubes are cylindrical conductors, the electrons can propagate in either the clockwise or the anticlockwise direction. These two 'paths' interfere, resulting in a periodic modulation of the electrical resistance as the magnetic flux through the tube is changed. In a carbon nanotube, the two paths are clockwise and anticlockwise around the nanotube, and the shift in the interference pattern manifests itself as a change in the electrical resistance along the nanotube as a function of magnetic field (*bottom*). The magnetic field at the peaks can be related to the quantum of magnetic flux and the cross-section of the nanotube. This effect is relatively robust and can be observed even if the electron transport in the nanotube is diffusive. In the right panel the measured magnetoresistance $R(B)$ at different temperatures T for a MWNT in a parallel magnetic field B, from [55]

regime (100°K), giant modulations of the conductance, mediated by the Fermi level location, are unveiled. The experimental data, consistent with the field-dependent density of states of the external shell, gave a first unambiguous experimental evidence of Aharonov-Bohm effect in clean multiwalled carbon nanotubes [56].

For what concerns SWNTs, as we showed above, theoretically the AB effect manifests itself in a SWNT by periodically modifying its band structure with a period of 1 Φ_0 in a magnetic flux (see Fig. 8.*right*) and about 1,000 T in field. However in a recent letter [57] it was shown that relatively low magnetic fields applied parallel to the axis of a chiral SWNT are found to cause large modulations to the p channel or valence band conductance of the nanotube in the Fabry-Perot interference regime. Beating in the Aharonov-Bohm type of interference between two field-induced nondegenerate subbands of spiraling electrons is responsible for the observed modulation with a pseudoperiod much smaller than that needed to reach the flux quantum Φ_0 through the nanotube cross section. Thus was shown that single-walled nanotubes represent the smallest cylinders exhibiting the Aharonov-Bohm effect with rich interference and beating phenomena arising from well defined molecular orbitals reflective of the nanotube chirality.

Spin Orbit Coupling in Carbon Nanotubes

The Spin Orbit interaction is a quantum relativistic effect due to the attractive potential of neighboring carbon atoms. It is given by

$$H_{SO} = \frac{\hbar}{4m^2c^2}(\nabla V \times p)\cdot\sigma,$$

where $V(r)$ is the atomic potential, m the free electron mass, p the electron momentum and σ the Pauli′s spin matrix.

Recently it has been proposed that a small gap can open on the two Dirac points of graphene due to spin-orbital coupling (SOC) [58], which at the same time makes the system a spin-Hall insulator [59] with quantized spin Hall conductance. However it was shown [60] that while the spin-orbit interaction in graphene is of the order of 4 meV, it opens up a gap of the order of 10^{-3}meV at the Dirac points, thus the predicted quantum spin Hall effect in graphene can only occur at unrealistically low temperature. The SOC effects was recently largely investigated [61, 62] also in CNs. In some papers was shown that local curvature of the graphene sheet induces an extra spin-orbit coupling term, thus the effect of SOC on derived materials of graphene like CNs can give a significant contribution.

We report here some results presented in a recent paper [63] and in agreement with previous calculations [62]. As we discussed above a continuum model for the effective spin orbit interaction in graphene can be derived from a tight-binding model which includes the π and σ bands and the combined effects of the intra-atomic spin orbit coupling (Δ) and curvature was analyzed. Thus was shown that local curvature of the graphene sheet induces an extra spin-orbit coupling term $\Delta_{curv} \propto \Delta$, similar to the Rashba interaction due to the electric field.

Although the spin-orbit coupling for flat graphene is rather weak, some significant effects can be found in CNs, especially when their radius is quite small in fact curvature effects on the scale of the distance between neighboring atoms could increase the strength of the spin-orbit coupling at least one order of magnitude with respect that obtained for a flat surface. In a curved graphene sheet, a hopping between the orbitals in the π and σ bands is induced [62]. This hopping terms break the isotropy of the lattice and lead to an effective anisotropic coupling between the π and σ bands in momentum space.

Here we start from Eq. 11. We use cylindrical coordinates, y, ϕ, and define the spin orientations $|\uparrow\rangle, |\downarrow\rangle$ as parallel and antiparallel to the y axis. Thus we introduce in the boundary $\nu \equiv (m_w - n_w + 3m)/3$. After integrating over the circumference of the CN $\int d\phi$, the Hamiltonian of a CN including SOC reads

$$H_{S-OR}\begin{pmatrix}|A\tau\rangle\\|B\tau\rangle\end{pmatrix} = \begin{pmatrix}0 & \hbar(k - i\nu/R)\hat{1} + \tau i\Delta_R\pi\hat{\sigma}_z\\ \hbar(k + i\nu/R)\hat{1} - \tau i\Delta_R\pi\hat{\sigma}_z & 0\end{pmatrix} \begin{pmatrix}|A\tau\rangle\\|B\tau\rangle\end{pmatrix} \tag{23}$$

where the $\tau = \pm 1$ corresponds to the $K(K')$ Dirac point, $|A\tau\rangle$ are envelope functions associated to the K and K' points of the Brillouin zone and corresponding to states located at the A and B sublattices, respectively. Notice that H has to be taken as a 4×4 Matrix, while $\hat{1}$ is the identity in the space of the spin. The basis states $|A\tau\rangle$ and $|B\tau\rangle$ are also spinors in spin subspace where the matrix $\hat{s}_z$ acts on with the spin orientations $|\uparrow\rangle, |\downarrow\rangle$ defined along the nanotube axis. This is different from the approach reported in [62] where the spins are defined perpendicular to the nanotube surface. However the spin-orbit term $i\Delta_R \pi \hat{s}_z$ is equivalent to the term proportional to $\hat{\sigma}_y$ obtained by Ando [62] while the the results obtained by applying Eq. 23 are in agreement with the ones reported in [61].

It follows that an energy gap $\pi\,\Delta_{\mathrm{R}}$ appears also for metallic CNs at low energies [62, 64]. This gap can be seen as a consequence of the Berry phase gained by the electron after completing a closed trajectory around the circumference of the CN under the effect of SOC (Δ_{R}) [62]. As a further effect Δ_{R} can also give rise to a small spin splitting [62, 64]

$$\varepsilon_q = \pm \frac{\hbar v_F}{R} \sqrt{z^2 + (q^2R^2 + \nu^2) + 2\nu z \hbar \hat{s}_z}, \tag{24}$$

where $q = k \pm K_s$ and $z = \pi \frac{R\Delta_R}{\hbar v_F}$. Now we want focus on the role of the curvature in small radius CNs. In fact it results that in absence of an external electric (Rashba) field (E =0). For a single wall nanotube of radius R we get $R\Delta_R$: 6.5 meV Å (see [63]) to be compared to $\hbar v_F$: 5 eV Å.

This effect can modify in a significant way the Fermi velocity for small radius CNs. Here we limit ourselves to the case of metallic CNs and to the lowest band so that, from Eq. 24 we obtain

$$\tilde{v}_F(\varepsilon_F) = \frac{\partial \varepsilon}{\hbar \partial k} = v_F \sqrt{1 - \left(\frac{\pi\,\Delta_R}{\varepsilon_F}\right)^2}, \tag{25}$$

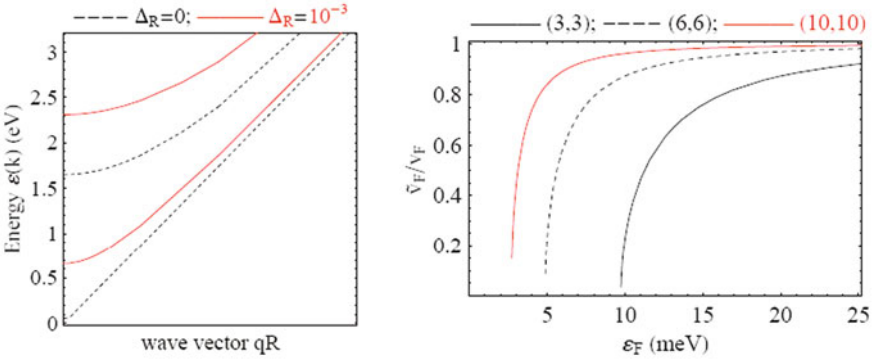

Fig. 10 (*Left*) Bandstructure of a metallic CN modified by the SOC. (*Right*) The renormalized Fermi velocity for three different metallic CNs as (10, 10) (R : 7Å), (6, 6) ((R : 4Å) and (3, 3) (R : 2Å) armchair ones

where ε_F can be taken as the doping level. The renormalized Fermi velocity for three different metallic CNs as $(10, 10)$, $(6, 6)$ and $(3, 3)$ armchair ones is plotted in Fig. 9 where also the corrections to the banstructure are reported.

Quantum Transport in Carbon Nanotubes

Ballistic Transport

When the length of the conductor is smaller than the electronic mean free path, then the electronic transport is ballistic. This ballistic regime refers to the transport of electrons in a medium where the electrical resistivity due to the scattering, by the atoms, molecules or impurities in the medium itself, is negligible or absent.

Conductance Quantization

The ballistic one-dimensional wire is a nanometric solid-state device in which the transverse motion (along φ for the CN in Fig. 5) is quantized into discrete modes, and the longitudinal motion (y direction for the for the CN in Fig. 5) is free. In this case, electrons propagate freely down to a clean narrow pipe and electronic transport with no scattering can occur. In this case each transverse wave guide mode or conducting channel contributes $G_0 = e^2/h (\approx 12.9\,\mathrm{k}\Omega)$ to the total conductance. Calculations indicate that conducting single-shell nanotubes have two conductance channels [39, 40, 65]. This predicts that the conductance of a single-wall nanotube is independent of diameter and length, i.e. according to the Landauer formula [66],

$$G(E) = \frac{2e^2}{h} N_\perp(E). \tag{26}$$

This value accounts for the contribution of the two spin projections and the two propagating modes of the nanotubes, while $N_\perp(E)$ is the energy-dependent number of available quantum channels.

Thus in the case of perfect (reflection less) or ohmic contacts between the CNT and the metallic voltage probes the expected energy-dependent conductance is easily obtained, from band structure calculations, or from the DOS, by counting the number of channels at a given energy. As we show in Fig. 11 a metallic nanotube present two quantum channels at the Fermi energy $E = 0$, or charge-neutrality point, resulting in $G(0) = 2G_0$. At higher energies, the conductance increases as more channels become available to conduction.

Thus in the ideal case CNs conduct current ballistically and do not dissipate heat. The nanotubes are several orders of magnitude greater in size and stability than other typical room-temperature quantum conductors.

The quantization of the conductance has been observed at room temperature in fibers of multiwall nanotubes [68]. The experimental method involved measuring the conductance of nanotubes by replacing the tip of a scanning probe microscope

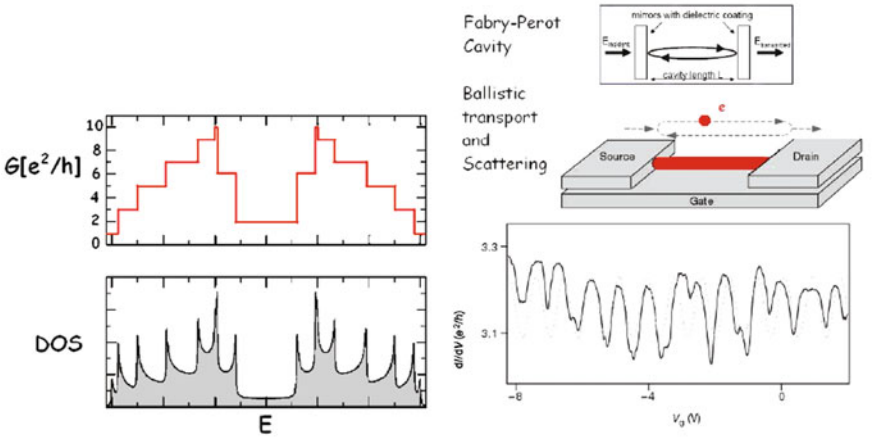

Fig. 11 (*Right*) Density of states and ideal ballistic conductance for a metallic nanotube. (*Left*) Schematic diagram of a SWNT device illustrating the multiple electron reflection that gives rise to the observed interference pattern. Below $T = 10°\text{K}$ oscillations in $\partial I/\partial V$ which are quasiperiodic in V_g due to resonant tunneling. Average differential conductance around $3.2e^2/h$. Adapted from [67]

with a nanotube fiber. The conductance of arc-produced MWNTs is one unit of the conductance quantum G_0. Since multiwall nanotubes consist of several concentrically arranged single-wall nanotubes, one would not expect them to behave as one-dimensional conductors. If adjacent carbon layers interact as in graphite, electrons would not be confined to one layer. The results of [68] suggest, however, that the current mainly flows through the outermost layer. However the coefficent of the conductance quantum was found to have some suprising integer and noninteger values, such as $0.5G_0$. Thus in a more recent letters [69] the authors, using a scattering technique calculated the ballistic quantum conductance and found that interwall interactions not only block some of the quantum conductance channels, but also redistribute the current nonuniformly over individual tubes across the structure. these results provide a natural explanation for the unexpected integer and noninteger conductance values reported for multiwall nanotubes in [68].

Some other experiments on metallic tubes have measured only a single channel G_0 at low bias, instead of the two theoretically predicted channels. Several theoretical papers have proposed an interpretation in terms of the hybridization between carbon and metal orbitals at the contact [70–77]. For higher bias voltage between conducting probes, in order to explain the experimental observation of limited turn-on current with increasing bias voltage, was supposed that the modifications of bands along the tube axis produce additional backscattering analogous to a Bragg reflection [78].

In more recent experiments was shown that also single-walled carbon nanotubes are 1D conductors that exhibit ballistic conduction [67, 79–82]. In Ref. [83] was shown a nonlinear resistance vs distance behavior as the nanotube is probed along

its length. This is an indication of elastic electronic transport in one-dimensional systems. This has been related to the ballistic transport in single wall nanotube.

Fabry-Perot Interference

In the ballistic regime the discussed wave nature of the propagating electrons yields also some interesting interference effects as the famous Fabry-Perot interference, light interference in cavity between multiply reflected light waves (see Fig. 10). In this case an analogous quantum interference can be observed between multiply reflected electron waves.

The latter interference becomes increasingly important, leading to dramatic changes in device properties when the size of a device becomes comparable to the electron coherence length [84–91], in a typical quantum ballistic regime which replaces the classical diffusive motion of electrons. The classical-to-quantum transition in device behaviour suggested the possibility for nanometer-sized electronic elements that make use of quantum coherence [84, 85, 90, 91] and among these CNs were promising candidates for realizing such device elements.

In Ref. [67] an example of a coherent molecular electronic device whose behaviour is explicitly dependent on quantum interference between propagating electron waves – a Fabry–Perot electron resonator based on individual single-walled carbon nanotubes with near-perfect ohmic contacts to electrodes. In these devices, the nanotubes act as coherent electron waveguides [68, 92, 93], with the resonant cavity formed between the two nanotube–electrode interfaces. The results were explained by using a theoretical model based on the multichannel Landauer–Buttiker formalism [94–96] to analyze the device characteristics and find that coupling between the two propagating modes of the nanotubes caused by electron scattering at the nanotube–electrode interfaces is important. in this model the nanotube is considered as a coherent waveguide with two propagating modes.

Thus in Ref. [67] a clear signature of interference effects was measured in the $\partial I/\partial V$ plots as a function of V and V_g measured at low temperatures. The data clearly indicated that the electrical behaviour of these nanotube devices is distinct from those reported that exhibited a Coulomb-blockade behaviour. An accurate data analysis provided experimental evidence that the electron scattering occurs mostly at the nanotube–metal interface and that electrons pass through the nanotube ballistically. A schematic diagram of a SWNT device illustrating the multiple electron reflection that gives rise to the observed interference pattern is reported in Fig. 11.

Coulomb-Blockade Regime

For low contact resistances transport is mainly determined by quantum interference discussed above whereas for high contact resistances, a nanotube can behave as a quantum dot, in which Coulomb blockade determines the transport properties, Here we discuss the latter regime in detail.

The Coulomb-Blockade Regime: General Theory

When two contacts not highly transparent are attached to a small device (next island or Quantum Dot (QD)), the measurements of the conductance and the differential conductivity reflect the strong Coulomb repulsion in the island. For temperatures that are typically below 1°K, the zero-bias conductance shows oscillations as a function of the gate voltage. This is characteristic of the so-called Coulomb blockade (CB) regime [97, 98], and the gate voltage between two peaks is related to the energy required to overcome the Coulomb repulsion when adding an electron between the barriers created by the contacts [99, 100]. Thus in these devices, because the thermal energy k_BT is below the energy for adding an additional electron to the device ($\mu_N = E(N) - E(N-1)$), low bias (small V_{sd}) transport is characterized by a current carried by successive discrete charging and discharging of the dot with a just one electron.

This phenomenon, known as single electron tunneling (SET or quantized charge transport), was observed in many experiments in vertical QDs at very small temperature [101–103]. In this regime the ground state energy determines strongly the conductance and the period in Coulomb Oscillations (COs). COs correspond to the peaks observed in conductance as a function of gate potential (V_g) and are crudely described by the Coulomb Blockade mechanism [104]: the $N-th$ conductance peak occurs when [105] $\alpha e V_g(N) = \mu_N$ where $\alpha = \frac{C_g}{C_\Sigma}$ is the ratio of the gate capacitance to the total capacitance of the device (see Fig. 12).

The peaks and their shape strongly depend on the temperature as explained by the Beenakker formula for the resonant tunneling conductance [104, 106]

$$G(V_g) = G_0 \sum_{q=1}^{\infty} \frac{V_g - \mu_q}{k_B T \sinh\left(\frac{V_g - \mu_q}{k_B T}\right)} \tag{27}$$

here $\mu_1, \ldots, \mu_N$ represent the positions of the peaks.

Microscopic Models

Here we introduce a simple microscopic model, which was developed for a metallic CN but can be easily extended to general CNs.

In a previous section we introduced the energy dispersion (Eq. 10) $\varepsilon(\vec{w}, m, k)$ by assuming an ideal CN of infinite length. When we take into account a CN between two contacts at a fixed distance (L) we can assume L as the CN length. It follows the quantization in the dispersion relation due to the finite longitudinal size of the tube, obtained by replacing the continuous values of k with the discrete values $k_n = n\pi/L$. The longitudinal quantization introduces a parameter which also gives a thermal limit for the atomic like behavior: in fact k wave vectors have to be taken as a continuum if k_BT is as a critical value $\varepsilon_c = v_F(h/L)$ and as a discrete set if the temperature is below (or near) ε_c.

Thus we can write the single electron energies near the Fermi points as

$$\varepsilon^{\vec{w}}_{n,m,p,s} \to \varepsilon_k \approx v_F \hbar \left(|n\frac{\pi}{L} - \alpha K_s| \right) \equiv v_F \bar{k},$$

the expression in the right corresponding to the lowest subband of a metallic CNs. Thus we introduce different operators for the electrons belonging to each branch: right going operators $c^{\dagger}_{R,\bar{k},s}$ and left going ones $c^{\dagger}_{L,\bar{k},s}$ for electrons with $\bar{k} > 0$ ($\bar{k} < 0$). In terms of these operators the free and interaction Hamiltonians can be written as

$$H_0 = v_F \sum_{\bar{k},s} \bar{k} c^{\dagger}_{R,\bar{k},s} c_{R,\bar{k},s} + v_F \sum_{\bar{k},s} \bar{k} c^{\dagger}_{L,\bar{k},s} c_{L,\bar{k},s} \tag{28}$$

$$H_{int} = \frac{1}{L} \sum_{k,k',q,s,s'} \left(V^{s,s'}_{k,p}(q) c^{\dagger}_{k+q,s} c^{\dagger}_{p-q,s'} c_{p,s'} c_{k,s} \right). \tag{29}$$

Here $c_k \equiv c_{R,k}$ if $k > 0$ and $c_k \equiv c_{L,k}$ if $k < 0$, while $V^{s,s'}_{k,p}(q)$ is the Fourier transform of the electron electron interaction.

Starting from the Hamiltonian above it is possible to take into account both the correlation effects and the influence of the long range component of the e–e interaction. However a short ranged interaction model [107] can simplify the calculations of the energies of the electrons in the QD. The Hamiltonian obtained by summing

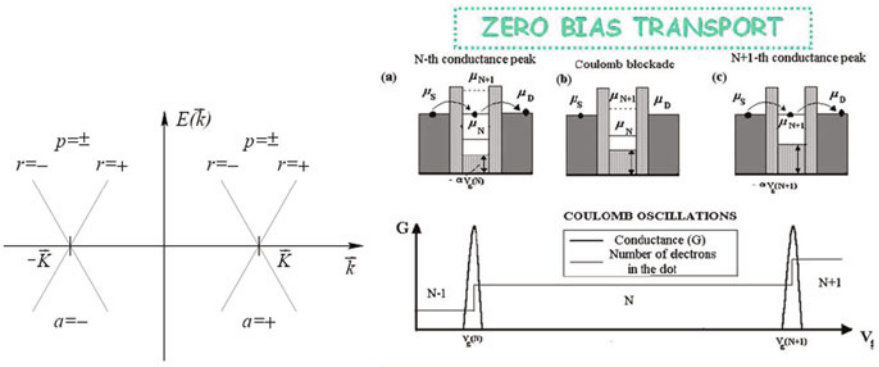

Fig. 12 (*Left*) The Model with linearized subbands near the Fermi points for a metallic CN. (*Right*) When the contacts are not highly transparent the conductance and the differential conductivity reflect the strong Coulomb repulsion in the CNs. (*Right*) In nanometric devices, when the thermal energy $k_B T$ is below the energy for adding an additional electron to the device $\mu_N = E(N) - E(N-1)$ Thus the low bias (small V_{sd}) transport is characterized by a current carried by successive discrete charging and discharging of the device with just one electron. It follows that the ground state energy determines strongly the conductance and the period in Coulomb Oscillations (COs).These COs correspond to the peaks observed in conductance as a function of gate potential V_g. The N-th conductance peak occurs when $\alpha e V_g(N) = \mu_N$. The Addition Energy needed to place an extra electron in the device is analogous to the electron affinity for a real atom $E^A_N = \mu_{N+1} - \mu_N$

Eqs. 28 and 29 in this approach just depends on two interaction parameters [107], J and V_0 so that

$$H = \sum_{n,\zeta,p,s} \varepsilon_{n,\zeta,p} \hat{n}_{n,\zeta,p,s} + V_0 \frac{N(N+1)}{2} - J \sum_{n,\zeta,p,s} \sum_{n',\zeta',p',s} \delta_{s,s'} \hat{n}_{n,\zeta,p,s} \hat{n}_{n,\zeta,p,s} \tag{30}$$

Symmetries in the Bandstructure. For a metallic CN near each Fermi point we obtain that the Hamiltonian above is represented by a typical bandstructure with linear branches depending on $\bar{k} = k + \alpha K_s$ ($\alpha = \pm 1$ labels the Fermi point). After the quantization, in the ideal case, we obtain shells with an 8-fold degeneracy (due to σ (spin symmetry), α ($K, -K$ lattice symmetry), ζ ($(k-K),(K-k)$) (see Fig. 13.C.*left*).

However some asymmetries in the bandstructure were both predicted and observed. In order to take into account the strong asymmetries measured we modify the dispersion relation. A first correction has to be introduced because of the *'longitudinal incommensurability'*: in general K is not a multiple of π/L so $K = (N + \delta N)\frac{\pi}{L}$ with $\delta N < 1$ and the energy shift is $\Delta\varepsilon = v_F \frac{h\delta N}{L}$. A second correction is due to the subband mismatch (δ_{SM}). The single electron energy levels are:

$$\varepsilon_{l,\sigma,p} = \hbar v_F |l\frac{\pi}{L} + pK| + \frac{(1-p)}{2}\delta_{SM} \tag{31}$$

where $p = \pm 1$.

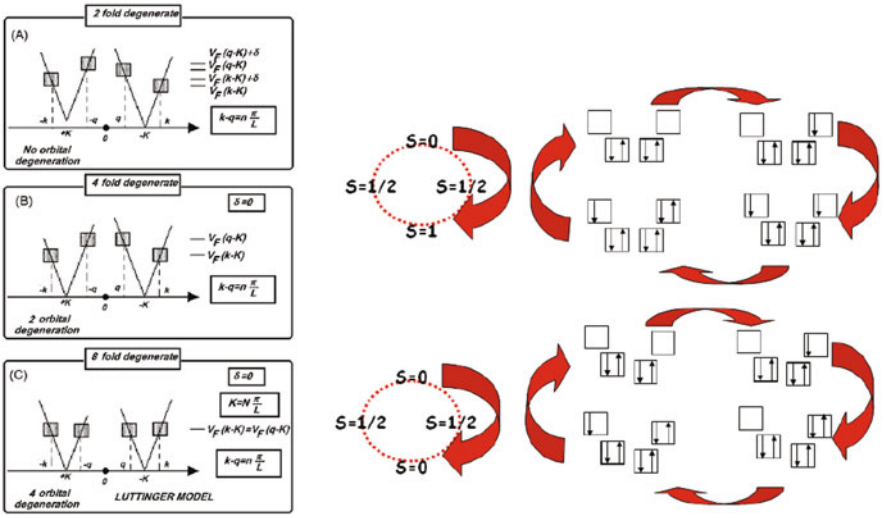

Fig. 13 (*Left*) The dispersion relation and the quantized levels. The boxes in the figure represent energy levels and can be filled by a pair of electrons with opposite spins. (**a**) The general case without any degeneracy. (**b**) The fourfold degeneracy case. (**c**) The eightfold degeneracy case. (*Left*) A simple scheme for the aufbau which takes in account the spin in the dot. (*Top*) The degenerate case with the spin period $=, 1/2, 1, 1/2, 0$. (*Bottom*) The non degenerate case with spin period $0, 1/2$

Each choice of parameters gives a different degeneracy for the quantum levels: 8-fold degeneracy corresponds to $\delta_{SM} = 0$ and $K = n\frac{\pi}{L}$; 4-fold degeneracy is found if we put just $\delta_{SM} = 0$ and 2 fold degeneracy in the general case.

Next we just consider particles near the same Fermi point and do not take into account the labels α. Obviously we have to consider also $\alpha - \alpha'$ interaction for particles near two different Fermi points.

Experiments and Theoretical Results about Coulomb Blockade

Many experiments showed Coulomb Oscillations in Carbon Nanotubes e. g. in 1997 Bockrath and coworkers [97] in a rope below about 10°K observed dramatic peaks in the conductance as a function of the gate voltage that modulated the number of electrons in the rope. These typical Coulomb blockade peaks in the zero bias conductance allowed to investigate the energy levels of interacting electrons. In fact in CB a CN behaves as an artificial atom and reveals its shell structure [98]. In this sense the measurements reported in [108] (see Fig. 14.*left*) for clean 'closed' nanotube dots showed complete Coulomb blockade and enable to deduce some properties from the addition energy of SWCNT. This 'addition energy', $E_A(n)$ is the energy needed to place an extra electron (the n-th) in a QD, defined analogously to the electron affinity for a real atom. It was extracted from measurements as $E_A \propto \Delta V_g$. Thus was possible discuss the role which the Coulomb interaction could play in a 1D at small temperatures($T = 0.1 \div 0.3°K$).

In Fig. 14.*left*, the small bias experimental conductance dI/dV as a function of gate voltage is shown. The SET prevails as revealed by the fine structure of the

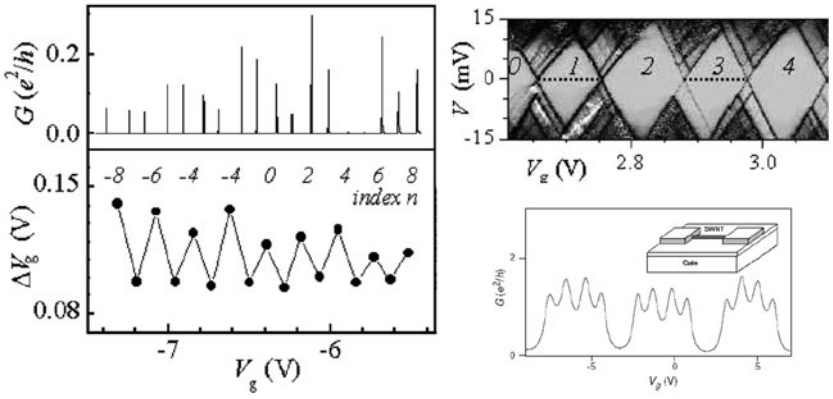

Fig. 14 (*Left*) Conductance vs gate voltage for a nanotube quantum dot at $T = 300$ mK with evident Coulomb blockade peaks. Spacings ΔV_g of the peaks in. The index n counts the added electrons relative to an arbitrary zero. For clarity only even n's are indicated. (*Right*) A greyscale plot (darker = more positive) of dI/dV vs V_g and V at $T = 100$ mK. The index n counts electrons added relative to the leftmost diamond. From Refs. [108, 109]

conductance spectrum. Each conductance peak represents the addition of an extra charge to the nanotube. The periodicity of the peaks is related to the size of the coherent conducting island. In the case of an irregular conductance spectrum, the nanotube is believed to be split into a series of conducting parts separated by local tunneling contacts.

The overall diagram of conductance of a QD as a function of bias and gate voltage generally appears as a diamond shaped structure referred to as the Coulomb diagram (see Fig. 14.*top.right*). For a fixed gate voltage, the current increases step wise with increasing bias voltage, producing the excited-state spectrum. Each step in the current is related to a new higher-lying energy level that enters the bias window. Within each diamond, the electron number of the nanotube is fixed and the current vanishes. The boundary of each diamond represents the transition between N and $N + 1$ electrons, and the parallel lines outside the diamonds correspond to excited states. Such a plot is well understood within the constant-interaction model (Eq. 30).

Some significant deviations from this simple picture were, however observed [110]. The ground-state spin configuration in a nanotube was determined by studying the transport spectrum in a magnetic field [111]; for a metallic CN the total spin of the ground state alternates between 0 and 1/2 as successive electrons are added, demonstrating a simple shell-filling, or even-odd, effect, i.e., successive electrons occupy the levels in spin-up and spin-down pairs (see Fig. 13.*right*). The semiconducting case was analyzed in [112]. In Ref. [113] the authors used magnetic field effect to lift the orbital degeneracy thus they were able to estimate some value of the orbital magnetic moment.

The CB measurements on suspended single-wall carbon nanotubes have also shown spectacular signatures of phonon assisted tunneling, mediated by stretching modes [114].

Effects of long range interaction. In Ref. [115] the effects of the long range terms of the interaction in a SWNT were investigated and the results were compared with the experiments at very low temperature T [108]. Thus was explained the observed damping in the addition energy for a SWNTs [108] at T : 200 mK as an effect of the long range of the e–e repulsion.

In order to investigate the effects on low dimensional electron systems due to the range of electron electron repulsion, was introduced a model for the interaction which interpolates well between short and long range regimes. This model predicts oscillations in the addition energy due to the Hund′s Rule quite similar to the ones observed in QDs (usually the Interaction between the electrons with momenta near the 2 Fermi Points is very small so that we have two independent 4-fold Degenerate Hamiltonians). The oscillations periodicity is 4 for the Model (8 for a system with two Fermi points, see Fig. 13.*right*). The oscillations amplitude is due to an exchange term corresponding to the short range interaction and the effect of a long range interaction is a damping of the oscillations when the number of electrons in the System increases (compare Fig. 15.*left* with the theoretical predictions in Fig. 15.*right*).

Asymmetries in the bandstructures The calculations above were based on the symmetric subbands. However the real band structures of measured CN's can show

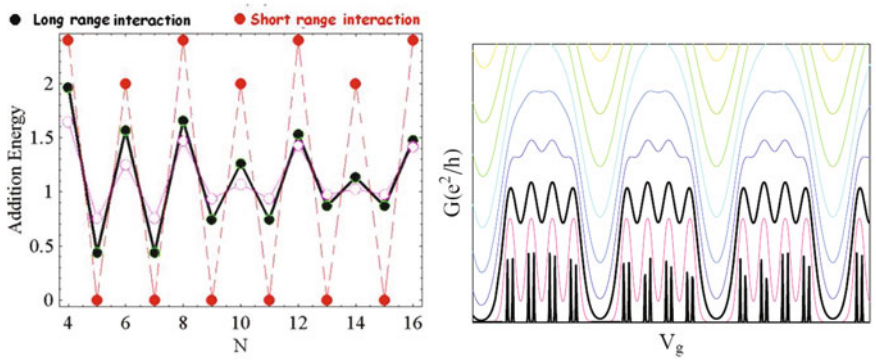

Fig. 15 On the left the analytical Aufbau results for the addition energy versus the number of electrons of a four fold degeneracy model corresponding to different values of the range (long range *black*, short range *dashed red line*). We show how the damping in the oscillations is due to a long range interaction while it does not appear for a short range model. The predictions can be compared with the measured addition energy in the experiment of [118]. (*Right*) COs conductance vs gate voltage at different temperatures calculated following the classical CB theory. Theoretical calculations show that the fine structure peaks are appreciable just for very low temperatures (*bottom black line*)

some differences with respect to the ideal case discussed above. In fact some experiments in recent years do not find this high symmetry as result and some different hypotheses in order to explain this discrepancy were formulated.

As was discussed in [115] this symmetry has relevant effects on the *Aufbau* of the CN's shells i.e. on the spin oscillations (see Fig. 15). In the experiments reported in [109] two different shell filling models are put forward: the first one, when the subband mismatch dominates, predicts that the spin in the SWCNT oscillates between $S = 0$ and $S = 1/2$ while when the subband mismatch is negligible the spin in the SWCNT oscillates between $S = 0$, $S = 1/2$ and $S = 1$ (see Fig. 13.*right*). In Ref. [108] the authors say *'the sole orbital symmetry is a two-fold one, corresponding to a K-K′ subband degeneracy and resulting from the equivalence of the two atoms in the primitive cell of graphene structure'*.

A secondary effect of the asymmetry in the Bandstructure is related to the positions of the CB peaks in the plot $V_g - G$. Thus experimentally we can understand the symmetry properties of a CN by observing the grouping of the peaks in the conductance versus gate potential. Thus in the experiment reported in [108] no four-fold grouping was observed because degeneracy was lifted by a mixing between states due either to defects or to the contacts. Nevertheless a different experiment [109] displays conductance peaks in clusters of four, indicating that there is a four fold degeneracy (see Fig. 14.*right.bottom* and compare with Fig. 15.*right* where also the temperature dependence according the Beenakker formula is included).

More recently spin states in carbon nanotube quantum dots have been revealed in various systems with the Kondo effect [116–118] and the simple shell structures [119–121]. These experiments allowed a comparison with the predicted

two or four-electron shell structures, depending on the relation between the zero-dimensional level spacing and the subband mismatch. In Ref. [119] low-temperature transport measurements have been carried out on single-wall carbon nanotube quantum dots in a weakly coupled regime in magnetic fields up to 8 Tesla. Four-electron shell filling was observed, and the magnetic field evolution of each Coulomb peak was investigated, in which magnetic field induced spin flip and resulting spin polarization were observed. Excitation spectroscopy measurements have revealed Zeeman splitting of single particle states for one electron in the shell, and demonstrated singlet and triplet states with direct observation of the exchange splitting at zero-magnetic field for two electrons in the shell, the simplest example of the Hund's rule. The total spin in an individual single-wall carbon nanotube quantum dot was also studied in [122] by using the ratio of the saturation currents of the first steps of Coulomb staircases for positive and negative biases. The current ratio reflects the total-spin transition that is increased or decreased when the dot is connected to strongly asymmetric tunnel barriers. The total spin states with and without magnetic fields can be also traced by this method.

Spin-orbit interaction Recently also the effects of the Spin-orbit interaction and anomalous spin relaxation was investigated in carbon nanotube quantum dots in order to propose the CN QD as devices for the spintronics. In this sense in a recent papers [123] was shown that the CNT Double Quantum Dot has clear shell structures of both four and eight electrons, with the singlet-triplet qubit present in the four-electron shells. In Ref. [123] the authors observed inelastic co-tunneling via the singlet and triplet states, which they used to probe the splitting between singlet and triplet, in good agreement with theory.

Luttinger liquid

Transport in 1 Dimension – Electronic correlations have been predicted to dominate the characteristic features in quasi one dimensional (1D) interacting electron systems. This property, commonly referred to as Tomonaga-Luttinger liquid (TLL or LL) behaviour [124–126], has recently moved into the focus of attention by physicists, also because in recent years several electrical transport experiments for a variety of 1D devices, such as semiconductor quantum wires [127] (QWs) and carbon nanotubes (CNs) [128, 129] have shown this behaviour.

In a 1D electron liquid Landau quasiparticles are unstable and the low-energy excitations take the form of plasmons (collective electron-hole pair modes): this is known as the breakdown of the Fermi liquid picture in 1D. The LL state has two main features: (1) the power-law dependence of physical quantities, such as the tunneling density of states (TDOS), as a function of energy or temperature; (2) the spin-charge separation: an additional electron in the LL decays into decoupled spin and charge wave packets, with different velocities for charge and spin. It follows that 1D electron liquids are characterized by the power-law dependence of some physical quantities as a function of the energy or the temperature. Thus the

tunneling conductance G reflects the power law dependence of the DOS in a small bias experiment [130, 131]

$$G = dI/dV \propto T^{\alpha_{bulk}} \tag{32}$$

for $eV_b = k_BT$, where V_b is the bias voltage, T is the temperature and k_B is Boltzmann′s constant. The exponent α_{bulk} known as *bulk critical exponent*, can be calculated in several different ways as we discuss below.

The Luttinger Model and the Bosonization Approach

A Tomonaga-Luttinger liquid is a theoretical model describing interacting electrons in a one-dimensional conductor [132–134]. The typical Luttinger model starts from the hypothesis that the Fermi surface consists of two Fermi points, in the neighborhood of which the dispersion curve can be approximated by straight lines with equations

$$\varepsilon_k \approx v_F(|k| - k_F) \equiv v_F\bar{k}. \tag{33}$$

Here we introduce the creation (annihilation) operators for the electrons $\hat{a}^\dagger_{k,s}$ with fixed momentum and spin, and we rewrite the Hamiltonian in Eqs. 28 and 41 in the limit of short range interactions. The scattering processes are usually classified according to the different electrons involved and the coupling strengths labeled with g are often taken as constants. In this case, as discussed in detail by Solyom [132], we can substitute $V^{s,s'}_{k,p}(q)$ with 8 constants (here we limit to 6 ones because we neglect the Umklapp scattering as we explain below). In general we should take into account the dependence on k, p and q, however in a model with a bandwidth cut-off, where all momenta are restricted to a small region near the Fermi points, the momentum dependence of the coupling is usually neglected. Thus the kinetic energy takes the form

$$\begin{aligned} H_0 &= v_{\mathrm{F}} \sum_{k,s} \left((k - k_{\mathrm{F}}) a^\dagger_{+,k,s} a_{+,k,s} + (-k - k_{\mathrm{F}}) a^\dagger_{-,k,s} a_{-,k,s} \right) \\ &= \frac{2\pi v_{\mathrm{F}}}{L} \sum_{q>0,\alpha=\pm,s} \rho_{\alpha,s}(q)\rho_{\alpha,s}(-q), \end{aligned} \tag{34}$$

where density operators for spin projections $s = \uparrow, \downarrow$ have been introduced:

$$\rho_{\pm,s}(q) = \sum_k a^\dagger_{\pm,k+q,s} a_{\pm,k,s}\,. \tag{35}$$

Interaction For what concerns the electron-electron interaction, the momentum conservation allows only for four processes, corresponding to $V^{s,s'}_{k,p}(q)$ in Eq. 29:

1. the *Forward Scattering in the same branch*, $g_4^{s,s'}$ for k and p in the same branch and small q (transferred momentum);
2. the *Forward Scattering involving two branches* $g_2^{s,s'}$ for where k and p are opposite and q is small;
3. the *Backward Scattering* ($g_1^{s,s'}$) which involves electrons in opposite branches with large transferred momentum (of order $2k_F$).
4. the *Umklapp scattering* ($g_3^{s,s'}$) additional process significant just at half-filling. Thus in our case we neglect $g_3^{s,s'}$ since the sample is assumed to be doped.

Here we take in account just two types of interaction. First, the "backward scattering" $(k_{\rm F}, s; -k_{\rm F}, t) \rightarrow (-k_{\rm F}, s; k_{\rm F}, t)$ which for $s \neq t$ cannot be rewritten as an effective forward scattering. The corresponding Hamiltonian is

$$H_{\rm int,1} = \frac{1}{L} \sum_{k,p,q,s,t} g_1 a^{\dagger}_{+,k,s} a^{\dagger}_{-,p,t} a_{+,p+2k_{\rm F}+q,t} a_{-,k-2k_{\rm F}-q,s}. \tag{36}$$

And, of course, there is also the forward scattering

$$H_{\rm int,2} = \frac{1}{2L} \sum_{q,\alpha,s,t} \left(g_2(q) \rho_{\alpha,s}(q) \rho_{-\alpha,t}(-q) + g_4(q) \rho_{\alpha,s}(q) \rho_{\alpha,t}(-q) \right). \tag{37}$$

Exact Solution. The full Hamiltonian above, $H_0 + H_{int}$ defines the simplest model for interacting electrons in 1D. A simple solvable case is the Tomonaga-Luttinger model [124, 125], where only forward scattering g_2 is taken into account ($g_1 = g_3 = g_4 = 0$). It has been solved by Mattis and Lieb [126], who showed that this model describes a particular type of system where the conventional Fermi surface, defined in terms of a step in the momentum distribution, does not exist for arbitrarily small g_2. Haldane [135] later extended their analysis to a more general situation and coined the term 'Luttinger liquid' in analogy with the Fermi liquid.

The usual diagonalization of the Tomonaga- Luttinger hamiltonian is based on the so-called bosonization scheme. The density operators $\rho(q)$ act like Bose creation and annihilation operators of elementary excitations with energy $v_F q$ and momentum q.

Several important quantities can be exactly calculated for the LL model, including the momentum distribution function [126] and various response functions [132], which generally exhibit power-law behavior [134, 136, 137].

All properties of a TL liquid can be described in terms of only two effective parameters per degree of freedom which take over in 1D the role of the Landau parameters familiar from Fermi liquid theory.

In particular the low-energy properties of a homogeneous 1D electron system could be completely specified by the TL coefficients corresponding to the interaction ($g_i^{s,\sigma}$) and the kinetic energy (v_F) in the limit of ideal TL liquid.

Four TL parameters, depending on g and v_F, characterize the low energy properties of interacting spinful electrons moving in one channel: the parameter K_ν fixes the exponents for most of the power laws and v_ν is the velocity of the long wavelength excitations: $\nu = \rho$ for the charge and $\nu = \sigma$ for the spin. The parameters [138] K_ρ and $v_{\rho/\sigma}$ are easily obtained as functions of $g_i^{s,\sigma}$ and v_F by various techniques found in textbooks [132].

$$K_\nu = \sqrt{\frac{\pi v_F + g_4^\nu - g_2^\nu}{\pi v_F + g_4^\nu + g_2^\nu}} \tag{38}$$

$$v_\nu = \sqrt{\left[v_F + \frac{g_4^\nu}{\pi}\right]^2 - \left(\frac{g_2^\nu}{\pi}\right)^2} \tag{39}$$

$$\alpha = \frac{1}{2}\left[\left(v_F + \frac{g_4^\sigma}{\pi}\right)\frac{1}{v_\sigma} + \left(v_F + \frac{g_4^\rho}{\pi}\right)\frac{1}{v_\rho} - 2\right] \tag{40}$$

where $g_i^\sigma = \frac{1}{2}(g_i^p - g_i^\perp)$ and $g_i^\rho = \frac{1}{2}(g_i^9 + g_i^\perp)$. Here α denotes the *bulk* critical exponent which characterizes many properties of the transport behaviour of a 1D device (e.g. the zero bias conductance as a function of $T\backslash,$). Notice that g_4 leads to a small renormalization of the Fermi velocity, which is usually neglected.

The model described above, with linear branches and constant interaction in momentum space is known as TL model and corresponds to a very short range interaction (Dirac delta). The presence of a long range interaction in a 1D electron system introduces in the model an infrared divergence and is quite difficult to solve. Next we discuss the solutions for the case of Carbon Nanotubes obtained with a Renormalization Group approach and a Dimensional Crossover.

Low-Energy Theory for Correlated Carbon Nanotubes

A formal description of the LL in CNs was developed at the end of 1990s because CNs display complex quasi-1D characteristics, which are required to reconsider and extend the basics of LL theory. In fact in CNs the Fermi surface is described by four points of the Brillouin zone, instead of the two points found for a single channel. Moreover the transport properties of a CN depend also on the diameter and chirality. Thus the LL theory was first developed for a metallic armchair SWCN [139]. There the low-energy theory including Coulomb interactions is derived and analyzed. It describes two fermion chains without interchain hopping but coupled in a specific way by the interaction. The strong-coupling properties were studied by bosonization, and consequences for experiments on single armchair nanotubes were discussed.

The electronic properties of carbon nanotubes are due to the special bandstructure of the π electrons in graphite [25, 27] as we discussed in Sect. "Electronic Structure of Single-Wall Nanotubes". The Fermi surface for a metallic CN, obtained starting from Eq. 10, consists of two distinct Fermi points αK with $\alpha = \pm$. As usually

here the y-axis points along the tube direction and the circumferential variable is $0 \leq \phi \leq 2\pi$. As we discussed above since the basis of graphite contains two carbon atoms, there are two sublattices $p = \pm$ shifted by the vector $\vec{d} = (0, d)$, and hence two degenerate Bloch states at each Fermi point αK_s. The quantization of transverse motion gives the 'mass' m_{eff} [26], according the Dirac fermions approach, which vanishes for the lowest subband of a metallic CN.

Because the excitation of other transversal bands costs energy, the bandwidth cutoff scale D we take in account just the lowest subband in the limit of linear dispersion as shown in Fig. (12.*left*). Thus, the non interacting part of Hamiltonian is a massless 1D Dirac Hamiltonian [26, 27]

$$H_0 = -v \sum_{p\alpha\sigma} p \int dy \; \psi^{\dagger}_{p\alpha\sigma} \partial_y \psi_{-p\alpha\sigma} \; . \tag{41}$$

Electron electron interaction. In order to introduce electron electron repulsion we have to introduce the Coulomb interactions mediated by a screened potential. Thus we start from the unscreened Coulomb repulsion$(a_0; a)$ in a wrapped 2D geometry

$$V_0(y - y', \varphi - \varphi') = \frac{e^2/\kappa}{\sqrt{(y - y')^2 + 4R^2 \sin^2(\varphi - \varphi')}}. \tag{42}$$

The Fourier transform $\hat{V}_0(q)$ reads

$$\hat{V}_0(q) \approx \frac{e^2/\kappa}{\sqrt{2}} \left[K_0\left(\frac{qR}{2}\right) I_0\left(\frac{qR}{2}\right) \right]. \tag{43}$$

Here the effects of electrons trapped in nonpropagating orbitals were incorporated in terms of a dielectric constant κ, $K_0(q)$ denotes the modified Bessel function of the second kind, $I_0(q)$ is the modified Bessel function of the first kind. The nanotube radius R yields a natural Ultra Violet (UV) cutoff (for $q \approx \frac{2\pi}{R}$) of the interaction.

We can also define a 1D potential V_0 (the 1D limit of the complete interaction) and the corresponding Fourier transform $V_0(k)$ for $|kR| = 1$,

$$V_0(y) = \frac{2e^2}{\kappa\pi\sqrt{a_0^2 + y^2 + 4R^2}} K\left(\frac{2R}{\sqrt{a_0^2 + y^2 + 4R^2}}\right);$$

$$V_0(k) = \frac{e^2}{\kappa} \left[2|\ln(kR)| + \pi \ln 2\right]. \tag{44}$$

with the complete elliptic integral of the first kind $K(z)$.

Scattering processes Thus we rewrite the coefficients g_i^{α} written for the short range interaction in Fourier transform by analyzing the scattering processes allowed for a CN. Thus we now distinguish four processes associated with the Fermi points $\alpha = \pm$:

1. the 'forward scattering' (αFS) where $\alpha_1 = \alpha_4$ and $\alpha_2 = \alpha_3$
2. the 'backscattering' (αBS) with $\alpha_1 = -\alpha_2 = \alpha_3 = -\alpha_4$ while
3. at half-filling there could be an additional 'Umklapp' process (αUS) characterized by $\alpha_1 = \alpha_2 = -\alpha_3 = -\alpha_4$ which we neglect in what follows.
4. In CNs an additional 'Forward scattering' term (f) which measures the difference between intra- and inter-sublattice interactions, can be introduced following [139, 140]. This term is due to the hard core of the Coulomb interaction. i.e. it follows from the unscreened short range component of the interaction.

These processes are different from the conventional ones discussed above since they do not necessarily mix right- and left-moving branches but rather involve different Fermi points.

Forward Scattering The αFS interaction couples only the total 1D charge densities,

$$H^{(0)}_{\alpha \mathrm{FS}} = \frac{1}{2} \int dy dy' \, \rho(y) V_0(y - y') \rho(y') \, , \tag{45}$$

with $\rho(y) = \sum_{p\alpha\sigma} \psi^{\dagger}_{p\alpha\sigma} \psi_{p\alpha\sigma}$. If we now introduce an infra red cut off given by the CN′s length, L as $k \geq q_c = \frac{2\pi}{L}$ we can define $g_2 \approx V_0(q_c)$.

Obviously the continuum argument (used obtaining $V(q)$ as a Fourier Transform in Eq. 29) plays for $|x| >> a$ while for $|x| \leq a$, an additional FS term arises due to the hard core of the Coulomb interaction,

$$H^{(1)}_{\alpha FS} = -f \int dx \sum_{p\alpha\alpha'\sigma\sigma'} \psi^{\dagger}_{p\alpha\sigma} \psi^{\dagger}_{-p\alpha'\sigma'} \psi_{-p\alpha'\sigma'} \psi_{p\alpha\sigma} \tag{46}$$

with $f/a = \gamma e^2/R$. Evaluating f on the wrapped graphite lattice yields

$$\gamma = \frac{\sqrt{3}a}{2\pi\kappa a_0} \left[1 - \frac{1}{\sqrt{1 + a^2/3a_0^2}} \right] \approx 0.1 \, . \tag{47}$$

This process was not analyzed in term of the g_i in the LL classical approach. In the language of a Hubbard model, we have $f/a = U - V$ where $U = e^2/R$ is the on-site and V the nearest-neighbor Coulomb interaction. According to Eq. 47, this difference is small compared to U.

Backward scattering. Thus we discuss αBS contributions. Since the discussed Fourier Transform involves a rapidly oscillating factor $\exp[2iK_x(x - x')]$, these are local processes which do not resolve sublattices,

$$H_{\alpha BS} = \frac{b}{2}\int dy \sum_{pp'\alpha\sigma\sigma'} \psi^{\dagger}_{p\alpha\sigma}\psi^{\dagger}_{p'-\alpha\sigma'}\psi_{p'\alpha\sigma'}\psi_{p-\alpha\sigma} \ . \tag{48}$$

Estimating the coupling constant we obtain $b \approx f$, while for well-screened short-ranged interactions, one has $b >> f$. In terms of g_i we have $b = g_1 = V_0(2K_s)$.

Bulk Critical exponent in CNs. For this LL model in the metallic armchair tube, a single interaction parameter, g,

$$\frac{1}{g} = K = \sqrt{1 + \frac{g_2}{(2\pi v_F)}} \approx \sqrt{1 + \frac{U_0(q_c)}{(2\pi v_F)}},$$

will drive the power-law temperature-dependent for $eV = k_BT$ and voltage-dependent for $eV = k_BT$ tunneling conductances.

Thus the critical exponent can be written in terms of g as

$$\alpha_{bulk} = \frac{1}{4}\left(g + 1/g - 2\right), \tag{49}$$

which depends just on the forward scattering part of the interaction. Here U_0 can be read as the charging energy, whereas $v_F h/2L$ is the single-particle level spacing. The charging energy follows from the capacitive properties of the metal-nanotube junction and from the electronic structure, so that no universal value can be derived.

Accordingly, the low-temperature conductance $dI/dV \propto V^{\alpha_{bulk}}$, while the linear conductance becomes $G(T) \propto T^{\alpha_{bulk}}$.

The conductance suppression at low temperature or bias has been shown to become even more dramatic for tunneling into the end of a long nanotube, with an exponent that we will calculate in a following section.

In order to estimate the value of the critical exponent we can follow the calculation of Egger and Gogolin [139, 141], where was obtained

$$g = \left\{1 + \frac{8e^2}{\pi\kappa\hbar v}[ln(L/2\pi R) + 0.51]\right\}^{-1/2}. \tag{50}$$

Thus, g is a function of the interaction strength and $g < 1$ corresponds to a repulsive interaction. In the experiments [129], bulk tunneling was measured fitting the high-temperature data, $\alpha \approx 0.34$ corresponding to a value of $g \approx 0.22$, in agreement with theoretical estimates [139, 140, 142].

Multi-wall carbon nanotubes and doping. The low-energy theory for multi-wall carbon nanotubes including the long-ranged Coulomb interactions, internal screening effects, and single-electron hopping between graphite shells was derived and analyzed by bosonization methods. Characteristic Luttinger liquid power laws are found for the tunneling density of states, with exponents approaching their Fermi liquid value only very slowly as the number of conducting shells, N, increases.

The bulk critical exponent was calculated by using bosonization techniques [143] and was obtained

$$\alpha_{bulk} \approx \frac{1}{4N}\left(K_N + \frac{1}{K_N} - 2\right), \tag{51}$$

where

$$\frac{1}{K_N} \approx \sqrt{1 + \frac{NU_0(q_c)}{(2\pi v_F)}}.$$

Afterwards the tunneling density of states of doped multiwall nanotubes including disorder and electron-electron interactions was computed and a non-conventional bahaviour was found [144]. In Ref. [144] this behaviour was explained in terms of a particularly effective and non-conventional Coulomb blockade (CB) for tunneling into a strongly interacting disordered metal.

The discussed explanation in terms of conducting shells does not agree with the measurements of the conductance which usually refer to the outer layer,also if the electronic properties are influenced by the interaction with inner metallic cylinders. Moreover MWNTs use to be significantly doped, which leads to the presence of a large number of subbands at the Fermi level [152] (see Fig. 16.*left*). Thus the number N in Eq. 51 is often assumed to be the number of subbands crossing the Fermi level.

The contribution of a large number of modes at low energies has then an appreciable impact on the enhancement of observables like the tunneling density of states. This issue is relevant for the investigation of the nanotubes of large radius that are present in the MWNTs, which may have a large N. Experiments reported in [153], where measurements of the tunneling conductance have been carried out in doped MWNTs, with a number of subbands at the Fermi level $N \approx 10 - 20$ (in the outer layer).

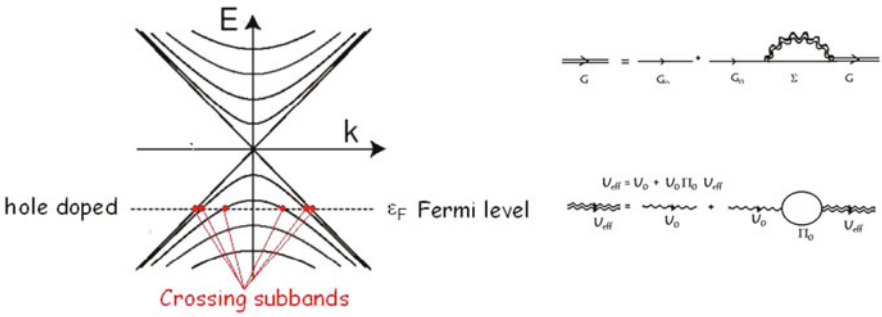

Fig. 16 The degree of doping in CNTs corresponds to the position of the Fermi energy. From a measurement of the conductance as a function of a gate voltage, which shifts the Fermi energy, we can argue the doping level. Nanotubes can be turned to n-type semiconducting by potassium Doping in a Vacuum, Vacuum Annealing or Electrostatic Doping while re-exposure to air reverts NT to p-type [145]. In fact several groups have concluded that charge transfer from oxygen to the nanotube leads to p-doping [146–149] while n-doping can be obtained by direct doping of the tube with an electropositive element such as potassium [150, 151]. In MWNTs the experimental conditions refer to a situation where $N_s = 5:10$ and the suppression of tunnelling in MWNT can be softened by increasing the doping level

We conclude that by doping carbon nanotubes it is possible to alter significantly the electronic, mechanical and chemical properties of the tubes.

RG Approach to the Luttinger Liquid

In Refs. [154–158], was introduced a Renormalization group (RG) method, in order to study the low-energy behaviour of the unscreened e–e repulsion in CNs. In some of these papers a dimensional regularization approach was presented, useful, when dealing with effects of the long-range Coulomb interaction. As we discuss below this method allows to avoid the infrared singularities arising from the long-range Coulomb interaction at $D = 1$.

Generalized Interaction

From the theoretical point of view, a relevant question is the determination of the effects of the long-range Coulomb interaction in CNs. It is known that the Coulomb interaction is not screened in one spatial dimension [159], although usually the e–e interaction is taken actually as short-range (TL model). Thus a dimensional regularization approach [160] was developed in order to analyze the low energy effects of the divergent long-range Coulomb interaction in one dimension. The interaction potential in arbitrary dimensions now reads

$$U_D(r-r') = \int_0^{2\pi}\int_0^{2\pi} \frac{c_D d\varphi d\varphi'}{4\pi^2|\bar{r}-\bar{r}'|} u_0(\varphi,k)\, u_0(\varphi,p)\, u_0\left(\varphi',(k+q)\right) u_0\left(\varphi',(p-q)\right)$$
$$= \frac{c_D}{|r-r'|}. \tag{52}$$

Here r is a vector in the D dimensional space and $\bar{r}$ is a vector in $D+1$ dimensions.

As it is known, the Coulomb potential $1/|r|$ can be represented in three spatial dimensions as the Fourier transform of the propagator $1/k^2$

$$\frac{1}{|r|} = \int \frac{d^3k}{(2\pi)^3} e^{ik\cdot r}\, \frac{1}{k^2}. \tag{53}$$

If the interaction is projected onto one spatial dimension, by integrating for instance the modes in the transverse dimensions, then the Fourier transform has the usual logarithmic dependence on the momentum [154]. We choose instead to integrate formally a number $3 - D$ of dimensions, so that the long-range potential gets the representation

$$\frac{1}{|x|} = \int \frac{d^Dk}{(2\pi)^D} e^{ikx}\, \frac{c(D)}{|k|^{D-1}}, \tag{54}$$

where $c(D) = \Gamma((D-1)/2)/(2\sqrt{\pi})^{3-D}$.

RG Solution for D=1

The starting Hamiltonian for the interacting 1D system is analogous to the sum of Eqs. 41 and 45,

$$H = \int_0^{\Lambda} \frac{dp}{(2\pi)} \psi^+(p)\varepsilon(p)\psi(p) + \int_0^{\Lambda} \frac{dp}{(2\pi)}\ \rho(p)\ U_0(p)\ \rho(-p) \tag{55}$$

where $\rho(p)$ are density operators made of the electron modes $\psi(p)$, and $U_0(p)$ corresponds to the Fourier transform of the 1D interaction potential. Here it also present an Ultra Violet cut-off, Λ, that can be estimated as the order of the bandwidth D.

In writing Eq. 55, were neglected backscattering processes that connect the two branches of the dispersion relation. This is justified, in a first approximation, as for the Coulomb interaction the processes with small momentum transfer have a much larger strength than those with momentum transfer $\approx 2k_F$. The backscattering processes give rise, however, to a marginal interaction.

The one-loop polarizability $\Pi_0(k, \omega_k)$ is given by the sum of particle-hole contributions within each branch

$$\Pi_0(k, \omega_k) = \frac{v_F k^2}{|v_F^2 k^2 - \omega_k^2|}\ . \tag{56}$$

The effective interaction is found by the Dyson equation (see Fig. 16.*right*)

$$U_{\mathit{eff}}(k, \omega_k) = \frac{U_0(k)}{1 - U_0(k)\Pi_0(k, \omega_k)}, \tag{57}$$

so that the self-energy follows: $\Sigma_{\mathit{eff}} = G_0 U_{\mathit{eff}} = G_0 U_{\mathit{eff}} = \frac{G_0 U_0}{1 - U_0 \Pi_0}$.

In the spirit of the GW approximation, v_F can be assumed as a free parameter that has to match the Fermi velocity in the fermion propagator after self-energy corrections.

The polarization gives the effective interaction U_{eff} as in Eq. 57 which incorporates the effect of plasmons in the model. We compute the electron self-energy by replacing the Coulomb potential by the effective interaction

$$\begin{aligned} i\Sigma(k, i\omega_k) =& i\frac{e^2}{2\pi} \int_{-E_c}^{E_c} \frac{dp}{2\pi} \int_{-\infty}^{+\infty} \frac{d\omega_p}{2\pi} \frac{1}{i(\omega_p + \omega_k) - v_F(p + k)} \\ & \frac{U_0(p)}{1 - \dfrac{e^2}{\pi} \dfrac{v_F p^2}{v_F^2 p^2 + \omega_p^2} U_0(p)}. \end{aligned} \tag{58}$$

This approximation reproduces the exact anomalous dimension of the electron field in the Luttinger model with a conventional short-range interaction [157]. The only contributions in (58) depending on the bandwidth cutoff are terms linear in ω_k an k. There is no infrared catastrophe at $\omega_k \approx v_F k$, because of the correction in the slope

of the plasmon dispersion relation, with respect to its bare value v_F. The result that we get for the renormalized electron propagator is

$$G^{-1}(k,\omega_k) = Z_\Psi^{-1}\,(\omega_k - v_F k) - \Sigma(k,\omega_k)$$

$$\approx Z_\Psi^{-1}\,(\omega_k - v_F k) + Z_\Psi^{-1}\,(\omega_k - v_F k)\int \frac{dp}{|p|}\frac{(1-f(p))^2}{2\sqrt{f(p)}\left(1+\sqrt{f(p)}\right)^2} + \ldots, \quad (59)$$

where $f(p) \equiv 1 + U_0(p,\omega_c)/(2\pi v_F)$ and $Z_\Psi^{1/2}$ is the scale of the bare electron field compared to that of the cutoff-independent electron field

$$\Psi_{bare}(E_c) = Z_\Psi^{1/2}\Psi\ . \quad (60)$$

The first RG flow equations, obtained analogously to the more general Eq. 67 obtained below, becomes

$$E_c\frac{d}{dE_c}\,\log\,Z_\Psi(E_c) = \frac{\left(1-\sqrt{f(E_c)}\right)^2}{8\sqrt{f(E_c)}}. \quad (61)$$

As it is known [156], the critical exponent can be easily obtained from the right side of Eq. 61 in the limit of $\log(E_c) \to 0$. If we assume $U(q)$ as a constant, g_2, it results

$$\sqrt{f(q)} = \sqrt{1+\frac{g_2}{(2\pi v_F)}} = K.$$

However as we discussed above the forward scattering involves small momentum transferred, q, thus if we suppose $q = q_c$ ($q \to q_c$ is a limit for the natural infrared cutoff), we obtain $g_2 = U(q_c)$. Hence, as it is clear from a comparison with Eqs. 49 and 61,

$$\alpha_Z = \frac{\left(1-\sqrt{f(q_c)}\right)^2}{8\sqrt{f(q_c)}} = \frac{1}{4}\left(K+\frac{1}{K}-2\right).$$

Dimensional Regularization Near D=1

A different approach was proposed in [155], where was developed an analytic continuation in the number of dimensions, in order to regularize the infrared singularity of the long-range Coulomb interaction at $D = 1$ [161]. The aim of this approach was to find the effective interaction between the low-energy modes of CNs, which have quite linear branches near the top of the subbands (K_S). For this purpose it needs to introduce the analytic continuation to a general dimension D of the linear dispersion around each Fermi point, i.e. the Hamiltonian

$$H = v_F \sum_{\alpha\sigma} \int_0^\Lambda dp|p|^{D-1} \int \frac{d\Omega}{(2\pi)^D}\ \psi^+_{\alpha\sigma}(p)\,\sigma\cdot p\ \psi_{\alpha\sigma}(p) + e^2 \int_0^\Lambda dp|p|^{D-1} \int \frac{d\Omega}{(2\pi)^D}\ \rho(p)\ \frac{c(D)}{|p|^{D-1}}\ \rho(-p), \tag{62}$$

where the σ_i matrices are defined formally by $\{\sigma_i, \sigma_j\} = 2\delta_{ij}$. Here $\rho(p)$ are density operators made of the electron modes $\psi_{\alpha\sigma}(p)$, and $c(D)/|p|^{D-1}$ corresponds to the Fourier transform of the Coulomb potential in dimension D. Its usual logarithmic dependence on $|p|$ at $D = 1$ is obtained by taking the 1D limit with $c(D) = \Gamma((D-1)/2)/(2\sqrt{\pi})^{3-D}$.

A self-consistent solution of the low-energy effective theory has been found in [154, 155, 162] by determining the fixed-points of the RG transformations implemented by the reduction of the cutoff Λ. The Renormalization Group theory with a dimensional crossover starts from Anderson suggestion [163] that the Luttinger model could be extended to 2D systems. The dimensional regularization approach of Refs. [154, 155, 162] overcomes the problem of introducing such an external parameter.

A phenomenological solution of the model was firstly obtained [154, 155, 162], carrying a dependence on the transverse scale needed to define the 1D logarithmic potential, which led to scale-dependent critical exponents and prevented a proper scaling behavior of the model [154, 155, 162, 164].

The long-range Coulomb interaction may lead to the breakdown of the Fermi liquid behavior at any dimension between $D = 1$ and $D = 2$, while the CN description lies between that of a pure 1D system and the 2D graphite layer. Then an analytic continuation is introduced in the number D of dimensions which allows to carry out the calculations needed, in order to accomplish the renormalization of the long-range Coulomb interaction at $D \to 1$.

In the vicinity of $D = 1$, a crossover takes place to a behavior with a sharp reduction of the electron quasiparticle weight and the DOS displays an effective power-law behavior, with an increasingly large exponent. For values of D above the crossover dimension, a clear signature of quasiparticles at low energies is obtained and the DOS approaches the well-known behavior of the graphite layer.

As in the previous section the one-loop polarizability $\Pi_0(k, \omega_k)$ is given by the sum of particle-hole contributions within each branch. Now it is the analytic continuation of the known result in Eq. 56, which we take away from $D = 1$, in order to carry out a consistent regularization of the Coulomb interaction

$$\Pi_0(k, \omega_k) = b(D) \frac{v_F^{2-D} k^2}{|v_F^2 k^2 - \omega_k^2|^{(3-D)/2}}, \tag{63}$$

where $b(D) = \frac{2}{\sqrt{\pi}} \frac{\Gamma((D+1)/2)^2 \Gamma((3-D)/2)}{(2\sqrt{\pi})^D \Gamma(D+1)}$. The effective interaction is found by the Dyson equation in Eq. 57, so that the self-energy Σ_{eff} follows. After dressing

the interaction with the polarization (63), the electron self-energy is given by the expression

$$\Sigma(k,\omega_k) = -e^2 \int_0^{E_c/v_F} dp|p|^{D-1} \int \frac{d\Omega}{(2\pi)^D} \int \frac{d\omega_p}{2\pi} G(k-p,\omega_k-\omega_p) \frac{-i}{\frac{|p|^{D-1}}{c(D)} + e^2\Pi(p,\omega_p)}. \tag{64}$$

At general D, the self-energy (64) shows a logarithmic dependence on the cutoff at small frequency ω_k and small momentum k. This is the signature of the renormalization of the electron field scale and the Fermi velocity. In the low-energy theory with high-energy modes integrated out, the electron propagator becomes

$$\frac{1}{G} = \frac{1}{G_0} - \Sigma \approx Z^{-1}(\omega_k - v_F\ \sigma\ \cdot k) - Z^{-1} f(D) \sum_{n=0}^{\infty} (-1)^n g^{n+1} \left(\frac{n(3-D)}{n(3-D)+2} \omega_k + \left(1 - \frac{2}{D} \frac{n(3-D)+1}{n(3-D)+2}\right) v_F\ \sigma\ \cdot k \right) h_n(D) \log(\Lambda), \tag{65}$$

where $g = (2b(D)c(D)e^2)/v_F$, $f(D) = \dfrac{1}{2^D \pi^{(D+1)/2} \Gamma(D/2) b(D)}$ and $h_n(D) = \dfrac{\Gamma(n(3-D)/2 + 1/2)}{\Gamma(n(3-D)/2+1)}$. The quantity $Z^{1/2}$ represents the scale of the bare electron field compared to that of the renormalized electron field for which G is computed.

The effective coupling g is a function of the cut off with an initial value obtained carrying out an expansion near $D = 1$ [156],

$$g_0(D) = c(D)\frac{e^2}{v_F} \approx \frac{e^2}{\pi^2 v_F} \frac{1}{D-1}. \tag{66}$$

The renormalized propagator G must be cutoff-independent, as it leads to observable quantities in the quantum theory. This condition is enforced by fixing the dependence of the effective parameters Z and v_F on Λ, as more states are integrated out from high-energy shells. We get the differential renormalization group equations

$$\Lambda \frac{d}{d\Lambda} \log Z(\Lambda) = -f(D) \sum_{n=0}^{\infty} \frac{n(3-D)(-g)^{n+1}}{n(3-D)+2} h_n(D) = -\gamma(g), \tag{67}$$

$$\Lambda \frac{d}{d\Lambda} g(\Lambda) = -f(D) \frac{2(D-1)}{D} g^2 \sum_{n=0}^{\infty} (-g)^n \frac{(3-D)n+1}{(3-D)n+2} h_n(D) = -\beta(g). \tag{68}$$

For $D = 1$ the function in the r.h.s. of Eq. 68 vanishes, so that the 1D model has formally a line of fixed-points, as it happens in the case of short-range interaction. In the crossover approach shown in this section, the effective coupling g is sent to strong coupling in the limit $D \to 1$, and the behavior of the RG flow in this regime

remains to be checked. The dependence on D of the functions appearing in the RG equations shows itself in the form of $D-1$ and $D-3$ factors, revealing that these are the two critical dimensions, corresponding to a marginal and a renormalizable theory, respectively.

In order to approach the limit $D \to 1$, we have to look for the asymptotic dependence on D of the functions appearing in the RG equations. We will see that this dependence appears as $D-1$ and $D-3$ factors, revealing that these are the two critical dimensions, corresponding to a marginal and a renormalizable theory, respectively.

Starting with the function $\beta(g)$, we need to carry out the sum at the right-hand-side of Eq. 67. This is given in terms of the hypergeometric special functions [156]. However the β function near $D=1$ can be approximated with the simple function of g and d to first order in $D-1$,

$$\beta(g) \approx -\frac{f(D)}{4}\frac{2(D-1)}{D}\sqrt{\pi}g\left(1-\frac{1}{\sqrt{1+g}}\right). \tag{69}$$

The γ function can be expressed in the form

$$\gamma(g) = \frac{f(D)}{4}\frac{3-D}{2}gT_D(g) \tag{70}$$

where the series $T_D(g)$ is available on tables. For $D=1$ it has the simple expression

$$T_1(g) = \sqrt{\pi}\frac{2\sqrt{g+1}-g-2}{g\sqrt{g+1}} \tag{71}$$

The scaling of the electron wave function near $D=1$ is therefore given by

$$\gamma(g) \approx \frac{f(D)}{4}\sqrt{\pi}\left(2-\sqrt{1+g}-\frac{1}{\sqrt{1+g}}\right) \tag{72}$$

This coincides formally with the anomalous dimension that is found at $D=1$ in the exact solution of the Luttinger model, what provides an independent check of our RG approach to the 1D system.

The dimensional crossover approach allows to calculate the critical exponent also in the case of a divergent interaction for $D \to 1$. The DOS computed at dimensions between 1 and 2 displays an effective power-law behavior which is given by $n(\varepsilon) : Z(\varepsilon)|\varepsilon|^{D-1}$, for several dimensions approaching $D=1$. Then by introducing the low-energy behavior of $Z(\varepsilon)$ in order to analyze the linear dependence of $\log(n(\varepsilon))$ on $x=-\log(\Lambda)$ it can be obtained

$$\log(n(\varepsilon)) \approx \log Z(\varepsilon) + (D-1)\log(|\varepsilon|) \approx (\alpha_Z - (D-1))\,x \equiv \alpha_D x. \tag{73}$$

Here α_Z can be easily written starting from Eq. 67, if we limit ourselves to a simple first order expansion near $x = 0$ with $(\log(Z) \approx \gamma(g_0)x)$, where g_0 is the initial value of the coupling (see Eq. 66)

$$\alpha_Z \approx T_1(\sqrt{1+g_0})g_0\frac{(3-D)f(D)(D+1)}{8}. \tag{74}$$

The analytic continuation in the number of dimensions allows to avoid the infrared singularities that the long-range Coulomb interaction produces at $D = 1$, providing insight, at the same time, about the fixed-points and universality classes of the theory in the limit $D \to 1$.

In order to compare the results of this approach with experiments, as in [156], a lower bound for the exponent of the DOS can be obtained by estimating the minimum of the absolute value of α_D, for dimensions ranging between $D = 1$ and $D = 2$. The evaluation can be carried out starting from Eqs. 73 and 74. A minimum value for $|\alpha_D|$ as a function of D, by introducing the expression of $g_0(D)$ in Eq. 66, was obtained. From Fig. 17 we can see that the maximum value for α_D (α_M) corresponds to a dimension between 1 and 1.2. If the number of subbands is increased, then the value of $|\alpha_M|$ decreases while the corresponding dimension approaches 1.

Doping in Multi Wall Carbon Nanotubes. In the case of doped MWNTs the effect of having a number N of subbands crossing the Fermi level, which multiply consequently the number of electron fields and terms in the hamiltonian has to be

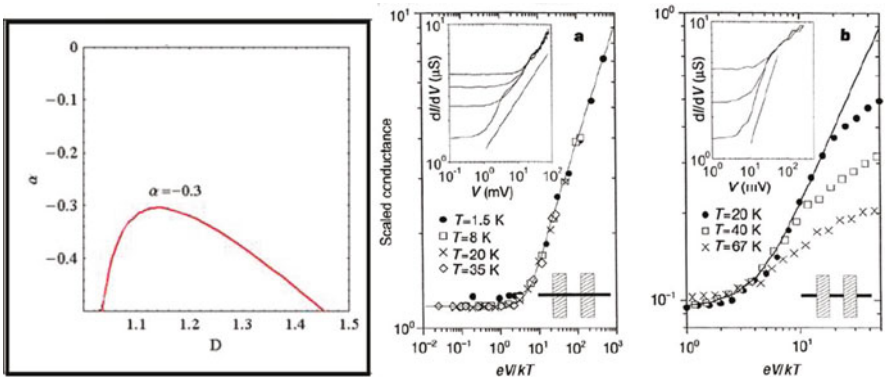

Fig. 17 (*Left*) α as a function of the dimension, and we choose the maximum value of this function between $D = 1$ and $D = 2$ as an estimate of the critical exponent. We find a value for α in the usual undoped nanotube that reproduces the anomalous exponent measured experimentally ($\alpha \approx -0.3$), corresponding to a dimension for the crossover between 1.1 and 1.2. (*Right*) Inset in a, dI/dV curves taken on a bulk-contacted rope at temperatures T = 1.6 K, 8 K, 20 K and 35 K. Inset in b, dI/dV curves taken on an end-contacted rope at temperatures T = 20 K, 40 K and 67 K. In both insets, a straight line on the log–log plot is shown as a guide to the eye to indicate power-law behaviour. The main panels a and b show these measurements collapsed onto a single curve by using the scaling relations described in the text. The solid line is the theoretical result fitted to the data by using as a fitting parameter. The values of resulting in the best fit to the data are = 0.46 in a and = 0.63 in b. From [165]

incorporated. Thus the analytic continuation to general dimension D of the one loop polarizability becomes

$$\Pi(k,\omega_k) = 2Nb(D)\frac{v_F^{2-D}k^2}{|v_F^2k^2-\omega_k^2|^{(3-D)/2}}. \tag{75}$$

The equations presented above have to be rewritten by including the number of subbands so that α_D in Eq. 73 becomes

$$\alpha_D \approx g_0 T_1(g_0)\frac{(3-D)f(D)(D+1)}{8\,N} - (D-1). \tag{76}$$

In [156] was obtained, in the limit of large N and small values of $D-1$,

$$\alpha_Z \approx -\frac{f(D)(3-D)(D+1)}{8\,N}\sqrt{\pi\, g_0}, \tag{77}$$

and was obtained that α_Z vanishes at large N as : $1/\sqrt{N}$, and it diverges at $D \to 1$ as $1/\sqrt{D-1}$.

Results and Experiments

Experimental Evidence of LL Behavior

In the last decade several transport and photoemission studies provided evidence for the existence of the TLL state in CNs. In these studies, power-law behavior of temperature and bias dependent conductivity and a power-law Fermi edge was observed, respectively.

The non-Ohmic behavior of the conductance at low bias voltage, the so called zero-bias anomaly (ZBA), is a clear signature of a tunneling contact between a Fermi liquid and a strongly correlated system. Thus evidence of LL behavior in CNs has been found in many experiments [129, 165], where a measurement of the temperature dependence of the resistance was carried out, above a crossover temperature T_c[166]. In Fig. 16.*right* are reported measurements of the conductance of bundles ('ropes') of SWNTs as a function of temperature and voltage that agree with predictions for tunnelling into a Luttinger liquid. In particular, we find that the conductance and differential conductance scale as power laws with respect to temperature and bias voltage, respectively, and that the functional forms and the exponents are in good agreement with theoretical predictions [165]. In these experiments (e.g. [129]), bulk tunnelling was measured fitting the high-temperature data, $\alpha \approx 0.34$ corresponding to a value of $g \approx 0.22$, in agreement with with theoretical estimates [139, 156].

Power-law conductance behavior with exponent values in the range of theoretical predictions was also found for crossed metallic junctions of SWNTs [167], giving confidence in the manifestation of a Luttinger liquid state in small-diameter SWNTs.

Alternatively, by means of angle-integrated photoemission measurements of SWNTs, some power-law behavior of the spectral function and intensities was also found to be in good agreement with LL model predictions [168].

Also the Nuclear magnetic resonance (NMR) can be a powerful method to characterize correlated states of materials as it is sensitive to the density of states near the Fermi edge. Recently experiments by Singer et al. [169] showed a deviation from Fermi-liquid behavior in carbon nanotubes with an energy gap evident at low temperatures.

Effects of Doping. The effect of doping was taken in account in [152]. There was explored the electric-field effect of carbon nanotubes (NTs) in electrolytes. Due to the large gate capacitance, Fermi energy shifts of order $\pm 1V$ can be induced, enabling to tune NTs from p to n-type. Consequently, large resistance changes are measured. The measurements of a power law behaviour were also carried out in the MWNTs by studying the tunneling of electrons into the CN. Nanotube/electrode interfaces with low transparency as well as nanotube/nanotube junctions created with atomic force microscope manipulation have been used. The tunneling conductance goes to zero as the temperature and bias are reduced, and the functional form is consistent with a power law suppression of tunneling as a function of energy. The exponent depends upon sample geometry. It has been reported that the values of the critical exponent α_{bulk} measured in 11 different samples range from 0.24 to 0.37 [153].

This variation can be accounted for within the RG approach reported above by assuming that a large number of subbands, N_s is involved (N = 2 to N = 10). Thus the effect of doping was studied in the suppression of tunneling observed in MWNTs, incorporating as well the influence of the finite dimensions of the system. The scaling approach reported above allowed to encompass the different values of the critical exponent measured for the tunneling density of states in carbon nanotubes. Thus was predicted that further reduction of α_{bulk} should be observed in multiwalled nanotubes with a sizeable amount of doping.

From a theoretical point of view, in the case of nanotubes with a very large radius, was found a pronounced crossover between a high-energy regime with persistent quasiparticles and a low-energy regime with the properties of a one-dimensional conductor.

Magnetic field effects on Luttinger Liquid behaviour. The effects of a transverse magnetic field B, acting on CNs were also investigated in the last years. Theoretically, it is predicted that a perpendicular B field modifies the DOS of a CN [40], leading to the Landau level formation as we discussed above. In a recent letter Kanda et al. [170] examined the dependence of G on perpendicular B fields in MWNTs (see Fig. 18). They found that, in most cases, G is smaller for higher magnetic fields, while α_{Bulk} is reduced by a factor $1/3$ to $1/10$, for B ranging from 0 to 4 T. Following the calculation proposed for a semiconducting quantum Wire [32] the effects of transverse magnetic field were analyzed in large radius CNs [157]. The presence of $B \neq 0$ produces the rescaling of all repulsive terms of the interaction between electrons, with a strong reduction of the backward scattering, due to the edge localization of the electrons. Our results imply a variation with B in the value

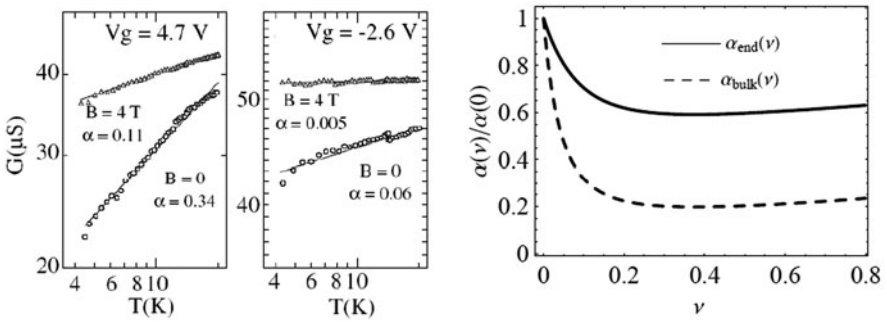

Fig. 18 (*Left*) Perpendicular magnetic field dependence of the $G - T$ data for two gate voltages $V_g = 4.7\text{V}$ (**a**), and 2.6V (**b**). In both cases, the data follow the power-law behavior, and the exponent depends on the magnetic field (from [170]. Critical exponents versus the magnetic field dependent parameter, ν, for a large radius CN: α_{bulk} is calculated following Eq. 51, α_{end} is calculated following Eq. 79. The magnetic field rescales the values of the Fermi velocity and the strength of e–e interaction. It follows that the effects of a transverse magnetic field also involve the value of K. Thus, we predict a reduction of the critical exponents α_{bulk} and α_{end}, by giving magnetic field dependent exponents for the power law behaviour of the conductance

of α_{Bulk}, which is in fair agreement with the value observed in transport experiments [170].

In order to obtain the critical exponent it is possible to calculate $U_0(q, \omega_c)$ starting from the eigenfunctions $\Psi_{0,k_F}(\varphi, y)$ and the potential in Eq. 42. We focus our attention on the forward scattering (FS) terms. We can obtain g_2, FS between opposite branches, corresponding to the interaction between electrons with opposite momenta, $\pm k_F$, with a small momentum transfer $\approx q_c$. The strength of this term reads

$$g_2 = U_0(q_c, B, k_F, -k_F)$$

$$= \frac{c_0}{N_2(\nu)} \left[K_0\left(\frac{q_c R}{2}\right) I_0\left(\frac{q_c R}{2}\right) + u_2(\nu) K_1\left(\frac{q_c R}{2}\right) I_1\left(\frac{q_c R}{2}\right) \right],$$

where $K_n(q)$ denotes the modified Bessel function of the second kind, $I_n(q)$ is the modified Bessel function of the first kind, while N_2 and u_2 are functions of the transverse magnetic field, as was discuss in the appendix of [171].

By introducing into Eq. 51 the calculated values of g_2 and g_4, it follows that the bulk critical exponent is reduced by the presence of a magnetic field, as we show in Fig. 18.

Intramolecular Devices

Impurity. Since 1995 intramolecular devices have also been proposed which should display a range of other device functions [172–177]. For example, by introducing

a pentagon and a heptagon into the hexagonal carbon lattice, two tube segments with different atomic and electronic structures can be seamlessly fused together to create intramolecular metal–metal, metal–semiconductor, or semiconductor–semiconductor junctions. Electrical transport SWNTs with intramolecular junctions was measured and was demonstrated that a metal–semiconductor junction behaves like a rectifying diode with nonlinear transport characteristics. In the case of a metal–metal junction, the conductance appears to be strongly suppressed and it displays a power-law dependence on temperatures and applied voltage, consistent with tunneling between the ends of two Luttinger liquids [129].

From a theoretical point of view the power-law behaviour characterizes also the thermal dependence of G when an impurity is present along the 1D devices. The theoretical approach to the presence of obstacles mixes two theories corresponding to the single particle scattering (by a potential barrier $V_B(r)$) and the TLL theory of interacting electrons. The single particle scattering gives the transmission, probability, $|t|^2$, depending in general on the single particle energy ε. Hence, following [134, 136], the conductance, G, as a function of the temperature and $|t|$ can be obtained

$$G \propto |t(\varepsilon, T)|^2 \equiv |t(\varepsilon)|^2 T^{2\alpha_{end}}, \tag{78}$$

where we introduced a second critical exponent [171], α_{end}

$$\alpha_{end} \approx \frac{1}{2}\left(\frac{1}{K} - 1\right). \tag{79}$$

The results obtained in [129] agreed with theoretical prediction.

Intrinsic Quantum Dot. Experiments [178, 179] show transport through an intrinsic quantum dot (QD) formed by a double barrier within a 1D electron system, allowing for the study of the resonant or sequential tunneling. The linear conductance typically displays a sequence of peaks, when the gate voltage, V_g, increases. Thus also the double-barrier problem has attracted a significant amount of attention among theorists [180–187], in particular for the case of two identical, weakly scattering barriers at a distance d. In general, the transmission is non-zero for particular values of the parameters corresponding to a momentum k_F, such that $\cos(k_F d/2) = 0$. It follows that, although in a 1D electron system for repulsive interaction the conductance is suppressed at zero temperature by the presence of one impurity (1D metal becomes a perfect insulator), the presence of an intrinsic QD gives rise to some peaks in the conductance at $T = 0$ corresponding to the perfect transmission. This *resonant scattering* condition corresponds to an average particle number between the two barriers of the form $\nu + 1/2$, with integer ν, i.e. the "island" between the two barriers is in a degenerate state. If interactions between the electrons in the island are included, one can recover the physics of the Coulomb blockade [188].

The power-law behaviour characterizes also the thermal dependence of G in the presence of an IQD. A first theory about the transport through an IQD is known as *Uncorrelated Sequential Tunneling* (UST), where an incoherent sequential

tunneling is predicted. It follows the dependence of the peaks of the conductance according to the power law

$$G_{max} \propto T^{\alpha_{end}-1}.$$

However in order to explain the unconventional power-law dependencies in the measured transport properties of a CN [178, 179], a different mechanism was proposed [178, 183], namely, *correlated sequential tunneling* (CST) through the island. The temperature dependence of the maximum G_{max} of the conductance peak, according to the CST theory, yields the power law behaviour

$$G_{max} \propto T^{\alpha_{end-end}-1} = T^{2\alpha_{end}-1}. \tag{80}$$

Recently a lot of theoretical work has been carried out on the double impurity problem in TLL systems. In an intermediate temperature range $\varepsilon_c << k_B T << \Delta_{dot}$, where ε_c is the Infra Red cut-off energy and Δ_{dot} is the level spacing of the dot, some authors [184, 185] predict a behaviour according to the UST, while others [187] find results in agreement with the CST theory. In a recent paper [189] the authors discussed how the critical exponent can depend on the size of the dot and on the temperature, by identifying three different regimes, i.e. the UST at low T, a Kirchoff regime at intermediate T ($G_{max} \propto T^{2\alpha_{end}}$) and a third regime for $T >> \Delta_{dot}$, with $G_{max} \propto T^{-1}$. Thus, in their calculations, obtained starting from spinless fermions on the lattice model, no evidence of CST is present.

Then, the problem of the transport through a Quantum Dot formed by two intramolecular tunneling barriers along the MWNT, weakly coupled to Tomonaga-Luttinger liquids is studied, including the action of a strong transverse magnetic field B. There were predicted [30] the presence of some peaks in the conductance G versus B, related to the magnetic flux quantization in the ballistic regime (at a very low temperature, T) and also at higher T, where the Luttinger behaviour dominates. The temperature dependence of the maximum G_{max} of the conductance peak according to the Sequential Tunneling follows a power law, $G \propto T^{\gamma_e - 1}$ with γ_e linearly dependent on the critical exponent, α_{end}, strongly reduced by B as shown in Fig. 18.*right*.

Intermediate Regimes and Crossover

Crossover from Luttinger liquid to Coulomb Blockade regime. Now we discuss the experimental data reported in a recent letter by Kanda et al. [170], in which the intermediate regime has been explored measuring the zero-bias conductance at temperatures where the thermal energy becomes comparable to the level spacing in the discrete single-particle spectrum. In Ref. [170] the authors have reported a systematic study of the gate voltage dependence of the LL-like behaviour in MWNTs, showing the dependence of the exponent α on gate voltage, with values of α ranging from 0.05 to 0.35. The main results of [170] are as follows:

1. the gate-voltage (V_g) dependence of the exponent α below 30 K exhibits periodic oscillations; the characteristic V_g scale for α variation, ΔV_g, is around 1 V;
2. changes in the exponent α are observed in the plots of the conductance at an inflection temperature $T^* \approx 30$ K, for values of V_g corresponding to peaks of α.

In their letter, Kanda et al. do not find plausible the explanation of the mentioned features starting from a LL description of the MWNTs. In this respect, Egger has considered in [143] a model for MWNTs composed of a number N_{SH} of ballistic metallic shells. The author has discussed there a low-energy theory for the MWNTs including long-ranged Coulomb interactions and internal screening effects. The theory may be also extended to include the effect of a variable number of conducting modes modulated by the doping level. However, Kanda et al. rule out the possibility that the change in the number of subbands at the Fermi level may be at the origin of the features observed in their experiment, as long as the subband spacing is too large to be consistent with the period of the oscillations.

Then, Kanda et al. turn to a different kind of theory that considers the MWNT as a diffusive conductor. Egger and Gogolin [144] have calculated the TDOS of doped MWNTs including disorder (with mean free path l smaller than the radius R) and electron-electron interactions. MWNTs may display an effective and nonconventional CB arising from tunneling into a strongly interacting disordered metal, leading to LL-like zero-bias anomalies: the exponent becomes $\alpha = (R/2\pi\hbar D\nu_0)\log(1+\nu_0 U)$, where D is the diffusion constant, $\nu_0 = N_s/2\pi\hbar v_F$ is the noninteracting density of states depending on the number of subbands N_s and the Fermi velocity v_F, and U_0 is an effectively short-ranged 1D interaction. Substituting these parameters by pertinent values yields an estimate α; $R/N_s l$, that is near the experimentally observed values.

Kanda and coworkers conclude that this second theory better explains the experimental results, by assuming that the mean-free path l may fluctuate with the gate voltage. This is based on the theoretical work by Choi et al. [190], that have studied the effects of single defects on the local density of states via resonant backscattering. However, the argument of Kanda et al. has not addressed the question of how a random distribution of defects may produce the oscillations observed in the experiment. We believe otherwise that the dependence of the α exponent on the gate voltage is in correspondence with a definite periodic structure of the single-particle density of states.

A theoretical approach was developed in [191, 192] to the low-energy properties of 1D electron systems aimed to encompass the mixed features of Luttinger liquid and Coulomb blockade behavior observed in the crossover between the two regimes. For this aim the Luttinger liquid description was extended by incorporating the effects of a discrete single-particle spectrum. The intermediate regime is characterized by a power-law behavior of the conductance, but with an exponent oscillating with the gate voltage, in agreement with recent experimental observations. This construction also accounts naturally for the existence of a crossover in the zero-bias conductance, mediating between two temperature ranges where the power-law behavior is preserved but with different exponent.

Crossover from Fabry-Perot to Coulomb Blockade regime. For good contact, the SWCNT acts as an electron wave guide creating resonances at certain energies and can be regarded as an open quantum dot with the resonances corresponding to the broad energy levels. As we discussed above in the opposite limit (CB regime) of very low transparency, the electrons are forced to tunnel one by one and the energy levels sharpens due to their longer life time.

An intermediate regime also exists in which the electron number on the dot is still fixed but significant cotunneling is allowed. This leads to different kinds of Kondo effects related to the total excess spin [193–195] and/or the orbital degree of freedom on the SWCNT quantum dot [196, 197].

The transition between these regimes was reported in [198] where the authors discussed how transport evolves from being wave-like transmission known as Fabry-Perot interference to single particle-like tunneling of electrons or holes. In the intermediate regime four Coulomb blockade peaks appear in each Fabry-Perot resonance, which is interpreted as entering the SU(4) Kondo regime. A bias shift of opposite polarity for the Kondo resonances for one electron and one hole in a shell is in some cases observed.

Superconducting Transition

The Superconductivity behaviour in low dimensional systems is a quite interesting question since 40 years ago Mermin and Wagner [199] proved a famous theorem stating that it is impossible for abrupt phase transitions with long-range order to occur in 1- or 2-D systems at finite temperature. Thus CNs are among the best candidates for investigating the possibility of (quasi)1D superconductivity. In general CNs do not show superconducting properties but some recent experiments found that they can can superconduct by showing also high superconducting transition temperature, $T_c \approx 10°$ K. [200, 201].

Experimental Evidence of Superconductivity in CNs

The field of SC in nanotubes started experimentally with the discovery of a strong proximity-induced SC in isolated or bundled SWNTs connected to superconducting leads [202, 203]. Proximity-induced superconductivity in single-walled carbon nanotubes below 1° both in a single tube 1 nm in diameter and in crystalline ropes containing about 100 nanotubes, was observed [202]. In these experiments, the CNs were assumed to be in the normal, N, state but with a phase coherence length L_ϕ and a thermal length L_T larger than the superconducting coherence length, allowing for the *SNS* junction to sustain a very high supercurrent below the lead transition temperature.

Measurements on ropes of single-walled carbon nanotubes (SWNT) in low-resistance contact to non-superconducting (normal) metallic pads were reported in [204]. It was found a 2 orders of magnitude resistance drop below 0.55°K, which

is destroyed by a magnetic field of the order of 1 T, or by a dc current greater than 2.5 μA. These features suggested the existence of intrinsic superconductivity in ropes of SWNT. Then in Ref. [205] were reported low-temperature transport measurements on suspended single-walled carbon nanotubes (both individual tubes and ropes) that indicated the presence of attractive interactions in carbon nanotubes which overcome Coulomb repulsive interactions at low temperature, and enabled investigation of superconductivity in a one-dimensional limit never explored before.

In 2001, ultra-small-diameter single wall nanotubes (USCN), with diameter of $\approx$ 0.4 nm, have been produced inside the channels of a zeolite matrix. Possible metallic geometries compatible with such a small radius are the armchair (3, 3) and the zig-zag (5, 0) ones. The ultra-small diameter of these tubes induces many unusual properties, such as a superconducting transition temperature $T_c \approx 15°$K [200], much larger than that observed in bundles of larger diameter tubes [204].

In MWNTs, where disorder and impurities can play a central role, supercurrents have been even harder to achieve. Enhanced conductance was observed near zero bias, which was interpreted in terms of multiple Andreev reflections in the presence of inelastic processes [206]. On the other hand, proximity induced supercurrent has been observed [207] also in an individual, diffusive MWNT using bulk(side)-contacted samples with Ti/Al contacts [208].

In Ref. [201] it was reported that there is a superconducting phase in entirely end-bonded MWNTs with a transition temperature $T_c \approx 12°$K. The TEM images showed a MWNT with an outer diameter of $2R_o = 7.4$ nm, and inner diameter of $2R_i < 2$ nm ($R < 1$ nm) while the emergence of this superconductivity is highly sensitive to the junction structures of the Au electrode/MWNTs and T_c depends on the numbers of electrically activated shells.

More recently a gradual magnetization drop with an onset temperature (Tc) of 18 23 K has been found in the honeycomb arrays of multiwalled CNTs (MWNTs) showing a slight resistance decrease due to superconductivity [209]. The disappearance of the Meissner effect after destroying the array structure suggested that intertube coupling of MWNTs in the honeycomb array is a dominant factor for the mechanism.

Theoretical Approach

The superconducting phase in 1D systems enters into competition with another type of quantum order, the charge-density-wave (CDW) phase, an instability very specific to 1D systems (while the SC one occurs irrespective of the dimension).

While the SC transition induces the creation or destruction of electron (Cooper) pairs, the CDW is induced by the spontaneous formation of electron-hole excitations.

The Phase Diagram and Breakdown of a Luttinger Liquid

Effective field theory was solved in practically exact way by Egger and Gogolin [139]. As we discussed above, they analyzed a (10, 10) SWNT, next CN_{10}. Thus

they showed that both g_1 and f scale as $1/R$ and in CN_{10} they are much smaller than g_2 [139] but at low temperature their effects should be included. In [139] this has been realized by means of a renormalization group calculation. The main result is the existence of two different crossover temperatures, namely

$$kT_f = De^{-\frac{2\pi v_F}{f}} \quad \text{and} \quad kT_b = De^{-\frac{2\pi v_F}{g_1}}$$

associated to the dominance of f and g_1 respectively. Below these temperatures the Luttinger liquid breaks down and a (quasi-) long-range order phase appears. Thus the presence of a SC phase due to the effect of the short range g_1 and f was predicted, but at very low temperatures ($T_b \approx 0.1$ m°K and $T_f \leq T_b$).

This behaviour can be summarized in the phase diagram reported in Fig. 19. Calculations for a CN_{10} predict that 1D superconductivity is the dominant instability only at $T < 1$ m°K with screened interactions thus a purely electronic mechanism is not sufficient. Moreover for long-ranged interactions (which is the case of nanotubes in typical conditions), we have $T_f \approx T_b$, while for short-ranged interactions it results $T_f < T_b$. In the latter case a superconducting instabilty is predicted at $T \approx T_f$ if the Luttinger liquid parameter g is larger than $1/2$.

Starting from these results a pure electronic mechanism which gives Superconductivity needs:

i) Screening of the forward scattering, g_2 (long range effect $g > 0.5$)
ii) Increasing of the backward scattering, g_1 (short range effect T_b)
iii) Relevant effects from the lattice (high value of the corresponding temperature, T_f)

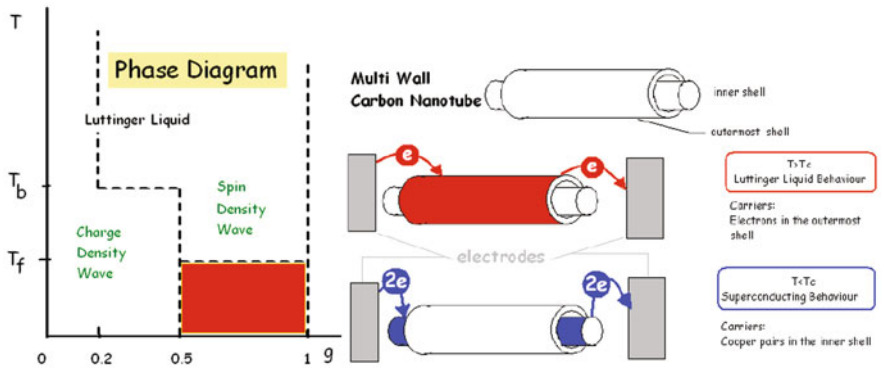

Fig. 19 The transition temperature for CN_{10} with the typical long-range interaction is estimated to be $T_f : T_b : 1$ mK, i.e. a value certainly hard to be observed. This is due to the smallness of g_1 and f (compared to g_2), since they scale as $1/R$ and are sizeable only for very thin tubes. (*left*) We assume that all shells of an entirely end bonded MWNT are resistors in a parallel connection. For $T > T_c$ the current is due to the flow of electrons in the outermost shells with the typical behaviour of a Luttinger Liquid. For $T < T_c$ a superconducting transition is allowed in the innermost shell; thus the transport is due to Cooper pairs

Some Phonon Based Theories

Many studies about the electron-phonon interaction focused on isolated tubes and in particular on the possible occurrence of a Peierls instability [210]. Such an instability is always expected to occur in 1D systems. Thus the coupling to long-wavelength acoustic modes such as twistons or radial breathing modes (derived from the transverse acoustic modes of graphite) was studied as a means to induce a CDW instability.

Superconductivity in carbon nanotube ropes – In order to explain superconductivity in the experiment of [205] was derived and analyzed the low-energy theory of superconductivity in carbon nanotube ropes [211]. The rope was modelled as an array of metallic nanotubes, taking into account phonon-mediated as well as Coulomb interactions, and arbitrary Cooper pair hopping amplitudes between different tubes. Quantum phase slips are shown to cause a depression of the critical temperature Tc below the mean-field value, and a temperature-dependent resistance below T_c. Thus was found a signature of the presence of attractive phonon-mediated interactions in carbon nanotubes, which can even overcome the repulsive Coulomb interactions [212].

According Ref. [213], the critical supercurrents found in experiments on the proximity effect of [202] can be explained by the presence of a short-range attractive interaction coming from the coupling to the elastic modes of the nanotube. In a further letter [214], the autor discussed the strong suppression of single-particle hopping between neighboring nanotubes in a disordered rope and conclude that the tunneling takes place in pairs of electrons, which are formed within each nanotube due to the existence of large superconducting correlations. Thus a model was developed to account that the single-particle hopping between neighboring nanotubes in a rope is strongly suppressed [215] because the different helical structure of the nanotubes leads to the misalignment of their lattices.

Thus the effect of superconductivity does not rely exclusively on the properties of the individual nanotubes in agreement with the discussed priciple that any correlation in a 1D system can only develop a divergence at zero temperature [216]. Moreover was demonstrated [217] that the interaction among a large number of metallic nanotubes favors the appearance of a metallic phase in the ropes, intermediate between respective phases with spin-density-wave and superconducting correlations. These arise in samples with about 100 metallic nanotubes or more, where the long-range Coulomb interaction is very effectively reduced and it may be overcome by the attractive interaction from the exchange of optical phonons within each nanotube.

Later were introduced the renormalization of intratube interactions and the effect of intertube Coulomb screening. Thanks to this aproach was possible to study both the limits of thin and thick ropes ranging from purely one-dimensional physics to the setting of 3D Cooper-pair coherence [218].

Superconductivity in small-diameter carbon nanotubes. The SC and instablities were investigated in CNs of small radius in order to explain the results of [200]. According to [219] the Luttinger liquid behavior breaks down in the undoped (3, 3)

nanotubes at low temperatures, due to the appearance of soft modes in the sector of current excitations. The instabilities that may lead to the breakdown of the Luttinger liquid in the small-diameter (5, 0) nanotubes were analyzed in [219]. There the authors focused on the competition between the effective interaction mediated by phonon exchange and the Coulomb interaction also by analyzing the effects of screening.

The softening of phonons by electron-phonon interactions and the Peierls transition was also studied in the specific case of small tubes [220, 221]. The increase of the coupling with radius was shown to lead to a Peierls distortion at several hundred Kelvin mediated by $2k_F$ phonons in the (3, 3) armchair case [220, 221].

Electronic instabilities of doped multi-walled nanotubes. In doped multi-walled nanotubes each shell has in general a manifold of Fermi points, thus an analysis based on the scale dependence of the different scattering processes, showed that a pairing instability arises for a large enough number of Fermi points as a consequence of their particular geometric arrangement. The instability is enhanced by the tunneling of Cooper pairs between nearest shells, giving rise to a transition from the Luttinger liquid to a superconducting state in a wide region of the phase diagram [222].

Isolated Single wall nanotube. Thus most of the studyes concluded that the sorrounding environment plays a central role on the SC transition of a CN. Thus in isolated nanotubes, Coulomb repulsion should easily overcome the attractive interaction mediated by phonons. However in [223], using a one-loop renormalization group method the authors concluded that a SC order may dominate in the (5, 0) tube provided that the electron-phonon interaction is strong enough. Moreover a possible dominant triplet-state superconducting instability was suggested to arise from the specific three-band topology at the Fermi level of isolated (5, 0) tubes [224].

Other Theories

A different mechanism of carbon nanotube superconductivity that originates from edge states which are specific to graphene was proposed in [225]. Using on-site and boundary deformation potentials which do not cause bulk superconductivity, was obtained an appreciable transition temperature for the edge state.

In Ref. [226] the issue was discussed, whether a superconducting behavior in small radius carbon nanotubes can arise by a purely electronic mechanism by a comparison between two different approaches, (1) the first one based on the Luttinger Model, (2) the second one, which emphasizes the role of the lattice and short range interaction, developed starting from the Hubbard Hamiltonian. By using the latter model a transition temperature of the same order of magnitude as the measured one was predicted.

By a Luttinger liquid-like approach, one finds enhanced superconducting correlations due to the strong screening of the long-range part of the Coulomb repulsion. It was shown that the presence of many nanotubes inside the zeolite matrix of the experiment in [200] provides a strong screening of the long range component of the electron-electron interaction (g_2), mainly due to the presence of electronic currents

in neighboring nanotubes, while the short range components (f and g_1) have to remain almost unchanged.

This allows for the occurrence of a sizable superconducting instability within the Luttinger liquid approach. Based on this finding, the autors performed a detailed analysis on the resulting Hubbard-like model, and calculated transition temperatures of the same order of magnitude as the measured ones [226].

In the experiment of [201] the authors claim that almost all the shells of the MWNTs are electrically active. Such a high quality of the contacts seems to be crucial, in order to observe the superconducting transition at such a high temperature. Moreover the clear power-law of the conductance observed for $T > T_c$ is consistent with the Luttinger liquid character of the normal state. Therefore the observed sharp breakdown of the power-law at T_c is an indication that an approach based on the superconducting instability of the Luttinger liquid is well posed.

Moreover, as we discussed above, in a typical transport experiment, only the outermost shell of the MWNT becomes electrically active. As a consequence the conducting channel is not efficiently screened and retains a strong 1D character. On the other hand, the activation of the internal shells gives a large dielectric effect, due to intra- and inter-shell screening, and at the same time it provides an incipient 3D character, which is crucial for establishing the superconducting coherence.

In Ref. [227], as reported in Fig. 19, all contacted shells can carry the normal current as resistors in parallel connection and at $T > T_c$, the electrons flow in each shell. It is however clear that the conductance G is mainly given by the outermost shells, because they have more conducting channels due to larger radius. For what concerns $T < T_c$, the theory predicts that superconductivity is favored in the inner part of the MWNT, where the radius of the shells is reduced, in particular, in the innermost shell which is able to support the transport of Cooper pairs. This scenario is in line with the prediction [228, 229] of an increase in pair binding energy with decreasing nanotube radius.

Notice that both the doping and the screening of long-range part of the electron-electron repulsion, needed to allow the SC phase, are related to the intrinsically 3D nature of the environment where the CNs operate [230].

Acknowledgments This work was supported in part by the EU under the 7th Framework Program ICT-2007.8.1 FET Proactive 1: Nano-scale ICT devices and systems Carbon nanotube technology for high-speed next-generation nano-Interconnects (CATHERINE) project, Grant Agreement n. 216215.

References

1. S. Iijima, Helical microtubules of graphitic carbon. Nature **354**, 56 (1991)
2. P.L. McEuen, Carbon-based electronics. Nature **393**, 15 (1998)
3. A. Oberlin, M. Endo, T. Koyama, Filamentous growth of carbon through benzene decomposition. J. Cryst. Growth **32**, 335–349 (1976)
4. H.W. Kroto, J.R. Heath, S.C. O'Brien, R.F. Curl, R.E. Smalley, C_{60}:Buckminsterfullerene. Nature **355**, 162–163 (1985)
5. T.W. Ebbesen, Carbon nanotubes. Phys. Today **49**(6), 26 (1996)

6. R.E. Smalley, Discovering the fullerenes. Rev. Mod. Phys. **69**, 723 (1997)
7. P.G. Collins, A. Zettl, H. Bando, A. Thess, R.E. Smalley, Nanotube nanodevice. Science **278**, 100 (1997)
8. A. Thess, R. Lee, P. Nikolaev, H. Dai, P. Petit, J. Robert, C. Xu, Y.H. Lee, S.G. Kim, A.G. Rinzler, D.T. Colbert, G. Scuseria, D. Tománek, J.E. Fischer, R.E. Smalley, Crystalline ropes of metallic carbon nanotubes. Science **273**, 483 (1996)
9. G. Gao, T. Cagin, W.A. Goddard III., Energetics, structure, mechanical and vibrational properties of single walled carbon nanotubes (SWNT). Nanotechnology **9**, 184–191 (1998)
10. M. Motta, Y.L. Li, I. Kinloch, A. Windle, Mechanical properties of continuously spun fibers of carbon nanotubes. Nano Lett. **5**(8), 1529–1533 (2005)
11. A.A. Puretzky, H. Schittenhelm, X.D. Fan, M.J. Lance, L.F. Allard, D.B. Geohegan, Investigations of single-wall carbon nanotube growth by time-restricted laser vaporization. Phys. Rev. B **65**(24), 245425 (2002)
12. P.X. Hou, S.T. Xu, Z. Ying, Q.H. Yang, C. Liu, H.M. Cheng, Hydrogen adsorption/desorption behavior of multi-walled carbon nanotubes with different diameters. Carbon **41**(13), 2471–2476 (2003)
13. R. Saito, G. Dresselhaus, M.S. Dresselhaus, *Physical Properties of Carbon Nanotubes* (Imperial College Press, London, 1998)
14. J. González, F. Guinea, M.A.H. Vozmediano, The electronic spectrum of fullerenes from the Dirac equation. Nucl. Phys. B **406**, 771 (1993)
15. A.H. Castro Neto, F. Guinea, N.M.R. Peres, K.S. Novoselov, A.K. Geim, The electronic properties of graphene. Rev. Mod. Phys. **81**, 109–162 (2008)
16. K.S. Novoselov, A.K. Geim, S.V. Morozov, D. Jiang, Y. Zhang, S.V. Dubonos, I.V. Gregorieva, A.A. Firsov, Electric field effect in atomically thin carbon films. Science **306**, 666 (2004)
17. A.H. Castro Neto, F. Guinea, N.M.R. Peres, Drawing conclusions from grapheme. Phys. World **19**, 33 (2006)
18. M.I. Katsnelson, K.S. Novoselov, A.K. Geim, Chiral tunnelling and the Klein paradox in grapheme. Nat. Phys. **2**, 620 (2006)
19. M.I. Katsnelson, K.S. Novoselov, Graphene: New bridge between condensed matter physics and quantum electrodynamics. Solid State Commun. **143**, 3 (2007)
20. N.M.R. Peres, F. Guinea, A.H. Castro Neto, Electronic properties of disordered two-dimensional carbon. Phys. Rev. B **73**, 125411 (2006)
21. V.P. Gusynin, S.G. Sharapov, Unconventional integer quantum hall effect in graphene. Phys. Rev. Lett. **95**, 146801 (2005)
22. K.S. Novoselov, A.K. Geim, S.V. Morozov, D. Jiang, M.I. Katsnelson, I.V. Grigorieva, S.V. Dubonos, A.A. Firsov, Two dimensional gas of massless Dirac fermions in graphene. Nature **438**, 197 (2005)
23. Y. Zhang, Y.-W. Tan, H.L. Stormer, P. Kim, Experimental observation of the quantum Hall effect and Berry's phase in graphene. Nature **438**, 201 (2005)
24. S. Reich, J. Maultzsch, C. Thomsen, P. Ordejón, Tight-binding description of grapheme. Phys. Rev. B **66**, 035412 (2002)
25. P.R. Wallace, The band theory of graphite. Phys. Rev. **71**, 622 (1947)
26. C.L. Kane, E.J. Mele, Size, Shape, and low energy electronic structure of carbon nanotubes. Phys. Rev. Lett. **78**, 1932 (1997)
27. D.P. Di Vincenzo, E.J. Mele, Self-consistent effective-mass theory for intralayer screening in graphite intercalation compounds. Phys. Rev. B **29**, 1685 (1984)
28. H.-W. Lee, D.S. Novikov, Supersymmetry in carbon nanotubes in a transverse magnetic field. Phys. Rev. B **68**, 155402 (2003)
29. X. Zhou, J.-Y. Park, S. Huang, J. Liu, P.L. McEuen, Band structure, phonon scattering, and the performance limit of single-walled carbon nanotube transistors. Phys. Rev. Lett. **95**, 146805 (2005)

30. S. Bellucci, P. Onorato, Transport through a double barrier in large radius carbon Nanotubes in the presence of a transverse magnetic field. Eur. Phys. J. B **52**, 469–476 (2006)
31. T. Ando, T. Seri, Quantum transport in carbon nanotubes in magnetic fields. J. Phys. Soc. Jpn. **66**, 3558 (1997)
32. S. Bellucci, P. Onorato, Transport through a double barrier for interacting quasi one-dimensional electrons in a quantum wire in the presence of a transverse magnetic field. Eur. Phys. J. B **45**, 87–96 (2005)
33. J.P. Lu, Novel magnetic properties of carbon nanotubes. Phys. Rev. Lett. **74**, 1123 (1995)
34. R. Saito, G. Dresselhaus, M.S. Dresselhaus, Erratum: Magnetic energy bands of carbon nanotubes. Phys. Rev. B **53**, 10408 (1996)
35. S. Bellucci, J. Gonzalez, F. Guinea, P. Onorato, E. Perfetto, Magnetic field effects in carbon nanotubes. J. Phys. Condens. Matter **19** 395017 (2007)
36. E. Perfetto, J. Gonzalez, F. Guinea, S. Bellucci, P. Onorato, Quantum hall effect in carbon nanotubes and curved grapheme strips. Phys. Rev. B **76**, 125430 (2007)
37. N. Nemec, G. Cuniberti, Phys. Rev. B **74**, 165411 (2006)
38. M.F. Lin, K.W.-K. Shung, Magnetoconductance of carbon nanotubes. Phys. Rev. B **51**, 7592 (1995)
39. W. Tian, S. Datta, Aharonov-Bohm-type effect in graphene tubules: A Landauer approach. Phys. Rev. B **49**, 5097 (1994)
40. H. Aiki, T. Ando, Electronic states of carbon nanotubes. J. Phys. Soc. Jpn. **62**, 1255 (1993)
41. H. Ajiki, T. Ando, Energy bands of carbon nanotubes in magnetic fields. J. Phys. Soc. Jpn. **65**, 505 (1996)
42. J.-O. Lee, J.-R. Kim, J.-J. Kim, J. Kim, N. Kim, J. W. Park, K.-H. Yoo, Observation of magnetic-field-modulated energy gap in carbon nanotubes. Solid State Commun. **115**, 467 (2000)
43. A. Rochefort, P. Avouris, F. Lesage, D.R. Salahub, Electrical and mechanical properties of distorted carbon nanotubes. Phys. Rev. B **60**, 13824 (1999)
44. M.S.C. Mazzoni, H. Chacham, Bandgap closure of a flattened semiconductor carbon nanotube: A first-principles study. Appl. Phys. Lett. **76**, 1561 (2000)
45. P.E. Lammert, P.H. Zhang, V.H. Crespi, Gapping by squashing: Metal-insulator and insulator-metal transitions in collapsed carbon nanotubes. Phys. Rev. Lett. **84**, 2453 (2000)
46. Ç. Kılıç, S. Ciraci, O. Gülseren, T. Yildirim, Variable and reversible quantum structures on a single carbon nanotube. Phys. Rev. B **62**, 16345 (2000)
47. M.T. Figge, M. Mostovoy, J. Knoester, Peierls transition with acoustic phonons and solitwistons in carbon nanotubes. Phys. Rev. Lett. **86**, 4572 (2001)
48. X. Zhou, H. Chen, O.-Y. Zhong-can, Can electric field induced energy gaps in metallic carbon nanotubes? J. Phys. Condens. Mattter **13**, L635 (2001)
49. D.S. Novikov, L.S. Levitov, Energy anomaly and polarizability of carbon nanotubes. Phys. Rev. Lett. **96**, 036402 (2006)
50. J. Jiang, J. Dong, D.Y. Xing, Zeeman effect on the electronic spectral properties of carbon nanotubes in an axial magnetic field. Phys. Rev. B **62**, 13209 (2000)
51. S. Roche, G. Dresselhaus, M.S. Dresselhaus, R. Saito, Aharonov-Bohm spectral features and coherence lengths in carbon nanotubes. Phys. Rev. B **62**, 16092 (2000)
52. F.L. Shyu, C.P. Chang, R.B. Chen, C.W. Chiu, M.F. Lin, Magnetoelectronic and optical properties of carbon nanotubes. Phys. Rev. B **67**, 045405 (2003)
53. Y. Aharonov, D. Bohm, Significance of electromagnetic potentials in the quantum theory. Phys. Rev. **115**, 485 (1959)
54. R.A. Webb, S. Washburn, C.P. Umbach, R.B. Laibowitz, Observation of *h*/*e* Aharonov-Bohm oscillations in normal-metal rings. Phys. Rev. Lett. **54**, 2696 (1985)
55. A. Bachtold, C. Strunk, J.-P. Salvetat, J.-M. Bonard, L. Forro, T. Nussbaumer, C. Schönenberger, Aharonov-Bohm oscillations in carbon nanotubes. Nature (London) **397**, 673 (1999)

56. B. Lassagne, J-P. Cleuziou, S. Nanot, W. Escoffier, R. Avriller, S. Roche, L. Forro, B. Raquet, J.-M Broto, Aharonov-Bohm conductance modulation in ballistic carbon nanotubes. Phys. Rev. Lett. **98**, 176802 (2007)
57. J. Cao, Q. Wang, M. Rolandi, H. Dai, Aharonov-Bohm interference and beating in single-walled carbon-nanotube interferometers. Phys. Rev. Lett. **93**, 216803 (2004)
58. C.L. Kane, E.J. Mele, Quantum spin hall effect in graphene. Phys. Rev. Lett. **95**, 226801 (2005)
59. S. Murakami, N. Nagaosa, S.-C. Zhang, Spin-hall insulator. Phys. Rev. Lett. **93**, 156804 (2004)
60. Y. Yao, F. Ye, X.-L. Qi, S.-C. Zhang, Z. Fang, Spin-orbit gap of graphene: First-principles calculations. Phys. Rev. B **75**, 041401 (R) (2007)
61. A. De Martino, R. Egger, K. Hallberg, C.A. Balseiro, Spin-orbit coupling and electron spin resonance theory for carbon nanotubes. Phys. Rev. Lett. **88** 206402 (2002); A. De Martino, R. Egger, F. Murphy-Armando, K. Hallberg, Spin–orbit coupling and electron spin resonance for interacting electrons in carbon nanotubes. J. Phys. Condens. Matter **16**, S1437 (2004)
62. T. Ando, Spin-Orbit Interaction in Carbon Nanotubes. J. Phys. Soc. Jpn. **69**, 1757 (2000)
63. D. Huertas-Hernando, F. Guinea, A. Brataas, Spin-orbit coupling in curved graphene, fullerenes, nanotubes, and nanotube caps. Phys. Rev. B **74**, 155426 (2006)
64. L. Chico, M.P. López-Sancho, M.C. Muñoz, Spin splitting induced by spin-orbit interaction in chiral nanotubes. Phys. Rev. Lett. **93**, 176402 (2004)
65. L. Chico, L.X. Benedict, S.G. Louie, M.L. Cohen, Quantum conductance of carbon nanotubes with defects. Phys. Rev. B **54**, 2600 (1996)
66. R. Landauer, IBM J. Res. Dev. **1**, 233 (1957); R. Landauer, Phil. Mag. **21**, 863 (1970)
67. W. Liang, M. Bockrath, D. Bozovic, J.H. Hafner, Tinkham, H. Park, Fabry-Perot interference in a nanotube electron waveguide. Nature (London) **411**, 665 (2001)
68. S. Frank, P. Poncharal, Z.L. Wang, W.A. De Heer, Carbon nanotube quantum resistors. Science **280**, 1744–1746 (1998)
69. S. Sanvito, Y.-K. Kwon, D. Tomànek, C.J. Lambert, Fractional quantum conductance in carbon nanotubes. Phys. Rev. Lett. **84**, 1974 (2000)
70. M.P. Anantram, Which nanowire couples better electrically to a metal contact: Armchair or zigzag nanotube? Appl. Phys. Lett. **78**, 2055 (2001)
71. N. Mingo, J. Han, Conductance of metallic carbon nanotubes dipped into metal. Phys. Rev. B **64**, 201401 (2001)
72. M.B. Nardelli, J.-L. Fattebert, J. Bernholc, *O*(*N*) real-space method for *ab initio* quantum transport calculations: Application to carbon nanotube–metal contacts. Phys. Rev. B **64**, 245423 (2001)
73. S. Dag, O. Gulseren, S. Ciraci, T. Yildirim, Electronic structure of the contact between carbon nanotube and metal electrodes. Appl. Phys. Lett. **83**, 3180 (2003)
74. J.J. Palacios, A.J. Perez-Jimenez, E. Louis, E. SanFabian, J.A. Verges, First-principles phase-coherent transport in metallic nanotubes with realistic contacts. Phys. Rev. Lett. **90**, 106801 (2003)
75. S. Okada, A. Oshiyama, Electronic structure of semiconducting nanotubes adsorbed on metal surfaces. Phys. Rev. Lett. **95**, 206804 (2005)
76. S.-H. Ke, W. Yang, H.U. Baranger, Nanotube-metal junctions: 2- and 3-terminal electrical transport. J. Chem. Phys. **124**, 181102 (2006)
77. N. Nemec, D. Tománek, G. Cuniberti, Contact dependence of carrier injection in carbon nanotubes: An *Ab Initio* study. Phys. Rev. Lett. **96**, 076802 (2006)
78. M.P. Anantram, Current-carrying capacity of carbon nanotubes. Phys. Rev. B **62**, R4837 (2000)
79. J. Kong, E. Yenilmez, T.W. Tombler, W. Kim, H.R.B. Laughlin, L. Liu, C.S. Jayanthi, S.Y. Wu, Quantum interference and ballistic transmission in nanotube electron waveguides. Phys. Rev. Lett. **87**, 106801 (2001)

80. D. Mann, A. Javey, J. Kong, Q. Wang, H. Dai, Ballistic transport in metallic nanotubes with reliable ohmic contacts. Nano Lett. **3**, 1541 (2003)
81. A. Javey, J. Guo, Q. Wang, M. Lundstrom, H.J. Dai, Ballistic carbon nanotube transistors. Nature (London) **424**, 654 (2003)
82. A. Javey, J. Guo, M. Paulsson, Q. Wang, D. Mann, Lundstrom, H. Dai, High-field quasiballistic transport in short carbon nanotubes. Phys. Rev. Lett. **92**, 106804 (2004)
83. P.J. de Pablo, C. Gomez-Navarro, J. Colchero, P.A. Serena, J. Gomez-Herrero, A. M. Baro, Nonlinear resistance versus length in single-walled carbon nanotubes. Phys. Rev. Lett. **88**, 036804 (2002)
84. T. Ando et al., *Mesoscopic Physics and Electronics* (Springer, Berlin, 1998)
85. S. Datta, *Electronic Transport in Mesoscopic Systems* (Cambridge University Press, Cambridge, 1995)
86. B.J. van Wees, L.P. Kouwenhoven, C.J.P.M. Harmans, J.G. Williamson, C.E. Timmering, M.E.I. Broekaart, C.T. Foxon, J.J. Harris, Observation of zero-dimensional states in a one-dimensional electron interferometer. Phys. Rev. Lett. **62**, 2523–2526 (1989)
87. M. Crommie, C.P. Lutz, D.M. Eigler, Confinement of Electrons to Quantum Corrals on a Metal Surface. Science **262**, 218–220 (1993)
88. Y. Ji et al., Science **290**, 779–783 (2000)
89. M.A. Topinka, B.J. LeRoy, S.E.J. Shaw, E.J. Heller, R.M. Westervelt, K.D. Maranowski, A.C. Gossard, Imaging coherent electron flow from a quantum point contact. Science **289**, 2323–2326 (2000)
90. H.C. Manoharan, C.P. Lutz, D.M. Eigler, Quantum mirages formed by coherent projection of electronic structure. Nature **403**, 512–515 (2000)
91. P. Debray, O.E. Raichev, P. Vasilopoulos, M. Rahman, R. Perrin, W.C. Mitchell, Ballistic electron transport in stubbed quantum waveguides: Experiment and theory. Phys. Rev. B **61**, 10950–10958 (2000)
92. C. Dekker, Carbon nanotubes as molecular quantum wires. Phys. Today **52**(5), 22–28 (1999)
93. C.T. White, T.N. Todorov, Carbon nanotubes as long ballistic conductors. Nature **393**, 240–242 (1998)
94. M. Buttiker, Y. Imry, R. Landauer, S. Pinhas, Generalized many-channel conductance formula with application to small rings. Phys. Rev. B **31**, 6207–6215 (1985)
95. M. Buttiker, Role of quantum coherence in series resistors. Phys. Rev. B **33**, 3020–3026 (1986)
96. M. Cahay, M. McLennan, S. Datta, Conductance of an array of elastic scatterers: A scattering-matrix approach. Phys. Rev. B **37**, 10125–10136 (1988)
97. M. Bockrath, D.H. Cobden, P.L. McEuen, N.G. Chopra, A. Zettl, A. Thess, R.E. Smalley, Single-electron transport in ropes of carbon nanotubes. Science **275**, 1922 (1997)
98. S.J. Tans, M.H. Devoret, R.J.A. Groeneveld, C. Dekker, Individual single-wall carbon nanotubes as quantum wires. Nature **386**, 474 (1997)
99. H.W.Ch. Postma, T. Teepen, Z. Yao, M. Grifoni, C. Dekker, Carbon nanotube single-electron transistors at room temperature. Science **293**, 76 (2001)
100. M.R. Buitelaar, A. Bachtold, T. Nussbaumer, M. Iqbal, C. Schönenberger, Multiwall carbon nanotubes as quantum dots. Phys. Rev. Lett. **88**, 156801 (2002)
101. L.P. Kouwenhoven, C. Marcus, Phys. World **11**, 35 (1998)
102. S. Tarucha, D.G. Austing, T. Honda, R.J. van der Hage, L.P. Kouwenhoven, Shell filling and spin effects in a few electron quantum dot. Phys. Rev. Lett. **77**, 3613 (1996)
103. T.H. Oosterkamp, J.W. Jansen, L.P. Kouwenhoven, D.G. Austing, T. Honda, S. Tarucha, Maximum-density droplet and charge redistributions in quantum dots at high magnetic fields. Phys. Rev. Lett. **82**, 2931 (1999)
104. C. Beenakker, Theory of Coulomb-blockade oscillations in the conductance of a quantum dot. Phys. Rev. B **44**, 1646 (1991)
105. O. Klein et al., Phase transitions in artificial atoms, in *Quantum Transport in Semiconductor Submicron Structures*, ed. by B. Kramer (Kluwer, Berlin, 1996)

106. L.P. Kouwenhoven, C.M. Marcus, P.L. McEuen, S. Tarucha, R.M. Westervelt, N.S. Wingreen, *Mesoscopic Electron Transport*, (Kluwer, Dordrecht, The Netherlands, 1997)
107. Y. Oreg, K. Byczuk, B.I. Halperin, Spin configurations of a carbon nanotube in a nonuniform external potential. Phys. Rev. Lett. **85**, 365 (2000)
108. D.H. Cobden, J. Nygard, Shell filling in closed single-wall carbon nanotube quantum dots. Phys. Rev. Lett. **89**, 46803 (2002)
109. W. Liang, M. Bockrath, H. Park, Shell filling and exchange coupling in metallic single-walled carbon nanotubes. Phys. Rev. Lett. **88**, 126801 (2002)
110. S.J. Tans, A.R.M. Verschueren, C. Dekker, Room-temperature transistor based on a single carbon nanotube. Nature **393**, 49 (1998)
111. D.H. Cobden, M. Bockrath, P.L. McEuen, A.G. Rinzler, R.E. Smalley, Spin splitting and even-odd effects in carbon nanotubes. Phys. Rev. Lett. **81**, 681 (1998)
112. P. Jarillo-Herrero, S. Sapmaz, C. Dekker, L.P. Kouwenhoven, H.S.J. van der Zant, Electron-hole symmetry in a semiconducting carbon nanotube quantum dot. Nature (London) **429**, 389 (2004)
113. P. Jarillo-Herrero, J. Kong, H.S.J. van der Zant, C. Dekker, L.P. Kouwenhoven, S. De Franceschi, Electronic transport spectroscopy of carbon nanotubes in a magnetic field. Phys. Rev. Lett. **94**, 156802 (2005)
114. S. Sapmaz, P. Jarillo-Herrero, Ya. M. Blanter, C. Dekker, H.S.J. van der Zant, Tunneling in suspended carbon nanotubes assisted by longitudinal phonons. Phys. Rev. Lett. **96**, 026801 (2006)
115. S. Bellucci, P. Onorato, Single-wall nanotubes: Atomiclike behavior and microscopic approach. Phys. Rev. B **71**, 075418 (2005)
116. J. Nygård, D.H. Cobden, P.E. Lindelof, Kondo physics in carbon nanotubes. Nature **408**, 342 (2000)
117. P. Jarillo-Herrero, J. Kong, H.S.J. van der Zant, C. Dekker, L.P. Kouwenhoven, S. De Franceschi, Orbital Kondo effect in carbon nanotubes. Nature **434**, 484 (2005)
118. B. Babić, T. Kontos, C. Schüonenberger, Kondo effect in carbon nanotubes at half filling. Phys. Rev. B **70**, 235419 (2004)
119. S. Moriyama, T. Fuse, M. Suzuki, Y. Aoyagi, K. Ishibashi, Four-electron shell structures and an tnteracting two-electron system in carbon-nanotube quantum dots. Phys. Rev. Lett. **94**, 186806 (2005)
120. S. Sapmaz, P. Jarillo-Herrero, J. Kong, C. Dekker, L.P. Kouwenhoven, H.S.J. van der Zant, Electronic excitation spectrum of metallic carbon nanotubes. Phys. Rev. B **71**, 153402 (2005)
121. A. Makarovski, L. An, J. Liu, G. Finkelstein, Evolution of transport regimes in carbon nanotube quantum dots. Phys. Rev. B **74**, 155431 (2006)
122. S. Moriyama, T. Fuse, T. Yamaguchi, K. Ishibashi, Phys. Rev. B **76**, 045102 (2007)
123. H. Ingerslev Jorgensen, K. Grove-Rasmussen, K.-Y. Wang, A.M. Blackburn, K. Flensberg, P.E. Lindelof, D.A. Williams, Nat. Phys. **4**, 536–539 (2008)
124. S. Tomonaga, Remarks on bloch's method of sound waves applied to many-fermion problems. Prog. Theor. Phys. **5**, 544 (1950)
125. J.M. Luttinger, An exactly soluble model of a many-fermion system. J. Math. Phys. **4**, 1154 (1963)
126. D.C. Mattis, E.H. Lieb, Exact solution of a many-fermion system and its associated boson field. J. Math. Phys. **6**, 304 (1965)
127. A. Yacoby, H.L. Stormer, N.S. Wingreen, L.N. Pfeiffer, K.W. Baldwin, K.W. West, Nonuniversal conductance quantization in quantum wires. Phys. Rev. Lett. **77**, 4612 (1996); O.M. Auslaender, A. Yacoby, R. de Picciotto, K.W. Baldwin, L.N. Pfeiffer, K.W. West, Experimental evidence for resonant tunneling in a Luttinger liquid. Phys. Rev. Lett. **84**, 1764 (2000)
128. S.J. Tans, M.H. Devoret, H. Dai, A. Thess, R.E. Smalley, L.J. Geerligs, C. Dekker, Individual single-wall carbon nanotubes as quantum wires. Nature **386**, 474 (1997)

129. Z. Yao, H.W.J. Postma, L. Balents, C. Dekker, Carbon nanotube intramolecular junctions. Nature **402**, 273 (1999)
130. C.L. Kane, M.P.A. Fisher, Experimental evidence for resonant tunneling in a Luttinger liquid. Phys. Rev. Lett. **68**, 1220 (1992)
131. C.L. Kane, M.P.A. Fisher, Resonant tunneling in an interacting one-dimensional electron gas. Phys. Rev. B **46**, R7268 (1992)
132. J. Sólyom, The Fermi gas model of one-dimensional conductors. Adv. Phys. **28**, 201 (1979)
133. J. Voit, One-dimensional Fermi liquids. Rep. Prog. Phys. **57**, 977 (1994)
134. H.J. Schulz, in *Proceedings of Les Houches Summer School LXI*, ed. by E. Akkermans, G. Montambaux, J. Pichard, J. Zinn-Justin (Elsevier, Amsterdam, 1995) p. 533
135. F.D.M. Haldane, Effective harmonic-fluid approach to low-energy properties of one-dimensional quantum fluids. Phys. Rev. Lett. **47**, 1840 (1981)
136. H.J. Schulz, G. Cuniberti, P. Pieri, in *Field Theories for Low-Dimensional Condensed Matter Systems*, ed. by G. Morandi (Springer, Berlin, 2000)
137. T. Giamarchi, *Quantum Physics in One Dimension* (Oxford, Clarendon, 2004)
138. W. Häusler, L. Kecke, A.H. MacDonald, Tomonaga-Luttinger parameters for quantum wires. Phys. Rev. B **65**, 085104 (2002)
139. R. Egger, A.O. Gogolin, Correlated transport and non-Fermi-liquid behavior in single-wall carbon nanotubes. Eur. Phys. J. B **3**, 281 (1998)
140. R. Egger, A.O. Gogolin, Effective low-energy theory for correlated carbon nanotubes. Phys. Rev. Lett. **79**, 5082 (1997)
141. R. Egger, A. Bachtold, M. Fuhrer, M. Bockrath, D. Cobden, P. McEuen, in *Interacting Electrons in Nanostructures*, ed. by R. Haug, H. Schoeller. Lecture Notes in Physics, vol 579 (Springer, Berlin, 2001)
142. C. Kane, L. Balents, M.P.A. Fisher, Coulomb interactions and mesoscopic effects in carbon nanotubes. Phys. Rev. Lett. **79**, 5086 (1997)
143. R. Egger, Luttinger liquid behavior in multiwall carbon nanotubes. Phys. Rev. Lett. **83**, 5547 (1999)
144. R. Egger, A.O. Gogolin, Bulk and boundary zero-bias anomaly in multiwall carbon nanotubes. Phys. Rev. Lett. **87**, 066401 (2001)
145. V. Derycke, R. Martel, J. Appenzeller, Ph. Avouris, Controlling doping and carrier injection in carbon nanotube transistors. Appl. Phys. Lett. **80**, 2773 (2002)
146. P.G. Collins, K. Bradley, M. Ishigami, A. Zettl, Extreme oxygen sensitivity of electronic properties of carbon nanotubes. Science, **287**, 1801 (2000)
147. G.U. Sumanasekera, C.K.W. Adu, S. Fang, P.C. Eklund, Effects of gas adsorption and collisions on electrical transport in single-walled carbon nanotubes. Phys. Rev. Lett. **85**, 1096 (2000)
148. K. Bradley, S.-H. Jhi, P.G. Collins, J. Hone, M.L. Cohen, S.G. Louie, A. Zettl, Is the intrinsic thermoelectric power of carbon nanotubes positive? Phys. Rev. Lett. **85**, 4361 (2000)
149. S.-H. Jhi, S.G. Louie, M.L. Cohen, Electronic properties of oxidized carbon nanotubes. Phys. Rev. Lett. **85**, 1710 (2000)
150. M. Bockrath, J. Hone, A. Zettl, P.L. McEuen, A.G. Rinzler, R.E. Smalley, Chemical doping of individual semiconducting carbon-nanotube ropes. Phys. Rev. B **61**, R10606 (2000)
151. C. Zhou, J. Kong, E. Yenilmez, H. Dai, Modulated chemical doping of individual carbon nanotubes. Science **290**, 1552 (2000)
152. M. Krüger, M.R. Buitelaar, T. Nussbaumer, C. Schönenberger, L. Forró, The electrochemical nanotube field-effect transistor. Appl. Phys. Lett. **78**, 1291 (2001)
153. A. Bachtold, M. de Jonge, K. Grove-Rasmussen, P.L. McEuen, M. Buitelaar, C. Schönenberger, Suppression of tunneling into multiwall carbon nanotubes. Phys. Rev. Lett. **87**, 166801 (2001)
154. S. Bellucci, in *Path Integrals from peV and TevV*, ed. by R. Casalbuoni et al. (World Scientific, Singapore, 1999) p. 363
155. S. Bellucci, J. González, Crossover from marginal Fermi liquid to Luttinger liquid behavior in carbon nanotubes. Phys. Rev. B **64**, 201106 (2001)

156. S. Bellucci, J. González, P. Onorato, Large N effects and renormalization of the long-range Coulomb interaction in carbon nanotubes. Nucl. Phys. B **663**, (2003)
157. S. Bellucci, P. Onorato, Magnetic field effects and renormalization of the long-range Coulomb interaction in Carbon Nanotubes. Ann. Phys. **321**, 934 (2006)
158. S. Bellucci, J. González, P. Onorato, Doping- and geometry-dependent suppression of tunneling in carbon nanotubes. Phys. Rev. B **69**, 085404 (2004)
159. R. Egger, H. Grabert, Electroneutrality and the Friedel sum rule in a Luttinger liquid. Phys. Rev. Lett. **79**, 3463 (1997)
160. S. Xu, J. Cao, C.C. Miller, D.A. Mantell, R.J.D. Miller, Y. Gao, Energy dependence of electron lifetime in graphite observed with femtosecond photoemission spectroscopy. Phys. Rev. Lett. **76**, 483 (1996)
161. C. Castellani, C. Di Castro, W. Metzner, Dimensional crossover from Fermi to Luttinger liquid. Phys. Rev. Lett. **72**, 316 (1994)
162. S. Bellucci, J. González, On the Coulomb interaction in chiral-invariant one-dimensional electron systems. Eur. Phys. J. B **18**, 3 (2000)
163. P.W. Anderson, *The Theory of Superconductivity in the High-T_c Cuprates* (Princeton University Press, Princeton, 1997)
164. D.W. Wang, A.J. Millis, S. Das Sarma, Coulomb Luttinger liquid. Phys. Rev. B **64**, 193307 (2001)
165. M. Bockrath, D.H. Cobden, J. Lu, A.G. Rinzler, R.E. Smalley, L. Balents, P.L. McEuen, Luttinger liquid behavior in carbon nanotubes. Nature (London) **397**, 598 (1999)
166. J.E. Fischer, H. Dai, A. Thess, R. Lee, N.M. Hanjani, D.L. Dehaas, R.E. Smalley, Metallic resistivity in crystalline ropes of single-wall carbon nanotubes. Phys. Rev. B **55**, R4921 (1997)
167. B. Gao, A. Komnik, R. Egger, D.C. Glattli, A. Bachtold, Evidence for Luttinger-liquid behavior in crossed metallic single-wall nanotubes. Phys. Rev. Lett. **92**, 216804 (2004)
168. H. Ishii et al., Direct observation of Tomonaga–Luttinger-liquid state in carbon nanotubes at low temperatures. Nature (London) **426**, 540 (2003)
169. P.M. Singer, P. Wzietek, H. Alloul, F. Simon, H. Kuzmany, NMR evidence for gapped spin excitations in metallic carbon nanotubes. Phys. Rev. Lett. **95**, 236403 12 (2005)
170. A. Kanda, K. Tsukagoshi, Y. Aoyagi, Y. Ootuka, Gate-voltage dependence of zero-bias anomalies in multiwall carbon nanotubes. Phys. Rev. Lett. **92**, 36801 (2004)
171. S. Bellucci, P. Onorato, Magnetic field effects on low dimensional electron systems: Luttinger liquid behaviour in a quantum wire. Eur. Phys. J. B **45**, 87 (2005)
172. L. Chico, V.H. Crespi, L.X. Benedict, S.G. Louie, M.L. Cohen, Pure carbon nanoscale devices: Nanotube heterojunctions. Phys. Rev. Lett. **76**, 971–974 (1996)
173. Ph. Lambin, A. Fonseca, J.P. Vigneron, J.B. Nagy, A.A. Lucas, Structural and electronic properties of bent carbon nanotubes. Chem. Phys. Lett. **245**, 85–89 (1995)
174. R. Saito, G. Dresselhaus, M.S. Dresselhaus, Tunneling conductance of connected carbon nanotubes. Phys. Rev. B **53**, 2044–2050 (1996)
175. J.-C. Charlier, T.W. Ebbesen, Ph. Lambin, Structural and electronic properties of pentagon-heptagon pair defects in carbon nanotubes. Phys. Rev. B **53**, 11108–11113 (1996)
176. M. Menon, D. Srivastava, Carbon nanotube "T junctions": Nanoscale metal-semiconductor-metal contact devices. Phys. Rev. Lett. **79**, 4453–4456 (1997)
177. L. Chico, M.P. López Sancho, M.C. Muñoz, Carbon-nanotube-based quantum dot. Phys. Rev. Lett. **81**, 1278–1281 (1998)
178. H.W.Ch. Postma, T. Teepen, Z. Yao, M. Grifoni, C. Dekker, Carbon nanotube single-electron transistors at room temperature. Science **293**, 76 (2001)
179. D. Bozovic, M. Bockrath, J.H. Hafner, C. M. Lieber, H. Park, M. Tinkham, Electronic properties of mechanically induced kinks in single-walled carbon nanotubes. Appl. Phys. Lett. **78**, 3693 (2001)
180. M. Sassetti, F. Napoli, U. Weiss, Coherent transport of charge through a double barrier in a Luttinger liquid. Phys. Rev. B **52**, 11213 (1995)

181. A. Furusaki, Resonant tunneling through a quantum dot weakly coupled to quantum wires or quantum Hall edge states. Phys. Rev. B **57**, 7141 (1998)
182. A. Braggio, M. Grifoni, M. Sassetti, F. Napoli, Plasmon and charge quantization effects in a double-barrier quantum wire. Europhys. Lett. **50**, 236 (2000)
183. M. Thorwart, M. Grifoni, G. Cuniberti, H.W.Ch. Postma, C. Dekker, Correlated tunneling in intramolecular carbon nanotube quantum dots. Phys. Rev. Lett. **89**, 196402 (2002)
184. Yu.V. Nazarov, L.I. Glazman, Resonant tunneling of interacting electrons in a one-dimensional wire. Phys. Rev. Lett. **91**, 126804 (2003)
185. D.G. Polyakov, I.V. Gornyi, Transport of interacting electrons through a double barrier in quantum wires. Phys. Rev. B **68**, 035421 (2003)
186. A. Komnik, A.O. Gogolin, Resonant tunneling between Luttinger liquids: A solvable case. Phys. Rev. Lett. **90**, 246403 (2003)
187. S. Hügle, R. Egger, Resonant tunneling in a Luttinger liquid for arbitrary barrier transmission. Europhys. Europhys. Lett. **66**, 565 (2004)
188. A. Furusaki, N. Nagaosa, Resonant tunneling in a Luttinger liquid. Phys. Rev. B **47**, 3827 (1993)
189. V. Meden, T. Enss, S. Andergassen, W. Metzner, K. Schönhammer, Correlation effects on resonant tunneling in one-dimensional quantum wires. Phys. Rev. B **71**, 041302(R) (2005)
190. H.J. Choi, J. Ihm, S.G. Louie, M.L. Cohen, Defects, quasibound states, and quantum conductance in metallic carbon nanotubes. Phys. Rev. Lett. **84**, 2917 (2000)
191. S. Bellucci, J. González, P. Onorato, Crossover from Luttinger liquid to Coulomb blockade regime in carbon nanotubes. Phys. Rev. Lett. **95**, 186403 (2005)
192. S. Bellucci, J. Gonzalez, P. Onorato, E. Perfetto, Modulation of Luttinger liquid exponents in multi-walled carbon nanotubes. Phys. Rev. B **74**, 045427 (2006)
193. D. Goldhaber-Gordon, H. Shtrikman, D. Mahalu, D. Abusch-Magder, U. Meirav, M.A. Kastner, Kondo effect in a single-electron transistor. Nature **391**, 156 (1998)
194. J. Nygard, D.H. Cobden, P.E. Lindelof, Kondo physics in carbon nanotubes. Nature **408**, 342 (2000)
195. J. Paaske, A. Rosch, P. Wolfle, N. Mason, C.M. Marcus, J. Nygard, Non-equilibrium singlet-triplet Kondo effect in carbon nanotubes. Nat. Phys. **2**, 460 (2006)
196. P. Jarillo-Herrero, J. Kong, H.S.J. van der Zant, C. Dekker, L.P. Kouwenhoven, S. De Franceschi, Orbital Kondo effect in carbon nanotubes. Nature **434**, 484 (2005)
197. A. Makarovski, J. Liu, G. Finkelstein, Evolution of transport regimes in carbon nanotube quantum dots. Phys. Rev. Lett. **99**, 066801 (2007)
198. J.V. Holm, H.I. Jorgensen, K. Grove-Rasmussen, J. Paaske, K. Flensberg, P.E. Lindelof, Gate-dependent tunneling-induced level shifts observed in carbon nanotube quantum dots. Phys. Rev. B **77**, 161406 (2008)
199. N.D. Mermin, H. Wagner, Absence of ferromagnetism or antiferromagnetism in one- or two-dimensional isotropic Heisenberg models. Phys. Rev. Lett. **17**, 1133 (1966)
200. Z.K. Tang, L. Zhang, N. Wang, X.X. Zhang, G.H. Wen et al., Superconductivity in 4 Angstrom single-walled carbon nanotubes. Science **292**, 2462 (2001)
201. I. Takesue, J. Haruyama, N. Kobayashi, S. Chiashi, S. Maruyama, T. Sugai, H. Shinohara, Superconductivity in entirely end-bonded multiwalled carbon nanotubes. Phys. Rev. Lett. **96**, 057001 (2006)
202. A.Yu. Kasumov, R. Deblock, M. Kociak, B. Reulet, H. Bouchiat, I.I. Khodos, Yu.B. Gorbatov, V.T. Volkov, C. Journet, M. Burghard, Supercurrent through single-walled carbon nanotubes. Science **284**, 1508 (1999)
203. A.F. Mopurgo, J. Kong, C.M. Marcus, H. Dai, Gate-controlled superconducting proximity effect in carbon nanotubes. Science **286**, 263 (1999)
204. M. Kociak, A.Yu. Kasumov, S. Guéron, B. Reulet, I.I. Khodos, Yu.B. Gorbatov, V.T. Volkov, L. Vaccarini, H. Bouchiat, Superconductivity in ropes of single-walled carbon nanotubes. Phys. Rev. Lett. **86**, 2416 (2001)

205. A.A. Kasumov, M. Kociak, M. Ferrier, R. Deblock, S. Guéron, B. Reulet, I. Khodos, O. Stéphan, H. Bouchiat, Quantum transport through carbon nanotubes: Proximity-induced and intrinsic superconductivity. Phys. Rev. B **68**, 214521 (2003)
206. M.R. Buitelaar, W. Belzig, T. Nussbaumer, B. Babic, C. Bruder, C. Schönenberger, Multiple Andreev reflections in a carbon nanotube quantum. Phys. Rev. Lett. **91**, 057005 (2003); E. Vecino, M.R. Buitelaar, A. Martýn-Rodero, C. Schönenberger, A.L. Yeyati, Conductance properties of nanotubes coupled to superconducting leads: signatures of Andreev states dynamics. Solid State Commun. **131**, 625 (2004)
207. J. Haruyama, A. Tokita, N. Kobayashi, M. Nomura, S. Miyadai et al., End-bonding multiwalled carbon nanotubes in alumina templates: Superconducting proximity effect. Appl. Phys. Lett. **84**, 4714 (2004)
208. T. Tsuneta, L. Lechner, P.J. Hakonen, Gate-controlled superconductivity in a diffusive multiwalled carbon nanotube. Phys. Rev. Lett. **98**, 087002 (2007)
209. N. Murata, J. Haruyama, Y. Ueda, M. Matsudaira, H. Karino, Y. Yagi, E. Einarsson, S. Chiashi, S. Maruyama, T. Sugai, N. Kishi, H. Shinohara, Meissner effect in honeycomb arrays of multiwalled carbon nanotubes. Phys. Rev. B **76**, 245424 (2007)
210. R.E. Peierls, *Quantum Theory of Solids* (Clarendon, Oxford, 1955)
211. M. Ferrier, A. De Martino, A. Kasumov, S. Gueron, M. Kociak, R. Egger, H. Bouchiat, Superconductivity in ropes of carbon nanotubes. Solid State Commun. **131**, 615 (2004)
212. A. De Martino, R. Egger, Effective low-energy theory of superconductivity in carbon nanotube ropes. Phys. Rev. B **70**, 014508 (2004)
213. J. González, Consistency of superconducting correlations with one-dimensional electron interactions in carbon nanotubes. Phys. Rev. Lett. **87**, 136401 (2001)
214. J. González, Microscopic model of superconductivity in carbon nanotubes. Phys. Rev. Lett. **88**, 076403 (2002)
215. A.A. Maarouf, C.L. Kane, E.J. Mele, Electronic structure of carbon nanotube ropes. Phys. Rev. B **61**, 11156 (2000)
216. H.J. Schulz, in *Correlated Electron Systems*, ed. by V.J. Emery, vol 9 (World Scientific, Singapore, 1993)
217. J. González, Superconductivity in carbon nanotube ropes. Phys. Rev. B **67**, 014528 (2003)
218. J.V. Alvarez, J. González, Insulating, superconducting, and large-compressibility phases in nanotube ropes. Phys. Rev. Lett. **91**, 076401 (2003)
219. J. González, Current instability and diamagnetism in small-diameter carbon nanotubes. Phys. Rev. B **72**, 073403 (2005)
220. K.-P. Bohnen, R. Heid, H.J. Liu, C.T. Chan, Lattice dynamics and electron-phonon interaction in (3,3) carbon nanotubes. Phys. Rev. Lett. **93**, 245501 (2004)
221. D. Connétable, G.-M. Rignanese, J.-C. Charlier, X. Blase, Room temperature Peierls distortion in small diameter nanotubes. Phys. Rev. Lett. **94**, 015503, (2005)
222. E. Perfetto, J. González, Theory of superconductivity in multiwalled carbon nanotubes. Phys. Rev. B **74**, 201403 (2006)
223. K. Kamide, T. Kimura, M. Nishida, S. Kurihara, Singlet superconductivity phase in carbon nanotubes. Phys. Rev. B **68**, 024506 (2003)
224. D. Carpentier, E. Orignac, Superconducting instability in three-band metallic nanotubes. Phys. Rev. B **74**, 085409 (2006)
225. K. Sasaki, J. Jiang, R. Saito, S. Onari, Y. Tanaka, Theory of superconductivity of carbon nanotubes and graphene. J. Phys. Soc. Jpn. **76**, 033702 (2007)
226. S. Bellucci, M. Cini, P. Onorato, E. Perfetto, Suppression of electron electron repulsion and superconductivity in ultra small carbon nanotubes. J. Phys. Condens. Matter **18**, S2115 (2006)
227. S. Bellucci, M. Cini, P. Onorato, E. Perfetto, Theoretical approach to electronic screening and correlated superconductivity in carbon nanotubes. Phys. Rev. B **75**, 014523 (2007)

228. E. Perfetto, G. Stefanucci, M. Cini, W=0 pairing in (N,N) carbon nanotubes away from half filling. Phys. Rev. B **66**, 165434 (2002)
229. E. Perfetto, G. Stefanucci, M. Cini, On-site repulsion as the origin of pairing in carbonnanotubes and intercalated graphite. Eur. Phys. J. B **30**, 139 (2002)
230. S. Bellucci, M. Cini, P. Onorato, E. Perfetto, Influence of dimensionality on superconductivity in carbon nanotubes. J. Phys. Condens. Matter **19**, 395016 (2007)

Nanotribology of Spiderman

Nicola M. Pugno

Abstract Spiders can produce cobwebs with high strength to density ratio and surprisingly display self-cleaning, strong and releasable adhesion (as geckos). Nanointerlocking, capillary and van der Waals forces, all potential adhesive mechanisms, were thus discussed, demonstrating the key role played by hierarchy to the design of super-hydrophobic, i.e. self-cleaning (by activating fakir drops as in lotus' leaves) and super-adhesive materials. The reversibility of the strong attachment was quantified thanks to an improved nonlinear peeling model, for which the solution in closed form was provided. Thus, mimicking Nature, thanks to carbon nanotube-based technology, we have suggested [N. Pugno, J. Phys. Condens. Matter **19**, 395001 (2007)] the feasibility of large invisible cables, as well as of self-cleaning, super-adhesive and releasable hierarchical smart materials. We have found that a man can be supported by a transparent cable with cross-section of 1 cm^2 and feasibly, with spider material gloves and boots, could remain attached even to a ceiling: a preliminary step towards a Spiderman suit.

Introduction

The gecko's ability to 'run up and down a tree in any way, even with the head downwards' was firstly observed by Aristotle, almost twenty-fifth centuries ago, in his *Historia Animalium*. A comparable 'adhesive' system is found in spiders, that in addition have the ability of producing fascinating cobwebs.

In general, when two solid (rough) surfaces are brought into contact with each other, physical/chemical/mechanical attractions occur (see [1]). The force developed that holds the two surfaces together is known as adhesion. Nanointerlocking

N.M. Pugno (✉)
Department of Structural Engineering and Geotechnics, Politecnico di Torino,
Corso Duca degli Abruzzi 24, 10129 Torino, Italy
e-mail: nicola.pugno@polito.it

S. Bellucci (ed.), *Physical Properties of Ceramic and Carbon Nanoscale Structures*,
Lecture Notes in Nanoscale Science and Technology 11,
DOI 10.1007/978-3-642-15778-3_3,

(or friction), intermolecular forces, including capillary and van der Waals forces, suction, secretion of sticky fluids and electrostatic attraction are all potential adhesive mechanisms in biological attachment systems (see the review by [2]).

Suction cups operate under the principle of air evacuation, i.e., when they come into contact with a surface, air is forced out of the contact area, creating a pressure differential. The adhesive force generated is simply the pressure differential multiplied by the cup area. Thus, in our (sea level) atmosphere the achievable suction strength is $\sigma_s \approx 0.1$ MPa, of the same order of magnitude of those observed in the other mentioned adhesive mechanisms or in spider/gecko adhesion. Even if suction can have an interesting role in producing synthetic adhesive materials, especially to be used in high-pressure environments, its mechanics is rather trivial. Moreover, although several insects and frogs rely on sticky fluids to adhere to surfaces, synthetic materials cannot evidently secrete these fluids without uncomfortable reservoirs. Furthermore, electrostatic attraction occurs only when two dissimilar heteropolar surfaces come in close contact. Accordingly, we will omit in our discussion these three mechanisms.

In geckos the main adhesive mechanisms are capillary [3] and van der Waals [4] forces, whereas in spiders [5], in addition to the main van der Waals adhesion, nanointerlocking could have a role (e.g., during cobweb gripping). Accordingly, in this paper, we focus our attention on these three adhesive mechanisms, with an eye to the role played by hierarchy and to reversibility.

Hierarchical miniaturized hairs without adhesive secretions are characteristic features of both spiders and geckos, see Fig. 1. In jumping spider *evarcha arcuata* [5], in addition to the tarsal claws (hooks with radius of $\sim$50 μm), a scopula (with surface area of 37,000 μm^2) is found at the tip of the foot; the scopula is differentiated in setae, each of them covered with numerous setules (with an average density of $\sim 2.1\,\mu m^{-2}$,) terminating in a triangular contact (with surface area of $\sim 0.17\,\mu m^2$.) The total number of setules per foot can be calculated at 78,000 and thus all 8 feet are provided with a total of $\sim$0.6 million points of contacts. The average adhesion force per setule was measured to be $\sim$41 nN, corresponding for the 8 feet or scopulae to $\sigma_{spider} \approx 0.24$MPa and to a safety factor, that is the adhesive force over the body weight ($\sim$15.1 mg), of $\lambda_{spider} \approx 173$.

Similarly, a tokay gecko (*gecko gecko*) foot consists of lamellae (soft ridges $\sim$1 mm in length), from which tiny curved setae ($\sim$10 μm in diameter, density of $\sim 0.014\,\mu m^{-2}$) extend, each of them composed by numerous spatulae (100–1,000 per seta, $\sim$0.1 μm in diameter) with terminal contact units (having surface area of $\sim 0.1\,\mu m^2$) [6, 7]. The adhesive force of a single seta and even of a single spatula has recently been measured to be respectively $\sim$194 μN [8] or $\sim$11 nN [9]. This corresponds to an adhesive strength of $\sigma_{gecko} \approx 0.58$ MPa [8] and a safety factor of $\lambda_{gecko} \approx 102$ (to compute this value we have assumed a weight of $\sim$250 g and a single foot surface area of $\sim 110\ mm^2$), comparable only with those of spiders ($\sim$173 [5]), cocktail ants (>100, [10]) or knotgrass leaf beetles ($\sim$50, [11]).

Note that such safety factors are ideal and thus are expected to be reduced by about one order of magnitude [12] as a consequence of the presence of 'defects' e.g. spurious particles, located at the contact interfacial zone. According to the previous

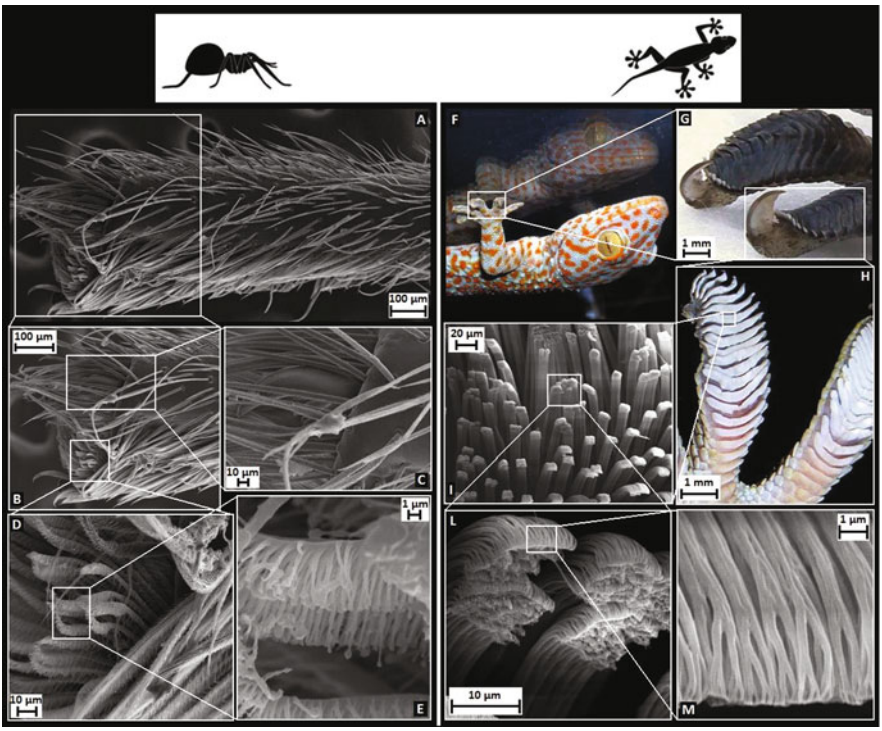

Fig. 1 Spider and gecko feet showed by SEM. In the Tokay gecko (Fig. 1f) the attachment system is characterized by a hierarchical hairy structures, which starts with macroscopic lamellae (soft ridges ∼1 mm in length, Fig. 1h), branching in setae (30–130 μm in length and 5–10 μm in diameter, Fig. 1i,l; [6, 70–72]. Each seta consists of 100–1,000 substructures called spatulae [6, 70], the contact tips (0.1–0.2 μm wide and 15–20 nm thick, Fig. 1M; [5, 69] responsible for the gecko's adhesion. Terminal claws are located at the top of each singular toe (Fig. 1g). Van der Waals and capillary forces are responsible for the generated adhesive forces [37, 73] whereas claws guarantee an efficient attachment system on surfaces with very large roughness. Similarly, in spiders (e.g. *Evarcha arcuata*, [74]) an analogous ultrastructure is found. Thus, in addition to the tarsal claws, which are present on the tarsus of all spiders (Fig. 1c), adhesive hairs can be distinguished in many species (Figs. 1d, e). Like for insects, these adhesive hairs are specialised structures that are not restricted only to one particular area of the leg, but may be found either distributed over the entire tarsus, as for lycosid spiders, or concentrated on the pretarsus as a tuft (scopula) situated ventral to the claws (Fig. 1a, 1b), as in the jumping spider *Evarcha arcuata* [74]

values, we estimate for a gecko a total number of points of contacts of ∼3 billions, thus much larger than in spiders, as required by their larger mass (the number of contacts per unit area must scale as the mass to 2/3, see [13]). The total adhesive force could easily be overcome by subsequently detaching single setules and not the whole foot at once [14, 15].

Moreover several natural materials exhibit super-hydrophobicity, with contact angles between 150° and 165°; often a strategy for allowing a safe interaction with

water. This is the case for the leaves of about 200 plants, including asphodelus, drosera, eucalyptus, euphorbia, ginkgo biloba, iris, tulipa and, perhaps the most famous, lotus [16, 17]. Similarly, animals can be super-hydrophobic, as for the case of water strider legs, butterfly wings, duck feathers and bugs [18–20]. These surfaces are generally composed of intrinsic hydrophobic material and $N=2$ hierarchical micro-sized levels [21].

Superhydrophobia is extremely important in micro/nano-fluidic devices for reducing the friction associated with the fluid flow, but also for self-cleaning: super-hydrophobic materials are often called self-cleaning materials since drops are efficiently removed taking with them the dirty particles which were deposit on them [17, 22]. This effect is extremely important in super-adhesive materials. Hansen and Autumn [23] have proved that gecko setae become cleaner with repeated use; this is probably a consequence of the hierarchical nature of the gecko foot, as we are going to demonstrate.

A replication of the characteristics of gecko [24] or spider feet would enable the development of a self-cleaning, as the lotus leaves (see the review by [21]), super-adhesive and releasable hierarchical material and, with the conjunction of large invisible cables [25], of a preliminary Spiderman suit, see Fig. 2 (Pugno, [26, 27].

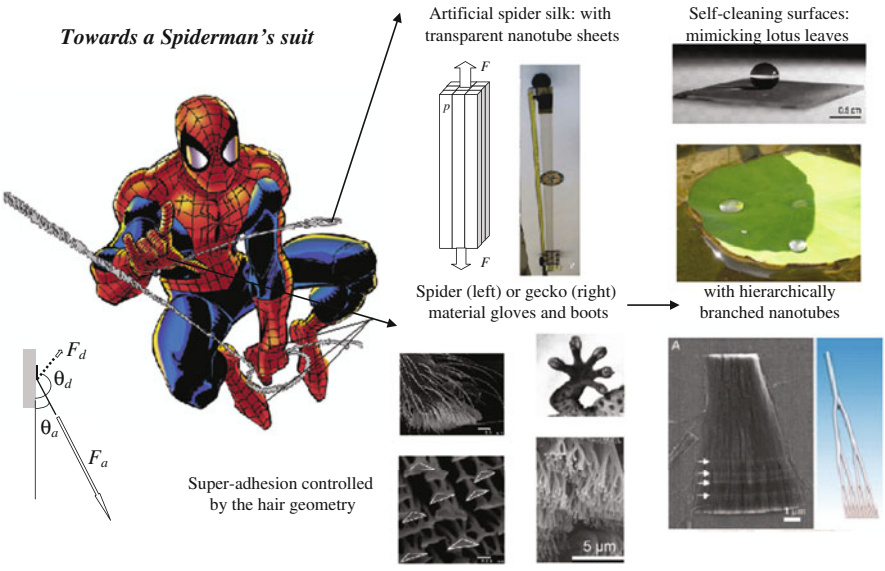

Fig. 2 Spiderman (related inset from the web) must have large cobwebs and self-cleaning, super-adhesive and releasable gloves and boots. Invisible large cables [25] could be realized with nanotube bundles (related inset from [28]), whereas gloves and boots, mimicking spider (related inset from [5]) or gecko (related inset from [51]) materials, with hierarchically branched nanotubes (related inset from [65]) as suggested by our analysis. Note that nanotube forest is super-hydrophobic (water repellent) and thus self-cleaning (related inset from [75]) as lotus leaves (related inset: photo by the Author)

Invisible Macroscopic Spider Silk

In this section we present just an idea, no more no less, for realizing large invisible cables [25]; a discussion on their technological feasibility is also included. The strength, stiffness and density of the invisible cable are estimated, and the condition of invisibility is provided.

Consider a rectangular cable having width W, thickness T and length L; the cross-section being composed of $n \times m$ (multiwalled) carbon nanotubes with inner and outer diameter d_- and d_+ respectively and length L. Let us assume that they are arranged in a square lattice with periodic spacing $p=W/n=T/m$ (see Fig. 2, related inset). Then, the strength σ_C of the bundle, defined as the failure tensile force divided by the nominal area $W \times T$, is predicted as:

$$\sigma_C = \frac{\pi}{4} \frac{d_+^2 - d_-^2}{p^2} \sigma_{NT}, \quad \sigma \rightarrow E, \rho \tag{1}$$

where σ_{NT} denotes the strength of the single carbon nanotube. To derive Eq. 1 we have assumed a full transfer load between the nanotube shells, which seems to be plausible if intertube bridgings are present, otherwise σ_{NT} would represent the nominal multiwalled nanotube strength. The same relationship is derived for the cable Young's modulus E_C considering in Eq. 1 the substitution $\sigma \rightarrow E$ and E_{NT} as the Young's modulus of the single carbon nanotube. Similarly, the cable density ρ_C, defined as the cable weight divided by the nominal volume $W \times T \times L$, is predicted according to Eq. 1 with the substitution $\sigma \rightarrow \rho$, where ρ_{NT} would denote the carbon (nanotube) density. Thus, the same (failure) strain $\varepsilon_C = \sigma_C / E_C = \sigma_{NT} / E_{NT}$ and strength over density ratio $\sigma_C / \rho_C = \sigma_{NT} / \rho_{NT}$ is expected for the bundle and for the single nanotube. This ratio is huge, at least theoretically, e.g., as required in the megacable of the space elevator [12]. Thus, Eq. 1 is a law to connect the nanoscale properties of the single nanotube with the macroscopic properties of the bundle.

On the other hand, indicating with λ the light wavelength, the condition for a nanotube to be invisible is:

$$d_+ << \lambda \tag{2a}$$

whereas to have a globally invisible cable, we require in addition to not have interference between single nanotubes, i.e.:

$$p >> \lambda \tag{2b}$$

We do not consider here the less strict limitations imposed by the sensitivity of the human eye, that can distinguish two different objects only if their angular distance is larger than ~1′. In other words, we want the cable to be intrinsically invisible.

Note that in the case of $p << \lambda$ a transparence is still achievable considering a sufficient thin sheet, as suggested by classical aerosol mixtures (here not applicable).

Assuming $d_+/\lambda \approx 1/10$, $p/\lambda \approx 10$, from the theoretical strength, Young's modulus and density of a single nanotube, we derive the following wavelength-independent invisible cable properties:

$$\sigma_C^{(theo)} \approx 10\,\text{MPa}, \quad E_C \approx 0.1\,\text{GPa}, \quad \rho_C \approx 0.1\,\text{kg}/\text{m}^3 \tag{3}$$

Meter-long multiwalled carbon nanotube cables can already be realized [28], suggesting that our proposal could became soon technologically feasible. For such a nanostructured macroscopic cable, a strength over density ratio of $\sigma_C/\rho_C \approx 120 - 144\text{KPa}/(\text{Kg}/\text{m}^3)$ was measured, dividing the breaking tensile force by the mass per unit length of the cable (the cross-section geometry was not of clear identification). Thus, we estimate for the single nanotube contained in such a cable $\sigma_{NT} \approx 170\text{MPa}$ ($\rho_{NT} \approx 1300\,\text{Kg}/\text{m}^3$), much lower than its theoretical or measured nanoscale strength [29]. This result was expected as a consequence of the larger probability to find critical defects in larger volumes [30]. Thus, defects limit the range of applicability of long bundles based on nanotubes, e.g. reducing their strength by about one order of magnitude [12]. However, the cable strength is expected to increase with the technological advancement. The cable density was estimated to be $\rho_C \approx 1.5\text{Kg}/\text{m}^3$ [28], thus resulting in a cable strength of $\sigma_C \approx 200\,\text{KPa}$. Note that a densified cable with a larger value of $\sigma_C/\rho_C \approx 465\,\text{KPa}/(\text{Kg}/\text{m}^3)$ was also realized [29], suggesting the possibility of a considerable advancement for this technology in the near future. For such cables a degree of transparency was observed, confirming that our proposal is realistic. Inverting Eq. 1 we deduce for them $p \approx 260\,\text{nm}$, in good agreement with the Scanning Electron Microscope (SEM) image analysis [28]. The nanotube characteristic diameter was $d_+ \approx 10\,\text{nm}$. Considering the visible spectrum, $\lambda \approx 400 - 600\,\text{nm}$, the condition (2a) was thus satisfied, whereas the condition (2b) was not satisfied. Thus, only a partial degree of transparency was to be expected (see Fig. 2, related inset).

Moreover, multiwalled carbon nanotubes with $d_+ \approx 50\text{nm}$ ($d_- \approx 0\text{nm}$) spaced by $p \approx 5\,\mu\text{m}$ are expected to realize an invisible cable with the mechanical properties given in Eq. 3. For example, this would correspond to an invisible cable with a cross-section of 1 cm^2 and weight per unit length of only $0.01\,\text{g}/\text{m}$, capable of supporting the weight of a man (1,000 N). However note that defects would decrease the cable strength, e.g., by one order of magnitude [12].

The nanotubes will remain parallel satisfying the condition (2b), if the cable will work under tension. A later force at the middle of the cable will tend to compact the nanotubes and at a strain of $\varepsilon \approx 8\,(W/L)^2$ all of them will be in contact. Since for a cable $W/L << 1$ (e.g., 10^{-2}), a strain of the order of $\varepsilon \approx 10^{-4}$, i.e. small if compared with that at failure $\varepsilon_{NT}^{(theo)} \approx \sigma_{NT}^{(theo)}/E_{NT} \approx 0.1$, will activate the nanotube interaction. In such a situation the cable would 'appear' near to the point of application of the lateral force, i.e. where the condition of Eq. 2b is not locally verified, to survive by activating the interaction; this behavior could help in visualizing the cable after having trapped a victim.

Obviously, reducing the requirement of invisibility to that of (a degree of) transparency would automatically lead to strongest macroscopic synthetic cobwebs. Graded cross-links are needed in order to improve the overall bundle strength [31].

Nanohooks

In this section an estimation of the elastic strength of hooks (Fig. 3a) with friction is summarized [32], treating them as elastic arcs (see [33]). We have quantified, as the intuition and Velcro® material suggest, that hooks allow reversible strong attachment, establishing elastic-plastic or hyper-elastic behaviours as dictated by the competition between friction and large displacements [32]. In addition, size-effects suggest that nano-contacts are safer. Thus, we describe here the main results of a 'Velcro nonlinear mechanics'[32], that could have interesting applications also in different fields, as suggested by its recent observation in wood [34].

The hook elastic critical force F_h (Fig. 3b) can be estimated according to:

$$F_h \approx \frac{\left(\pi/2+\varphi\right) EI}{\pi R^2} \tag{4}$$

where φ is the friction coefficient between hook and substrate (or loop), E is the material Young modulus, I is the cross-sectional moment of inertia and R is the hook radius. Thus, if a number of hooks per unit area $\rho_h = m/\left[\pi\ (2R)^2\right]$ is present, corresponding to an equivalent number m of hooks per clamp, the corresponding nominal strength will be:

$$\sigma_h = \rho_h F_h = \frac{m\left(\pi/2+\varphi\right) EI}{4\pi^2 R^4} = \frac{m\left(\pi/2+\varphi\right) E}{16\pi\ \left(R/r\right)^4} \tag{5}$$

where r is the equivalent radius (in terms of inertia) of the cross-section. For example, considering m=10, $\varphi = 0$, E=10 GPa (Young's modulus for keratin

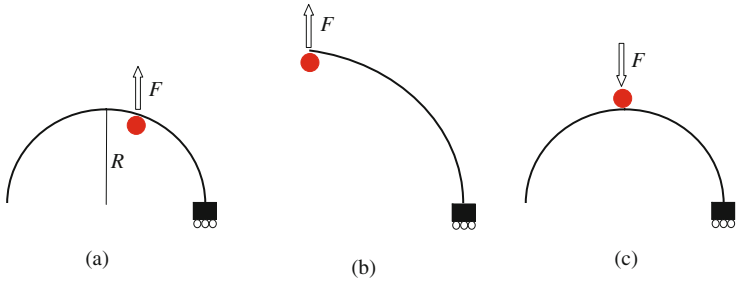

Fig. 3 Elastic hook with friction. Conditions of interlocking (**a**), ultimate "elastic" strength (**b**) and hauling (**c**)

material is E=1–20 GPa, see [35], and [36]) and $R/r = 10$ corresponds to $\sigma_h \approx 0.3$ MPa, comparable with the strength observed in *evarcha arcuata* spiders of ~0.24 MPa ([5], note the two spider hooks in the related inset of Fig. 2).

On the other hand, the maximum force for hooking (Fig. 3c) is:

$$F_h^* = -\frac{\varphi EI}{R^2} \tag{6}$$

Consequently the ratio:

$$\mu = \frac{F_h}{|F_h^*|} = \frac{1}{\pi} + \frac{1}{2\varphi} \tag{7}$$

is expected to be very large ($\mu(\varphi \to 0) \to \infty$), and thus strong and 'reversible' adhesion is expected in hooked materials. This can be easily verified in our own home making experiments on Velcro materials, directly measuring μ and thus deducing the related friction coefficient φ. For example for $\mu \approx 10 - 100$, $\varphi \approx 5 \times 10^{-(2-3)}$.

If a contact area A supports the (e.g., animal body) weight W, the safety factor, i.e. the ratio between the attachment force and the weight $W = Mg = \rho Vg = \rho ALg$ (ρ is the density, g is the gravitational acceleration, V is the body volume and M its mass) is:

$$\lambda = \frac{\sigma_h A}{W} = \frac{1}{\rho g}\frac{\sigma_h}{L} \tag{8}$$

in which L=V/A is a characteristic size of the supported weight. Thus, smaller is safer. For example, since we expect $L \propto M^{1/3}$, assuming $\sigma_h \approx const$, the predicted scaling is $\lambda = kM^{-1/3}$; noting that in the *evarcha arcuata* spiders [5] $\lambda_{spider} \approx 173$ and $M_{spider} \approx 15$mg we deduce $k_{spider} \approx 43\text{g}^{1/3}$. Thus for a Spiderman ($M_{man} \approx 70$ kg), defined as a man having gloves and shoes composed of spider material, we roughly (because self-similarity is assumed) expect $\lambda_{spiderman} \approx 1$. For gecko gloves, since for geckos $\lambda_{geckos} \approx 102$ and $M_{geckos} \approx 250$ g, we would deduce $k_{geckos} \approx 643\, g^{1/3}$ and thus $\lambda_{spiderman} \approx 15$. Accordingly, such gloves are sufficient to support Spiderman even on a ceiling.

The force carried by one hook scales as $F_1 \equiv F_h \propto r^4/R^2$, thus the bending, tensile, and nominal stresses in the hook must scale as $\sigma_b \propto r/R$, $\sigma_t \propto (r/R)^2$ and $\sigma_h \propto (r/R)^4$ respectively. Accordingly, size-effects can be predicted. For example, splitting up the contact into n sub-contacts, i.e., $R \to R/\sqrt{n}$, would result in a force $F_n = n^\beta F_1$ with $\beta = 0$ if $r \propto R$ but $\beta = 2$ if $r = const$. Thus, for this last case, sub-contacts are found to be stronger, even if the hook will be higher stressed and its mechanical strength will impose a lower-bound to the radius of the smallest hook. This explains why Nature uses nano-sized bio-contacts, since usually $0 < \beta < 2$, as recently discussed on the basis of contact mechanics (for which $\beta = 1/2$, see [13]). Pugno [26] has shown that this enhancement cannot continue ad infinitum. If the

hook weight is a constant fraction of the body weight, the scaling of the safety factor is $\lambda \propto r^2/R^3$, similarly to the prediction of Eq. 8.

Finally, the work of adhesion per unit area can be computed according to:

$$2\gamma_h = \rho_h \int_0^{F_h} \delta\,(F)\,\mathrm{d}F = \left(\frac{1}{2} + \kappa\right)\sigma_h \delta\,(F_h) \tag{9}$$

where $\kappa = 0$ for linear systems. For example, considering $\kappa = 0$, $\sigma_h = 0.3$ MPa as previously computed, and $\delta\,(F_h) \approx R = 100$ nm we get $\gamma_h \approx 0.03\mathrm{N}/\mathrm{m}$, comparable with the work of adhesion observed in geckos (0.05 N/m, see [37]).

Nanohooks could be useful, in addition to classical mechanisms, in order to reduce the dramatic role played by the surface roughness, that will imply contact 'defects' during especially macroscopic adhesion.

Self-Cleaning Super-Adhesive Materials

The contact angle (Fig. 4a) between a liquid drop and a solid surface was found by Young [38] according to $\cos\theta = (\gamma_{SV} - \gamma_{SL})/\gamma_C$, where $\gamma_C \equiv \gamma_{LV}$ and the subscripts of the surface tensions describe the solid (S), liquid (L) and vapour (V) phases. Note that for $(\gamma_{SV} - \gamma_{SL})/\gamma_C > 1$ the drop tends to spread completely on the surface and $\theta = 0°$, whereas for $(\gamma_{SL} - \gamma_{SV})/\gamma_C > 1$ the drop is in a pure non-wetting state and $\theta = 180°$. According to the well-known Wenzel's model [39, 40] the apparent contact angle θ_W is a function of the surface roughness w, defined as the ratio of rough to planar surface areas, namely, $\cos\theta_W = w\cos\theta$ (Fig. 4b). The apparent contact angle varies also with the heterogeneous composition of the solid surface, as shown by Cassie and Baxter [41]. Consider a heterogeneous surface made up of different materials characterized by their intrinsic contact angles θ_i and let φ_i be the area fraction of each of the species; the individual areas are assumed to be much smaller than the drop size. Accordingly, the apparent contact angle θ_{CB} can be derived as $\cos\theta_{CB} = \sum_i \varphi_i \cos\theta_i$ [41].

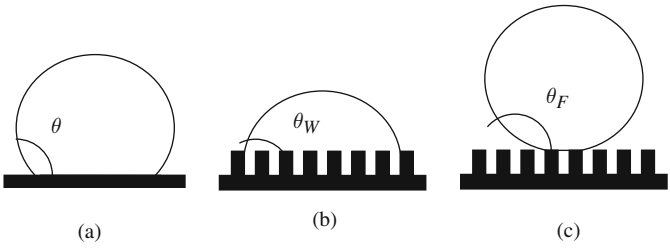

Fig. 4 Contact angles for a drop on a flat surface (**a**) or on a rough surface in the Wenzel (**b**) or Fakir (**c**) state

A droplet can sit on a solid surface in two distinct configurations or states (Fig. 4b, c). It is said to be in Wenzel state (Fig. 4b) when it is conformal with the topography. The other state in which a droplet can rest on the surface is called the Fakir state, after Quéré [42], where it is not conformal with the topography and only touches the tops of the protrusions on the surface (Fig. 4c). The observed state should be the one of smaller contact angle, as can be evinced by energy minimization [43].

Let us consider a hierarchical surface (Fig. 5). The first level is composed by pillars in fraction φ (as in Fig. 4b, c). Each pillar is itself structured in n sub-pillars in a self-similar (fractal) manner, and so on. Thus, the pillar fraction at the hierarchical level N is φ^N, whereas the related number of pillars at the level N is n^N. Applying the Cassie and Baxter law [41] for the described composite (solid/air) hierarchical surface (the contact angle in air is by definition equal to 180°) we find for the hierarchical fakir state:

$$\cos\theta_F^{(N)} = \varphi^N (\cos\theta + 1) - 1 \tag{10}$$

Note that for $N = 0$ $\cos\theta_F^{(0)} = \cos\theta$ as it must be, whereas for N=1 $\cos\theta_F^{(1)} = \varphi(\cos\theta + 1) - 1$, as already deduced for the case described in Fig. 4c [44]. Equation 10 quantifies the crucial role of hierarchy and suggests that hierarchical surfaces are fundamental to realize super-hydrophobic materials (effective contact angle larger than $\theta_{SHpho} \approx 150°$), since we predict $\theta_F^{(\infty)} = 180°$. The minimum number of hierarchical levels necessary to achieve super-hydrophobia in the Fakir state is thus:

$$N_{SHpho}^{(F)} = \frac{\log\left(\frac{1+\cos\theta_{SHpho}}{1+\cos\theta}\right)}{\log\varphi} \tag{11}$$

and the logarithmic dependence suggests that just a few hierarchical levels are practically required.

By geometrical argument the roughness w of the introduced hierarchical surface Fig. 5 can be calculated in closed form. The roughness at the hierarchical level k is given by $w^{(k)} = 1 + S_L^{(k)} \big/ A$ in which A is the nominal contact area and $S_L^{(k)}$ is the total lateral surface area of the pillars. The pillar at the level k has an equivalent radius r_k and a length l_k and the pillar slenderness s, defined as the ratio between its lateral and base areas, is $s = 2l_k \big/ r_k$. The air surface area at the level k can be computed as $A\left(1 - \varphi^k\right)$ or equivalently as $A - n^k \pi r_k^2$, thus we deduce $r_k = r_0 \left(\varphi \big/ n\right)^{k/2}$, with $A \equiv A_0 \equiv \pi r_0^2$. Consequently:

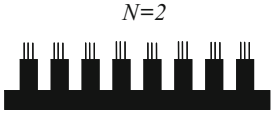

Fig. 5 A hierarchical surface with N=2 levels

$$w^{(N)} = 1 + \frac{1}{\pi r_0^2} \sum_{k=1}^{N} 2\pi r_k l_k n^k = 1 + s \sum_{k=1}^{N} \varphi^k = 1 + s\frac{\varphi - \varphi^{N+1}}{1-\varphi} \quad \forall n \tag{12}$$

Note that the result becomes independent from n (and that $w^{(0)}(\varphi) = 1 = w^{(N)}(\varphi = 0)$, $w^{(1)} = 1 + s\varphi$, whereas $w^{(N\neq 1)}(\varphi = 1) = \infty$). Thus we find for the hierarchical Wenzel state:

$$\cos\theta_W^{(N)} = w^{(N)} \cos\theta = \left(1 + s\frac{\varphi - \varphi^{N+1}}{1-\varphi}\right)\cos\theta \tag{13}$$

Equation 13 suggests that hierarchical surfaces can be interesting also to realize super-hydrophilic materials, since we predict $\cos\theta_W^{(\infty)} = w^{(\infty)}\cos\theta$ with $w^{(\infty)} = 1 + s\varphi/(1-\varphi)$; thus if $\cos\theta > 0$ $\theta_W^{(\infty)} \to 0$, for $s \to \infty$ or $\varphi \to 1$. However note that for $\cos\theta < 0$, $\theta_W^{(\infty)} \to 180°$ ($s \to \infty$ or $\varphi \to 1$), and thus super-hydrophobia can take place also in the Wenzel state, without invoking fakir drops. The minimum number of hierarchical levels necessary to render the surface super-hydrophobic/hydrophilic in the Wenzel state is thus:

$$N_{SHpho,phi}^{(W)} = \frac{\log\left(1 + \frac{(1-\varphi)}{s\varphi}\left(1 - \frac{\cos\theta_{SHpho,phi}}{\cos\theta}\right)\right)}{\log\varphi} \tag{14}$$

where effective contact angles smaller than θ_{SHphi} define super-hydrophily.

Comparing $\theta_W^{(N)}$ and $\theta_F^{(N)}$, we find that the Fakir state is activated at each hierarchical level for (we omit here second order problems, related to metastability, contact angle hysteresis and limit of the Wenzel's approach, for which the reader should refer to the review by [21]):

$$\theta > \theta_{WF},\ \cos\theta_{WF} = -\frac{1-\varphi^N}{w^{(N)} - \varphi^N} = -\frac{1}{w^{(\infty)}} = -\frac{1-\varphi}{1+\varphi\,(s-1)} \quad \forall N \tag{15}$$

Note that the result is independent from N and $\theta_{WF} \to 90°$ for $s \to \infty$ or $\varphi \to 1$, and thus a hydrophobic\hydrophilic material composed by sufficiently slender or spaced pillars surely will/will not activate fakir drops and will become super-hydrophobic\hydrophilic for a large enough number of hierarchical levels. Thus hierarchy can enhance the intrinsic property of a material. The role of hierarchy is summarized in the phase diagram of Fig. 6.

For example, for plausibly values of $\varphi = 0.5$ and s=10 we find from Eq. 15 $\theta_{WF} = 95.2°$; thus assuming $\theta = 95°$ the Fakir state is not activated and the Wenzel state prevails (if the Fakir state still prevails it is metastable, see [21]). From Eq. 12 $w^{(1)} = 6$, $w^{(2)} = 8.5$, $w^{(3)} = 9.75$ and $w^{(4)} = 10.375$; accordingly from Eq. 13 $\theta_W^{(1)} \approx 122°$, $\theta_W^{(2)} \approx 138°$, $\theta_W^{(3)} \approx 148°$ and $\theta_W^{(4)} \approx 155°$, thus N=4 hierarchical levels are required for activating super-hydrophobia (from Eq. 14 $N_{SHpho}^{(W)} = 3.2$). On the other hand, assuming $\theta = 100°$ fakir drops are activated and from Eq. 10

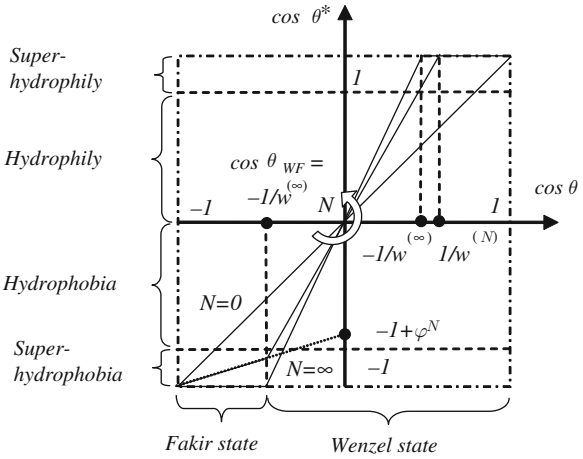

Fig. 6 Effective contact angle $\theta^* = \theta_{F,W}^{(N)}$ as a function of the intrinsic one θ by varying the number N of hierarchical levels. Thus, super-hydrophobic/hydrophilic surfaces can be obtained by an opportune design of the hierarchical architecture, according to this phase diagram and reported equations (note that metastable fakir drops could be observed also in the Wenzel region, dotted line, see [21])

$\theta_F^{(1)} \approx 126°$, $\theta_F^{(2)} \approx 143°$ and $\theta_F^{(3)} \approx 154°$, thus N=3 hierarchical levels are sufficient to achieve super-hydrophobia (from Eq. 11 $N_{SHpho}^{(F)} = 2.6$).

Some insects, such as the beetle *Hemisphaerota cyanea*, use capillary to stick to their substrate, generating a force close to 1 g (i.e. 60 times its body mass) for more than 2 min [45], allowing them to resist attacking ants; tokay geckos use the same principle (in addition to van der Waals forces) to generate their tremendous adhesion [3].

Between a spherical surface (contact angle θ) of radius r_0 and a flat plate (contact angle θ_P), the capillary attractive or repulsive force is predicted to be $F_C = 2\pi r_0 \gamma_C (\cos\theta + \cos\theta_P)$ [46]. Thus, for a pillar of size r_0 composed by N hierarchical levels the force is $F_C^{(N)} = n^N 2\pi r_N \gamma_C (\cos\theta + \cos\theta_P)$ and the nominal strength $\sigma_C^{(N)} = F_C^{(N)} \Big/ (\pi r_0^2)$ becomes:

$$\sigma_C^{(N)} = \frac{2(\varphi n)^{N/2}}{r_0} \gamma_C \left(\cos\theta_{W,F}^{(N)} + \cos\theta_P\right) \tag{16}$$

Note that for N=0 such a capillary strength corresponds to the previously discussed law. For N=1 the strength scales as $\sqrt{n}$, in agreement with a recent discussion [14]: splitting up the contact into n sub-contacts would result in a stronger interaction (with a cut-off at the theoretical strength): smaller is stronger (see [30]). This explains the observed miniaturized size of biological contacts. Introducing the previously computed contact angle related to the hierarchical surface allows one to

evaluate the hierarchical capillary force, with or without activation of the Fakir state. Super-attraction/repulsion can thus be achieved thanks to hierarchy, since $\sigma_C^{(N)} \approx \sigma_C^{(0)} (\varphi n)^{N/2}$.

Thus, the analysis demonstrates and quantifies that super-hydrophobic/hydrophilic and simultaneously super-attractive/repulsive surfaces can be realized, mimicking Nature thanks to hierarchical architectures. Assuming $\varphi = 0.5$, n=s=10 and $\theta \approx 120°$ (as in lotus leaves), the analysis shows that fakir drops are activated and only two hierarchical levels are required to achieve super-hydrophobia ($\theta > \theta_{WF} = 95.2°$, $N_{SHpho}^{(F)} = 1.9$; $\theta_F^{(1)} \approx 139°$, $\theta_F^{(2)} \approx 151°$), in agreement with direct observations on super-hydrophobic plants (see our discussing in the Introduction). Simultaneously, we deduce $\sigma_C^{(1)} \approx 2.2\sigma_C^{(0)}$, $\sigma_C^{(2)} \approx 5.0\sigma_C^{(0)}$ and $\sigma_C^{(3)} \approx 11.2\sigma_C^{(0)}$, i.e. just three hierarchical levels (or even two, if $\varphi \approx 1$ and $n \approx 10$) are sufficient to enhance the capillary strength by one order of magnitude, generating super-attractive ($\sigma_C^{(0)} > 0$) or super-repulsive ($\sigma_C^{(0)} < 0$) surfaces. Thus, the analysis suggests the feasibility of innovative self-cleaning and simultaneously super-adhesive hierarchical materials, as observed in spiders and geckos.

Analogously, hierarchy simultaneously enhances the work of adhesion, and thus the corresponding force, per unit nominal area, due to the larger effective surface area. Accordingly, the maximum (assuming all the surfaces in contact) effective work of adhesion can be derived by the following energy equivalence:

$$\gamma_{\max}^{(N_1,N_2)} \approx \gamma_C \left(w_1^{(N_1)} + w_2^{(N_2)} \right) \tag{17}$$

in which the subscripts 1 and 2 refer to the two surfaces in contact. For example, the adhesive force between two-hierarchical level surfaces, defined by $w_{1,2}^{(2)} = 1.75$ ($\varphi = 0.5$, s=1), is enhanced by hierarchy by a factor of 3.5 (with respect to the two corresponding flat surfaces). Note that for s=10 this factor becomes 18 and remains significantly larger than one (i.e. 10) even if one of the two surfaces becomes perfectly flat.

However we have to note that the Wenzel approach must loose its validity for large roughness w, for which an effective micro- (rather than macro-) roughness have to be considered.

Capillary and van der Waals Forces

The capillary force can also be derived according to the well-known Laplace's law [47]. The attractive force between two flat plates of areas A, separated by a liquid of thickness t, with (liquid/vapour) surface tension γ_C and (liquid/solid) contact angle θ is (see the review by [21]):

$$F_C = \frac{2A\gamma_C \cos\theta}{t} \tag{18}$$

Note that $\sigma_C = F_C/A$ is a function of the liquid thickness but not of the size of the contact. Considering for example $\gamma_C = 0.05\text{N/m}$, $\theta = 80°$ and t=1 nm would yield $\sigma_C \approx 9\,\text{MPa}$. The force described by Eq. 17 is attractive for $\theta < 90°$ (hydrophilic) or repulsive for $\theta > 90°$ (hydrophobic). An additional viscous force can be generated $F_C^{(\eta)} \propto \eta/\tau$, where η is the dynamic viscosity of the liquid and τ is the separation time interval.

Note the differences between the force predictions of Eq. 18 and that considered in the previous section [46], i.e.:

$$F_C = 2\pi r_0 \gamma_C (\cos\theta + \cos\theta_P) \tag{19}$$

in the limit of $r_0 \to \infty$, which suggest that we are far from a full understanding of the mechanism. In addition, both the approaches predict $\sigma_C = F_C/A = F_C/(\pi r_0^2) \to \infty$ for $t, r_0 \to 0$ in contrast to the common sense of a finite theoretical strength $\sigma_C^{(th)}$. This cut-off could be a consequence of a quantized (instead of a continuous) crack propagation, as discussed in the example reported by Pugno [26]. Thus, the following asymptotic matching can be straightforwardly proposed:

$$\sigma_C \approx \left(\frac{2}{r_0 + c} + \frac{1}{t + c}\right) \gamma_C (\cos\theta + \cos\theta_P)\,, c \approx 3\gamma_C (\cos\theta + \cos\theta_P) \Big/ \sigma_C^{(th)} \tag{20}$$

Similarly, the van der Waals force between two parallel surfaces of area A is ([48]; see also [49]):

$$F_{vdW} = \frac{HA}{6\pi t^3} \tag{21}$$

where H is the Hamaker's constant, with a typical value around 10^{-20}J (as before, t<30 nm is the separation between the two surfaces). Note that $\sigma_{vdW} = F_{vdW}/A$ is a function of the liquid thickness but not of the size of the contact. Considering for example t=1 nm would yield $\sigma_{vdW} \approx 0.5\,\text{MPa}$.

For the case of a spherical surface of radius r_0 and a flat plate, the contact force predicted according to the 'JKR' model of contact mechanics [50] is:

$$F_{vdW} = 3/2\pi \gamma_{vdW} r_0 \tag{22}$$

Thus also in this case, as formerly discussed by Arzt et al. [13], $F_n = \sqrt{n} F_1$. Moreover, since $F_{vdW} \propto r_0$ the results reported in the previous section are still applicable.

As for capillary, note the differences between the two approaches summarized in Eqs. 21 and 22, which suggest that we are far from a full understanding of the mechanism. In addition, Eqs. 21 and 22 predict $\sigma_{vdW} = F_{vdW}/A = F_{vdW}/(\pi r_0^2) \to \infty$

for $t, r_0 \to 0$ in contrast to the common sense of a finite theoretical strength $\sigma_{vdW}^{(th)}$ (and of a quantized crack propagation, see [26]). Thus, the following asymptotic matching can be straightforwardly proposed:

$$\sigma_{vdW} \approx 3/2\gamma_{vdW}\left(\frac{1}{r_0+c}+\frac{H}{9\gamma_{vdW}\pi\,(t+c)^3}\right), c = X\left(6\pi\sigma_{vdW}^{(th)}\,;-9\pi\,\gamma_{vdW}\,;0;-H\right) \tag{23}$$

where $X\,(a\,;b\,;c;d)$ denotes the solution of the three-order polynomial equation $ax^3+bx^2+cx+d=0$, derived imposing $c:\sigma_{vdW}\,(r_0,t\to 0)=\sigma_{vdW}^{(th)}$ (one could also consider valid Eq. 23 with $c\to 0$, with a cut-off at $\sigma_{vdW}^{(th)}$). To have an idea of the theoretical strength note that $\sigma_{vdW}^{(th)} \approx 20\,\text{MPa}$ (see [51]).

The different force predictions for plausible values are of the same order of magnitude. Using Eq. 22, as done by Autumn et al. [4] and Arzt et al. [13], ($\gamma_{vdW} \approx 0.05\,\text{N/m}$) for the gecko spatula ($r_0 \approx 0.05\,\mu\text{m}$) we get $F_{spatula} \approx 12\,\text{nN}$, comparable to the observed value of ~11 nN [9]. Thus, for a seta composed by 1,000 spatulae, $F_{seta} \approx 12\,\mu\text{N}$ [4, 8] measured values of ~194 and ~40 μN respectively); for a non hierarchical seta from Eq. 22 one would deduce ($r_0 \approx 5\,\mu\text{m}$) $F'_{seta} \approx 1.2\,\mu\text{N}$ and thus for a real, thus hierarchical, seta having 1,000 spatulae, $F_{seta} \approx \sqrt{1000}\times 1.2\,\mu\text{N} \approx 38\,\mu\text{N}$. Similarly for the setula of a spider $R_{eq} \approx \sqrt{0.17/\pi}\,\mu\text{m} \approx 0.2\,\mu\text{m}$ (terminal surface area of $\sim 0.17\,\mu\text{m}^2$) and $F_{setula} \approx 47\,\text{nN}$ (observed value ~41 nN, [5]).

Finally, we note that since different mechanisms could be simultaneously activated, the real adhesive force (or strength or fracture energy) could be computed as:

$$F = \sum_i F_i f_i \tag{24}$$

in which F_i is the force activated by the i-th mechanism having weight f_i $\left(\sum_i f_i = 1\right)$.

For example, for geckos a still partially unsolved question is to quantify the participation of capillary and van der Waals forces in their adhesion (nanohook and suction mechanisms in geckos have been ruled out, see the review by [2]). We note that Huber et al. [3] observed a humidity (U) dependence of the adhesion force in gecko spatulae, thus, from Eq. 24 we could write:

$$F = F_{dry}f_{dry} + F_{wet}f_{wet} \approx F_{vdW}\,(1-U) + (F_{vdW}+F_C)\,U \tag{25}$$

By fitting their data we find $F_{vdW} \approx 7\text{nN}$ and $F_C \approx 5\text{nN}$, thus $F_{vdW}/F_C \approx 1.4$, i.e., van der Waals are expected to be the main adhesive forces in geckos even if capillary ones play a significant role too.

Equations 20 and 23 can be straightforwardly extended to hierarchical surfaces according to our findings reported in the previous Section.

Smart Adhesion

Consider the detachment as the peeling of a thin film of (free-) length l, width b and thickness h, pulled at an angle ϑ by a force F Fig. 7. A non-linear stress-strain relationship $\sigma = E(\varepsilon)\,\varepsilon$ is considered. The total potential energy (elastic energy minus external work) of the film is $\Phi = bhl\int_0^{\varepsilon} E(\varepsilon)\,\varepsilon\,\mathrm{d}\varepsilon - Fl(1-\cos\vartheta+\varepsilon)$. Thus, the energy release rate is:

$$2\Delta\gamma \equiv -\frac{1}{b}\frac{\mathrm{d}\Phi}{\mathrm{d}l} = -h\int_0^{\varepsilon} E(\varepsilon)\,\varepsilon\,\mathrm{d}\varepsilon + \frac{F}{b}(1-\cos\vartheta+\varepsilon) \tag{26}$$

The detachment will take place when $\Delta\gamma \equiv \gamma \equiv \gamma_1+\gamma_2-\gamma_{12}$, where $\gamma_{1,2}$ are the surface energies of the two materials in contact and γ_{12} is that of the interface.

For quadratic nonlinearities, i.e., $E(\varepsilon) = E + E'\varepsilon$, a closed form solution is still reachable. Note that $E' < 0$ describes elastic-plastic materials (e.g., hooked surface with $\varphi > \varphi_C \approx \pi/39$, see [26]), whereas $E' > 0$ hyper-elastic ones (e.g., hooked surface with $\varphi < \varphi_C$). The detachment force is found in the following form:

$$\begin{aligned}\varepsilon_C =& X\left(4E';\ 3E+6E'(1-\cos\vartheta)\ ;\ 6E(1-\cos\vartheta)\ ;\ -12\gamma/h\right), F_C\\ =& AE(\varepsilon_C)\,\varepsilon_C\end{aligned} \tag{27}$$

(as before $X(a;b;c;d)$ denotes the solution of the three-order polynomial equation $ax^3+bx^2+cx+d=0$). For $E' \to 0$ the classical Kendall [52] prediction is recovered. Varying the pulling angle strong force variations are found, as can easily be evinced considering the simplest case in the limit of $E^{-1}, E' \to 0$, deducing $F_C = 2\gamma b/(1-\cos\vartheta)$. Note that, also according to fracture mechanics, subcontacts are safer ($b \to b/\sqrt{n}, F_n = \sqrt{n}F_1$; the paper by Pugno [26] shows that this cannot be ad infinitum).

Moreover the strongest attachment is achieved for $\vartheta = 0$ whereas the easier detachment for $\vartheta = \pi$. The ratio between the corresponding forces is:

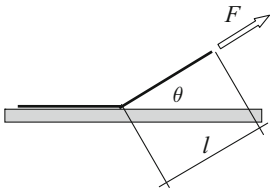

Fig. 7 Peeling of a thin film

$$\frac{F_a}{F_d} \equiv \frac{F_C\left(\vartheta = 0\right)}{F_C\left(\vartheta = \pi\right)} = g\left(E^{/}\right)\frac{1+\sqrt{\chi+1}}{\sqrt{\chi}}, \chi \equiv \gamma\big/(hE) \tag{28}$$

where $g\left(E^{/}\right)$ is a known function describing the constitutive nonlinearity, which could have an important role for soft matter, and in particular $g\left(0\right) = 1$; in this case $F_a\big/F_d \to 1, \infty$ for $\chi \to \infty, 0$. For example taking $\gamma = 0.05\text{N}\big/\text{m}$ (of the order of the previously discussed $\gamma_{h,C,vdW}$), h=100 nm, E=10 GPa we find $F_a\big/F_d \approx 283$. *This value is of the same order of magnitude of the safety factor found in spiders* [5], i.e., 173. Such a geometrical control can thus explain the smart safety factor reduction during detachment up to ∼1, needed for animal walk. Thus, this pulling angle control can represent the main mechanism to achieve reversible adhesion. For example, for a man with adhesive gloves capable of supporting 300 kg at $\vartheta \approx \pi$, only ∼1 kg must be applied at $\vartheta \approx 0$ to detach them. Probably the proper use of such hypothetical gloves would require opportune training, similarly to the use of a pair of skis, a paragliding or a wet suit.

The value of F_C corresponds to a delamination (opening and/or sliding) and not necessarily to a detachment (opening prevails on sliding). To distinguish between these two different mechanisms we note that $2\gamma = \left(K_{op}^2 + K_{sl}^2\right)\Big/E$, where $K_{op,sl}$ are the stress intensity factors at the tip of the interfacial crack for opening (mode I) or sliding (mode II) and $K_{op} \propto F_{\perp} \propto \sin\vartheta$ whereas $K_{sl} \propto F_{//} \propto \cos\vartheta$; assuming as a first approximation a detachment for $K_{sl}\big/K_{op} \approx \tan^{-1}\vartheta < 1$ we derive a critical value of ∼45°. A similar behaviour has recently been confirmed by numerical simulations on gecko seta [51]: for forces applied at an angle less than ∼30° the predominant failure mode was sliding, whereas larger angles correspond to detachment. Using the previous parameters we find $F_C\left(\vartheta = 30°\right)\big/F_C\left(\vartheta = 150°\right) \approx 14$, which can still be sufficient to control adhesion of nonideal contacts, for which the strength is expected to be reduced by a factor of about one order of magnitude [12]. However note that in any case (i.e., also at $\vartheta \approx 0$) the total adhesive force could be overcome by subsequently detaching single points of contacts and not the whole surface at once [14], even if, when not in vivo, this mechanism could be hard to be activated. Note that the ratio predicted by Eq. 28 is compatible with homemade experiments that we have performed using adhesive tape. For larger thickness the behaviour would be that of a beam rather than of a film [26].

Observation on Living Geckos

In this section we summarize recent observations on adhesion of living geckos [53]. We report experimental observations on the times of adhesion of living Tokay geckos (*Gekko geckos*) on polymethylmethacrylate (PMMA) inverted surfaces. Two different geckos (male and female) and three surfaces with different root mean square (RMS) roughness (RMS=42, 618 and 931 nm) have been considered, for a total of 72 observations. The measured data are proved to be statistically significant, following the Weibull Statistics with coefficients of correlation between

0.781 and 0.955. The unexpected result is the observation of a maximal gecko adhesion on the surface with intermediate roughness of RMS=618 nm, that we note has waviness comparable to the seta size.

Surface roughness strongly influences the animal adhesion strength and ability. Its role was shown in different measurements on flies and beetles, walking on surfaces with well defined roughness [54], [55, 56], on the chrysomelid beetle *Gastrophysa viridula* [57], on the fly *Musca domestica* ([56]) as well as on the Tokay geckos [58]. Peressadko and Gorb [56] and Gorb [57] report a minimum of the adhesive/frictional force, spanning surface roughness from 0.3 to 3 μm. The experiments on the reptile Tokay gecko [58] showed a minimum in the adhesive force of a single spatula at an intermediate root mean square (RMS) surface roughness around 100–300 nm, and a monotonic increase of adhesion times of living geckos by increasing the RMS, from 90 to 3,000 nm. There are several observations and models in the literature, starting with the pioneer paper by Fuller and Tabor [59], in which roughness was seen to decrease adhesion monotonically. But there is also experimental evidence in the literature, starting with the pioneer paper by Briggs and Briscoe [60], which suggests that roughness need not always reduce adhesion. For example, Persson and Tosatti [61] and Persson [62], in the framework of a reversible model, have shown that for certain ranges of roughness parameters, it is possible for the effective surface energy to first increase with roughness amplitude and then eventually decreasing. Including irreversible processes, due to mechanical instabilities, Guduru [63] has demonstrated, under certain hypotheses, that the pull-out force must increase by increasing the surface wave amplitude. We have suggested [53] that roughness alone could not be sufficient to describe the three-dimensional topology of a complex surface and additional parameters have to be considered for formulating a well-posed problem.

Accordingly, we have machined and characterized three different Polymethylmethacrylate surfaces (PMMA 1,2,3; surface energy of ∼41 mN/m) with a full set of roughness parameters, as reported in Table 1: Sa represents the surface arithmetical average roughness; Sq=RMS is the classical mean square roughness; Sp and Sv are respectively the height of the highest peak and the deepness of the deepest valley (absolute value); Sz is the average distance between the five highest peaks and the five deepest valleys (detected in the analyzed area);

Table 1 Roughness parameters for the three different Polymethylmethacrylate (PMMA 1,2,3) surfaces

	PMMA1	PMMA2	PMMA3
Sa(μm)	0.033±0.0034	0.481±0.0216	0.731±0.0365
Sq(μm)	0.042±0.0038	0.618±0.0180	0.934±0.0382
Sp(μm)	0.252±0.0562	2.993±0.1845	4.620±0.8550
Sv(μm)	0.277±0.1055	2.837±0.5105	3.753±0.5445
Ssk	−0.122±0.1103	0.171±0.1217	0.192±0.1511
Sz (μm)	0.432±0.1082	4.847±0.2223	6.977±0.2294
Sdr (%)	0.490±0.0214	15.100±1.6093	28.367±2.2546

Ssk indicates the surface skewness; Sdr is the effective surface area minus the nominal one and divided by the last one.

Two different Tokay gecko's, female (G1, weight of ∼46 g) and male (G2, weight of ∼72 g), have been considered. The gecko is first placed in its natural position on the horizontal bottom of a box ($50 \times 50 \times 50$ cm^3). Then, slowly, we rotated the box up to the gecko reaches a natural downwards position and, at that time, we start the measurement of the gecko time of adhesion. We excluded any trial in which the gecko walks on the inverted surface. The time measurement was stopped when gecko breaks loose from the inverted surface and falls on the bottom of the box (for G1) or at the first detachment movement of the gecko's foot (for G2). The time between one measurement and the following, pertaining to the same set, is only that needed to rotate the box and placed the gecko again on the upper inverted surface (∼14 s). The experiments were performed at ambient temperature (∼22°C) and humidity (∼75%). The measured adhesion times are summarized in Table 2 and confirmed to be statistically significant by applying Weibull Statistics, see Fig. 8.

Table 2 Gecko adhesion times on PMMA 1,2,3 surfaces

Test No.	PMMA 1	PMMA 2	PMMA 3
1	8	137	15
2	13	215	22
3	36	243	22
4	37	280	25
5	48	498	27
6	62	610	29
7	67	699	32
8	87	900	35
9	88	945	48
10	93	1,194	51
11	116	1,239	53
12	134	1,320	91
13	145	2,275	97
14	160	2,740	102
15	197	4,800	109
16	212		114
17	215		148
18	221		207
19	228		424
20	292		645
21	323		
22	369		
23	474		
24	550		
25	568		
26	642		
27	660		
28	700		
29	707		
30	936		

Table 2 (continued)

Test No.	PMMA 1	PMMA 2	PMMA 3
31	1,268		
32	1,412		
33	1,648		
34	1,699		
35	2,123		
36	2,703		
37	2,899		
Scale Parameter t_0 (s)	800	1,251.7	108.4
Sq (μm)	0.042±0.0038	0.618±0.0180	0.934±0.0382

Note that, as an index of the gecko adhesion ability, here we use the Weibull scale parameter t_0 (in seconds) of the distribution of the detachment/failure F (closely related to its mean value)

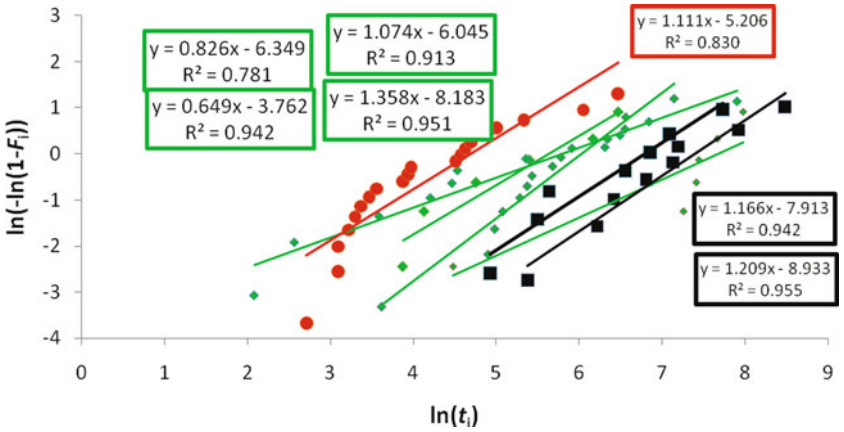

Fig. 8 Weibull Statistics (F is the cumulative probability of detachment/failure and t_i are the measured adhesion times) applied to the measured adesion times on PMMA surfaces. PMMA 1 (green, for which we made the measurements in four different days and with both geckos G1 and G2), PMMA 2 (black, for which we made the measurements in two different days, one with gecko G1 and one with gecko G2) and PMMA 3 (red, for which we made the measurements in a single day with gecko G2)

We have observed a maximum in the gecko's adhesion times on PMMA 2, having an intermediate roughness of RMS=618 nm. An oversimplified explanation could be the following. For PMMA 1 (Sq=42 nm, waviness of $\lambda \approx 3$–4 μm, $h \approx 0.1$ μm), the gecko's seta (diameter of ~10 μm, represented in blue in Fig. 9, that must not be confused with the terminal nearly two dimensional spatualae) cannot penetrate in the characteristic smaller valleys and adhere on the side of each single one Fig. 9a, thus cannot optimally adapt to the surface roughness. For PMMA 2 (Sq=618 nm, $\lambda \approx 7$–8 μm, $h \approx 1$ μm) the gecko's setae are able to adapt better to the roughness, adhering this time on the top of and on the side of a single asperity: in this way the effective number of setae in contact increases and, as a direct consequence, also

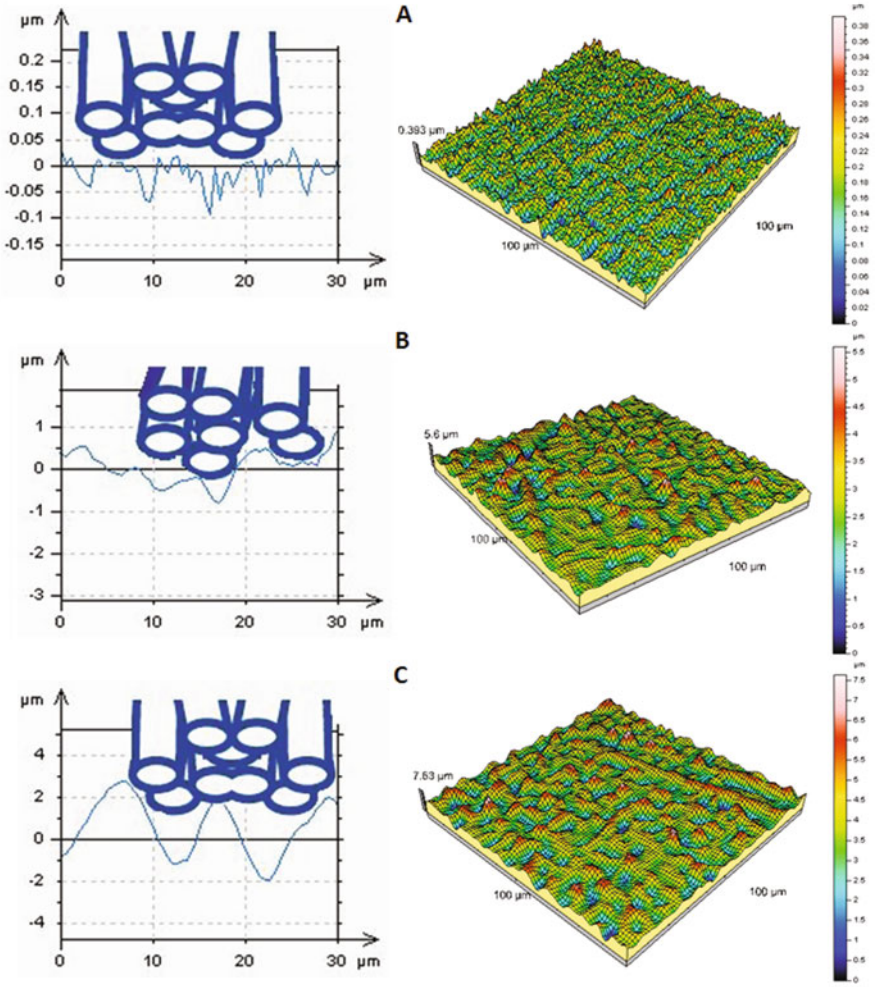

Fig. 9 A simple interpretation of our experimental results on the adhesion tests of living geckos on PMMA surfaces having different roughness. (**A**) Setae cannot adapt well on PMMA 1; (**B**) on PMMA 2 the adhesion is enhanced thanks to the higher compatibility in size between setae and roughness; (**C**) on PMMA 3 only partial contact is achieved. On the right, we report the analyzed three-dimensional profiles of the roughness for all the three investigated surfaces (from the top: PMMA 1,2 and 3)

the adhesion ability of the gecko increases Fig. 9b. On PMMA 3 (Sq=931 nm, $\lambda \approx 10$–12 μm and $h \approx 2$ μm) the waviness characterizing the roughness is larger than the seta's size: as a consequence, a decrease in the number of setae in contact is expected Fig. 9c . As a result, on PMMA 2 an adhesion increment, of about 45%, is observed. According to Briggs and Briscoe [60] an increment of 40%, thus close to our observation, is expected for an adhesion parameter α equal to 1/3. Such a

parameter was introduced as the key parameter in governing adhesion by Fuller and Tabor [59] as:

$$\alpha = \frac{4\sigma}{3}\left(\frac{4E}{3\pi\sqrt{\beta}\gamma}\right)^{2/3} \tag{29}$$

where σ is the standard deviation of the asperity height distribution (assumed to be Gaussian), β is the mean radius of curvature of the asperity, γ is the surface energy and E is the Young modulus of the soft solid (gecko foot). Even if the value of E of the entire foot cannot be simply defined, as a consequence of its non compact structure, we note that considering it to be of the order of 10 MPa (thus much smaller than that of the keratin material), with $\gamma \approx 0.05\text{N}/\text{m}$ [8], $\sigma \approx \text{Sq}$, $\beta \approx \lambda$ would correspond to values of α close to 0.5.

The reported maximal adhesion was not observed by Huber et al. [58]. Note that their tested polished surfaces were of five different types, with a nominal asperity size of 0.3, 1, 3, 9 and 12 μm, which correspond to RMS values of 90, 238, 1,157, 2,454 and 3,060 nm respectively. Huber et al. [58] have observed sliding of geckos on polishing paper with a RMS value of 90 nm for slopes larger than 135°. On a rougher substrate, with a RMS value of 238 nm, two individual geckos were able to cling to the ceiling for a while, but the foot-surface contact had to be continuously renewed because gecko toes slowly tend to slid off the substrate. Finally, on the remaining tested rougher substrates, animals were able to adhere stably to the ceiling for more than 5 min.

These different observations (assuming that the influences of claws and moult were minimized also by Huber et al. [58] suggest that the RMS parameter is not sufficient alone to describe all the aspects of the surface roughness. The use of a 'complete'set of roughness parameters could help in better understanding the animal adhesion and thus in optimizing the Spiderman suit design.

Towards a Spiderman Suit

According to our analysis, a man (palm surfaces of ∼200 cm^2) and gecko-material gloves ($\sigma_{gecko} \approx 0.58$ MPa) could support a mass of ∼1,160 kg (safety factor ∼14), or with spider-material gloves ($\sigma_{spider} \approx 0.24$ MPa) a mass of ∼480 kg (safety factor ∼6). We expect, due to non ideal contact, a safety factor reduction of about one order of magnitude [12], thus we still conclude that Spiderman suits could become feasible in the near future. Note that theoretical van der Waals gloves ($\sigma_{vdW}^{(th)} \approx 20$ MPa) would allow one to support a mass of ∼40,000 kg (safety factor of ∼500). Carbon nanotubes could be one of the most promising candidates for our applications: on a small scale a carbon nanotube surface was able to achieve adhesive forces ∼200 times greater than those of gecko foot hairs [64], even if it could not replicate large scale gecko adhesion perhaps due to a lack of compliance and hierarchy. Thus, we propose the use of hierarchical branched long (to have the

sufficient compliance) nanotubes [65] as good material for a Spiderman suit, with a number of hierarchical levels sufficient to activate self-cleaning, as quantifiable by our calculations. Their aspect ratio must not be too large, to avoid bunching [66, 67] and elastic self-collapse under their own weight, but sufficiently large to conform to a rough surface by buckling under the applied stress (see [2]), similar to the optimization done by Nature in spiders and geckos. In particular, following Glassmaker et al. [67] and Yao and Gao [68] for the bunching and introducing our result for the pillar radius at the level N ($r_N = r_0 \left(\varphi/n\right)^{N/2}$) we find the anti-bunching and anti-self-collapse [69] conditions at the hierarchical level N in the following form:

$$s < \min \left\{ 2 \left(\frac{3^3 \pi^4}{2^5 \left(1 - \nu^2\right)} \right)^{1/12} \left(\frac{E r_0}{\gamma} \right)^{1/3} \left(\frac{\varphi}{n} \right)^{N/6} \left(\sqrt{\left(\varphi_{\max}/\varphi^N\right)} - 1 \right)^{1/2}, \right.$$
$$\left. \left(\frac{8\pi^2 E}{r_0 \left(\varphi/n\right)^{N/2} \rho g} \right)^{1/3} \right\}, \tag{29}$$

where ν is the Poisson's ratio, ρ is the material density and $\varphi_{\max} = \pi/2\sqrt{3}$, $\varphi_{\max} = \pi/4$ or $\varphi_{\max} = \pi/3\sqrt{3}$ for triangular, square or hexagonal pillar lattices respectively. In order to have a uniform contact, the buckling [69] must be activated under the applied stress σ_a (e.g., ~10 KPa, see [2]), thus imposing:

$$s > \pi \sqrt{4/3} \varphi^{N/2} \sqrt{\left(\sigma_a/E\right)}, \tag{30}$$

Equations 29 and 30 can be used for an optimal design of hierarchical super-adhesive materials.

Accompanied by large transparent (if not fully invisible, to dispose of a higher strength) nanotube based cobwebs, a complete preliminary Spiderman suit could be realized, Fig. 2.

Conclusions

We have proposed [26] new laws to design futuristic self-cleaning, super-adhesive and releasable hierarchical smart materials, as well as large invisible cables, based on carbon nanotube technology.

Thus the formulas suggest the possibility of scaling up the amazing adhesion properties of a spider to the size of a man, thus the feasibility of a Spiderman suit. Strong attachment and self-cleaning are all properties that must be achieved simultaneously. Even if this seems to be impossible, since these mechanisms are in strong competitions, lotus leaves and gecko feet suggest the opposite. But one could deduce that this high nanotech project is unfeasible, since no adhesive-based animals larger than geckos exist in Nature. This is not fully right: Nature has often different scopes

with respect to ours, for example animals are not interested in going into space, as we are. Consequently, rather than mimicking Nature we must be inspired by Nature: an airplane is not a big bird. Thus, the project could be feasible. We think that it is feasible, since for a Spiderman Suit we need an adhesive strength that is much lower (two order of magnitudes) than the theoretical (e.g. van der Waals) strength. This safety factor could allow us to produce a flaw-tolerant, a very important requirement since larger contact imperfections are expected at larger size scales, super-adhesive smart material.

The analysis thus represents a first step towards the feasibility of a Spiderman suit [26].

Acknowledgments The author thanks Dorothy Hesson for the English grammar final supervision and the MIUR and PROMOMAT financial supports.

References

1. B. Bhushan, J.N. Israelachvili, U. Landman, Nanotribology: friction, wear and lubrication at the atomic scale. Nature **374**, 607–616 (1995)
2. B. Bhushan, A. Sayer, *Gecko Feet: Natural Attachment Systems for Smart Adhesion*, Applied Scanning Probe Methods – Biomimetics and Industrial Applications, vol 7 (Springer-Verlag, Heidelberg, Germany, 2007), p. 41–76
3. G. Huber, H. Mantz, R. Spolenak, K. Mecke, K. Jacobs, S.N. Gorb, E. Arzt, Evidence for capillarity contributions to gecko adhesion from single spatula and nanomechanical measurements. Proc. Natl. Acad. Sci. U.S.A. **102**, 16293–16296 (2005)
4. K. Autumn, M. Sitti, Y.A. Liang, A.M. Peattie, W.R. Hansen, S. Sponberg, T.W. Kenny, R. Fearing, J.N. Israelachvili, R.J. Full, Evidence for van der Waals adhesion in gecko setae. Proc. Natl. Acad. Sci. U.S.A. **99**, 12252–12256 (2002)
5. A.B. Kesel, A. Martin, T. Seidl, Getting a grip on spider attachment: an AFM approach to microstructure adhesion in arthropods. Smart Mater. Struct. **13**, 512–518 (2004)
6. R. Ruibal, V. Ernst, The structure of the digital setae of lizards. J. Morph. **117**, 271–294 (1965)
7. H.H. Schleich, W. Kästle, Ultrastrukturen an Gecko-Zehen. Amphib. Reptil. **7**, 141–166 (1986)
8. K. Autumn, Y.A. Liang, S.T. Hsieh, W. Zesch, W.P. Chan, T.W. Kenny, R. Fearing, R.J. Full, Adhesive force of a single gecko foot-hair. Nature **405**, 681–685 (2000)
9. G. Huber, S.N. Gorb, R. Spolenak, E. Arzt, Resolving the nanoscale adhesion of individual gecko spatulae by atomic force microscopy. Biol. Lett. **1**, 2–4 (2005)
10. W. Federle, K. Rohrseitz, B. Hölldobler, Attachment forces of ants measured with a centrifuge: better 'wax-runners' have a poorer attachment to a smooth surface. J. Exp. Biol. **203**, 505–12 (2000)
11. N.E. Stork, Experimental analysis of adhesion of *Chrysolina polita* (Chrysomelidae: Coleoptera) on a variety of surfaces. J. Exp. Biol. **88**, 91–107 (1983)
12. N. Pugno, On the strength of the nanotube-based space elevator cable: from nanomechanics to megamechanics. J. Phys. Condens. Matter **18**, S1971–S1990 (2006)
13. E. Arzt, S. Gorb, R. Spolenak, From micro to nano contacts in biological attachment devices. Proc. Natl. Acad. Sci. U.S.A. **100**, 10603–10606 (2003)
14. S. Niederegger, S. Gorb, Tarsal movements in flies during leg attachment and detachment on a smooth substrate. J. Insect Physiol. **49**, 611–20 (2003)
15. M. Varenberg, N. Pugno, S. Gorb, Spatulae structures in biological fibrillar adhesion. SOFT MATTER **6**, 3269–3272 (2010)
16. C. Neinhuis, W. Barthlott, Characterisation and distribution of water-repellent, self-cleaning plant surfaces. Ann. Bot. **79**, 667–677 (1997)

17. W. Barthlott, C. Neinhuis, Purity of scared lotus or escape from contamination in biological surfaces. Planta **202**, S1–8 (1997)
18. T. Wagner, C. Neinhuis, W. Barthlott, Wettability and contaminability of insect wings as a function of their surface sculture. Acta Zool. **77**, 213–225 (1996)
19. W. Lee, M.K. Jin, W.C. Yoo, J.K. Lee, Nanostructuring of a polymeric substrate with well- defined nanometer-scale topography and tailored surface wettability. Langmuir **20**, 7665–7669 (2004)
20. X. Gao, L. Jiang, Biophysics: water-repellent legs of water striders. Nature **432**, 36 (2004)
21. D. Quéré, Non-sticking drops. Rep. Prog. Phys. **68**, 2495–2532 (2005)
22. R. Blossey, Self-cleaning surfaces – virtual realities. Nat. Mater. **2**, 301–306 (2003)
23. W.R. Hansen, K. Autumn, Evidence for self-cleaning in gecko setae. Proc. Natl. Acad. Sci. U.S.A. **102**, 385–389 (2005)
24. A.K. Geim, S.V. Dubonos, I.V. Grigorieva, K.S. Novoselov, A.A. Zhukov, S.Y. Shapoval, Microfabricated adhesive mimicking gecko foot-hair. Nat. Mater. **2**, 461–463 (2003)
25. N. Pugno, Large invisible cables Arxiv: cond-mat/0601369 (2006)
26. N. Pugno, Towards a Spiderman suit: large invisible cables and self-cleaning releasable super-adhesive materials. J. Phys. Condens. Mater **19**, 395001–395018 (2007)
27. N. Pugno, Spiderman gloves. Nano Today **3**, 35–41 (2008)
28. M. Zhang, S. Fang, A.A. Zakhidov, S.B. Lee, A.E. Aliev, C.D. Williams, K.R. Atkinson, R.H., Strong, transparent, multifunctional, carbon nanotube sheets. Science **309**, 1215–1219 (2005)
29. M.F. Yu, O. Lourie, M.J. Dyer, K. Moloni, T.F. Kelly, R.S. Ruoff, Strength and breaking mechanism of multiwalled carbon nanotubes under tensile load. Science **287**, 637–640 (2000)
30. A. Carpinteri, N. Pugno, Are the scaling laws on strength of solids related to mechanics of to geometry? Nat. Mater. **4**, 421–423 (2005)
31. N. Pugno, Graded cross-links for stronger nanomaterials. Mater. Today **13**, 40–43 (2010)
32. N. Pugno, Velcro® nonlinear mechanics. Appl. Phys. Lett. **90**, 121918 (2007)
33. A. Carpinteri, *Structural Mechanics: A Unified Approach* (E & FN Spon, London, UK, 1997)
34. D. Kretschmann, Velcro mechanics in wood. Nat. Mater. **2**, 775–776 (2003)
35. A.P. Russell, The morphological basis of weight-bearing in the scansors of the tokay gecko. Can. J. Zool. **64**, 948–955 (1986)
36. J.E.A. Bertram, J.M. Gosline, Functional design of horse hoof keratin: the modulation of mechanical properties through hydration effects. J. Exp. Biol. **130**, 121–136 (1987)
37. K. Autumn, A.M. Peattie, Mechanisms of adhesion in geckos. Integr. Comp. Biol. **42**, 1081–1090 (2002)
38. T. Young, An essay on the cohesion of fluids. Phil. Trans. R. Soc. (London) **95**, 65–87 (1805)
39. R.N. Wenzel, Resistance of solid surfaces to wetting by water. Ind. Eng. Chem. **28**, 988–994 (1936)
40. R.N. Wenzel, Surface roughness and contact angle. J. Phys. Chem. **53**, 1466–70 (1949)
41. A.B.D. Cassie, S. Baxter, Wettability of porous surfaces. Trans. Faraday Soc. **40**, 546–551 (1944)
42. D. Quéré, Fakir droplets. Nat. Mater. **1**, 14–15 (2002)
43. J. Bico, U. Thiele, D. Quèrè, Wetting of textured surfaces. Colloids Surf. A **206**, 41–46 (2002)
44. J. Bico, C. Marzolin, D. Quèrè, Pearl drops. Europhys. Lett. **47**, 220–226 (1999)
45. T. Eisner, D.J. Aneshansley, Defense by foot adhesion in a beetle (Hemisphaerota cyanea). Proc. Natl Acad. Sci. U.S.A. **97**, 6568–6573 (2000)
46. J.S. McFarlane, D. Tabor, Adhesion of solids and the effects of surface films. Proc. R. Soc. (London) A **202**, 224–243 (1950)
47. P.S. Laplace, *Oeuvres Complètes* (Imprimerie Royale, Paris, 1847)
48. H.C Hamaker, The London-van der Waals attraction between spherical particles. Physica **4**, 1058–1072 (1937)
49. J.N. Israelachvili, *Intermulecular and Surface Forces, with Application to Colloidal and Biological Systems* (Colloid Science S.) (Academic Press Inc., San Diego, CA, 1991)
50. K.L. Johnson, K. Kendall, A.D. Roberts, Surface energy and the contact of elastic solids. Proc. R. Soc. (London) A **324**, 301–313 (1971)

51. H. Gao, X. Wang, H. Yao, S. Gorb, E. Arzt, Mechanics of hierarchical adhesion structures of geckos. Mech. Mater. **37**, 275–285 (2005)
52. K. Kendall, Thin-film peeling-elastic term. J. Phys. D: Appl. Phys. **8**, 1449–1452 (1975)
53. N. Pugno, E. Lepore, Observation of optimal gecko's adhesion on nanorough surfaces. Biosystems **94**, 218–222 (2008)
54. Z. Dai, S.N. Gorb, U. Schwarz, Roughness-dependent friction force of the tarsal claw system in the beetle Pachnoda marginata (Coleoptera Scarabaeidae). J. Exp. Biol. **205**, 2479–2485 (2002)
55. B.N.J. Persson, S. Gorb, The effect of surface roughness on the adhesion of elastic plates with application to biological systems. J. Chem. Phys. **119**, 11437–11444 (2003)
56. A.G. Peressadko, S.N. Gorb, *Surface Profile and Friction Force Generated by Insects*, vol 15, ed. by I. Boblan, R. Bannasch (Bionik, Hannover; 2004) p. 237
57. S.N. Gorb, *Attachment Devices of Icuticle* (Dordrecht: Kluwer Academic Publishers, Boston, 2001)
58. G. Huber, S.N. Gorb, N. Hosoda, R. Spolenak, E. Arzt, Influence of surface roughness on gecko adhesion. Acta Biomater. **3**, 607–610 (2007)
59. K.N.G. Fuller, D. Tabor, The effect of surface roughness on the adhesion of elastic solids. Proc. Royal Soc. Lond. A **345**, 327–342 (1975)
60. G.A.D. Briggs, B.J. Briscoe, The effect of surface topography on the adhesion of elastic solids. J. Phys. D: Appl. Phys. **10**, 2453–2466 (1977)
61. B.N.J. Persson, E. Tosatti, The effect of surface roughness on the adhesion of elastic solids. J. Chem. Phys. **115**, 5597–5610 (2001)
62. B.N.J. Persson, Adhesion between and elastic body and a randomly hard surface. Eur. Phys. J. E **8**, 385–401 (2002)
63. P.R. Guduru, Detachment of a rigid solid from an elastic wavy surface: theory. J. Mech. Phys. Solids **55**, 445–472 (2007)
64. B. Yurdumakan, N.R. Raravikar, P.M. Ajayan, A. Dhinojwala, Synthetic gecko foot hairs from multiwalled carbon nanotubes. Chem. Comm. **30**, 3799–3801 (2005)
65. G. Meng, Y.J. Jung, A. Cao, R. Vajtai, P.M. Ajayan, Controlled fabrication of hierarchically branched nanopores, nanotubes, and nanowires. Proc. Natl. Acad. Sci. U.S.A. **102**, 7074–7078 (2005)
66. C.Y. Hui, A. Jagota, Y.Y, Lin, E.J. Kramer, Constraints on micro-contact printing imposed by stamp deformation. Langmuir **18**, 1394–1404 (2002)
67. N.J. Glassmaker, A. Jagota, C.Y. Hui, J. Kim, Design of biomimetic fibrillar interface: 1. Making contact. J. R. Soc. Interface London **1**, 23–33 (2004)
68. H. Yao, H. Gao, Mechanics of robust and releasable adhesion in biology: bottom-up designed of hierarchical structures of gecko. J. Mech. Phys. Sol. **54**, 1120–1146 (2006)
69. S.P. Timoshenko, J.M. Gere, *Theory of Elastic Stability* (McGraw-Hill, New York, 1961)
70. U. Hiller, Untersuchungen zum Feinbau und zur Funktion der Haftborsten von Reptilien. Z Morphol Tiere **62**, 307–362 (1968)
71. A.P. Russell, A contribution to the functional morphology of the foot of the tokay, Gekko gecko. J. Zool. Lond. **176**, 437–476 (1975)
72. E.E. Williams, J.A. Peterson, Convergent and alternative designs in the digital adhesive pads of scincid lizards. Science **215**, 1509–1511 (1982)
73. W. Sun, P. Neuzil, T.S. Kustandi, S. Oh, V.D. Samper, The nature of the gecko Lizard Adhesive Force. Biophys. J. **89**, L14–L17 (2005)
74. A.B. Kesel, A. Martin, T. Seidl, Adhesion measurements on the attachment devices of the jumping spider Evarcha arcuata. J. Exp. Biol. **206**, 2733–2738 (2003)
75. K.K.S. Lau, J. Bico, K.B.K. Teo, M. Chhowalla, G.A.J. Amaratunga, W.I. Milne, G.H. McKinley, K.K., Superhydrophobic carbon nanotube forests. Nanoletters **3**, 1701–1705 (2003)

Strength of Nanotubes and Megacables

Nicola M. Pugno

Abstract In this chapter my findings [mainly reported in N. Pugno, J. Phys.–Condens. Matter, **18**, S1971–S1990 (2006); N. Pugno, Acta Mater. **55**, 5269–5279 (2007); N. Pugno, Nano Today **2**, 44–47 (2007)] on the mechanical strength of nanotubes and megacables are reviewed, with an eye to the challenging project of the carbon nanotube-based space elevator megacable. Accordingly, basing the design of the megacable on the theoretical strength of a single carbon nanotube, as originally proposed at the beginning of the third millennium, has been demonstrated to be naïve. The role on the fracture strength of thermodynamically unavoidable atomistic defects with different size and shape is thus here quantified on brittle fracture both numerically (with *ad hoc* hierarchical simulations) and theoretically (with quantized fracture theories), for nanotubes and nanotube bundles. Fatigue, elasticity, non-asymptotic regimes, elastic-plasticity, rough cracks, finite domains and size-effects are also discussed.

Introduction

A space elevator basically consists of a cable attached to the Earth surface for carrying payloads into space [1]. If the cable is long enough, i.e. around 150 Mm (a value that can be reduced by a counterweight), the centrifugal forces exceed the gravity of the cable, that will work under tension [2]. The elevator would stay fixed geosynchronously; once sent far enough, climbers would be accelerated by the Earth's rotational energy. A space elevator would revolutionize the methodology for carrying payloads into space at low cost, but its design is very challenging. The most critical component in the space elevator design is undoubtedly the cable [3–5], that requires a material with very high strength and low density.

N.M. Pugno (✉)
Department of Structural Engineering and Geotechnics, Politecnico di Torino,
Corso Duca degli Abruzzi 24, 10129 Torino, Italy
e-mail: nicola.pugno@polito.it

S. Bellucci (ed.), *Physical Properties of Ceramic and Carbon Nanoscale Structures*,
Lecture Notes in Nanoscale Science and Technology 11,
DOI 10.1007/978-3-642-15778-3_4,

Considering a cable with constant cross-section and a vanishing tension at the planet surface, the maximum stress-density ratio, reached at the geosynchronous orbit, is for the Earth equal to 63 GPa/(1,300 kg/m^3), corresponding to 63 GPa if the low carbon density is assumed for the cable. Only recently, after the re-discovery of carbon nanotubes [6], such a large failure stress has been experimentally measured, during tensile tests of ropes composed of single walled carbon nanotubes [7] or multiwalled carbon nanotubes [8] both expected to have an ideal strength of ~100 GPa. Note that for steel (density of 7,900 kg/m^3, maximum strength of 5 GPa) the maximum stress expected in the cable would be of 383 GPa, whereas for kevlar (density of 1,440 kg/m^3, strength of 3.6 GPa) of 70 GPa, both much higher than their strengths [3].

However, an optimized cable design must consider a uniform tensile stress profile rather than a constant cross-section area [2]. Accordingly, the cable could be built of any material by simply using a large enough taper-ratio, that is the ratio between the maximum (at the geosynchronous orbit) and minimum (at the Earth's surface) cross-section area. For example, for steel or kevlar a giant and unrealistic taper-ratio would be required, 10^{33} or 2.6×10^8 respectively, whereas for carbon nanotubes it must theoretically be only 1.9^9. Thus, the feasibility of the space elevator seems to become only currently plausible [9, 10] thanks to the discovery of carbon nanotubes. The cable would represent the largest engineering structure, hierarchically designed from the nano- (single nanotube with length of the order of a hundred nanometers) to the mega-scale (space elevator cable with a length of the order of a hundred megameters).

In this chapter the asymptotic analysis on the role of defects for the mega-cable strength, based on new theoretical deterministic and statistical approaches of quantized fracture mechanics proposed by the author [11–14], is extended to non asymptotic regimes, elastic-plasticity, rough cracks and finite domains. The role of thermodynamically unavoidable atomistic defects with different size and shape is thus quantified on brittle fracture, fatigue and elasticity, for nanotubes and nanotube bundles. The results are compared with atomistic and continuum simulations and nano-tensile tests of carbon nanotubes. Key simple formulas for the design of a flaw-tolerant space elevator megacable are reported, suggesting that it would need a taper-ratio (for uniform stress) of about two orders of magnitude larger than as today erroneously proposed.

The chapter is organized in 10 short sections, as follows. After this introduction, reported as the first section, we start calculating the strength of nanotube bundles by using *ad hoc* hierarchical simulations, discussing the related size-effect. In Sect. 'Brittle Fracture' the strength reduction of a single nanotube and of a nanotube bundle containing defects with given size and shape is calculated; the taper-ratio for a flaw-tolerant space elevator cable is accordingly derived. In Sect. 'Elastic-Plasticity, Fractal Cracks and Finite Domains' elastic-plastic (or hyper-elastic) materials, rough cracks and finite domains are discussed. In Sect. 'Fatigue' the fatigue life time is evaluated for a single nanotube and for a nanotube bundle. In Sect. 'Elasticity' the related Young's modulus degradations are quantified. In Sects. 'Atomistic Simulations', 'Nanotensile Tests' we compare our results on strength

and elasticity with atomistic simulations and tensile tests of carbon nanotubes. In Sect. 'Thermodynamic Limit' we demonstrate that defects are thermodynamically unavoidable, evaluating the minimum defect size and corresponding maximum achievable strength. The last section presents our concluding remarks.

Hierarchical Simulations and Size-Effects

To evaluate the strength of carbon nanotube cables, the SE^3 algorithm, formerly proposed [3] has been adopted [15]. Multiscale simulations are necessary in order to tackle the size scales involved, spanning over ~10 orders of magnitude from nanotube length (~100 nm) to kilometre-long cables, and also to provide useful information about cable scaling properties with length.

The cable is modelled as an ensemble of stochastic 'springs', arranged in parallel sections. Linearly increasing strains are applied to the fibre bundle, and at each algorithm iteration the number of fractured springs is computed (fracture occurs when local stress exceeds the nanotube failure strength) and the strain is uniformly redistributed among the remaining intact springs in each section.

In-silico stress-strain experiments have been carried out according to the following hierarchical architecture. Level 1: the nanotubes (single springs, Level 0) are considered with a given elastic modulus and failure strength distribution and composing a $40\times1{,}000$ lattice or fibre. Level 2: again a $40\times1{,}000$ lattice composed by second level 'springs', each of them identical to the entire fibre analysed at the first level, is analysed with in input the elastic modulus and stochastic strength distribution derived as the output of the numerous simulations to be carried out at the first level. And so on. Five hierarchical levels are sufficient to reach the size-scale of the megametre from that of the nanometre, Fig. 1.

The level 1 simulation is carried out with springs $L_0 = 10^{-7}$ m in length, $w_0 = 10^{-9}$ m in width, with Young's modulus $E_0 = 10^{12}$ Pa and strength σ_f randomly distributed according to the nanoscale Weibull statistics [16] $P\left(\sigma_f\right) = 1 - \exp[-(\sigma_f/\sigma_0)^m]$, where P is the cumulative probability. Fitting to experiments [7, 8], we have derived for carbon nanotubes $\sigma_0 = 34$ GPa and $m = 2.7$ [16]. Then the level 2 is computed, and so on. The results are summarized in Fig. 2, in which a strong size-effect is observed, up to length of ~1 m.

Given the decaying σ_f vs. cable length L obtained from simulations, it is interesting to fit the behaviour with simple analytical scaling laws. Various exist in the literature, and one of the most used is the Multi-Fractal Scaling Law (MFSL [17], see also [18]) proposed by Carpinteri. This law has been recently extended towards the nanoscale [19]:

$$\frac{\sigma_f}{\sigma_{macro}} = \sqrt{1 + \frac{l_{ch}}{L + l_0}} \tag{1}$$

where σ_f is the failure stress, σ_{macro} is the macrostrength, L is the structural characteristic size, l_{ch} is a characteristic internal length and l_0 is defined via

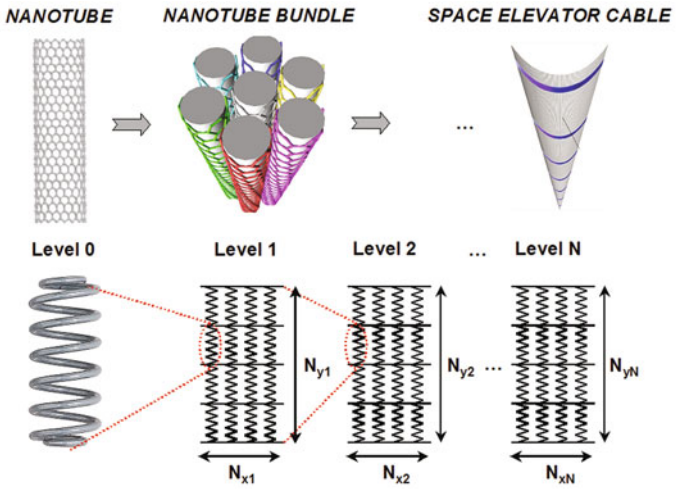

Fig. 1 Schematization of the adopted multiscale simulation procedure to determine the space elevator cable strength. Here, $N=5$, $N_{x1}=N_{x2}=\ldots N_{x5}=40$ and $N_{y1}=N_{y2}=\ldots N_{y5}=1{,}000$, so that the total number of nanotubes in the space elevator cable is $N_{tot}=(1{,}000\times 40)^5\approx 10^{23}$ [15]

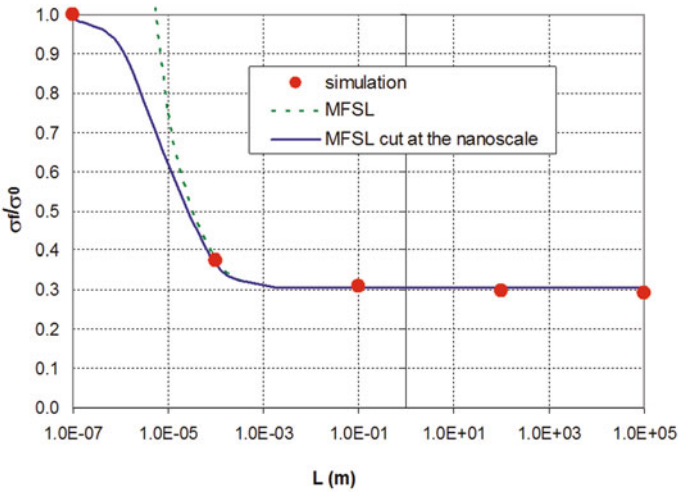

Fig. 2 Comparison between simulations and analytical scaling law Eq. 1 for the failure strength of the nanotube bundle as a function of its length; the asymptote is at 10.20 GPa [15]

$\sigma_f\,(l=0) = \sigma_{macro}\sqrt{1+\frac{l_{ch}}{l_0}} \equiv \sigma_{nano}$, where σ_{nano} is the nanostrength. Note that for $l_0 = 0$ this law is identical to the Carpinteri' scaling law [17]. Here, we can choose σ_{nano} as the nanotube stochastic strength, i.e. $\sigma_{nano}=34$ GPa. The computed macrostrength is $\sigma_{macro}=10.20$ GPa. The fit with Eq. 1 is shown in

Fig. 1 ('MFSL cut at the nanoscale'), for the various L considered at the different hierarchical levels (and compared with the classical 'MFSL'). The best fit is obtained for $l_{ch} = 5 \times 10^{-5}$ m, where the analytical law is practically coincident with the simulated results. Thus, for a carbon nanotube megacable we have numerically derived a plausible strength $\sigma_C = \sigma_{macro} \approx 10$ GPa.

Brittle Fracture

By considering Quantized Fracture Mechanics (QFM; [11–14]), the failure stress σ_N for a nanotube having atomic size q (the 'fracture quantum') and containing an elliptical hole of half-axes a perpendicular to the applied load (or nanotube axis) and b can be determined including in the asymptotic solution [12] the contribution of the far field stress. We accordingly derive:

$$\frac{\sigma_N(a,b)}{\sigma_N^{(theo)}} = \sqrt{\frac{1+2a/q\,(1+2a/b)^{-2}}{1+2a/q}}, \quad \sigma_N^{(theo)} = \frac{K_{IC}}{\sqrt{q\pi/2}} \tag{2}$$

where $\sigma_N^{(theo)}$ is the theoretical (defect-free) nanotube strength (∼100 GPa, see Table 1) and K_{IC} is the material fracture toughness. The self-interaction between the tips has been here neglected (i.e. $a << \pi R$, with R nanotube radius) and would further reduce the failure stress. For atomistic defects (having characteristic length of few Ångstrom) in nanotubes (having characteristic diameter of several nanometers) this hypothesis is fully verified. However, QFM can easily treat also the self-tip interaction starting from the corresponding value of the stress-intensity factor (reported in the related Handbooks). The validity of QFM has been recently confirmed by atomistic simulations [3–5, 12, 13, 20], but also at larger size-scales [12, 13, 21] and for fatigue crack growth [14, 22, 23].

Table 1 Atomistic simulations [30–33] vs. QFM predictions, for nano-cracks of size n or nano-holes of size m [4]

Nanotube type	Nanocrack (n) and nanohole (m) sizes	Strength (GPa) by QM (MTB-G2) and MM (PM3; M) QM/MM atomistic or QFM calculations
[5, 5]	Defect-free	105 (MTB-G2); 135 (PM3)
[5, 5]	$n = 1$ (Sym.+H)	85 (MTB-G2), 79 (QFM); 106 (PM3), 101 (QFM)
[5, 5]	$n = 1$ (Asym. +H)	71 (MTB-G2), 79 (QFM); 99 (PM3), 101 (QFM)
[5, 5]	$n = 1$ (Asym.)	70 (MTB-G2), 79 (QFM); 100 (PM3), 101 (QFM)
[5, 5]	$n = 2$ (Sym.)	71 (MTB-G2), 63 (QFM); 105 (PM3), 81 (QFM)
[5, 5]	$n = 2$ (Asym.)	73 (MTB-G2), 63 (QFM); 111 (PM3), 81 (QFM)
[5, 5]	$m = 1$ (+H)	70 (MTB-G2), 68 for long tube, 79 (QFM); 101 (PM3), 101 (QFM)
[5, 5]	$m = 2$ (+H)	53 (MTB-G2), 50 for long tube, 67 (QFM); 78 (PM3), 86 (QFM)

Table 1 (continued)

Nanotube type	Nanocrack (n) and nanohole (m) sizes	Strength (GPa) by QM (MTB-G2) and MM (PM3; M) QM/MM atomistic or QFM calculations
[10, 10]	Defect-free	88 (MTB-G2); 124 (PM3)
[10, 10]	$n = 1$ (sym.+H)	65 (MTB-G2), 66 (QFM)
[10, 10]	$n = 1$ (Asym. +H)	68 (MTB-G2), 66 (QFM)
[10, 10]	$n = 1$ (Sym.)	65 (MTB-G2), 66 (QFM); 101 (PM3), 93 (QFM)
[10, 10]	$n = 2$ (Sym.)	64 (MTB-G2), 53 (QFM); 107 (PM3), 74 (QFM)
[10, 10]	$n = 2$ (Asym.)	65 (MTB-G2), 53 (QFM); 92 (PM3), 74 (QFM)
[10, 10]	$m = 1$ (+H)	56 (MTB-G2), 52 for long tube, 66 (QFM); 89 (PM3), 93 (QFM)
[10, 10]	$m = 2$ (+H)	42 (MTB-G2), 36 for long tube, 56 (QFM); 67 (PM3), 79 (QFM)
[50, 0]	Defect-free	89 (MTB-G2)
[50, 0]	$m = 1$ (+H)	58 (MTB-G2); 67 (QFM)
[50, 0]	$m = 2$ (+H)	46 (MTB-G2); 57 (QFM)
[50, 0]	$m = 3$ (+H)	40 (MTB-G2); 44 (QFM)
[50, 0]	$m = 4$ (+H)	36 (MTB-G2); 41 (QFM)
[50, 0]	$m = 5$ (+H)	33 (MTB-G2); 39 (QFM)
[50, 0]	$m = 6$ (+H)	31 (MTB-G2); 37 (QFM)
[100, 0]	Defect-free	89 (MTB-G2)
[100, 0]	$m = 1$ (+H)	58 (MTB-G2); 67 (QFM)
[100, 0]	$m = 2$ (+H)	47 (MTB-G2); 57 (QFM)
[100, 0]	$m = 3$ (+H)	42 (MTB-G2); 44 (QFM)
[100, 0]	$m = 4$ (+H)	39 (MTB-G2); 41 (QFM)
[100, 0]	$m = 5$ (+H)	37 (MTB-G2); 39 (QFM)
[100, 0]	$m = 6$ (+H)	35 (MTB-G2); 37 (QFM)
[29, 29]	Defect-free	101 (MTB-G2)
[29, 29]	$m = 1$ (+H)	77 (MTB-G2); 76 (QFM)
[29, 29]	$m = 2$ (+H)	62 (MTB-G2); 65 (QFM)
[29, 29]	$m = 3$ (+H)	54 (MTB-G2); 50 (QFM)
[29, 29]	$m = 4$ (+H)	48 (MTB-G2); 46 (QFM)
[29, 29]	$m = 5$ (+H)	45 (MTB-G2); 44 (QFM)
[29, 29]	$m = 6$ (+H)	42 (MTB-G2); 42 (QFM)
[47, 5]	Defect-free	89 (MTB-G2)
[47, 5]	$m = 1$ (+H)	57 (MTB-G2); 67 (QFM)
[44, 10]	Defect-free	89 (MTB-G2)
[44, 10]	$m = 1$ (+H)	58 (MTB-G2); 67 (QFM)
[40, 16]	Defect-free	92 (MTB-G2)
[40, 16]	$m = 1$ (+H)	59 (MTB-G2); 69 (QFM)
[36, 21]	Defect-free	96 (MTB-G2)
[36, 21]	$m = 1$ (+H)	63 (MTB-G2); 72 (QFM)
[33, 24]	Defect-free	99 (MTB-G2)
[33, 24]	$m = 1$ (+H)	67 (MTB-G2); 74 (QFM)

Table 1 (continued)

Nanotube type	Nanocrack (n) and nanohole (m) sizes	Strength (GPa) by QM (MTB-G2) and MM (PM3; M) QM/MM atomistic or QFM calculations
[80, 0]	Defect-free	93 (M)
[80, 0]	$n=2$	64 (M); 56 (QFM)
[80, 0]	$n=4$	50 (M); 43 (QFM)
[80, 0]	$n=6$	42 (M); 35 (QFM)
[80, 0]	$n=8$	37 (M); 32 (QFM)
[40, 0] (nested by a [32, 0])	Defect-free	99 (M)
[40, 0] (nested by a [32, 0])	$n=2$	73 (M); 69 (QFM + vdW interaction ~10GPa)
[40, 0] (nested by a [32, 0])	$n=4$	57 (M); 56 (QFM + vdW interaction ~10GPa)
[40, 0] (nested by a [32, 0])	$n=6$	50 (M); 48 (QFM + vdW interaction ~10GPa)
[40, 0] (nested by a [32, 0])	$n=8$	44 (M); 44 (QFM + vdW interaction ~10GPa)
[100, 0]	Defect-free	89 (MTB-G2)
[100, 0]	$n=4$	50 (M); 41 (QFM)
[10, 0]	Defect free	124 (QM); 88 (MM);
[10, 0]	$n=1$	101 (QM) 95 (QM/MM) 93 (QFM); 65 (MM) 66 (QFM)

The QFM predictions are here obtained simply considering in Eq. 2 $2a/q = n$, $2b/q = 1$ for cracks of size n or $a/q = b/q = (2m-1)/\sqrt{3}$ for holes of size m. Quantum mechanics (QM) semi-empirical calculations (PM3 method), Molecular Mechanics (MM) calculations (modified Tersoff-Brenner potential of second generation (MTB-G2), modified Morse potential (M)) and coupled QM/MM calculations. The symbol (+H) means that the defect was saturated with hydrogen. Symmetric and asymmetric bond reconstructions were also considered; the tubes are 'short', if not otherwise specified. We have roughly ignored in the QFM predictions the difference between symmetric and asymmetric bond reconstruction, hydrogen saturation and length-effect (for shorter tubes an increment in the strength is always observed, as an intrinsic size-effect), noting that the main differences in the atomistic simulations are imputable to the used potential. For nested nanotubes a strength increment of ~10 GPa is here assumed to roughly take into account the van der Walls (vdW) interaction between the walls

Regarding the defect shape, for a sharp crack perpendicular to the applied load $a/q = \text{const}$ & $b/q \to 0$, thus $\sigma_N \approx \sigma_N^{(theo)}/\sqrt{1+2a/q}$, and for $a/q >> 1$, i.e. large cracks, $\sigma_N \approx K_{IC}/\sqrt{\pi a}$ in agreement with Linear Elastic Fracture Mechanics (LEFM); note that LEFM can (1) only treat sharp cracks and (2) unreasonably predicts an infinite defect-free strength. On the other hand, for a crack parallel to the applied load $b/q = \text{const}$ & $a/q \to 0$ and thus $\sigma_N = \sigma_N^{(theo)}$, as it must be. In addition, regarding the defect size, for self-similar and small holes $a/b = \text{const}$ & $a/q \to 0$ and coherently $\sigma_N = \sigma_N^{(theo)}$; furthermore, for self-similar and large holes $a/b = \text{const}$ & $a/q \to \infty$ and we deduce $\sigma_N \approx \sigma_N^{(theo)}/(1+2a/b)$ in agreement with the stress-concentration posed by Elasticity; but Elasticity (coupled with a

maximum stress criterion) unreasonably predicts (3) a strength independent from the hole size and (4) tending to zero for cracks. Note the extreme consistency of Eq. 2, that removing all the limitations (1–4) represents the first law capable of describing in a unified manner all the size- and shape-effects for the elliptical holes, including cracks as limit case. In other words, Eq. 2 shows that the two classical strength predictions based on stress-intensifications (LEFM) or -concentrations (Elasticity) are only reasonable for 'large' defects; Eq. 2 unifies their results and extends its validity to 'small' defects ('large' and 'small' are here with respect to the fracture quantum). Eq. 2 shows that even a small defect can dramatically reduces the mechanical strength.

An upper bound of the cable strength can be derived assuming the simultaneous failure of all the defective nanotubes present in the bundle. Accordingly, imposing the critical force equilibrium (mean-field approach) for a cable composed by nanotubes in numerical fractions f_{ab} containing holes of half-axes a and b, we find the cable strength σ_C (ideal if $\sigma_C^{(theo)}$) in the following form:

$$\frac{\sigma_C}{\sigma_C^{(theo)}} = \sum_{a,b} f_{ab} \frac{\sigma_N(a,b)}{\sigma_N^{(theo)}} \tag{3}$$

The summation is extended to all the different holes; the numerical fraction f_{00} of nanotubes is defect-free and $\sum_{a,b} f_{ab} = 1$. If all the defective nanotubes in the bundle contain identical holes $f_{ab} = f = 1 - f_{00}$, and the following simple relation between the strength reductions holds: $1 - \sigma_C/\sigma_C^{(theo)} = f\left(1 - \sigma_N/\sigma_N^{(theo)}\right)$.

Thus, the taper-ratio λ needed to have a uniform stress in the cable [2], under the centrifugal and gravitational forces, must be larger than its theoretical value to design a flaw-tolerant megacable. In fact, according to our analysis, we deduce ($\lambda = e^{const \cdot \rho_C/\sigma_C} \geq \lambda^{(theo)} \approx 1.9$ for carbon nanotubes; ρ_C denotes the material density):

$$\frac{\lambda}{\lambda^{(theo)}} = \lambda^{(theo)\left(\frac{\sigma_C^{(theo)}}{\sigma_C} - 1\right)} \tag{4}$$

Equation 4 shows that a small defect can dramatically increase the taper-ratio required for a flaw-tolerant megacable.

Elastic-Plasticity, Fractal Cracks and Finite Domains

The previous equations are based on linear elasticity, i.e., on a linear relationship $\sigma \propto \varepsilon$ between stress σ and strain ε. In contrast, let us assume $\sigma \propto \varepsilon^{\kappa}$, where $\kappa > 1$ denotes hyper-elasticity, as well as $\kappa < 1$ elastic-plasticity. The power of the stress-singularity will accordingly be modified [24] from the classical value 1/2 to

$\alpha = \kappa/(\kappa + 1)$. Thus, the problem is mathematically equivalent to that of a re-entrant corner [25], and consequently we predict:

$$\frac{\sigma_N(a,b,\alpha)}{\sigma_N^{(theo)}} = \left(\frac{\sigma_N(a,b)}{\sigma_N^{(theo)}}\right)^{2\alpha}, \quad \alpha = \frac{\kappa}{\kappa+1} \tag{5}$$

A crack with a self-similar roughness, mathematically described by a fractal with non-integer dimension $1 < D < 2$, would similarly modify the stress-singularity, according to [18, 26] $\alpha = (2 - D)/2$; thus, with Eq. 5, we can also estimate the role of the crack roughness. Both plasticity and roughness reduce the severity of the defect, whereas hyper-elasticity enlarges its effect. For example, for a crack composed by n adjacent vacancies, we found $\sigma_N/\sigma_N^{(theo)} \approx (1+n)^{-\alpha}$.

However, note that among these three effects only elastic-plasticity may have a significant role in carbon nanotubes; in spite of this, fractal cracks could play an important role in nanotube bundles as a consequence of their larger size-scale, which would allow the development of a crack surface roughness. Hyper-elasticity is not expected to be relevant in this context.

According to LEFM and assuming the classical hypothesis of self-similarity ($a_{\max} \propto L$), i.e., the largest crack size is proportional to the characteristic structural size L, we expect a size-effect on the strength in the form of the power law $\sigma_C \propto L^{-\alpha}$. For linear elastic materials $\alpha = 1/2$ as classically considered, but for elastic-plastic materials or fractal cracks $0 \leq \alpha \leq 1/2$ [24], whereas for hyper-elastic materials $1/2 \leq \alpha \leq 1$, suggesting an unusual and super-strong size-effect. This parameter would represent the maximum slope (in a bi-log plot) of the scaling reported in Fig. 1.

Equation 2 does not consider the defect-boundary interaction. The finite width $2W$, can be treated by applying QFM starting from the related expression of the stress-intensity factor (reported in Handbooks). However, to have an idea of the defect-boundary interaction, we apply an approximated method [27], deriving the following correction $\sigma_N(a,b,W) \approx C(W)\,\sigma_N(a,b)$, $C(W) \approx (1 - a/W)/\left(\sigma_N(a,b)\big|_{q \to W-a}/\sigma_N^{(theo)}\right)$ (note that such a correction is valid also for $W \approx a$, whereas for $W >> a$ it becomes $C(W >> a) \approx 1 - a/W$). Similarly, the role of the defect orientation β could be treated by QFM considering the related stress-intensity factor; roughly, one could use the self-consistent approximation $\sigma_N(a,b,\beta) \approx \sigma_N(a,b)\cos^2\beta + \sigma_N(b,a)\sin^2\beta$.

Fatigue

The space elevator cable will be cyclically loaded, e.g., by the climbers carrying the payloads, thus fatigue could play a role on its design. By integrating the quantized Paris' law, that is an extension of the classical Paris' law recently proposed

especially for nanostructure or nanomaterial applications [14, 22, 23], we derive the following number of cycles to failure (or life time):

$$\frac{C_N(a)}{C_N^{(theo)}} = \frac{(1+q/W)^{1-m/2} - (a/W+q/W)^{1-m/2}}{(1+q/W)^{1-m/2} - (q/W)^{1-m/2}}, \quad m \neq 2 \tag{6a}$$

$$\frac{C_N(a)}{C_N^{(theo)}} = \frac{\ln\{(1+q/W)/(a/W+q/W)\}}{\ln\{(1+q/W)/(q/W)\}}, \quad m = 2 \tag{6b}$$

where $m>0$ is the material Paris' exponent. Note that according to Wöhler $C_N^{(theo)} = K\Delta\sigma^{-k}$, where K and k are material constants and $\Delta\sigma$ is the amplitude of the stress range during the oscillations. Even if fatigue experiments in nanotubes are still to be performed, their behaviour is expected to be intermediate between those of Wöhler and Paris, as displayed by all the known materials, and the quantized Paris' law basically represents their asymptotic matching (as quantized fracture mechanics basically represents the asymptotic matching between the strength and toughness approaches).

Only defects remaining self-similar during fatigue growth have to be considered, thus only a crack (of half-length a) is of interest in this context. By means of Eq. 6 the time to failure reduction can be estimated, similarly to the brittle fracture treated by Eq. 2.

For a bundle, considering a mean-field approach (similarly to Eq. 3) yields:

$$\frac{C_C}{C_C^{(theo)}} = \sum_a f_a \frac{C_N(a)}{C_N^{(theo)}} \tag{7}$$

Better predictions could be derived integrating the quantized Paris' law for a finite width strip. However, we note that the role of the finite width is already included in Eq. 6, even if these are rigorously valid in the limit of W tending to infinity.

Elasticity

Consider a nanotube of lateral surface A under tension and containing a transversal crack of half-length a. Interpreting the incremental compliance, due to the presence of the crack, as a Young's modulus (here denoted by E) degradation we find $\frac{E(a)}{E^{(theo)}} = 1-2\pi\frac{a^2}{A}$ [28]. Thus, recursively, considering Q cracks (in the megacable $10^{12}-10^{20}$ defects are expected, see Sect. 'Hierarchical Simulations and Size-Effects') having sizes a_i or, equivalently, M different cracks with multiplicity Q_i ($Q = \sum_{i=1}^{M} Q_i$), noting that $n_i = \frac{2a_i}{q}$ represents the number of adjacent vacancies in a crack of half-length a_i, with q atomic size, and $v_i = \frac{Q_i n_i}{A/q^2}$ its related numerical (or volumetric) vacancy fraction, we find [28]:

$$\frac{E}{E^{(theo)}} = \prod_{i=1}^{Q} \frac{E\left(a_i\right)}{E^{(theo)}} \approx 1 - \xi \sum_{i=1}^{M} v_i n_i \tag{8}$$

with $\xi \geq \pi/2$, where the equality holds for isolated cracks. Eq. 8 can be applied to nanotubes or nanotube bundles containing defects in volumetric percentages v_i.

Forcing the interpretation of our formalism, we note that $n_i = 1$ would describe a single vacancy, i.e., a small hole. Thus, as a first approximation, different defect geometries, from cracks to circular holes, e.g., elliptical holes, could in principle be treated by Eq. 8; we have to interpret n_i as the ratio between the transversal and longitudinal (parallel to the load) defect sizes ($n_i = a_i/b_i$). Introducing the i-th defect eccentricity e_i as the ratio between the lengths of the longer and shorter axes, as a first approximation $n_i\left(\beta_i\right) \approx e_i \cos^2 \beta_i + 1/e_i \sin^2 \beta_i$, where β_i is the defect orientation. For a single defect typology $\frac{E}{E^{(theo)}} \approx 1 - \xi v n$, in contrast to the common assumption $\frac{E}{E^{(theo)}} \approx 1 - v$, rigorously valid only for the cable density, for which $\frac{\rho_C}{\rho_C^{(theo)}} \equiv 1 - v$. Note that the failure strain for a defective nanotube or nanotube bundle can also be predicted, by $\varepsilon_{N,C}/\varepsilon_{N,C}^{(theo)} = \left(\sigma_{N,C}/\sigma_{N,C}^{(theo)}\right) / \left(E/E^{(theo)}\right)$.

In contrast to what happens for the strength, large defectiveness is required to have a considerable elastic degradation, even if we have shown that sharp transversal defects could have a role. For example, too soft space elevator cables would become dynamically unstable [29].

Atomistic Simulations

Let us study the influence on the strength of nano-cracks and circular nano-holes. n atomic adjacent vacancies perpendicular to the load, correspond to a blunt nano-crack of length $2a \approx nq$ and thickness $2b \approx q$ (or $2a \approx nq$ with a radius at tips of $b^2/a \approx q/2$). Similarly, nano-holes of size m can be considered: the index $m = 1$ corresponds to the removal of an entire hexagonal ring, $m = 2$ to the additional removal of the six hexagons around the former one (i.e. the adjacent perimeter of 18 atoms), $m = 3$ to the additional removal of the neighbouring 12 hexagonal rings (next adjacent perimeter), and so on (thus $a = b \approx q(2m-1)/\sqrt{3}$). Quantum mechanics (QM), semi-empirical (PM3 method), Molecular Mechanics (MM; with a modified Tersoff-Brenner potential of second generation (MTB-G2) or a modified Morse potential (M)) and coupled QM/MM calculations [30–33] are reported and extensively compared in Table 1 with the QFM non-asymptotic predictions of Eq. 2 (differently from the asymptotic comparison reported in [3, 12]). The comparison shows a relevant agreement, confirming and demonstrating that just a few vacancies can dramatically reduce the strength of a single nanotube, or of a nanotube bundle as described by Eq. 3 that predicts for $f \approx 1$, $\sigma_C/\sigma_C^{(theo)} \approx \sigma_N/\sigma_N^{(theo)}$. Assuming large holes ($m \to \infty$) and applying QFM to a defective bundle ($f \approx 1$), we predict $1 - \sigma_C/\sigma_C^{(theo)} \approx 1 - \sigma_N/\sigma_N^{(theo)} \approx 67\%$; but nano-cracks surely would be even

more critical, especially if interacting with each other or with the boundary. Thus, the expectation for the megacable of a strength larger than ~33 GPa is unrealistic.

Note that an elastic ($\kappa \approx 1$) nearly perfectly plastic ($\kappa \approx 0$) behaviour, with a flow stress at ~30–35 GPa for strains larger than ~3–5%, has been recently observed in tensile tests of carbon nanotubes [34], globally suggesting $\kappa \approx 0.6 - 0.7$; similarly, numerically computed stress-strain curves [35] reveal for an armchair (5, 5) carbon nanotube $\kappa \approx 0.8$, whereas for a zig-zag (9, 0) nanotube $\kappa \approx 0.7$, suggesting that the plastic correction reported in Sect. 'Elastic-Plasticity, Fractal Cracks and Finite Domains' could have a role.

Regarding elasticity, we note that Eq. 8 can be viewed as a generalization of the approach proposed in [36], being able to quantify the constants k_i fitted by atomistic simulations for three different types of defect [28]. In particular, rearranging Eq. 8 and in the limit of three small cracks, we deduce $\frac{E_{th}}{E} \approx 1 + k_1 c_1 + k_2 c_2 + k_3 c_3$, identical to their law (their Eq. 15), in which $c_i = Q_i/L$ is the linear defect concentration in a nanotube of length L and radius R and $k_i = \frac{\xi c_i n_i^2 q^2}{\pi^2 R}$. These authors consider 1, 2 and 3 atoms missing, with and without reconstructed bonds; for non-reconstructed bonds two alternative defect orientations were investigated for 2 and 3 atoms missing. Even if their defect geometries are much more complex than the nanocracks that we here consider, the comparison between our approach and their atomistic simulations, which does not involve best-fit parameters, shows a good agreement [28].

Nanotensile Tests

The discussed tremendous defect sensitivity, described by Eq. 2, is confirmed by a statistical analysis based on Nanoscale Weibull Statistics [16] applied to the nanotensile tests. According to this treatment, the probability of failure P for a nearly defect-free nanotube under a tensile stress σ_N is independent from its volume (or surface), in contrast to classical Weibull Statistics [37], namely:

$$P = 1 - \exp -N_N \left(\frac{\sigma_N}{\sigma_0}\right)^w \tag{9}$$

where w is the nanoscale Weibull modulus, σ_0 is the nominal failure stress (i.e. corresponding to a probability of failure of 63%) and $N_N \equiv 1$. In classical Weibull statistics $N_N \equiv V/V_0$ for volume dominating defects (or $N_N = A/A_0$ for surface dominating defects), i.e., N_N is the ratio between the volume (or surface) of the structure and a reference volume (or surface). The experimental data on carbon nanotubes [7, 8] were treated [16] according to nanoscale and classical Weibull statistics: the coefficients of correlation were found to be much higher for the nanoscale statistics than for the classical one (0.93 against 0.67, $w \approx 2.7$ and $\sigma_0 \approx 31 - 34$ GPa). The data set on MWCNT tensile experiments [38] has also been statistically treated [3]. The very large highest measured strengths denotes interactions between the external and internal walls, as pointed out by the same authors [38] and recently quantified [14]. Thus, the measured strengths cannot be

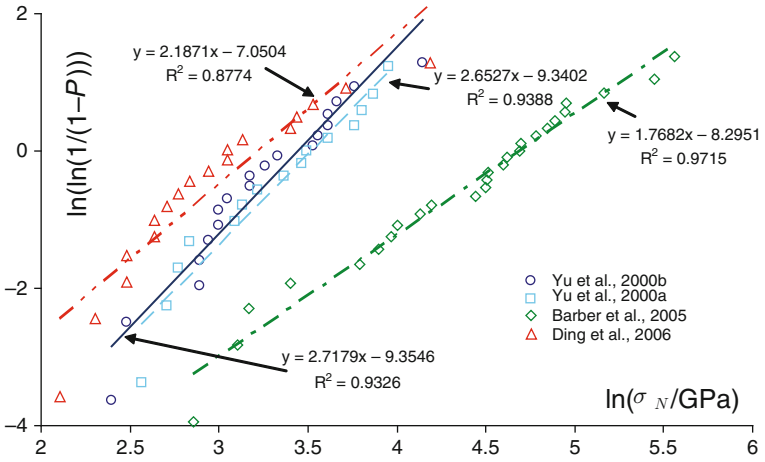

Fig. 3 Nanoscale Weibull Statistics, straight lines, applied to the new nanotensile experiments on carbon nanotubes [4]

considered plausible for describing the strength of a SWCNT. Such experiments were best-fitted with $\sigma_0 \approx 108$ GPa (but not significant for the strength of a single nanotube) and $w \approx 1.8$ (coefficient of correlation 0.94). In Fig. 3, the new data set [39] is treated [4] by applying NWS ($N_N \equiv 1$, $w \approx 2.2$, $\sigma_0 \approx 25$ GPa) and compared with the other nanoscale statistics [3, 4] deduced from the other data sets [7, 8, 38]. Note that volume- or surface-based Weibull statistics are identical in treating the external wall of the tested nanotubes, just an atomic layer thick. We have found a poor coefficient of correlation also treating this new data set with classical Weibull statistics, namely 0.51 (against 0.88 for NWS, see Fig. 3).

All these experimental data [7, 8, 38, 39] are treated in Table 2, by applying QFM in the form of Eq. 2: non-linear multiple solutions for identifying the defects corresponding to the measured strength clearly emerge; however these are quantifiable, showing that a small defect is sufficient to rationalize the majority of the observed strong strength reductions.

Finally, the new experimental results [38] are differently treated in Table 3, with respect to both strength and elasticity, assuming the presence of transversal nanocracks. The ideal strength is assumed to be of 100 GPa and the theoretical Young's modulus of 1 TPa; by Eq. 2 the crack length n is calculated and introduced in Eq. 8 to derive the related vacancy fraction v ($\xi = \pi/2$).

Thermodynamic Limit

Defects are thermodynamically unavoidable, especially at the megascale. At the thermal equilibrium the vacancy fraction $f = n/N << 1$ (n is the number of vacancies and N is the total number of atoms) is estimated as [40]:

$$f \approx e^{-E_1/k_B T_a} \tag{10}$$

Table 2 Experiments vs. QFM predictions; strength reduction $\sigma_N\,(a,b)/\sigma_N^{(theo)}$ derived according to Eq. 2 [4]

$\sigma_N/\sigma_N^{(theo)}$ $2b/q$ $2a/q$	0	1	2	3	4	5	6	7	8	9	10	∞
0	1.00*	1.00*	1.00*	1.00*	1.00*	1.00*	1.00*	1.00*	1.00*	1.00*	1.00*	1.00
1	0.71*	0.75	0.79	0.82	0.85	0.87*	0.88*	0.90	0.91	0.91	0.92	1.00
2	0.58	0.60*	0.64*	0.68	0.71*	0.73	0.76	0.78*	0.79	0.81	0.82	1.00
3	0.50	**0.52**	0.54*	0.58	0.61	0.64*	0.66*	0.68	0.70*	0.72	0.74	1.00
4	**0.45**	0.46	**0.48**	0.51*	0.54*	0.56	0.59	0.61	*0.63*	0.65	0.67	1.00
5	0.41	0.42	0.44*	0.46	**0.48**	0.51*	0.53*	0.55*	0.58	0.59	0.61	1.00
6	0.38	0.38	0.40	0.42	0.44*	0.47	0.49*	0.51*	0.53*	0.55*	0.57	1.00
7	*0.35*	0.36	***0.37***	*0.39*	0.41	***0.43***	**0.45**	0.47	0.49*	0.51*	0.53*	1.00
8	**0.33**	*0.34*	*0.35*	***0.37***	0.38	0.40	0.42	0.44*	0.46	**0.48**	0.49*	1.00
9	**0.32**	**0.32**	**0.33**	*0.34*	0.36	0.38	0.40	0.41	***0.43***	**0.45**	0.46	1.00
10	0.30*	0.30*	0.31	**0.33**	*0.34*	0.36	***0.37***	*0.39*	0.41	0.42	0.44*	1.00
11	**0.29**	**0.29**	0.30*	0.31	**0.32**	*0.34*	*0.35*	***0.37***	*0.39*	0.40	0.42	1.00
12	*0.28*	*0.28*	**0.29**	0.30*	0.31	**0.32**	*0.34*	*0.35*	***0.37***	0.38	0.40	1.00
13	0.27	0.27	*0.28*	**0.29**	0.30*	0.31	**0.32**	*0.34*	*0.35*	0.36	0.38	1.00
14	*0.26*	*0.26*	0.27	0.27	**0.29**	0.30*	0.31	**0.32**	*0.34*	*0.35*	0.36	1.00
15	**0.25**	**0.25**	*0.26*	0.27	0.27	**0.29**	0.30*	0.31	**0.32**	*0.34*	*0.35*	1.00
16	*0.24**	*0.24**	**0.25**	*0.26*	0.27	*0.28*	**0.29**	0.30*	0.31	0.32	**0.33**	1.00
17	*0.24**	*0.24**	*0.24**	**0.25**	*0.26*	0.27	*0.28*	**0.29**	0.30*	0.31	**0.32**	1.00
18	**0.23**	**0.23**	*0.24**	*0.24**	**0.25**	*0.26*	0.27	*0.28*	**0.29**	0.30*	0.31	1.00
19	**0.22***	**0.22***	**0.23**	**0.23**	*0.24**	**0.25**	*0.26*	0.27	*0.28*	**0.29**	0.30*	1.00
20	**0.22***	**0.22***	**0.22***	**0.23**	*0.24**	*0.24**	**0.25**	*0.26*	0.27	*0.28*	**0.29**	1.00
21	*0.21*	*0.21*	**0.22***	**0.22***	**0.23**	*0.24**	**0.25**	**0.25**	*0.26*	0.27	*0.28*	1.00
22	*0.21*	*0.21*	*0.21*	**0.22***	**0.22***	**0.23**	*0.24**	**0.25**	*0.26*	0.27	*0.28*	1.00
23	*0.20*	*0.21*	*0.21*	*0.21*	**0.22***	**0.23**	**0.23**	*0.24**	**0.25**	*0.26*	0.27	1.00
24	*0.20*	*0.20*	*0.20*	*0.21*	*0.21*	**0.22***	**0.23**	*0.24**	*0.24**	**0.25**	*0.26*	1.00
25	*0.20*	*0.20*	*0.20*	*0.20*	*0.21*	**0.22***	**0.22***	**0.23**	*0.24**	**0.25**	*0.26*	1.00
26	*0.19*	*0.19*	*0.20*	*0.20*	*0.20*	*0.21*	**0.22***	**0.22***	**0.23**	*0.24**	**0.25**	1.00
27	*0.19*	*0.19*	*0.19*	*0.20*	*0.20*	*0.21*	*0.21*	**0.22***	**0.23**	*0.24**	*0.24**	1.00
28	*0.19*	*0.19*	*0.19*	*0.19*	*0.20*	*0.20*	*0.21*	**0.22***	**0.22***	**0.23**	*0.24**	1.00
29	*0.18*	*0.18*	*0.19*	*0.19*	*0.19*	*0.20*	*0.20*	*0.21*	**0.22***	**0.23**	**0.23**	1.00
30	*0.18*	*0.18*	*0.18*	*0.19*	*0.19*	*0.19*	*0.20*	*0.21*	*0.21*	**0.22***	**0.23**	1.00
31	*0.18*	*0.18*	*0.18*	*0.18*	*0.19*	*0.19*	*0.20*	*0.20*	*0.21*	**0.22***	**0.22***	1.00
32	**0.17***	**0.17***	*0.18*	*0.18*	*0.18*	*0.19*	*0.19*	*0.20*	*0.21*	*0.21*	**0.22***	1.00
33	**0.17***	**0.17***	**0.17***	*0.18*	*0.18*	*0.19*	*0.19*	*0.20*	*0.20*	*0.21*	*0.21*	1.00
34	**0.17***	**0.17***	**0.17***	**0.17***	*0.18*	*0.18*	*0.19*	*0.19*	*0.20*	*0.20*	*0.21*	1.00
35	**0.17***	**0.17***	**0.17***	**0.17***	**0.17***	*0.18*	*0.18*	*0.19*	*0.19*	*0.20*	*0.21*	1.00
36	**0.16**	**0.16**	**0.17***	**0.17***	**0.17***	*0.18*	*0.18*	*0.19*	*0.19*	*0.20*	*0.20*	1.00
37	**0.16**	**0.16**	**0.16**	**0.17***	**0.17***	**0.17***	*0.18*	*0.18*	*0.19*	*0.19*	*0.20*	1.00
38	**0.16**	**0.16**	**0.16**	**0.16**	**0.17***	**0.17***	*0.18*	*0.18*	*0.19*	*0.19*	*0.20*	1.00
39	**0.16**	**0.16**	**0.16**	**0.16**	**0.17***	**0.17***	**0.17***	*0.18*	*0.18*	*0.19*	*0.19*	1.00
40	**0.16**	**0.16**	**0.16**	**0.16**	**0.16**	**0.17***	**0.17***	*0.18*	*0.18*	*0.19*	*0.19*	1.00
41	**0.15**	**0.15**	**0.16**	**0.16**	**0.16**	**0.16**	**0.17***	**0.17***	*0.18*	*0.18*	*0.19*	1.00
42	**0.15**	**0.15**	**0.15**	**0.16**	**0.16**	**0.16**	**0.17***	**0.17***	*0.18*	*0.18*	*0.19*	1.00
43	**0.15**	**0.15**	**0.15**	**0.15**	**0.16**	**0.16**	**0.16**	**0.17***	**0.17***	*0.18*	*0.18*	1.00
44	**0.15**	**0.15**	**0.15**	**0.15**	**0.16**	**0.16**	**0.16**	**0.17***	**0.17***	*0.18*	*0.18*	1.00
45	**0.15**	**0.15**	**0.15**	**0.15**	**0.15**	**0.16**	**0.16**	**0.16**	**0.17***	**0.17***	*0.18*	1.00
46	**0.15**	**0.15**	**0.15**	**0.15**	**0.15**	**0.15**	**0.16**	**0.16**	**0.17***	**0.17***	*0.18*	1.00
47	0.14	0.14	**0.15**	**0.15**	**0.15**	**0.15**	**0.16**	**0.16**	**0.16**	**0.17***	**0.17***	1.00

Table 2 (continued)

$\sigma_N/\sigma_N^{(theo)}$ $2b/q$ $2a/q$	0	1	2	3	4	5	6	7	8	9	10	∞
48	0.14	0.14	0.14	**0.15**	**0.15**	**0.15**	**0.15**	**0.16**	**0.16**	**0.17***	**0.17***	1.00
49	0.14	0.14	0.14	0.14	**0.15**	**0.15**	**0.15**	**0.16**	**0.16**	**0.16**	**0.17***	1.00
50	0.14	0.14	0.14	0.14	**0.15**	**0.15**	**0.15**	**0.15**	**0.16**	**0.16**	**0.17***	1.00
∞	0.00	0.00	0.00	0.00	0.00	0.00	0.00	0.00	0.00	0.00	0.00	$(1+2a/b)^{-1}$

In **bold** type are represented the 15 different nanostrengths measured on single walled carbon nanotubes in bundle [7]; whereas in *italic* we report the 19 nanostrengths measured on multi walled carbon nanotubes [8], and in underlined type the most recent 18 observations [34]. All the data are reported with the exception of the five smallest values of 0.08, 0.10 [34], 0.11 [8], 0.12 [8, 34] and 0.13 [7], for which we would need for example adjacent vacancies ($2b/q$~1) in number $n = 2a/q =$ 138–176, 90–109, 75–89, 64–74 and 55–63 respectively. The 26 strengths measured in [38] are also treated (asterisks), simply assuming two interacting walls for $100 < \sigma_N^{(exp)} \leq 200$ gigapascals (thus $\sigma_N = \sigma_N^{(exp)}/2$) or 3 interacting walls for $200 < \sigma_N^{(exp)} \leq 300$ gigapascals ($\sigma_N = \sigma_N^{(exp)}/3$). All the experiments are referred to $\sigma_N^{(theo)} = 100$GPa (q~0.25 nm). If all the nanotubes in the cable contain identical holes, $\sigma_C/\sigma_C^{(theo)} = \sigma_N/\sigma_N^{(theo)}$

where $E_1 \approx 7$ eV is the energy required to remove one carbon atom and T_a is the absolute temperature at which the carbon is assembled, typically in the range between 2,000 and 4,000 K. Thus, $f \approx 2.4 \times 10^{-18} - 1.6 \times 10^{-9}$. For the megacable, having a carbon weigh of ~5,000 kg, the total number of atoms is $N \approx 2.5 \times 10^{29}$ thus a huge number of equilibrium defects, in the range $n \approx 0.6 \times 10^{12} - 3.9 \times 10^{20}$ is expected, in agreement with a recent discussion [41] and observations [42].

The strength of the cable will be dictated by the largest transversal crack on it, according to the weakest link concept. The probability of finding a nanocrack of size m in a bundle with vacancy fraction f is $P(m) = (1-f)f^m$, and thus the number M of such nanocracks in a bundle composed by N atoms is $M(m) = P(m)N$[27]. The size of the largest nanocrack, which typically occurs once, is found from the solution to the equation $M(m) \approx 1$, which implies [43]:

$$m \approx -\ln\left[(1-f)N\right]/\ln f \approx -\ln N/\ln f \tag{11}$$

Accordingly, we deduce a size $m \approx 2-4$ for the largest thermodynamically unavoidable defect in the megacable. Inserting Eqs. 11 and 10 into Eq. 2 evaluated for a transversal crack ($b \approx 0$ and $2a/q \approx m$), we deduce the statistical counterpart of Eq. 2 and thus the following thermodynamical maximum achievable strength:

$$\frac{\sigma_N(N)}{\sigma_N^{(theo)}} \leq \frac{\sigma_N^{(\max)}(N)}{\sigma_N^{(theo)}} = \frac{1}{\sqrt{1 + \frac{k_B T_a}{E_1}\ln N}} \tag{12}$$

Then, inserting Eq. 12 into Eqs. 3 and 4, the maximum cable strength and minimum taper-ratio can be statistically deduced. The corresponding maximum achievable

Table 3 The new results [34] are here treated with respect to both strength and elasticity, assuming the presence of transversal nanocracks composed by n adjacent vacancies [4]

MWCNT number and fracture typology	Strength (GPa)	Young's modulus (GPa)	κ	n	V (%)
1 (multiple load A)	8.2	1,100	1.01	148	0.07
2 (clamp failed)	10	840	0.98	100	0.23
3	12	680	1.00	69	0.44
4 (failure at the clamp)	12	730	0.98	69	0.40
5 (multiple load B)	14	1,150	1.02	51	0.14
6 (multiple load a)	14	650	0.97	51	0.62
7	15	1,200	1.05	44	0.11
8	16	1,200	1.02	39	0.13
9	17	960	1.00	34	0.49
10	19	890	0.97	27	0.74
11 (multiple load b)	21	620	0.99	22	1.51
12 (multiple load I)	21	1,200	0.99	22	0.22
13 (multiple load II)	23	1,250	0.99	18	0.17
14	30	870	1.00	11	1.92
15 (plasticity observed)	31	1,200	0.59 (0.99)	10	0.49
16 (plasticity observed)	34	680	0.69 (1.02)	8	3.80
17 (multiple load III)	41	1,230	1.03	5	0.69
18 (failure at the clamp)	66	1,100	0.98	2	4.90

The constitutive parameter κ has been estimated as $\kappa \approx \ln(\varepsilon_N)/\ln(\sigma_N/E)$ for all the tests: note the low values for the two nanotubes that revealed plasticity (in brackets the values calculated up to the incipient plastic flow are also reported). The ideal strength is assumed to be of 100GPa and the theoretical Young's modulus of 1,300 GPa; by Eq. 2 the crack length n is calculated and introduced in Eq. 8 to derive the related vacancy fraction v ($\xi = \pi/2$)

Fracture in two cases was observed at the clamp; in one case the clamp itself failed, thus the deduced strength represents a lower bound of the nanotube strength. Three nanotubes were multiple loaded (in two a,b and A,B or in three I,II,III steps), i.e., after the breaking in two pieces of a nanotube, one of the two pieces was again tested and fractured at a higher stress. Two nanotubes displayed a plastic flow

A vacancy fraction of the order of few ‰ is estimated, suggesting that such nanotubes are much more defective than as imposed by the thermodynamic equilibrium, even if the defects are small and isolated. However, note that other interpretations are still possible, e.g., assuming the nanotube is coated by an oxide layer and rationalizing the ratio between the observed Young's modulus and its theoretical value as the volumetric fraction (for softer coating layers) of carbon in the composite structure

strength, a unavoidable limit (at least at the thermodynamic equilibrium), is ∼45 GPa and the corresponding flaw-tolerant taper-ratio is ∼4.6. But the larger taper-ratio implies a large cable mass and thus a large number N of atoms. Updating N in our statistical calculation yields the same, thus self-consistent, predictions. Statistically we expect and even smaller strength, as previously discussed.

Conclusions

The strength of a real, thus defective, carbon nanotube macroscopic cable is expected to be strongly reduced with respect to the theoretical strength of a carbon nanotube. Accordingly, in this chapter key simple formulas for the design of nanotube bundles (e.g. the space elevator megacable) have been reported.

References

1. Y.V. Artsutanov, Kosmos na Elektrovoze, Komsomol-skaya Pravda, July 31 (1960); contents described in Lvov, V. Science **158**, 946–947 (1967)
2. J. Pearson, The orbital tower: a spacecraft launcher using the Earth's rotational energy. Acta Astronaut. **2**, 785–799 (1975)
3. N. Pugno, On the strength of the nanotube-based space elevator cable: from nanomechanics to megamechanics. J. Phys. Condens. Matter **18**, S1971–S1990 (2006)
4. N. Pugno, The role of defects in the design of the space elevator cable: from nanotube to megatube. Acta Mater. **55**, 5269–5279 (2007)
5. N. Pugno, Space elevator: out of order? Nano Today **2**, 44–47 (2007)
6. S. Iijima, Helical microtubules of graphitic carbon. Nature **354**, 56–58 (1991)
7. M.F. Yu, B.S. Files, S. Arepalli, R. Ruoff, Tensile loading of ropes of single wall carbon nanotubes and their mechanical properties. Phys. Rev. Lett. **84**, 5552–5555 (2000)
8. M.F. Yu, O. Lourie, M.J. Dyer, K. Moloni, T.F. Kelly, R. Ruoff, Strength and breaking mechanism of multiwalled carbon nanotubes under tensile load. Science **287**, 637–640 (2000)
9. B.C. Edwards, Design and deployment of a space elevator. Acta Astronaut. **10**, 735–744 (2000)
10. B.C. Edwards, E.A. Westling, *The Space Elevator: A Revolutionary Earth-to-Space Transportation System* (Spageo Inc., San Francisco, CA, 2003)
11. N. Pugno, A quantized Griffith's criterion, Fracture Nanomechanics, Meeting of the Italian Group of Fracture, Vigevano, Italy, 25–26 Sept 2002
12. N. Pugno, R. Ruoff, Quantized fracture mechanics. Phil. Mag. **84**, 2829–2845 (2004)
13. N. Pugno, Dynamic quantized fracture mechanics. Int. J. Fract. **140**, 158–168 (2006)
14. N. Pugno, New quantized failure criteria: application to nanotubes and nanowires. Int. J. Fract. **141**, 311–328 (2006)
15. N. Pugno, F. Bosia, A. Carpinteri, Multiscale stochastic simulations as in-silico tensile testing of nanotube-based megacables. Small **4**, 1044–1052 (2008)
16. N. Pugno, R. Ruoff, Nanoscale Weibull statistics. J. Appl. Phys. **99**, 1–4 (2006)
17. A. Carpinteri, Scaling laws and renormalization groups for strength and toughness of disordered materials. Int. J. Solid Struct. **31**, 291–302 (1994)
18. A. Carpinteri, N. Pugno, Are the scaling laws on strength of solids related to mechanics or to geometry? Nat. Mater. **4**, 421–423, (2005)
19. N. Pugno, A general shape/size-effect law for nanoindentation. Acta Mater. **55**, 1947–1953 (2007)
20. M. Ippolito, A. Mattoni, L. Colombo, N. Pugno, The role of lattice discreteness on brittle fracture: how to reconcile atomistic simulations to continuum mechanics. Phys. Rev. B **73**, 104111–1/6 (2006)
21. D. Taylor, P. Cornetti, N. Pugno, The fracture mechanics of finite crack extensions. Eng. Fract. Mech. **72**, 1021–1028 (2005)
22. N. Pugno, M. Ciavarella, P. Cornetti, A. Carpinteri, A unified law for fatigue crack growth. J. Mech. Phys. Solid. **54**, 1333–1349 (2006)
23. N. Pugno, P. Cornetti, A. Carpinteri, New unified laws in fatigue: from the Wöhler's to the Paris' regime. Eng. Fract. Mech. **74**, 595–601 (2007)

24. J.R. Rice, G.F. Rosengren, Plane strain deformation near a crack tip in a power-law hardening material. J. Mech. Phys. Solid. **16**, 1–12 (1968)
25. A. Carpinteri, N. Pugno, Fracture instability and limit strength condition in structures with re-entrant corners. Eng. Fract. Mech. **72**, 1254–1267 (2005)
26. A. Carpinteri, B. Chiaia, Crack-resistance behavior as a consequence of self-similar fracture topologies. Int. J. Fract. **76**, 327–340 (1996)
27. Q.Z. Wang, Simple formulae for the stress-concentration factor for two- and three-dimensional holes in finite domains. J. Strain Anal. **73**, 259–264 (2002)
28. N. Pugno, Young's modulus reduction of defective nanotubes. Appl. Phys. Lett. **90**, 043106 (2007)
29. N. Pugno, H. Troger, A. Steindl, M. Schwarzbart, On the stability of the track of the space elevator. Proceedings of the 57th international astronautical congress, Valencia, Spain, 2–6 October 2007
30. S.L. Mielke, D. Troya, S. Zhang, J.-L. Li, S. Xiao, R. Car, R.S. Ruoff, G.C. Schatz, T. Belytschko, The role of vacancy defects and holes in the fracture of carbon nanotubes. Chem. Phys. Lett. **390**, 413–420 (2004)
31. T. Belytschko, S.P. Xiao, R. Ruoff, Effects of defects on the strength of nanotubes: experimental-computational comparisons, Los Alamos National Laboratory, Preprint Archive, Physics, arXiv:physics/0205090 (2002)
32. S. Zhang, S.L. Mielke, R. Khare, D. Troya, R.S. Ruoff, G.C. Schatz, T. Mechanics of defects in carbon nanotubes: atomistic and multiscale simulations. Phys. Rev. B **71**, 115403 1–12 (2005)
33. R. Khare, S.L. Mielke, J.T. Paci, S. Zhang, R. Ballarini, G.C. Schatz, T. Belytschko, Coupled quantum mechanical/molecular mechanical modelling of the fracture of defective carbon nanotubes and grapheme sheets. Phys. Rev. B **75**, 075412 (2007)
34. W. Ding, L. Calabri, K.M. Kohlhaas, X. Chen, D.A. Dikin, R.S. Ruoff, Modulus, fracture strength, and britlle vs. plastic response of the outer shell of arc-grown multiwalled carbon nanotubes. Exp. Mech. **47**, 25–36 (2006)
35. M. Meo, M. Rossi, Tensile failure prediction of single wall carbon nanotube. Eng. Fract. Mech. **73**, 2589–2599 (2006)
36. M. Sammalkorpi, A. Krasheninnikov, A. Kuronen, K. Nordlund, K. Kaski, Mechanical properties of carbon nanotubes with vacancies and related defects. Phys. Rev. B **70**, 245416–1/8 (2004)
37. W. Weibull, *A Statistical Theory of the Strength of Materials* (Ingeniörsvetenskapsakademiens, Handlingar, 1939), p. 151
38. A.H. Barber, I. Kaplan-Ashiri, S.R. Cohen, R. Tenne, H.D. Wagner, Stochastic strength of nanotubes: an appraisal of available data. Compos. Sci. Tech. **65**, 2380–2386 (2005)
39. I. Kaplan-Ashiri, S.R. Cohen, K. Gartsman, V. Ivanovskaya, T. Heine, G. Seifert, I. Wiesel, H.D. Wagner, R. Tenne, On the mechanical behavior of WS2 nanotubes under axial tension and compression. Proc. Natl. Acad. Sci. U.S.A. **103**, 523–528 (2006)
40. C. Kittel, *Introduction to Solid State Physics* (John Wiley & Sons, New York, 1966)
41. H.K.D.H. Bhadeshia, 52nd Hatfield Memorial Lecture – Large chunks of very strong steel. Mater. Sci. Tech. **21**, 1293–1302 (2005)
42. Y. Fan, B.R. Goldsmith, P.G. Collins, Identifying and counting point defects in carbon nanotubes. Nat. Mater. **4**, 906–911 (2005)
43. P.D. Beale, D.J. Srolovitz, Elastic fracture in random materials. Phys. Rev. B **37**, 5500–5507 (1988)

Physics of Carbon Nanostructures

Stefano Bellucci and Alexander Malesevic

Abstract We consider the multidisciplinary topic of the physics of carbon nanostructures, limiting ourselves to examining in some detail only graphitic allotropes, Our main aim is to illustrate the impact of carbon nanostructures on certain research and application areas. We provide, firstly, an historical overview, moving then to discussing the structure of graphene and carbon nanotubes. We place a special emphasis on the description of various techniques used to deposit carbon nanotubes and graphene, and then enter the study of the physical properties of the latter systems. We end our treatment with a general overview of the broad range of applications graphene and carbon nanotubes are finding.

Abbreviations

AFM	Atomic force microscopy
ARXPS	Angle resolved X-ray photoelectron spectroscopy
C_2H_2	Acetylene
CCD	charge-coupled device
CCNT	Coiled carbon nanotubes
CH_4	Methane
CNF	Carbon nanofibre
CNT	Carbon nanotube
CNW	Carbon nanowall
CVD	Chemical vapor deposition
DC	Direct current
DWCNT	Double-wall carbon nanotube
FET	Field-effect transistor
FLG	Few layer graphene
FN	Fowler-Nordheim

S. Bellucci (✉)
INFN, Laboratori Nazionali di Frascati, P.O. Box 13, 00044 Frascati, Italy
e-mail: stefano.bellucci@lnf.infn.it

S. Bellucci (ed.), *Physical Properties of Ceramic and Carbon Nanoscale Structures*,
Lecture Notes in Nanoscale Science and Technology 11,
DOI 10.1007/978-3-642-15778-3_5,

H_2	Hydrogen
LEED	Low energy electron diffraction
MBE	Molecular beam epitaxy
MW	Microwave
MWCNT	Multi-wall carbon nanotube
PECVD	Plasma enhanced chemical vapor depostion
QED	Quantum electrodynamics
RF	Radio frequency
SEM	Scanning electron microscopy
SPM	Scanning probe microscopy
SiC	Silicon carbide
SiO_2	Silicon oxide
STM	Scanning tunnelling microscopy
SWCNT	Single-wall carbon nanotube
SW	Stone-Wales
TEM	Transmission electron microscope
XPS	X-ray photoelectron spectroscopy
XRD	X-ray diffraction

Introduction

It is practically impossible to grasp the entire scope of carbon nanostructure physics, considering the multidisciplinary character of this widely studied subject. Focusing on graphitic allotropes, this chapter tries to give a flavor of the widespread implications carbon nanostructures have on research and applications. It will start with an historical overview, followed by a discussion of the structure of CNTs and graphene. Next, several different synthesis techniques for carbon nanotubes and graphene are explored, followed by a study of their physical properties. A summary of the broad range of applications concludes this chapter.

Historical Overview

In the scientific community, impact is not only dependent on the talent of the researcher, but also on the choice of journal and the maturity of the community. This last parameter results from a combination of available investigation tools, theories and scientific open-mindedness and explains why certain discoveries are not always accredited to the correct persons. This is certainly the case for the history of CNTs and graphene, two carbon nanostructures that are among the hottest and most exciting physics topics in decades [1].

Dimensionality is the most important parameter to distinguish between different carbon nanostructures, since it not only affects the morphology but also the physical properties. For carbon nanostructures and according to popular belief, quasi zero-, one- and two-dimensional crystal structures were subsequently discovered.

Because probing the nano-world assumes the availability of appropriate tools, it is quite delicate to discuss the discovery of carbon nanostructures before 1939, when Siemens introduced the first commercial transmission electron microscope (TEM). But worth mentioning in this context is the famous blacksmith Assad Ullah, who lived in the seventeenth century and empirically optimized techniques for steel forging and annealing to produce the legendary Damascus sabers. Careful high resolution TEM analysis of these sabers led to the finding that CNTs were formed in the sophisticated thermomechanical forging process which explains the sabers' exceptional quality [2, 3].

The first TEM evidence of hollow CNTs was presented by Radushkevich and Lukyanovich in 1952 [4], even though the term CNT had not yet been postulated. This discovery was not widely acknowledged due to the combined facts that the article was written in Russian, published in a Russian journal not mentioned in global literature databases and because access to Russian journals was not straightforward considering the cold war.

The well-known history of carbon nanostructures starts in 1985 when Harry Kroto and Richard Smalley decided to investigate the mechanism of carbon chain formation in interstellar space [5]. They investigated the mass spectra of carbon species that were evaporated from a graphite target by laser ablation techniques and discovered a remarkable stable cluster consisting of 60 carbon atoms [6]. In search for a spherical geometry to visualize this structure and arrange all 60 carbon atoms to satisfy sp^2 valences, they consulted architect Buckminster Fuller's studies on the construction of geodesic domes [7]. It was concluded that the carbon atoms must be arranged in the shape of a soccer ball, consisting of 12 pentagons and 20 hexagons with a carbon atom on every vertex. This structure can be thought of as a huge quasi zero-dimensional molecule and became known as a fullerene. Harry Kroto and Richard Smalley were rewarded with the 1997 Nobel price for outstanding work in physics for their discovery.

Six years later, in the fall of 1991, Sumio Iijima's efforts to synthesize fullerenes by arc discharge evaporation techniques resulted in the discovery of quasi one-dimensional needle-like concentric crystal carbon tubules [8]. The carbon atoms in these structures were arranged in a hexagonal network, like rolled up graphite sheets. Similar to the Russian dolls, these so-called CNTs consisted of several nested tubes, hence the term multi-wall carbon nanotubes (MWCNTs). As a result of the worldwide interest in carbon nanostructures following the work of Harry Kroto and Richard Smalley, and because Sumio Iijima is a gifted writer and talented scientist and due to the high impact of a Nature article, Iijima became known as the CNT pioneer.

Two years later, the synthesis of single-wall carbon nanotubes (SWCNTs), a single atomic sheet of graphite rolled up into a cylinder, was reported simultaneously by IBM scientists Bethune et al. [9] and the NEC research group of Iijima and coworkers [10].

In the years that followed, a vast amount of papers reported on the remarkable physical properties of nanotubes which were used for the benefit of ingenious CNT based applications like e.g. innovative composites, prototype transistors and electron field emission devices. Numerous synthesis techniques emerged for the production

of tailor-made CNTs with controlled length, diameter and electrical properties on one hand and for mass production of CNTs on the other hand.

The short history of graphene, defined as a monolayer of graphite, resembles the chronological history of CNTs closely. In 1974, Blakely et al. discovered the strictly two-dimensional carbon crystal signature of graphene in Auger spectra by studying the equilibrium segregation of carbon on nickel surfaces [11–13]. Because of the little interest in carbon nanostructures at that time and because Blakely didn't manage to isolate the graphene film and therefore couldn't investigate graphene's physical properties, this discovery remained largely unknown.

In 2004, Kostya Novoselov and Andre Geim were able to peel off a single layer of graphene from a graphite crystal by using straightforward, yet elaborate exfoliation techniques [14, 15]. Supported by the global interest in carbon nanostructures and because they were able to provide detailed information about the extraordinary electrical properties of graphene, Kostya Novoselov and Andre Geim are nowadays considered the graphene pioneers.

Structural Characterization

A single atomic sheet of graphene can be considered the mother of all graphitic allotropes, since it is the elementary building block of graphite as well as CNTs and fullerenes. As illustrated in Fig. 1, graphene can be stacked to form graphite, rolled up into a CNT cylinder and wrapped up to form a fullerene.

Stacking two sheets of graphene produces graphite by definition, but the physical properties of stacks consisting of less than ten graphene sheets are significantly different from the physical properties of bulk graphite. Therefore, a different terminology is applied to distinguish few-layer graphene (FLG) stacks from bulk graphite as discussed in Sect. 'Graphene Classification'.

Rolling up a graphene sheet to form a CNT is no arbitrary process, since it determines not only the nanotube morphology but also the physical properties of the resulting CNT, as discussed in Sects. 'Nanotube Classification' and 'Physical Properties'. It is therefore appropriate to define some structural parameters to facilitate the discussion about the CNT morphology.

Atomic Structure

Graphene is defined as a two-dimensional carbon crystal with a strictly hexagonal lattice structure. But perfect two-dimensional crystals cannot exist in the free state, as first theoretically established by Peierls [17, 18] and Landau [19] more than 70 years ago. They showed that thermal fluctuations should destroy long-range order, resulting in melting of a two-dimensional lattice at finite temperature. Mermin and Wagner further confirmed these findings and extended the proof to two-dimensional crystals in general [20, 21]. Numerous experiments have validated the theoretical conclusions, presenting thermodynamical instabilities in thin films unless the films constitute a three-dimensional system [22–24].

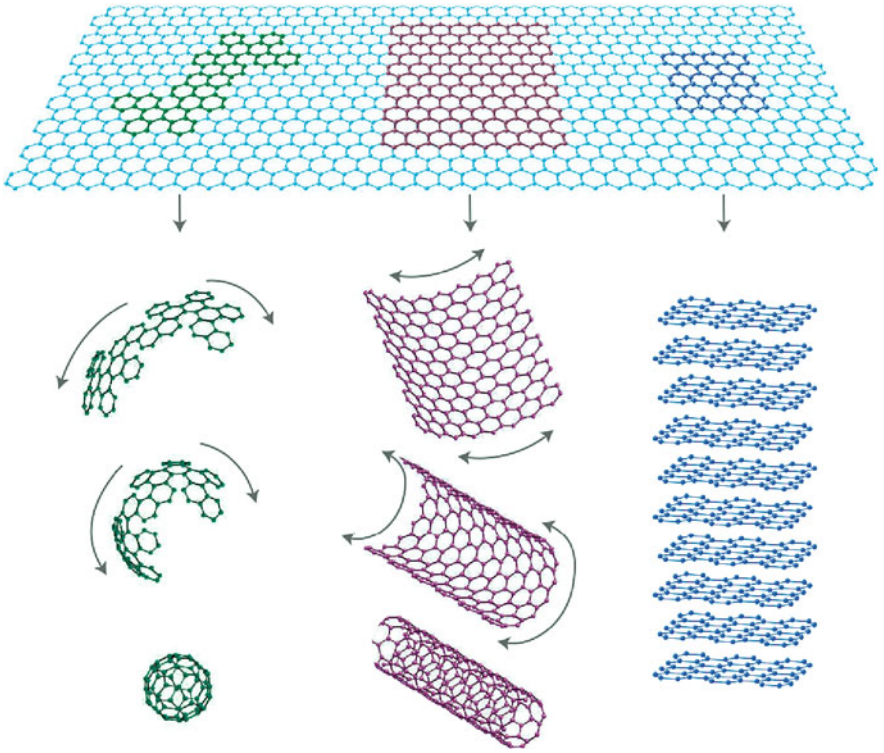

Fig. 1 Artist impression of graphene's versatile nature [16]. A sheet of graphene can be wrapped to form a fullerene (*left*), rolled up into a CNT (*middle*) and stacked to form graphite (*right*)

However, although theory forbids strictly two-dimensional crystals, it does allow structural deformations, like bending, to stabilize atomically thin graphene in the third dimension [25]. High resolution TEM and electron diffraction studies have confirmed the deformation of suspended graphene by periodic rippling of the surface [26, 27]. This intrinsic microscopic roughening results in an average out of plane curvature of 1 nm corresponding to a surface normal deviation of about 5°. Even though these are large values, they do not immediately cause plastic deformation and generation of defects [28, 29].

Because CNTs can be considered rolled-up graphene sheets, all parameters determining CNT morphology are defined in the graphene plane to facilitate further calculations.

Two unit vectors $\vec{a}_1$ and $\vec{a}_2$ are selected in the graphene plane, making an angle of 60° relative to each other, as visualized in Fig. 2. The chiral vector $\vec{C}_h$ is defined as the roll-up vector, perpendicular to the nanotube axis. If a nanotube is formed by cutting the graphene sheet depicted in Fig. 2 along OB and AB' and rolling the sheet from OB to AB', then the tip of $\vec{C}_h$ should touch its tail. The length of the chiral vector $\vec{C}_h$ corresponds to the nanotube circumference and the nanotube diameter d can be calculated from $d = \left|\vec{C}_h\right| / \pi$.

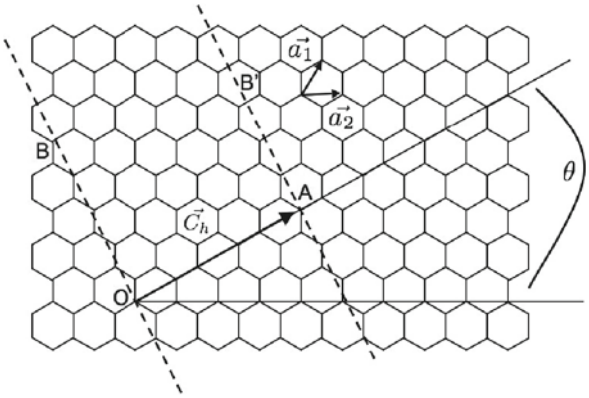

Fig. 2 Scheme of the planar CNT parameters. The unit vectors $\vec{a_1}$ and $\vec{a_2}$, chiral vector $\vec{C_h}$ and chiral angle θ are all depicted

The chiral vector $\vec{C_h}$ can be written in function of the unit vectors as

$$\vec{C_h} = n\vec{a_1} + m\vec{a_2}. \tag{1}$$

Often it is more convenient to work with the shorthand notation (n, m) instead of with $\vec{C_h}$, which alters the expression for the diameter to

$$d = \frac{\left|\vec{C_h}\right|}{\pi} = \frac{3}{\pi}\, a_{C-C}\, \sqrt{m^2 + n^2 + mn}\,, \tag{2}$$

where a_{C-C} is the interatomic distance between neighboring carbon atoms. It turns out that the complete structure and morphology of a carbon nanotube depends only on the parameters m and n.

In order to describe chirality for a CNT analogous to DNA, the chiral angle θ is defined as the angle between $\vec{C_h}$ and $\vec{a_1}$. This extra parameter is complementary to $\vec{C_h}$ and necessary for a complete description of the twist in the hexagonal structure of a nanotube. The honeycomb lattice limits the value of θ to $0 \leq \theta \leq 30$ and like the CNT diameter, θ can be expressed in function of the parameters n and m as

$$\cos\theta = \frac{\vec{C_h}.\vec{a_1}}{\left|\vec{C_h}\right| . |\vec{a_1}|} = \frac{2n + m}{2\sqrt{m^2 + n^2 + mn}}. \tag{3}$$

Graphene Classification

Graphite is the three-dimensional equivalent resulting from stacking the strictly two-dimensional crystal graphene. The definitions of graphite and graphene are solely based on structural differences and are therefore inappropriate to denote stacks of less than ten layers graphene, whose structure resembles graphite but whose physical properties correspond more to graphene than to graphite. This class of

graphitic material is therefore denoted by the term FLG. To further differentiate nano-structured graphite from bulk graphite, the term carbon nanowall or CNW indicates nano-structured graphite with physical properties that correspond closely to graphite, but whose behavior in prototype applications is similar to CNTs.

In an attempt to optimize the synthesis of CNTs by means of microwave plasma enhanced chemical vapor deposition (see Sect. 'Carbon Nanotube Synthesis Techniques'), Wu et al. discovered the formation of freestanding flakes of carbon hence denoted CNWs [30]. No TEM studies were undertaken at that time, but Raman spectroscopy analysis identified defective graphite as the structure of the as grown flakes. CNWs always grow vertically aligned to the substrate and subsequent studies showed how the orientation of the flakes could be controlled during synthesis by localized electric fields [31].

Due to the global interest in carbon nanostructures, more diverse reports on the plasma synthesis of CNWs presented qualitative structural studies demonstrating that CNWs are on the average 10–60 nm thick, 1–3 μm high and 0.5–2 μm wide [32–39]. Their large thickness clearly indicates that CNWs resemble graphite more than graphene.

CNWs are in general defective graphite nanostructures [40, 41] and detailed TEM analysis revealed that CNWs are polycrystalline flakes consisting of nanographite domains [42]. By optimizing the CNW synthesis technique, it is possible to decreases the number of defects and the flake thickness in order to transform the as grown flakes from CNWs to FLG [43–45].

Nanotube Classification

The worldwide interest in carbon nanostructures resulted in an increased electron microscopy analysis of carbon containing soot from various origin. Many interesting crystalline tubular carbon nanostructures were identified and will be discussed in this section. An overview of the rich variety of tubular carbon nanostructures is presented in Fig. 3. Because branched CNTs [46–48] are not structurally different from ordinary CNTs, they will not be discussed here.

CNTs can be roughly divided into categories according to the number of concentric tubes, ranging from a single-wall over a double-wall to multi-wall CNTs. Typical diameters vary between 1–2 nm for SWCNTs [10, 9, 49], between 2 and 5 nm for double-wall CNTs (DWCNTs) [50] and between 5 and 30 nm for MWCNTs [8, 49]. There are no limitations on the length of nanotubes and values of more than 7 mm are reported,[1] which give CNTs an incredible aspect ratio. High resolution TEM images of a SWCNT and a MWCNT are presented in Fig. 3a, b.

Every individual nanotube, whether a SWCNT or part of a MWCNT, can be categorized in function of its chirality using the parameters n and m [52]. If the hexagons are arranged in such a way that $\theta = 0°$, which implies that either n or m

[1]This data was published online by Wendy Beckman in a newsletter from the University of Cincinnati on 29 November 2006.

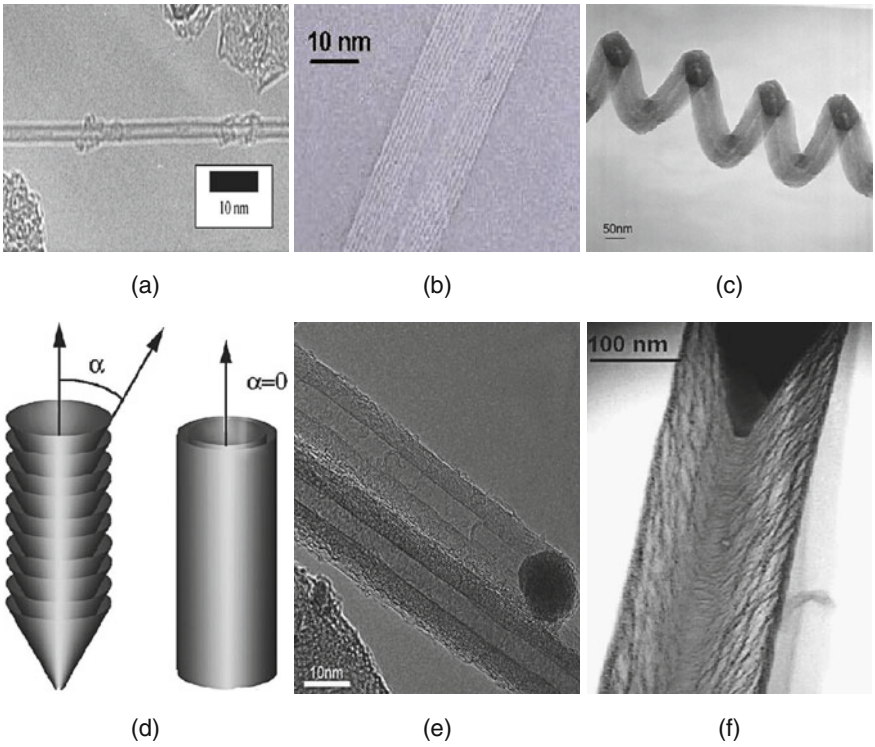

Fig. 3 High resolution TEM micrographs of different carbon nanostructure morphologies: (**a**) SWCNT, (**b**) MWCNT, (**c**) coiled CNT, (**e**) bamboo carbon nanofiber and (**f**) herringbone carbon nanofiber. In (**d**) depicts a scheme the difference between nanotubes and nanofibers: $\alpha = 0$ for CNTs and $\alpha > 0$ for CNFs [51]

are zero, the CNT is called a *zig-zag* nanotube. In the other limiting case when $\theta = 30°$, which implies that $n = m$, the CNT is an *armchair* nanotube. For all other combinations of n and m, the term *chiral nanotube* is used. The notations zigzag and armchair become clear in Fig. 4, by using some imagination.

Just one year after the report of MWCNTs by Iijima [8], the existence of a class of coiled CNTs (CCNTs) was predicted by molecular dynamics simulations [53]. Shortly after, the first experimental observations of coiled MWCNTs was reported by Amelinckx et al. [54]. A high resolution TEM micrograph of an individual CCNT is presented in Fig. 3c. Like straight CNTs, CCNTs can be of the single-wall or multi-wall type with varying diameters and without limitations on their length. Coiling a straight CNT creates pentagon-heptagon pairs in the hexagonal carbon atom arrangement and two extra parameters are necessary in order to completely describe CCNT morphology: The coil diameter and the coil pitch, which is the distance between adjacent corresponding points along the axis of the helix, similar to half the period of an electromagnetic wave [55, 56].

The origin of CNT coiling has been quite strongly debated over the last years. It was not clear whether coiling had a structural origin, thereby establishing CCNTs

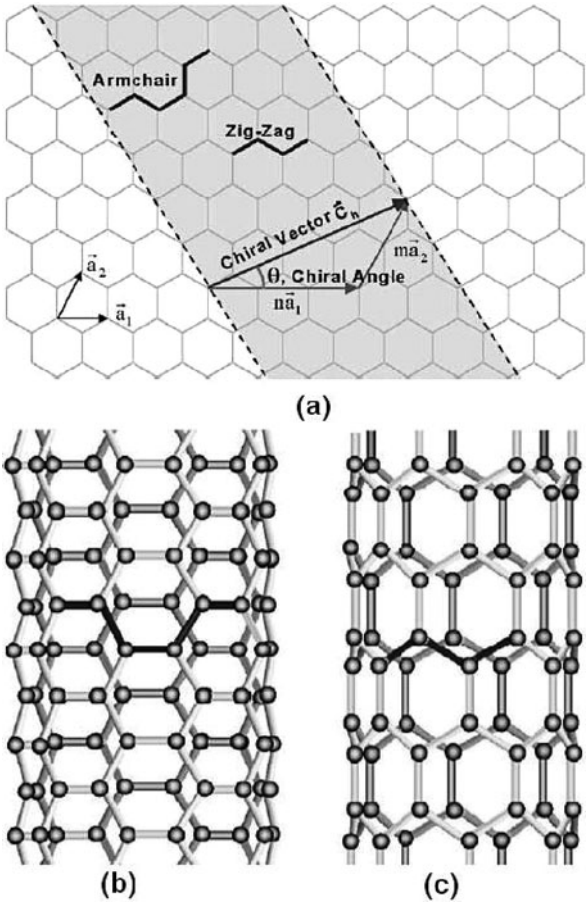

Fig. 4 Description of the classification of nanotubes (**a**). Illustrations of armchair (**b**) and zigzag nanotubes (**c**) are presented

as a different class of nanotubes, or whether coiling resulted from a faulted shape that straight CNTs adopt due to external conditions. Statistical analysis of a large number of helically coiled CNTs evidenced that the helical morphology was rather decided by intrinsic structural factors than by external parameters [57]. However, external factors may contribute in creating specific growth conditions that favor coiled instead of straight morphology.

The walls of CNTs are by definition aligned parallel to the axis of the tube, spanning the complete length of the tube, but this is no necessary requirement for all the tubular crystalline carbon nanostructures known. The term carbon nanofibers (CNFs) is used for a distinct class of MWCNTs consisting of stacked curved graphene layers that form *cones* or *cups* [51]. The stacked cone structure is often referred to as *herringbone* as its structure resembles a fish skeleton in TEM analysis, depicted in Fig. 3f. The stacked cup structure, presented in Fig. 3e, is often denoted *bamboo* for the same reason.

Contrary to CNTs, the graphene layers span only a limited region of the CNF length, are relatively short, poorly connected and are aligned under a nonzero angle

α with the CNF axis. Therefore, the mechanical and electrical properties of CNFs differ greatly from the properties of CNTs. A scheme presenting the difference between CNTs and CNFs is depicted in Fig. 3d.

Structural Defects

Often theoretical predictions and experimental observations do not quite match expectations in the field of carbon nanostructures because structural defects influence the physical properties of the nanostructures. Because CNTs and graphene are typically supported by a substrate, structural corrugations due to the underlying substrate should also be taken into account. Substrate-induced structural distortion, adsorbates and local charge disorder could be very important for transport properties of carbon nanostructures. Specifically lithography resist, commonly used in the device fabrication procedures, is observed to introduce unknown and uncontrollable perturbations of graphene structure, as investigated with scanning tunneling microscopy [58].

Besides substrate-induced structural distortion, are atmospheric species a source of structure corrugation, since it was noticed that the measured thickness of graphene was larger when measured in air when compared to vacuum [58]. The presence of ambient species like nitrogen, oxygen, argon, water or other contamination on the surface of graphene impedes quantum electron transport studies of undoped graphene devices. This problem can be resolved by a current-induced cleaning of graphene in which contamination is observed to cluster and migrate away from the graphene surface to the contact electrodes [59].

Atomic-scale structural defects in the hexagonal carbon lattice were predicted by theoretical simulations and can be induced by energetic particles like electrons and ions. These predicted stable polymorphic atomic defects include pentagon-heptagon pairs [60], mono-vacancies and multi-vacancies [61] and adatoms [62].

Pentagon-heptagon pair formation is the consequence of a $C-C$ bond rotation as indicated in Fig. 5 and denoted Stone-Wales (SW) transformation after its discoverers. In situ high resolution TEM revealed that SW transformations promote the formation of further topological defects and act as an accumulation site of topological defects. SW transformations are immobile and induce kinks in CNTs and curvature in graphene. Topological defects close to the kink structure would be more likely to move there because of the involved elastic strain in the kink region [63].

The most expected and experimentally studied point defects comprises one carbon atom vacancies, two neighboring vacancies, a pentagon-octagon-pentagon defect and a carbon adatom [64, 65].

Accumulation of structural defects causes breakdown of the hexagonal carbon lattice and this has been explored by heating CNTs in air [66], exposing them to laser irradiation [67] and to beams of energetic particles like electrons [68, 69], but also less conventional techniques like camera flashes are known to cause CNT segmentation [70].

Contrary to a general tendency to decrease nanostructure quality after exposure to severe physical conditions is a proposed technique to eliminate SW transformation

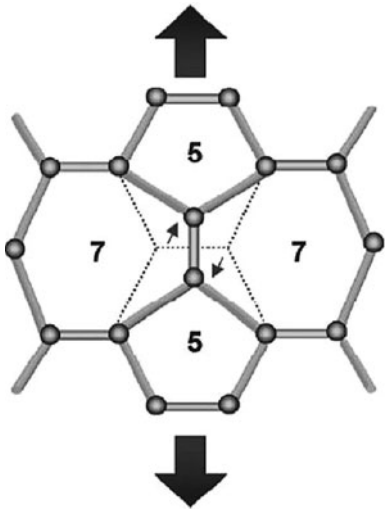

Fig. 5 Scheme of a Stone-Wales transformation in which four hexagons are converted to two pentagon-heptagon pairs [52]

efficiently with the help of femtosecond laser pulses [71]. Further positive effects of physical treatments include joining two CNTs together in a controlled manner by heating [72], transforming herringbone CNFs to straight CNTs by electric fields [73] and converting SWCNTs from metallic to semiconducting by hydrogen plasma treatment [74].

Synthesis Techniques

Strictly speaking, the only two requirements for the synthesis of carbon nanostructures are a carbon and an energy source. The carbon source can be any carbon containing chemical compound ranging from solids like graphite over liquids such as ethylene to gases like methane. Thermal, electrical, mechanical or optical energy sources are applied to break the existing bonds of the carbon source in an optimized environment to assist the formation of carbon nanostructures. Based on this general principle, various ingenious techniques have been developed for the synthesis of CNTs and graphene.

The main challenges for the synthesis techniques of carbon nanostructures are the possibility of mass production and control over the structural properties such as chirality, diameter, length, area and defects. The majority of synthesis techniques for the production of graphene and CNTs will be discussed in this section as well as their ability to manage the challenges of mass production and structural control.

Graphene Synthesis Techniques

Like writing with a pencil, a single layer of graphene can be peeled off a graphite crystal by mechanical exfoliation. This technique is a straightforward route for

the production of high quality graphene for tabletop experiments and does not require expensive tools, hence it is the most utilized technique for the preparation of graphene and FLG. However, mechanical exfoliation is not suited for mass production of graphene and several other approaches prevailed recently that address the requirement for mass production more efficiently.

Mechanical Exfoliation

Mechanical exfoliation of graphene is performed by rubbing bulk graphite against a Si wafer like a *cheese greater* technique [75] or by repeated peeling off thin graphite flakes with adhesive tape until the thinnest flakes are found on the surface of a silicon wafer [14].

The problem with this technique is that graphene crystallites left on the substrate are extremely rare and hidden in a *haystack* of thousands of thick graphite flakes. Scanning the substrate in search for graphene can not rely on scanning probe microscopy (SPM) because of the low throughput, whereas SEM is unsuitable to identify the number of atomic layers. The solution for this problem comes from the observation that graphene becomes visible on top of a Si substrate with a carefully chosen thickness of silicon oxide (SiO_2) equal to 300 nm, owing to a feeble interference-like contrast with respect to an empty substrate [76, 77]. If not for this simple yet effective way to scan substrates in an optical microscope, graphene would probably remain undiscovered today. After optical identification of graphene, further confirmation of the one atom thickness can be derived from SPM analysis and Raman recognition of the characteristic graphene signature [78].

Epitaxial Growth

The epitaxial growth of a graphene film on carbon doped nickel, platinum, palladium and cobalt was already observed by Blakely et al. in as early as 1979 [11, 13, 79], Blakely. Single crystalline metal samples were doped with carbon and afterwards loaded in a ultrahigh vacuum chamber and cleaned by annealing at elevated temperatures around 1,200°C prior to carbon segregation experiments. By gradually decreasing the temperature after annealing, the carbon coverage at the surface of the samples was studied in function of temperature with in situ Auger spectroscopy and low energy electron diffraction (LEED).

The general results obtained on the (111) nickel surface of a carbon doped nickel single crystal are presented in Fig. 6. By decreasing the temperature, an abrupt transition of a clean surface to a monolayer of segregated carbon was attributed to a surface phase condensation at the temperature T_s. The carbon signal remained constant over a temperature range of more or less 100 K before graphite precipitation occurred at the temperature T_p.

More recently it was presented that films of graphene and FLG can be grown epitaxially on the silicon-terminated face of a silicon carbide (SiC) wafer by thermal desorption of silicon [80]. For this procedure, single crystalline SiC wafers are loaded in an ultrahigh vacuum chamber and cleaned in situ by annealing up to

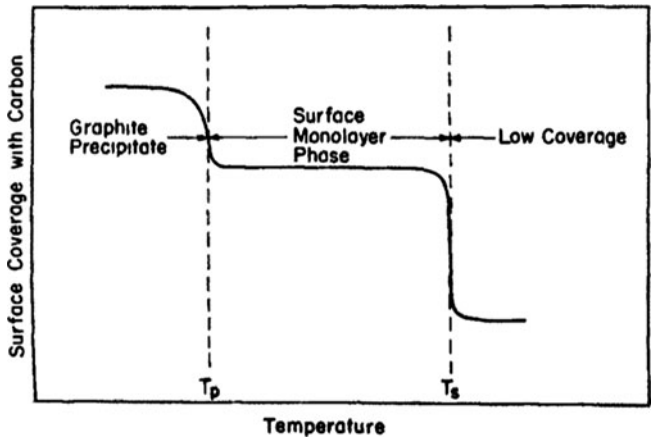

Fig. 6 Schematic equilibrium temperature dependence of carbon coverage on the (111) nickel surface of a carbon doped nickel single crystal [11]

850°C under silicon flux for half an hour. The silicon flux removes native oxide by the formation of volatile SiO, that sublimes at this temperature. It is also possible to grow graphene films at more moderate vacuum conditions using ovens with controlled background gas [81]. The as prepared wafers are subsequently annealed in the absence of a silicon flux at approximately 1200°C for about 20 min. The silicon atoms in the top atomic layer of the SiC wafer desorb as a result of the thermal treatment and a single layer of graphene is produced. The resulting graphene film covering the entire wafer is not continuous but exhibits a single-crystal grain size of several hundreds of nanometers [82]. The growth of the graphene film is not self-limited so that longer growth times produces relatively thick graphite films up to 100 atomic layers.

Careful investigation of the as prepared FLG films revealed that the distance between the first atomic graphene layer and the last SiC layer is nearly equal to the diamond bond length [81]. This suggests that the substrate bond to the first graphene layer is much stronger than a van der Waals interaction and simulations suggest that this layer is insulating [83]. However, the second graphene layer is semiconducting. Thus, the first graphene layer can be interpreted as a buffer layer between the substrate and an isolated layer with the electronic properties of a graphene sheet.

Another remark concerning epitaxial grown FLG is the observed larger interlayer spacing when compared to the bulk graphite interlayer spacing [84]. This larger interlayer spacing suggest a significant amount of stacking faults.

Chemical Routes

Oxidation of graphite produces graphite oxide, which is water dispersible due to the presence of oxygen-containing groups and readily exfoliates upon sonication

in water [85]. Several functional groups characterize exfoliated graphite oxide flakes and lead to an enhanced dispersion in water [86]. After a good dispersion is achieved, an intermediate centrifugation step separates the large from the small flakes [87] and the selected graphite oxide flakes can be deposited on SiO_2 wafers using standard drop-casting, dip-coating or spray-coating techniques [88, 86]. Alternatively, the graphite oxide can be deposited using vacuum filtration methods [89], which has been successfully used for the deposition of SWCNTs [90]. Once the spray-coated graphite oxide flakes are deposited, they can be chemically reduced and if well prepared, graphene and FLG flakes result from this procedure.

Depending on the experimental details, the resulting FLG either has a wide area up to several micrometers [86, 88, 89] or either has the shape of a thin ribbon with controlled width ranging from several nanometers down to less than 10 nm [91].

A variant technique on the exfoliation in water is thermal exfoliation of graphite oxide by rapid heating up to 1000°C in argon environment [92, 93]. In this process, graphite oxide is observed to split into individual single and few-layer sheets through evolution of CO_2.

Chemical Vapor Deposition

Over the years, the formation of graphene via absorption and thermal decomposition of hydrocarbons at appropriate temperatures is extensively studied on the surface of cobalt [94], nickel [95], platinum [96], palladium [97], ruthenium [98], titanium carbide [99, 100] and iridium [101, 102].

In 1983, Tontegode et al. studied the adsorption of benzene vapors on the surface of iridium crystals in situ by Auger spectroscopy and discovered the formation of a monolayer graphite on the (111) surface of iridium [103]. The resulting graphene film was self-limiting since no increase in film thickness was observed by additional exposure.

Thermal chemical vapor deposition (CVD) experiments are performed in ultra-high vacuum at elevated temperatures up to 1,600°C and the metal surfaces are thoroughly cleaned by thermal procedures prior to synthesis of graphene. A hydrocarbon gas, typically ethylene, is decomposed while heating the metal and a carbon monolayer is formed on its surface. The resulting graphene film is observed to completely cover the metal surface.

Instead of thermal energy, a plasma can be used as the energy source for the decomposition of a hydrocarbon gas. This so called plasma enhanced CVD (PECVD) technique has produced nanometer thin films of crystalline FLG completely covering the nickel substrate surfaces [104]. However, the films are not continuous and have grain sizes of a few micrometer with edges that curl upward from the nickel surface and small islands of amorphous carbon are also visible on the grains.

The CVD and PECVD route for the synthesis of graphene only recently emerged and is currently thoroughly explored with high expectations for mass production of high quality graphene.

Carbon Nanotube Synthesis Techniques

Over the last fifteen years, many ingenious techniques were developed for the synthesis of CNTs, but only three of them matured and established a widespread general production scheme for the large scale synthesis of high quality CNTs with controlled diameter, length and sometimes also chirality. Nearly all commercially available CNTs are produced by one of these three synthesis techniques that are covered in this section.

Arc Discharge

Originally developed for the synthesis of fullerenes, arc discharge techniques produce carbon soot containing many interesting carbon nanostructures including CNTs, as discovered by Iijima in 1991 [8]. Besides its pioneering role for the synthesis of CNTs, arc discharge evolved as a trustful technique for the mass production of CNTs.

At the heart of an arc discharge setup are two graphite electrodes, mounted at a controlled distance of ± 1 mm from each other in a sealed environment [105]. Classically, air is evacuated from the reactor chamber and replaced by a buffer gas like helium, hydrogen or argon to stabilize the electric arc. More recently, the gaseous medium is reportedly substituted by liquids like water [106, 107] or liquid nitrogen [108] which yield many interesting carbon nanostructures.

A constant voltage of ± 20 V in combination with a high current up to 100 A is applied between the two electrodes which causes sublimed carbon atoms from the positive electrode or anode to be deposited primarily on the negative electrode or cathode. Throughout the ± 2 min during experiments, the distance between the anode and cathode is kept constant to assure a stable electric arc.

The as described technique is only accommodated for the synthesis of MWCNTs. For the production of SWCNTs, a metal catalyst like iron, cobalt, nickel, yttrium or a combination of metals need to be added to the anode.

Arc discharge is no clean technique since the produced carbon soot not only covers the cathode but also the walls of the reactor, that need to be cleaned prior to subsequent experiments. Only 20% of the carbon soot consists of CNTs, mostly arranged in bundles, that need to be segregated from amorphous carbon by subsequent purification steps. Even though arc discharge is an elaborate synthesis technique that offers limited control over the CNT orientation and chirality, it is an inexpensive route for the mass production of high quality CNTs [109].

Laser Ablation

Synthesis of CNTs via laser ablation of a graphite target is similar to arc discharge since the carbon source in both techniques is graphite. For the synthesis of CNTs by the laser ablation technique, a continuous or pulsed laser is directed at a graphite target located in a heated quartz tube at ± 1,200°C. The quartz tube is continuously flushed with argon or helium gas and the sublimed carbon species are transported by

the gas flow and recombine on a cold finger to form bundles of CNTs. If the graphite target is not doped, only MWCNTs prevail. Doping of the graphite target with metals like nickel and cobalt is a prerequisite for the synthesis of SWCNTs [110].

The advantages of pulsed over continuous lasers are a higher achievable laser power, an increased quality of the as prepared CNTs and a decreased amorphous carbon formation. Operating a free electron laser with a pulse frequency around 75 Mhz causes the graphite target to sublime without thermally heating which dramatically improves the CNT purity by nearly eliminating the formation of amorphous carbon [111].

The laser ablation technique is characterized by a higher CNT yield and more narrow CNT diameter distribution when compared to arc discharge synthesis of CNTs. Using a free electron laser enables synthesis of CNTs with a purity of 90% [112], which eliminates the need for post synthesis purification steps. Disadvantages of the laser ablation technique are the high cost, limited mass production opportunities and no control over CNT orientation and chirality.

Chemical Vapor Deposition

The main advantages of CVD and its derivative PECVD are the low cost, high throughput, high quality of the as grown CNTs, negligible amorphous carbon formation and controlled tube diameter, length and orientation. All these features established CVD and PECVD as the most widespread synthesis technique for CNTs [51, 113].

The main requirements for CVD synthesis of CNTs are a hydrocarbon gas, a metal catalyst and a plasma or thermal energy source. Because the plasma characteristics are dependent on the frequency of the voltage applied to ignite the plasma, three types of different situations must be distinguished. Direct current (DC) [114, 115], radio frequency (RF) [116, 117] and microwave (MW) [118, 119] plasmas each have their own characteristics that require slightly different CNT synthesis conditions.

Contrary to arc discharge and laser ablation techniques, CVD requires a metal catalyst for the synthesis of MWCNTs as well as SWCNTs [120]. Ideal metals are characterized by a high carbon absorption and typical examples include nickel, iron and cobalt [121]. The metal catalyst is typically deposited as a thin continuous film on a substrate and afterwards annealed and reshaped into small catalyst islands. The size and density of the islands is directly related to the diameter and density of the as grown CNTs.

The substrates supporting the catalyst islands are placed in a vacuum chamber and exposed to a gas mixture of a hydrocarbon gas diluted with a buffer gas. The most popular gas mixtures are acetylene diluted with ammonia and methane diluted with hydrogen. The hydrocarbon gas mixture is decomposed by thermal energy or by a plasma and the carbon radicals diffuse towards the catalyst islands where many different processes drive the nucleation of CNTs [122, 123, 124, 125] as depicted in Fig. 7.

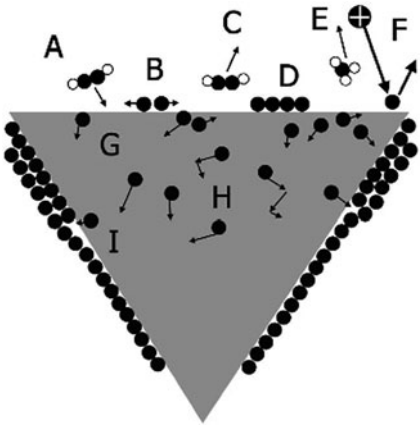

Fig. 7 Schematic representation of the different processes driving CNT nucleation [51]

The carbon radicals arrive at the catalyst surface (A) and are further dissociated (B) or depart from the surface without dissociation (C). Dissociated carbon dissolves into the catalyst particle (G) and diffuses through or around the catalyst (H) before recombining at the surface and forming a graphene layer (I). PECVD introduces a few additional processes due to application of an electrical field and partial ionization of the gas, such as sputtering due to ion bombardment (F) and chemical etching (E) [51].

The shape of the catalyst defines the nanotube morphology because the growing graphene sheets are tangent to the catalyst surface. If the catalyst particle has a more triangular shape like in Fig. 7, CNFs prevail since the growing graphene sheets make an angle with the tube axis. If the catalyst has a rounded shape, CNTs are produced.

CNTs and CNFs grow by incorporation of carbon atoms at the edges of the graphene layer that is formed on the catalyst surface. Elongation of the graphene layer can push the catalyst particle upward from the substrate surface if the substrate wetting of the catalyst particle is poor. Strong interaction between the catalyst and the substrate keeps the catalyst at the bottom of the growing graphene layers. The position of the catalyst in the growing tube differentiates between two growth modes as schematically depicted in Fig. 8. CNTs and CNFs are commonly stated to grow according to a so-called *tip* or *base* growth mechanism [126, 127], depending on whether the catalyst particles are pushed upwards from the substrate by the growing CNTs or remain attached to the substrate during the growth.

The length of the tubes is controlled by the growth time and it is clear from Fig. 7 that the diameter of the tubes is proportional to the catalyst size.

The orientation of the tubes can be controlled by the gas flow [128, 129] or by applying electric fields [130, 131] to guide the growing CNTs in thermal CVD. This way, straight and aligned CNTs are produced. DC and RF PECVD setups usually do not require extra efforts for the alignment of the tubes since the catalyst supporting substrates are generally positioned on an electrode which implies the presence of electric field lines perpendicular to the substrate surface. The as produced CNTs

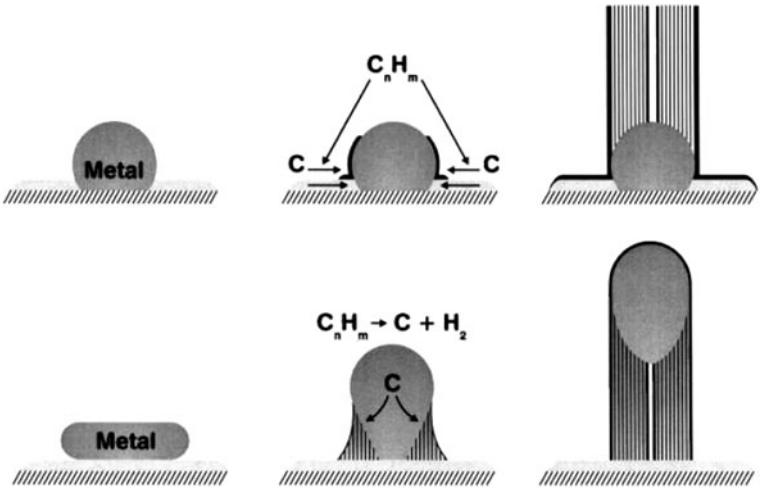

Fig. 8 Schematic representation of the two different CNT and CNF growth modes. The top panel depicts base growth and the bottom panel depicts tip growth of a MWCNT [126]

and CNFs are therefore aligned vertically to the supporting substrate. Inductively coupled RF plasmas [132] and MW plasmas generally can not take advantage of the plasma's intrinsic electric field and therefore rely on external fields for the alignment of the CNTs.

Selective Synthesis

Controlling the chirality of CNTs is of great importance since CNTs are either metallic or semiconducting depending on the chirality, and many applications require CNTs with controlled electrical properties.

Elaborate techniques have been developed for sorting semiconducting and metallic CNTs after synthesis [133, 134], but these techniques offer little outlook for high throughput facilities (see also Sect. 'Activation, Purification and Functionalisation').

Because of the relationship between chirality and CNT structure on one hand and CNT structure and metal catalyst on the other, the catalyst is expected to determine the chirality. So far, only few attempts succeeded. Preferential growth of semiconducting SWCNTs by RF PECVD was achieved with nearly 90% of the CNTs being semiconducting [135]. The relative abundances of semiconducting and metallic CNTs grown by various methods were confirmed to be dependent on the synthesis technique and conditions. Further, the preparation of the catalyst was demonstrated to influence and restrict the different (n, m) possibilities to only two [136].

Not only the catalyst, but also the hydrocarbon gas mixture and the substrate material determine the CNT chirality. In CVD synthesis of SWCNTs, changing

the hydrocarbon gas from methane to carbon monoxide was shown to restrict the variation of (n, m) indices to only three possibilities and altering the substrate material from silicon oxide to magnesium oxide also limits the different (n, m) possibilities to three [137].

Physical Properties

It is due to their physical properties that CNTs and graphene caused so much excitement among researchers worldwide. Considering thermal behavior, CNTs exhibit thermal stability in vacuum up to 2,800°C [138] and graphene studies reveal superb thermal conductivity [139], which might be beneficial in thermal management applications. Further, magnetization measurements along the axis of iron filled CNTs revealed excellent coercivities, a strong uniaxial anisotropy and high saturation magnetization moments [140].

Over the last 2 decades, the electrical and mechanical properties of CNTs and graphene were among the most intense studied topics, attracting attention from a broad audience and suggesting a large potential for these graphitic nanostructures in a broad range of nano-electronic applications and composites. It is therefore relevant to discuss the electrical and mechanical properties of CNTs and graphene in more detail.

Electrical Properties

The hexagonal carbon lattice of graphene consists of two interpenetrating triangular sub-lattices pictured in Fig. 9a. The atom sites of one sub-lattice (green) are the centers of the other (orange) [141]. The graphene lattice thus has two carbon atoms, designated A and B in Fig. 9a, per unit cell and is invariant under 120° rotations around any lattice site.

Every carbon atom has four orbitals, one *s* and three *p* orbitals, from which just one *p* orbital remains free of participating in the covalent binding with the three nearest neighbor atoms. This free *p* orbital is oriented perpendicular to the graphene plane and hybridizes to form the valence and conduction band.

Due to quantum mechanical hopping of charge carriers between the two sub-lattices of graphene, the conduction and valence band touch each other in the K and K' points of the Brillouin zone, which makes graphene a zero-gap semiconductor as depicted in Fig. 9b. Near these points the bands form conical valleys and the energy varies linearly with the magnitude of momentum measured from the Brillouin zone corners [142, 143]. This behavior implies that the speed of electrons in graphene is a constant, independent of momentum, alike the speed of light is a constant c.

Due to the interaction with the graphene potential, electrons give rise to new charge carriers, quasiparticles that can be described by the Dirac equation and move with an effective speed of light $v_f \approx 10^6\ \mathrm{ms}^{-1} \approx c/300$. These quasiparticles are

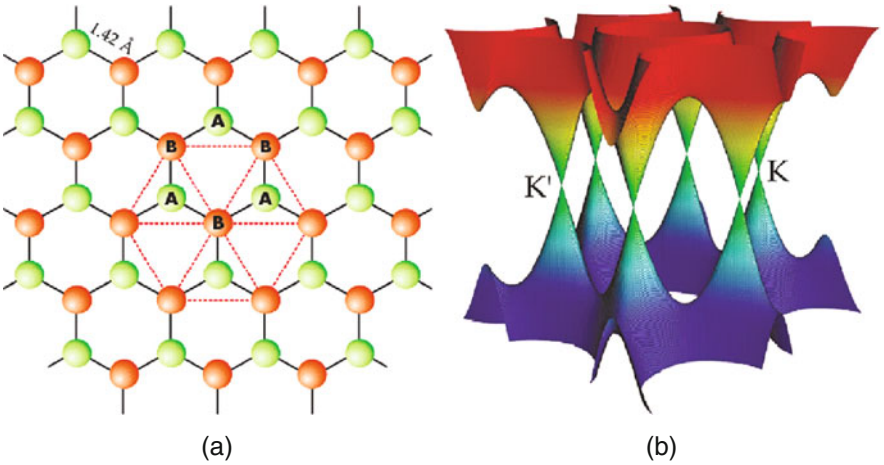

Fig. 9 Scheme of the graphene lattice depicting the two sub-lattices (**a**) [141], and electronic band structure of graphene according to the Bloch band description (**b**) [142]

called massless Dirac fermions and can be thought of as electrons that have lost their rest mass m_0 or neutrinos that acquired the electron charge e [16].

Because of the relativistic description of graphene's charge carriers, several interesting phenomena from the theory of quantum electrodynamics (QED) can be probed in graphene. The so-called Klein paradox is the most counterintuitive consequence of QED and refers to the relativistic process in which the amplitude of the electron wave function remains constant during tunneling through a potential barrier if the height of the barrier exceeds the electron's rest energy, mc^2 (where m is the electron mass and c is the speed of light) [142, 144]. Graphene offers a way to probe the Klein paradox in a bench-top experiment.

Graphene's unusual electronic behavior reveals itself in a pronounced ambipolar electric field effect such that charge carriers can be tuned in concentrations as high as 10^{13} cm^{-2} with a mobility exceeding 15000 cm^2 V^{-1}s^{-1} even under ambient conditions [145, 146]. This translates into ballistic transport on the sub-micrometer scale [147]. As the Fermi energy approaches zero in field effect experiments, a minimum conductivity of about e^2/h remains (where e is the electron charge and h is the Planck constant), partly because of the difficulty of localizing massless Dirac fermions which can slip through a rough potential landscape that would trap non-relativistic electrons [145]. Even more surprising than graphene's non-zero conductivity is the experimental behavior that this minimum conductivity is about π times larger than expected. This disagreement between theory and experiment has become known as *the mystery of a missing pie* and remains unsolved up to this moment.

Another consequence of graphene's atypical electronic behavior is the expression of an anomalous quantum Hall effect where the sequence of equidistant steps in the Hall conductivity σ_{xy} is shifted by $1/2$ due to the existence of a quantized level at zero E, which is shared by electrons and holes [148–150].

The band structure changes dramatically when stacking layers of graphene. Where a single layer of graphene is a zero-gap semiconductor, bilayer graphene already is a semimetal like graphite [151–153]. However, the band overlap in bilayer graphene is only very small, but increases when adding more layers. For eleven and more layers, the difference in band overlap with graphite is smaller than 10%.

The conducting states at the Fermi energy of graphene's electronic structure are restricted to the corners of the first Brillouin zone as depicted in Fig. 9b, which reduces the Fermi surface of graphene to the six corners of a hexagon.

For a SWCNT, the wavevector $\vec{k}$ of the electrons moving around the circumference is quantized due to a periodic boundary condition: The wave function at the endpoint of $\vec{C}_h$ is the one at the origin multiplied by the Bloch factor $\exp(i\vec{k}\cdot\vec{C}_h)$. The cyclic boundary condition imposes $\exp(i\vec{k}\cdot\vec{C}_h) = 1$ which implies that $\vec{k}\cdot\vec{C}_h = 2\pi q$, where q is an integer [154–156]. Therefore, only states perpendicular to $\vec{C}_h$ with a spacing of $2/d$, where d is the nanotube diameter, are allowed. Along these states, the electronic structure of graphene is probed, which leads to a metallic SWCNT if one of the allowed wavevectors passes through a corner of the Fermi surface. From the criterion $\vec{K}_b \cdot \vec{C}_h = 2\pi q$, where $\vec{K}_b$ is the wavevector of a corner in the first Brillouin zone, this situation occurs when the coordinates of a corner point K_1 and K_2 satisfy $nK_1 + mK_2 = q$. Taking for instance $K_1 = 1/3$ and $K_2 = -1/3$ leads to the conclusion that a SWCNT should be metallic if $n - m = 3q$ and otherwise the tube should be semiconducting [157]. The energy gap scales with the nanotube diameter as $1/d$ and is on the order of $0.5eV$ for a SWCNT with typical diameter $d \approx 1.4$ nm [49].

The finite curvature of SWCNTs induces orbital re-hybridization effects and is found to induce shifts in the Fermi points, along the circumference direction for zigzag CNTs and along the axis for armchair CNTs [158–160]. For zigzag CNTs, this shift implies that wavevectors predicted to yield metallic SWCNTs no longer pass through the shifted Fermi points and hence the tubes will be semiconducting. To summarize, CNTs are metallic when $n = m$, they have a small gap when $n - m = 3q$ and they are truly semiconducting in all other situations. This behavior is illustrated in Fig. 10 where four different SWCNTs and their corresponding electronic structure are schematically depicted.

MWCNTs consist of concentric SWCNTs and therefore a more complex electronic structure is expected, also taking into account interactions between adjacent tubes. Electrical resistance measurements on an individual MWCNT revealed a logarithmic decrease of the conductance with decreasing temperature, followed by a saturation below $T \approx 0.3$ K [161]. An ingenious experiment established that all MWCNTs have nearly the same conductance $G_0 = 2e^2/h$, where e is the electron charge and h is Planck's constant [162]. The MWCNTs appeared to be ballistic conductors, despite interactions between different layers.

For CNFs, the graphene planes are not continuous along the entire length and make an angle with the fiber axis, which is expressed in a dominant inter-plane tunneling of electrons during electrical measurements. The main contribution to the resistance of an individual CNF is attributed to inter-plane tunneling [163].

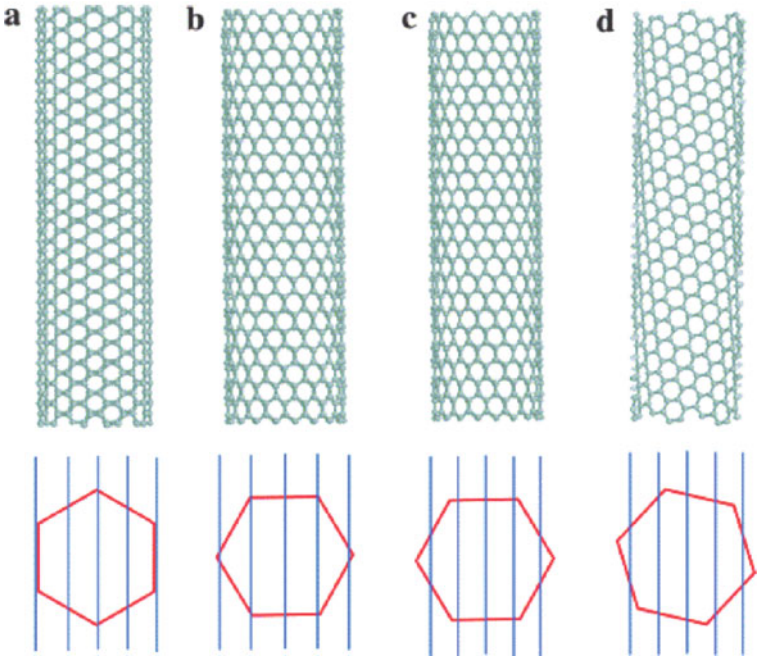

Fig. 10 Scheme depicting the relation between CNT morphology and electronic properties. The top panel illustrates different SWCNT morphologies: (10,10) armchair nanotube (**a**), (12,0) zigzag nanotube (**b**), (14,0) zigzag nanotube (**c**) and (7,6) chiral nanotube (**d**). The hexagon in the bottom panel represents the first Brillouin zone and the vertical lines represent the electronic states of the nanotube [49]

Mechanical Characteristics

The mechanical properties of a solid depends ultimately on the strength of the interatomic bonds. For the case of graphene and CNTs, this is an encouraging fact since the sp^2 carbon bond is among the strongest covalent bonds known. But mechanical characterization of graphene and CNTs is challenged by tremendous limitations of specimen size, uncertainty in data obtained from indirect measurements and inadequacy in test specimen preparation due to a tough control in sample alignment and distribution [164, 165].

Graphene's spring constant was recently determined by pressing an atomic force microscopy (AFM) tip on freely suspended graphene sheets. By examining how the spring constants vary with size dimensions of the suspended sheets, graphene's Young's modulus could be determined [166]. Values for the measured spring constant range from 1 to 5 Nm^{-1} from which a Young's modulus of 0.5 TPa was extracted, compared to 1 TPa for in plane bulk graphite [167] and diamond [168].

The Young's modulus of MWCNTs was first determined by measuring the amplitude of their intrinsic thermal vibration in TEM [169]. An average value of 1.8 TPa was obtained, nearly double the value for bulk graphite. This result was confirmed

by measuring the compressive response of CNTs using micro-Raman spectroscopy, which returned values of ∼2 TPa, respectively ∼3 TPa, for the Young's modulus of MWCNTs, respectively SWCNTs [170].

Dedicated direct measurements of the Young's modulus of CNTs was carried out by attaching individual MWCNTs and ropes of SWCNTs between two AFM tips and monitoring the strain in function of the applied stress, while recording the CNT deformation behavior in a scanning electron microscope (SEM) [28, 171], Yu. For MWCNTs, a sliding of the inner tubes out of the outer tube was observed and a Young's modulus ranging from 0.3 to 1 TPa was extracted. This telescoping *sword and sheath* failure mechanism was ascribed to the weak van der Waals binding between adjacent layers compared to the strong interatomic covalent bonds. For SWCNTs, it was assumed that the load applied to the ropes was only carried by the outermost tubes in agreement to a well fit model. Based on this model, a SWCNT Young's modulus ranging from 0.3 to 1.4 TPa was deduced. Large variations between the various reported values are due to atomic defects in the lattice structure and therefore it is generally accepted to state the Young's modulus of CNTs around 1 TPa.

Contrary to what is expected from their high Young's modulus, CNTs are remarkably flexible with completely reversible bending up to angles in excess of 110° [172]. Films of vertically aligned CNTs behave like a super-compressible foam [173, 174]. Under compression, the nanotubes collectively form zigzag buckles that can fully unfold to their original length upon release. Under compressive cyclic loading of the vertically aligned CNT forest, no fatigue failure is observed at high strain amplitudes up to half a million cycles [175].

Because CNFs consist of stacks of graphene cones or cups held together mainly by van der Waals forces, their mechanical properties are inferior to CNTs. The bending modulus of CNFs was measured in TEM by electromechanical resonance, which returned typical values of ∼ 30 GPa for bamboo CNFs with point defects compared to 2–3 GPa for bamboo CNFs with volume defects [176].

Applications

Applications are often the driving force behind research, since the promise of implementation assures the abundance of funds for scientific research. This is certainly the case for carbon nanostructures who's novel physical properties can be explored in a wide range of interesting practices. In this section, the most appealing and feasible applications of graphene, CNTs and CNFs will be discussed.

Possible applications of carbon nanostructures surpass the conventional scope of electronics and composites, and are seemingly only limited by scientific creativity. As an example, a straightforward technique allows spinning forests of vertically aligned CNTs into self-supporting sheets with a gravimetric strength that exceeds that of steel [177, 178] and chemically derived graphene oxide paper is found to outperform many other paper-like materials in stiffness and strength [179]. In photovoltaic devices, CNTs were configured as energy conversion material with

an efficiency greater than 1% [180] and composites of CNTs or graphene and conjugated polymers were shown to act as a good electrode material [181, 182].

Activation, Purification and Functionalisation

Many synthesis techniques for CNTs and graphene require additional purification and functionalisation steps in order to dispose the catalyst particles and amorphous carbon and only select particular nanostructures corresponding to applications' demands. Several nanostructure characteristics, like diameter, length and morphology (tube vs fiber), can already be controlled in-situ during synthesis, while other requirements have to be addressed afterwards.

For CNTs, the selection of chirality imposes the biggest challenge, since it determines the nanotube's electronic behavior. While some successful attempts have resulted in chirality selective synthesis of CNTs (see Sect. 'Selective Synthesis'), sorting metallic and semiconducting CNTs is also possible after growth. For bulk amounts of purified CNTs, the volume fraction of metallic and semiconducting SWCNTs can be effectively estimated by measuring the spectral response of a pyroelectric detector [183]. Selecting specific SWCNTs from the bulk is achieved by applying the ability of specific aromatic polymers to efficiently disperse certain SWCNTs with a high degree of selectivity. Relatively small changes in the polymer structure lead to selection on the basis of both chirality and diameter [184]. A more primitive, but nevertheless efficient way to eliminate metallic SWCNTs in nanoelectronic systems, is burning them off by applying a relatively high current [185]. Semiconducting SWCNTs are more resistant to current and sustain the treatment.

Plasma processing and wet chemical techniques are widely explored for the purification and functionalisation of CNTs. Efficient elimination of catalyst impurities was accomplished by acid treatment followed by a thermal process [186]. This technique also introduced intercalated nitric acid molecules into SWCNT bundles. Wet chemical techniques further realized CNT functionalisation by attachment of small molecules like thionine [187], enzymes [188], thiol [189], alkyl-halides [190] and polymers [191].

Plasma functionalisation is often more efficient and practical than wet chemical processing since it can be accomplished in-situ after PECVD synthesis of CNTs. A RF plasma source is the most widely used tool for the plasma treatment of CNTs, accommodating the preparation of e.g. fluorinated CNTs [192, 193]. The versatility of RF plasma's was presented by the successful binding of polystyrene, oxygen and amine on the surface of CNTs [194]. It was demonstrated that an argon plasma treatment generates defect sites at the CNT walls, which act as the active sides for the subsequent binding of molecules [195, 196].

Nano-Electronics

Graphene's touching conduction and valence band accounts for the majority of excitement over this two-dimensional crystal since it gives rise to graphene's

unusual electronic properties. However, despite its intriguing properties, the lack of a band-gap also presents the biggest hurdle for many graphene based nano-electronic applications like transistors. Many of the proposals to open a gap in graphene's electronic spectra require complex engineering of the graphene layer, which is elaborate and not very practical [197–199]. Nevertheless, when synthesizing graphene by epitaxial growth on SiC substrates a small band-gap of ∼0.26 eV can be induced [200]. This realization presents a great step towards graphene based nano-electronic applications [201].

Graphene field effect transistor devices have been fabricated by a conventional top-down CMOS-compatible process [202]. Electrical measurements of graphene transistors revealed that the resistivity of the graphene ribbon increases as its width decreases, indicating the impact of edge states [203].

For CNTs, there are two main areas being considered in integrated circuits, namely as interconnects between transistors and as the channel material in field-effect transistors (FET) [204]. Every transistor is connected by two leads or interconnects classified according to their orientation: vertical interconnects, also denoted *vias*, and horizontal interconnects. Scaling down the processor architecture implies thinner interconnects for the same amount of current, which imposes large constraints on the interconnect material. MWCNTs and CNFs are the ideal candidate to replace copper which is currently used for interconnects. Vias are the simplest component that can be replaced by vertically aligned MWCNTs and CNFs. In this arrangement, either one thick tube [205] or several thin tubes fill the hole in the dielectric [206]. The only challenge in the latter case is to control the density of the tubes to construct a dense forest in order to assure sufficient electrical conduction [207]. However, the successful fabrication of an integrated circuit combining silicon transistors and CNT interconnects has recently been achieved [208].

Constructing a FET with a CNT channel is challenging since it requires a semiconducting CNT and chirality selection of CNTs remains delicate. Further, CNT contacts behave as Schottky barriers, compared to ohmic contacts in conventional FETs. Nevertheless, a CNT based FET can be constructed and by applying a gate voltage, the CNT can be switched from a conducting to an insulating state [209]. The CNT FET performance can be optimized by using a thin silane-based organic monolayer as gate dielectric [210].

The next step towards CNT CMOS technology is the construction of an integrated logic circuit, which was accomplished by assembling a ring oscillator on a single CNT [211]. However, proof-of-work for an individual CNT based FET is not sufficient for CMOS industry, that demands several million devices per square centimeter. A major step to overcome this challenge applies a novel aspect of CNT dielectrophoresis to realize the controlled assembly of CNTs on determined positions of patterned transistors [212]. The CNTs are committed to bridge the gap between source and drain, thereby forming the gate material.

Besides applications in integrated circuits are CNTs and graphene extensively explored as nonvolatile random access memory device [213–216], as supercapacitor electrodes for compact energy-storage devices [217, 218] and as antennas in radios [219–221].

Compared to straight CNTs, the helical morphology of CCNTs can be advantageous in developing CNT based applications. Force modulation measurements of the coils revealed elastic behavior in agreement with classical theory [222], and CCNTs were shown to behave like nano-springs able to elongate up to 40% when applying tension [223]. The CCNT behavior analogous to classical theory has been exploited for the development of a self-sensing mechanical resonators able to detect mass changes of a few attograms [224]. In nano-electronics, an electric current passed through CCNTs could induce magnetic fields to manipulate electromagnetic nano-transformers or nano-switches [225].

Field Emission

CNTs provide high potential as electron sources in field emission practices with potential applications including microwave amplifiers [226], SEM electron sources [227], field emission displays [228–230] and portable X-ray sources [231].

The principle of field emission experiments is applying an electric field to lower the potential barrier that electrons in a metal must overcome to tunnel into vacuum [232]. The height of the potential barrier is denoted as the work function ϕ. In the absence of an electric field, only electrons that are excited either thermally of by incident radiation, can overcome the potential barrier.

The situation changes significantly when an electric field is applied between the metal and a counter electrode. As a result of the electric field and the image charge effect, the potential barrier changes from a semi-infinite step function to the shape drawn in Fig. 11 [233]. The height of the barrier is lowered by an amount $\triangle\phi$ and for increasing field strength, the width of the barrier becomes so small that the electrons can tunnel through it. This situation is not only restricted to zero temperature since the highest occupied electron levels in a metal at room temperature are still close to the Fermi energy.

The locally applied electric field is not simply V/d, which is the macroscopic field obtained between two planar electrodes separated by a distance d. In most case,

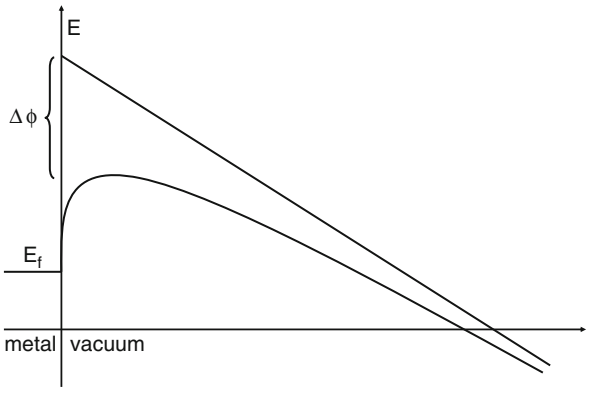

Fig. 11 Schematic drawing of the field emission concept: applying an electric field reshapes the potential barrier and lowers the work function by a factor $\triangle\phi$. This facilitates tunneling of electrons through the potential barrier [233]

the local field will be higher by a factor β, which gives the aptitude of the emitter to amplify the field and is accordingly termed the field amplification factor [234]. β is determined solely by the geometrical shape of the emitter, and the corresponding local electric field at the emitter surface becomes $E = V\beta/d$.

CNTs and CNFs are excellent field emitters due to their sharp tips that imply large amplification factors and therefore reduce the necessary electric field strength for electron tunneling to only a few V/μm [235]. The ability to modify the tip geometry provides a way to control the field emission properties of CNTs and CNFs [236].

The density of CNTs or CNFs strongly influences the field emission behavior since close proximity of neighboring tubes causes electrostatic screening and prevents potential penetration along the tube walls [237]. The minimal distance between neighboring tubes in order to eliminate screening effects should be equal to or greater than the height of the tubes [238].

Sensors

Sensors continue to make a significant impact on everyday life. The main requirements of a good sensor are high sensitivity, fast response, low cost, high volume production, and high reliability. Due to their exceptional physical properties, CNTs have been explored as the sensing material in pressure, flow, thermal, gas, optical, mass, position, stress, strain, chemical, and biological sensors [239].

Micrometer-Size sensors made of graphene were noticed to be capable of detecting individual gas molecules attaching or detaching from graphene's surface [240]. The adsorbed molecules change the local carrier concentration in graphene by one electron, which results in step-like changes in resistance. The achieved sensitivity is due to the fact that graphene is an extremely electronically low-noise material.

Resistive CNT gas sensors have been mainly evaluated for detection of ammonia, hydrogen, nitrogen oxide and carbon oxide [241–245] and operate by measuring a change in resistance of a thin CNT film or composite. Impedance spectroscopy revealed that chemisorption processes were responsible for the recorded resistance change [246]. The electrical response of the CNT based gas sensors can be optimized by temperature treatment to yield sensitivities as high as 10–50 parts per billion [242, 247, 248].

Composites

Polymers, ceramics and metals have all been studied as the matrix material for CNT and graphene composites, but polymers are the most explored system due to their relatively convenient possibility [249]. As structural nanotube reinforcements, SWCNTs are favored over MWCNTs or CNFs because only the outer shell of MWCNTs is found to contribute in tensile loading and CNFs have

inferior mechanical properties compared to CNTs [250]. For graphene, a bottom-up chemical approach for the preparation of graphene polymer composites results in a material with similar characteristics as SWCNT polymer composites [251].

Experimental research on CNT reinforced nano-composites has presented exciting results, although published data are often contradictory and experimental values do not reach the level predicted by theory [252, 253]. Improvements as well as worsening of the mechanical properties of CNT composites have all been reported, even for similar systems tested in different laboratories. The contradictory nature of the results expresses the challenges that remain to overcome before CNT composites reach full maturity.

In the field of CNT and graphene based polymer composites, significant mechanical improvements have been obtained by mixing only 1–2 wt% CNTs or graphene in the polymer matrix. Reported achievements include a shift in glass transition temperature of over 40° [254], a 80% increase in tensile modulus [255], a 140% enhancement in ductility [256], a 241% amelioration of elastic modulus and a 162% rise of yield strength [257]. In addition to mechanical improvement, the introduction of CNTs into insulating polymers can avoid electrostatic charging [258] and improve thermal stability [259].

The interfacial area in CNT composites is extremely large due to the CNTs' high aspect ratio and causes interfacial interactions to be critical for the composite's performance. Because of contradictory reports on strong bonding on one hand [260] and poor interfacial interaction on the other [261], it is clear that the preparation technique for CNT composites is crucial for its performance and need to be better controlled.

Another important factor to determine CNT composite performance is dispersion of the CNT bundles, since poor dispersion results in slipping of individual CNTs from bundles during load-carrying experiments [262]. Dispersion of CNTs is dependent on the matrix material [263] and can be enhanced by modification of the CNT surface [264] or by justified choice of processing technique such as e.g. shear mixing and melt compounding [253].

The exceptional resilience of CNTs is particularly desirable to compensate for the brittleness of ceramics and a surfactant-assisted method describes how to achieve a good CNT dispersion in a ceramic matrix [265]. The highly shear deformable SWCNTs in the ceramic composite help redistribute the stress under indentation, imparting the composites with contact-damage resistance [266].

In addition to straight CNTs, composites based on CCNTs can enhance the fracture toughness as well as mechanical strength, even if there is no direct chemical bonding between the nanotubes and the matrix [56].

Medical Applications and Concerns

Graphene and CNTs may be an important tissue engineering material for improved tracking of cells, sensing of micro-environments [267], delivering of transfection agents [268], and scaffolding for incorporating with the host's body [269].

However, toxicological tests unambiguously revealed that CNTs induce inflammation, fibrosis, and biochemical and toxicological changes in the lungs [270]. These results raise questions on the applicability of carbon nanostructures and justify concern and precaution among users and researchers worldwide.

References

1. M. Monthioux, V.L. Kuznetsov, Who should be given the credit for the discovery of carbon nanotubes? Carbon **44**, 1621 (2006)
2. M. Reibold, P. Paufler, A.A. Levin, W. Kochmann, N. Pätzke, D.C. Meyer, Carbon nanotubes in an ancient Damascus sabre. Nature **444**, 286 (2006)
3. A.A. Levin, D.C. Meyer, M. Reibold, W. Kockmann, N. Pätzke, P. Paufler, Microstructure of a genuine Damascus sabre. Crystal Res. Crystal Technol. **40**, 905 (2005)
4. L.V. Radushkevich, V.M. Lukyanovich, O. strukture ugleroda, obrazujucegosja pri termiceskom razlozenii okisi ugleroda na zeleznom kontakte. Zurn. Fisic. Chim. **26**, 88 (1952)
5. J.R. Heath, Long carbon chain molecules in circumstellar shells. Astrophys. J. **314**, 352 (1986)
6. H.W. Kroto, J.R. Heath, S.C. O'Brien, R.F. Curl, R.E. Smalley, C60: Buckminsterfullerene. Nature **318**, 162 (1985)
7. R.W. Marks, *The Dymaxion World of Buckminster Fuller* (Reinhold, New York, USA, 1960)
8. S.Iijima, Helical microtubules of grafitic carbon. Nature **354**, 56 (1991)
9. D.S. Bethune, C.H. Kiang, M.S. De Vries, G. Gorman, R. Savoy, J. Vazquez, R. Beyers, Cobalt-catalysed growth of carbon nanotubes with single-atomic-layer walls. Nature **363**, 605 (1993)
10. S. Iijima, T. Ichihashi, Single-shell carbon nanotubes of 1-nm diameter. Nature **363**, 603 (1993)
11. J.C. Shelton, H.R. Patil, J.M. Blakely, Equilibrium segregation of carbon to a nickel (111) surface: a surface phase transition. Surf. Sci. **43**, 493 (1974)
12. L.C. Iseti, J.M. Blakely, Segregation isosteres for carbon at the (100) surface of nickel. Surf. Sci. **58**, 397 (1976)
13. M. Eizenberg, J.M. Blakely, Carbon monolayer phase condensation on Ni(111). Surf. Sci. **82**, 228 (1979)
14. K.S. Novoselov, D. Jiang, F. Schedin, T.J. Booth, V.V. Khotkevich, S.V. Morozov, A.K. Geim, Two-dimensional atomic crystals. Proc. Nat. Acad. Sci. **102**, 10451 (2005)
15. K.S. Novoselov, A.K. Geim, S.V. Morozov, D. Jiang, Y. Zhang, S.V. Dubonos, I.V. Grigorieva, A.A. Firsov, Electric field effect in atomically thin carbon films. Science **306**, 666 (2004)
16. A.K. Geim, K.S. Novoselov, The rise of graphene. Nat. Mater. **6**, 183 (2007)
17. R.E. Peierls, Bemerkungen uber Umwandlungstemperaturen. Helvetica Phys. Acta **7**, 81 (1934)
18. R.E. Peierls, Quelques proprietes typiques des corpses solides. Ann. Inst. Henri Poincare **5**, 177 (1935)
19. L.D. Landau, Zur Theorie der Phasenumwandlungen II. Physikalische Zeitschrift der Sowjetunion **11**, 26 (1937)
20. N.D. Mermin, H. Wagner, Absence of ferromagnetism or antiferromagnetism in one- or two-dimensional isotropic Heisenberg models. Phys. Rev. Lett. **17**, 1133 (1966)
21. N.D. Mermin, Crystalline order in two dimensions. Phys. Rev. **176**, 250 (1968)
22. J.W. Evans, P.A. Thiel, M.C. Bartelt, Morphological evolution during epitaxial thin film growth: formation of 2D islands and 3D mounds. Surf. Sci. Rep. **61**, 1 (2006)
23. M. Zinkeallmang, L.C. Feldman, M.H. Grabow, Clustering on surfaces. Surf. Sci. Rep. **16**, 377 (1992)

24. J.A. Venables, G.D.T. Spiller, M. Hanbucken, Nucleation and growth of thin-films. Rep. Prog. Phys. **47**, 399 (1984)
25. D.R. Nelson, T. Piran, S. Weinberg, *Statistical Mechanics of Membranes and Surfaces* (World Scientific, Singapore, 2004)
26. J.C. Meyer, A.K. Geim, M.I. Katsnelson, K.S. Novoselov, T.J. Booth, S. Roth, The structure of suspended graphene sheets. Nature **446**, 60 (2007)
27. J.C. Meyer, A.K. Geim, M.I. Katsnelson, K.S. Novoselov, D. Obergfell, S. Roth, C. Girit, A. Zettl, On the roughness of single- and bi-layer graphene membranes. Solid State Commun. **143**, 101 (2007)
28. M.F. Yu, B.S. Files, S. Arepalli, R.S. Ruoff, Tensile loading of ropes of single wall carbon nanotubes and their mechanical properties. Phys. Rev. Lett. **84**, 5552 (2000)
29. J.Y. Huang, S. Chen, Z.Q. Wang, K. Kempa, Y.M. Wang, S.H. Jo, G. Chen, M.S. Dresselhaus, Z.F. Ren, Superplastic carbon nanotubes. Nature **439**, 281 (2006)
30. Y. Wu, P. Qiao, T. Chong, Z. Shen, Carbon nanowalls grown by microwave plasma enhanced chemical vapor deposition. Adv. Mater. **14**, 64 (2002)
31. Y. Wu, B. Yang, Effects of localized electric field on the growth of carbon nanowalls. Nano Lett. **2**, 355 (2002)
32. M. Hiramatsu, K. Shiji, H. Amano, M. Hori, Fabrication of vertically aligned carbon nanowalls using capacitively coupled plasma-enhanced chemical vapor deposition assisted by hydrogen radical injection. Appl. Phys. Lett. **84**, 4708 (2004)
33. A.T.H. Chuang, B.O. Boskovic, J. Robertson, Freestanding carbon nanowalls by microwave plasma-enhanced chemical vapour deposition. Diam. Relat. Mater. **15**, 1103 (2006)
34. A. Yoshimura, S. Kurita, M. Tachibana, K. Kojima, P. Molina Morales, H. Nakai, in *Fabrication of Carbon Nanowalls by dc Plasma-Enhanced Chemical Vapor Deposition and Characterization of thei Structures* (IEEE, Nagoya, Japan, 2005)
35. M. Hiramatsu, M. Hori, Fabrication of carbon nanowalls using novel plasma processing. Jpn. J. Appl. Phys. **45**, 5522 (2006)
36. A.T.H. Chuang, J. Robertson, B.O. Boskovic, K.K.K. Koziol, Three-dimensional carbon nanowall structures. Appl. Phys. Lett. **90**, 123107 (2007)
37. G. Sata, T. Morio, T. Kato, R. Hatakeyama, Fast growth of carbon nanowalls from pure methane using helicon plasma-enhanced chemical vapor deposition. Jpn. J. Appl. Phys. **45**, 5210 (2006)
38. Y. Wu, B. Yang, B. Zong, H. Sun, Z. Shen, Y. Feng, Carbon nanowalls and related materials. J. Mater. Chem. **14**, 469 (2004)
39. K. Shiji, M. Hiramatsu, A. Enomoto, M. Nakamura, H. Amano, M. Hori, Vertical growth of carbon nanowalls using rf plasma-enhanced chemical vapor deposition. Diam. Relat. Mater. **14**, 831 (2005)
40. Z.H. Ni, H.M. Fan, Y. P. Feng, Raman spectroscopic investigation of carbon nanowalls. J. Chem. Phys. **124**, 204703 (2006)
41. S. Kurita, A. Yoshimura, H. Kawamoto, T. Uchida, K. Kojima, M. Tachibana, Raman spectra of carbon nanowalls grown by plasma-enhanced chemical vapor deposition. J. Appl. Phys. **97**, 104320 (2005)
42. K. Kobayashi, M. Tanimura, H. Nakai, A. Yoshimura, H. Yoshimura, K. Kojima, M. Tachibana, Nanographite domains in carbon nanowalls. J. Appl. Phys. **101**, 094306 (2007)
43. K. Nishimura, N. Jiang, A. Hiraki, Growth and characterization of carbon nanowalls. IEICE Trans. Electron. **E86-C**, 821 (2003)
44. L. Giorgi, Th.D. Makris, R. Giorgi, N. Lisi, E. Salernitano, Electrochemical properties of carbon nanowalls synthesized by HF-CVD. Sens. Actuators B Chem. **126**, 144 (2007)
45. M. Zhu, J. Wang, R.A. Outlaw, K. Hou, D.M. Manos, B.C. Holloway, Synthesis of carbon nanosheets and carbon nanotubes by radio frequency plasma enhanced chemical vapor deposition. Diam. Relat. Mater. **16**, 196 (2007)

46. J.F. AuBuchon, L.H. Chen, C. Daraio, S.H. Jin, Multibranching carbon nanotubes via self-seeded catalysts. Nano Lett. **6**, 324 (2006)
47. O.T. Heyning, P. Bernier, M. Glerup, A low cost method for the direct synthesis of highly Y-branched nanotubes. Chem. Phys. Lett. **409**, 43 (2005)
48. D. Wei, Y. Liu, L. Cao, L. Fu, X. Li, Y. Wang, G. Yu, D. Zhu, A new method to synthesize complicated multibranched carbon nanotubes with controlled architecture and composition. Nano Lett. **6**, 186 (2006)
49. H. Dai, Carbon nanotubes: opportunities and challenges. Surf. Sci. **500**, 218 (2002)
50. T. Yamabe, T. Namai, K. Hata, D.N. Futaba, K. Mizuno, J. Fan, M. Yudasaka, M. Yumura, S. Iijima, Size-selective growth of double-walled carbon nanotube forests from engineered iron catalysts. Nat. Nanotechnol. **1**, 131 (2006)
51. A.V. Melechko, V.I. Merkulov, T.E. McKnight, M.A. Guillorn, K.L. Klein, D.H. Lowndes, M.L. Simpson, Vertically aligned carbon nanofibers and related structures: controlled synthesis and directed assembly. J. Appl. Phys. **97**, 41301 (2005)
52. E.T. Thostenson, Z. Ren, T.W. Chou, Advances in the science and technology of carbon nanotubes: a review. Compos. Sci. Technol. **61**, 1899 (2001)
53. B.I. Dunlap, Connecting carbon tubules. Phys. Rev. B **46**, 1933 (1992)
54. S. Amelinckx, X.B. Zhang, D. Bernaerts, X.F. Zhang, V. Ivanov, J.B. Nagy, A formation mechanism for catalytically grown helix-shaped graphite nanotubes. Science **265**, 635 (1994)
55. M. Lu, K.T. Lau, J.C. Xu, H.L. Li, Coiled carbon nanotubes growth and DSC study in epoxy-based composites. Colloids Surf. A **257**, 339 (2005)
56. K.T. Lau, M. Lu, D. Hui, Coiled carbon nanotubes: Synthesis and their potential applications in advanced composite structures. Composites B **37**, 437 (2006)
57. A. Szabo, A. Fonseca, J.B. Nagy, Ph Lambin, L.P. Biro, Structural origin of coiling in coiled carbon nanotubes. Carbon **43**, 1628 (2005)
58. M. Ishigami, J.H. Chen, W.G. Cullen, M.S. Fuhrer, E.D. Williams, Atomic structure of Graphene on SiO2. Nano Lett. **7**, 1643 (2007)
59. J. Moser, A. Barreiro, A. Bachtold, Current-induced cleaning of graphene. Appl. Phys. Lett. **91**, 163513 (2007)
60. A.J. Stone, D.J. Wales, Theoretical studies of icosahedral C60 and some related species. Chem. Phys. Lett. **128**, 501 (1986)
61. A.V. Krasheninnikov, K. Nordlund, M. Sirvio, E. Salonen, J. Keinonen, Formation of ion-irradiation-induced atomic-scale defects on walls of carbon nanotubes. Phys. Rev. B **63**, 245405 (2001)
62. K. Nordlund, J. Keinonen, T. Mattila, Formation of ion irradiation induced small-scale defects on graphite surfaces. Phys. Rev. Lett. **77**, 699 (1996)
63. K. Suenaga, H. Wakabayashi, M. Koshino, Y. Sato, K. Urita, S. Iijima, Imaging active topological defects in carbon nanotubes. Nat. Nanotechnol. **2**, 358 (2007)
64. A. Hashimoto, K. Suenaga, A. Gloter, K. Urita, S. Iijima, Direct evidence for atomic defects in graphene layers. Nature **430**, 870 (2004)
65. J.C. Charlier, Defects in carbon nanotubes. Acc. chem. res. **35**, 1063 (2002)
66. K. Molhave, S.B. Gudnason, A.T. Pedersen, C.H. Clausen, A. Horsewell, P. Boggild, Transmission electron microscopy study of individual carbon nanotube breakdown caused by Joule heating in air. Nano Lett. **6**, 1663 (2006)
67. C. Kramberger, A. Waske, K. Biedermann, T. Pichler, T. Gemming, B. Buchner, H. Kataura, Tailoring carbon nanostructures via temperature and laser irradiation. Chem. Phys. Lett. **407**, 254 (2005)
68. S. Gupta, R.J. Patel, R.E. Giedd, Electron beam-induced surface modification and nano-engineering of carbon nanotubes: single-walled and multiwalled. J. Mater. Res. **21**, 3109 (2006)
69. T.D. Yuzvinsky, W. Mickelson, S. Aloni, G.E. Begtrup, A. Kis, A. Zettl, Shrinking a carbon nanotube. Nano Lett. **6**, 2718 (2006)

70. L. Der Hsien, K. Hsin Fu, H. Wen Kuang, Segmentation of single-walled carbon nanotubes by camera flash. Appl. Phys. Lett. **88**, 093113 (2006)
71. A.H. Romero, M.E. Garcia, F. Valencia, H. Terrones, M. Terrones, H.O. Jeschke, Femtosecond laser nanosurgery of defects in carbon nanotubes. Nano Lett. **5**, 1361 (2005)
72. C. Jin, K. Suenaga, S. Iijima, Plumbing carbon nanotubes. Nat. Nanotechnol. **3**, 17 (2008)
73. Q. Bao, H. Zhang, C. Pan, Electric-field-induced microstructural transformation of carbon nanotubes. Appl. Phys. Lett. **89**, 063124 (2006)
74. G. Zheng, Q. Li, K. Jiang, X. Zhang, J. Chen, Z. Ren, S. Fan, Transition of single-walled carbon nanotubes from metallic to semiconducting in field-effect transistors by hydrogen plasma treatment. Nano Lett. **7**, 1622 (2007)
75. J.S. Bunch, A.M. van der Zande, S.S. Verbridge, I.W. Frank, D.M. Tanenbaum, J.M. Parpia, H.G. Craighead, P.L. McEuen, Electromechanical resonators from graphene sheets. Science **315**, 490 (2007)
76. P. Blake, E.W. Hill, A.H.C. Neto, K.S. Novoselov, D. Jiang, R. Yang, T.J. Booth, A.K. Geim, Making graphene visible. Appl. Phys. Lett. **91**, 063124 (2007)
77. D.S.L. Abergel, A. Russell, V.I. Fal'ko, Visibility of graphene flakes on a dielectric substrate. Appl. Phys. Lett. **91**, 063125 (2007)
78. A.C. Ferrari, J.C. Meyer, V. Scardaci, C. Casiraghi, M. Lazzeri, F. Mauri, S. Piscanec, D. Jiang, K.S. Novoselov, S. Roth, A.K. Geim, Raman spectrum of graphene and graphene layers. Phys. Rev. Lett. **97**, 187401 (2006)
79. J.C. Hamilton, J.M. Blakely, Carbon segregation to single crystal sufaces of Pt, Pd and Co. Surf. Sci. **91**, 199 (1980)
80. C. Berger, Z.M. Song, T.B. Li, X.B. Li, A.Y. Ogbazghi, R. Feng, Z.T. Dai, A.N. Marchenkov, E.H. Conrad, P.N. First, W.A. de Heer, Ultrathin epitaxial graphite: 2D electron gas properties and a route toward graphene-based nanoelectronics. J. Phys. Chem. B **108**, 19912 (2004)
81. W.A. de Heer, C. Berger, X. Wu, P.N. First, E.H. Conrad, X. Li, T. Li, M. Sprinkle, J. Hass, M.L. Sadowski, M. Potemski, G. Martinez, Epitaxial graphene. Solid State Commun. **143**, 92 (2007)
82. E. Rollings, G.H. Gweon, S.Y. Zhou, B.S. Mun, J.L. McChesney, B.S. Hussain, A. Fedorov, P.N. First, W.A. de Heer, A. Lanzara, Synthesis and characterization of atomically thin graphite films on a silicon carbide substrate. J. Phys. Chem. Solids **67**, 2172 (2006)
83. F. Varchon, R. Feng, J. Hass, X. Li, B. Ngoc Nguyen, C. Naud, P. Mallet, J.Y. Veuillen, C. Berger, E.H. Conrad, L. Magaud, Electronic structure of epitaxial graphene layers on SiC: effect of the substrate. Phys. Rev. Lett. **99**, 126805 (2007)
84. J. Hass, F. Varchon, J.E. Millan Otoya, M. Sprinkle, W.A. de Heer, C. Berger, P.N. First, L. Magaud, E.H. Conrad (unpublished)
85. N.I. Kovtyukhova, P.J. Ollivier, B.R. Martin, T.E. Mallouk, S.A. Chizhik, E.V. Buzaneva, A.D. Gorchinskiy, Layer-by-layer assembly of ultrathin composite films from micron-sized graphite oxide sheets and polycations. Chem. Mater. **11**, 771 (1999)
86. D. Li, M.B. Muller, S. Gilje, R.B. Kaner, G.G. Wallace, Processable aqueous dispersions of graphene nanosheets. Nat. Nanotechnol. **3**, 101 (2008)
87. Y. Xu, H. Bai, G. Lu, C. Li, G. Shi, Flexible graphene films via the filtration of water-soluble noncovalent functionalized graphene sheets. J. Am. Chem. Soc. **130**, 5856 (2008)
88. S. Gilje, S. Han, M. Wang, K.L. Wang, R.B. Kaner, A chemical route to graphene for device applications. Nano Lett. **7**, 3394 (2007)
89. G. Eda, G. Fanchini, M. Chhowalla, Large-area ultrathin films of reduced graphene oxide as a transparent and flexible electronic material. Nat. Nanotechnol. **3**, 270 (2008)
90. Z. Wu, Z. Chen, X. Du, J.M. Logan, J. Sippel, M. Nikolou, K. Kamaras, J.R. Reynolds, D.B. Tanner, A.F. Hebard, A.G. Rinzler, Transparent, conductive carbon nanotube films. Science **305**, 1273 (2004)
91. X. Li, X. Wang, L. Zhang, S. Lee, H. Dai, Chemically derived, ultrasmooth graphene nanoribbon semiconductors. Science **319**, 1229 (2008)

92. H.C. Schniepp, J.L. Li, M.J. McAllister, H. Sai, M. Herrera Alonso, D.H. Adamson, R.K. Prud'homme, R. Car, D.A. Saville, I.A. Aksay, Functionalized single graphene sheets derived from splitting graphite oxide. J. Phys. Chem. B **110**, 8535 (2006)
93. Z. Osvath, A. Darabont, P. Nemes Incze, E. Horvath, Z.E. Horvath, L.P. Biro, Graphene layers from thermal oxidation of exfoliated graphite plates. Carbon **45**, 3022 (2007)
94. J. Vaari, J. Lahtinen, P. Hautojärvi, The adsorption and decomposition of acetylene on clean and K-covered Co(0001). Catal. Lett. **44**, 43 (1997)
95. Y. Gamo, A. Nagashima, M. Wakabayashi, M. Terai, C. Oshima, Atomic structure of monolayer graphite formed on Ni(111). Surf. Sci. **374**, 61 (1997)
96. T.A. Land, T. Michely, R.J. Behm, J.C. Hemminger, G. Comsa, STM investigation of single layer graphite structures produced on Pt(111) by hydrocarbon decomposition. Surf. Sci. **264**, 261 (1992)
97. C. Oshima, A. Nagashima, Ultra-thin epitaxial films of graphite and hexagonal boron nitride on solid surfaces. J. Phys. Condens. Matter **9**, 1 (1997)
98. A.L. Vazquez de Parga, F. Calleja, B. Borca, M.C.G. Passeggi Jr., J.J. Hinarejos, F. Guinea, R. Miranda, Periodically rippled graphene: growth and spatially resolved electronic structure. Phys. Rev. Lett. **100**, 056807 (2008)
99. B. Tilley, T. Aizawa, R. Souda, W. Hayami, S. Otani, Y. Ishizawa, Monolayer graphite on a tungsten-segregated TiC(100) surface. Solid State Commun. **94**, 685 (1995)
100. M. Terai, N. Hasegawa, M. Okusawa, S. Otani, C. Oshima, Electronic states of monolayer micrographite on TiC(111)-faceted and TiC(410) surfaces. Appl Surf. Sci. **130**, 876 (1998)
101. E.V. Rut'kov, A. Ya Tontegode, A study of the carbon adlayer on iridium. Surf. Sci. **161**, 373 (1985)
102. J. Coraux, A.T. N'Diaye, C. Busse, T. Michely, Structural coherency of graphene on Ir(111). Nano Lett. **8**, 565 (2008)
103. A. Ya Tontegode, N.A. Kholin, Poverkhnost **1**, 41 (1983)
104. A.N. Obraztsov, E.A. Obraztsova, A.V. Tyurnina, A.A. Zolotukhin, Chemical vapor deposition of thin graphite films of nanometer thickness. Carbon **45**, 2017 (2007)
105. M.V. Antisari, R. Marazzi, R. Krsmanovic, Synthesis of multi-walled carbon nanotubes by electric arc discharge in liquid environments. Carbon **41**, 2393 (2003)
106. N. Sano, H. Wang, M. Chhowalla, I. Alexandru, G.A.J. Amaratunga, Synthesis of carbon onions in water. Nature **414**, 506 (2001)
107. H. Lange, M. Sioda, A. Huczko, Y.Q. Zhu, H.W. Kroto, D.R.M. Walton, Nanocarbon production by arc discharge in water. Carbon **41**, 8 (2003)
108. M. Ishigami, J. Cummings, A. Zettl, S. Chen, A simple method for the continuous production of carbon nanotubes. Phys. Lett. **319**, 457 (2000)
109. C. Journet, W.K. Maser, P. Bernier, A. Loiseau, M. Lamy de la Chapelle, S. Lefrant, P. Deniard, R. Lee, J.E. Fischer, Large-scale production of single-walled carbon nanotubes by the electric-arc technique. Nature **388**, 756 (1997)
110. T. Gue, P. Nikolaev, A. Thess, D.T. Colbert, R.E. Smalley, Catalytic growth of single-walled nanotubes by laser vaporization. Chem. Phys. Lett. **243**, 49 (1995)
111. P.C. Eklund, B.K. Pradhan, U.J. Kim, Q. Xiong, J.E. Fischer, A.D. Friedman, B.C. Holloway, K. Jordan, M.W. Smith, Large-scale production of single-walled carbon nanotubes using ultrafast pulses from a free electron laser. Nano Lett. **2**, 561 (2002)
112. A.G. Rinzler, J. Liu, H. Dai, P. Nikolaev, C.B. Huffman, F.J. Rodríguez Macías, P.J. Boul, A.H. Lu, D. Heymann, D.T. Colbert, R.S. Lee, J.E. Fischer, A.M. Rao, P.C. Eklund, R.E. Smalley, Large-scale purification of single-wall carbon nanotubes: process, product, and characterization. Appl. Phys. A **67**, 29 (1998)
113. M. Meyyappan, Delzeit Lance, Cassell Alan, and Hash David, Carbon nanotube growth by PECVD: a review. Plasma Sources Scie. Technol. **12**, 205 (2003)
114. R.E. Morjan, V. Maltsev, O. Nerushev, Y. Yao, L.K.L. Falk, E.E.B. Campbell, High growth rates and wall decoration of carbon nanotubes grown by plasma-enhanced chemical vapour deposition. Chem. Phys. Lett. **383**, 385 (2004)

115. L.H. Chen, J.F. AuBuchon, I.C. Chen, C. Daraio, X.R. Ye, A. Gapin, S. Jin, C.M. Wang, Growth of aligned carbon nanotubes on carbon microfibers by dc plasma-enhanced chemical vapor deposition. Appl. Phys. Lett. **88**, 033103 (2006)
116. T. Nozaki, T. Goto, K. Okazaki, K. Ohnishi, L. Mangolini, J. Heberlein, U. Kortshagen, Deposition of vertically oriented carbon nanofibers in atmospheric pressure radio frequency discharge. J. Appl. Phys. **99**, 024310 (2006)
117. N. Satake, G.H. Jeong, T. Hirata, R. Hatakeyama, H. Ishida, K. Tohji, K. Motomiya, Production of carbon nanotubes by controlling radio-frequency glow discharge with reactive gases. Phys. B **323**, 290 (2002)
118. T. Iwasaki, G.F. Zhong, T. Aikawa, T. Yoshida, H. Kawarada, Direct evidence for root growth of vertically aligned single-walled carbon nanotubes by microwave plasma chemical vapor deposition. J. Phys. Chem. B **109**, 19556 (2005).
119. W.S. Choi, S.H. Choi, B. Hong, J.H. Lee, Growth of carbon nanotubes on glass substrate by MPECVD. Mater. Sci. Eng. C **26**, 1215 (2006)
120. P.B. Balbuena, J. Zhao, S.P. Huang, Y.X. Wang, N. Sakulchaicharoen, D.E. Resasco, Role of the catalyst in the growth of single-wall carbon nanotubes. J. Nanosci. Nanotechnol. **6**, 1247 (2006).
121. A. Moisala, A.G. Nasibulin, E.I. Kauppinen, The role of metal nanoparticles in the catalytic production of single-walled carbon nanotubes – a review. J. Phys. Condens. Matter **15**, S3011 (2003)
122. F. Ding, K. Bolton, A. Rosen, Molecular dynamics study of bamboo-like carbon nanotube nucleation. J. Electron. Mater. **35**, 207 (2006)
123. Y. Homma, Y. Kobayashi, T. Ogino, D. Takagi, I. Roichi, Y.J. Jung, P.M. Ajayan, Role of transition metal catalyst in single-walled carbon nanotube growth in chemical vapor deposition. J. Phys. Chem. B **107**, 12161 (2003)
124. F. Beuneu, Nucleation and growth of single wall carbon nanotubes. Solid State Commun. **136**, 462 (2005)
125. J. Gavillet, J. Thibault, O. Stéphan, H. Amara, A. Loiseau, Ch. Bichara, J.P. Gaspard, F. Ducastelle, Nucleation and growth of single wall carbon nanotubes: the role of metallic catalysts. J. Nanosci. Nanotechnol. **4**, 346 (2004)
126. R.T.K. Baker, Catalytic growth of carbon filaments. Carbon **27**, 315 (1989)
127. M.S. Bell, R.G. Lacerda, K.B.K. Teo, W.I. Milne, *Characterisation of the Growth Mechanism during PECVD of Multiwalled Carbon Nanotubes*, vol 100 of *Topics In Applied Physics* (Springer-Verlag, Berlin, Germany, 2006), pp. 77–93
128. S. Huang, X. Cai, J. Liu, Growth of millimeter-long and horizontally aligned single-walled carbon nanotubes on flat substrates. J. Am. Chem. Soc. **125**, 5636 (2003)
129. Y. Zhang, A. Chang, J. Cao, Q. Wang, W. Kim, Y. Li, N. Morris, E. Yenilmez, J. Kong, H. Dai, Electric-field-directed growth of aligned single-walled carbon nanotubes. Appl. Phys. Lett. **79**, 3155 (2001).
130. E. Joselevich, C.M. Lieber, Vectorial growth of metallic and semiconducting single-wall carbon nanotubes. Nano Lett. **2**, 1137 (2002)
131. Z. Jin, H. Chu, J. Wang, J. Hong, W. Tan, Y. Li, Ultralow feeding gas flow guiding growth of large-scale horizontally aligned single-walled carbon nanotube arrays. Nano Lett. **7**, 2073 (2007)
132. J.H. Yen, I.C. Leu, M.T. Wu, C.C. Lin, M.H. Hon, Effect of nanowire catalyst for carbon nanotubes growth by ICP-CVD. Diam. Relat. Mater. **14**, 841 (2005)
133. M.S. Arnold, A.A. Green, J.F. Hulvat, S.I. Stupp, M.C. Hersam, Sorting carbon nanotubes by electronic structure using density differentiation. Nat. Nanotechnol. **1**, 60 (2006)
134. Y. Maeda, S. Kimura, M. Kanda, Y. Hirashima, T. Hasegawa, T. Wakahara, Y.F. Lian, T. Nakahodo, T. Tsuchiya, T. Akasaka, J. Lu, X.W. Zhang, Z.X. Gao, Y.P. Yu, S. Nagase, S. Kazaoui, N. Minami, T. Shimizu, H. Tokumoto, R. Saito, Large-scale separation of metallic and semiconducting single-walled carbon nanotubes. J. Am. Chem. Soc. **127**, 10287 (2005)

135. Y. Li, D. Mann, M. Rolandi, W. Kim, A. Ural, S. Hung, A. Javey, J. Cao, D. Wang, E. Yenilmez, Q. Wang, J.F. Gibbons, Y. Nishi, H. Dai, Preferential growth of semiconducting single-walled carbon nanotubes by a plasma enhanced CVD Method. Nano Lett. **4**, 317 (2004)
136. S.M. Bachilo, L. Balzano, J.E. Herrera, F. Pompeo, D.E. Resasco, R.B. Weisman, Narrow (n,m)-distribution of single-walled carbon nanotubes grown using a solid supported catalyst. J. Am. Chem. Soc. **125**, 11186 (2003)
137. G. Lolli, L. Zhang, L. Balzano, N. Sakulchaicharoen, Y. Tan, D.E. Resasco, Tailoring (n,m) structure of single-walled carbon nanotubes by modifying reaction conditions and the nature of the support of CoMo catalysts. J. Phys. Chem. B **110**, 2108 (2006)
138. P.G. Collins, P. Avouris, Nanotubes for electronics. Sci. Am. **283**, 62 (2000)
139. A.A. Balandin, S. Ghosh, W. Bao, I. Calizo, D. Teweldebrhan, F. Miao, C.N. Lau, Superior thermal conductivity of single-layer graphene. Nano Lett. **8**, 902 (2008)
140. C. Muller, S. Hampel, D. Elefant, K. Biedermann, A. Leonhardt, M. Ritschel, B. Buchner, Iron filled carbon nanotubes grown on substrates with thin metal layers and their magnetic properties. Carbon **44**, 1746 (2006)
141. A.K. Geim, A.H. MacDonald, Graphene: exploring carbon flatland. Phys. Today **60**, 35 (2007)
142. M.I. Katsnelson, Graphene: carbon in two dimensions. Mater. Today **10**, 20 (2007)
143. A. Bostwick, T. Ohta, J.L. McChesney, T. Seyller, K. Horn, E. Rotenberg, Band structure and many body effects in graphene. Eur. Phys. J. Special Topics **148**, 5 (2007)
144. M.I. Katsnelson, K. Novoselov, A.K. Geim, Chiral tunnelling and the Klein paradox in graphene. Nat. Phys. **2**, 620 (2006)
145. K.S. Novoselov, A.K. Geim, S.V. Morozov, D. Jiang, M.I. Katsnelson, I.V. Grigorieva, S.V. Dubonos, A.A. Firsov, Two-dimensional gas of massless Dirac fermions in graphene. Nature **438**, 197 (2005)
146. J. Yan, Y.B. Zhang, P. Kim, A. Pinczuk, Electric field effect tuning of electron-phonon coupling in graphene. Phys. Rev. Lett. **98**, 166802 (2007)
147. D.A. Areshkin, D. Gunlycke, C.T. White, Ballistic transport in graphene nanostrips in the presence of disorder: importance of edge effects. Nano Lett. **7**, 204 (2007)
148. K.S. Novoselov, Z. Jiang, Y. Zhang, S.V. Morozov, H L. Stormer, U. Zeitler, J.C. Maan, G.S. Boebinger, P. Kim, A.K. Geim, Room-temperature quantum hall effect in graphene. Science **315**, 1137201 (2007)
149. Y. Zhang, J.W. Tan, H.L. Stormer, P. Kim, Experimental observation of the quantum Hall effect and Berry's phase in graphene. Nature **438**, 201 (2005)
150. C.P. Burgess, B.P. Dolan, Quantum Hall effect in graphene: emergent modular symmetry and the semicircle law. Phys. Rev. B **76**, 113406 (2007)
151. B. Partoens, F.M. Peeters, From graphene to graphite: electronic structure around the K point. Phys. Rev. B **74**, 075404 (2006)
152. T. Ohta, A. Bostwick, T. Seyller, K. Horn, E. Rotenberg, Controlling the electronic structure of bilayer graphene. Science **313**, 951 (2006)
153. M. Aoki, H. Amawashi, Dependence of band structures on stacking and field in layered graphene. Solid State Commun. **142**, 123 (2007)
154. P. Lambin, Electronic structure of carbon nanotubes. Comptes Rendus Physique **4**, 1009 (2003)
155. M.S. Ouyang, J.H. Huang, C.M. Lieber, Fundamental electronic properties and applications of single-walled carbon nanotubes. Acc. Chem. Res. **35**, 1018 (2002)
156. P.L. McEuen, M.S. Fuhrer, H. Park, Single-walled carbon nanotube electronics. IEEE Trans. Nanotechnol. **1**, 78 (2002)
157. N. Hamada, S.I. Sawada, A. Oshiyama, New one-dimensional conductors: graphitic microtubules. Phys. Rev. Lett. **68**, 1579 (1992)
158. M.S. Ouyang, J.L. Huang, C.M. Lieber, Scanning tunneling microscopy of the one-dimensional electronic properties of single-walled carbon nanotubes. Ann. Rev. Phys. Chem. **53**, 201 (2002)

159. M. Ouyang, J.L. Huang, C.L. Cheung, C.M. Lieber, Energy gaps in "Metallic" single-walled carbon nanotubes. Science **292**, 702 (2001)
160. A. Kleiner, S. Eggert, Band gaps of primary metallic carbon nanotubes. Phys. Rev. B **63**, 073408 (2001)
161. L. Langer, V. Bayot, E. Grivei, J.P. Issi, J.P. Heremans, C.H. Olk, L. Stockman, C. Van Haesendonck, Y. Bruynseraede, Quantum transport in a multiwalled carbon nanotube. Phys. Rev. Lett. **76**, 479 (1996)
162. S. Frank, P. Poncharal, Z.L. Wang, W.A. de Heer, Carbon nanotube quantum resistors. Science **280**, 1744 (1998)
163. L. Zhang, D. Austin, V.I. Merkulov, A.V. Meleshko, K.L. Klein, M.A. Guillorn, D.H. Lowndes, M.L. Simpson, Four-probe charge transport measurements on individual vertically aligned carbon nanofibers. Appl. Phys. Lett. **84**, 3972 (2004)
164. R.S. Ruoff, D. Qian, W.K. Liu, Mechanical properties of carbon nanotubes: theoretical predictions and experimental measurements. Comptes Rendus Physique **4**, 993 (2003)
165. J.P. Salvetat-Delmotte, A. Rubio, Mechanical properties of carbon nanotubes: a fiber digest for beginners. Carbon **40**, 1729 (2002)
166. I.W. Frank, D.M. Tanenbaum, A.M. van der Zande, P.L. McEuen, Mechanical properties of suspended graphene sheets. J. Vac. Sci. Technol. B **25**, 2558 (2007)
167. E.W. Wong, P.E. Sheehan, C.M. Lieber, Nanobeam mechanics: elasticity, strength, and toughness of nanorods and nanotubes. Science **277**, 1971 (1997)
168. W.D.J. Callister, *Materials Science and Engineering an Introduction*, 6th edn. (Wiley, New York, USA, 2003)
169. M.M.J. Treacy, T.W. Ebbesen, J.M. Gibson, Exceptionally high Young's modulus observed for individual carbon nanotubes. Nature **381**, 678 (1996)
170. O. Lourie, H.D. Wagner, Evaluation of Young's modulus of carbon nanotubes using micro-Raman spectroscopy. J. Mater. Res. **13**, 2418 (1998)
171. M.F. Yu, O. Lourie, M.J. Dyer, K. Moloni, T.F. Kelly, R.S. Ruoff, Strength and breaking mechanism of multiwalled carbon nanotubes under tensile load. Science **287**, 637 (2000)
172. S. Iijima, C. Brabec, A. Maiti, J. Bernholc, Structural flexibility of carbon nanotubes. J. Chem. Phys. **104**, 2089 (1996)
173. A. Cao, P.L. Dickrell, W.G. Sawyer, M.N. Ghasemi Nejhad, P.M. Ajayan, Super-compressible foamlike carbon nanotube films. Science **310**, 1307 (2005)
174. C. Daraio, V.F. Nesterenko, S. Jin, W. Wang, A.M. Rao, Impact response by a foamlike forest of coiled carbon nanotubes. J. Appl. Phys. **100**, 064309 (2006)
175. J. Suhr, P. Victor, L. Ci, S. Sreekala, X. Zhang, O. Nalamasu, P.M. Ajayan, Fatigue resistance of aligned carbon nanotube arrays under cyclic compression. Nat. Nanotechnol. **2**, 417 (2007)
176. R. Gao, Z.L. Wang, Z. Bai, W.A. de Heer, L. Dai, M. Gao, Nanomechanics of individual carbon nanotubes from pyrolytically grown arrays. Phys. Rev. Lett. **85**, 622 (2000)
177. M. Zhang, S. Fang, A.A. Zakhidov, S.B. Lee, A.E. Aliev, C.D. Williams, K.R. Atkinson, R.H. Baughman, Strong, transparent, multifunctional, carbon nanotube sheets. Science **309**, 1215 (2005)
178. K. Liu, Y. Sun, L. Chen, C. Feng, X. Feng, K. Jiang, Y. Zhao, S. Fan, Controlled growth of super-aligned carbon nanotube arrays for spinning continuous unidirectional sheets with tunable physical properties. Nano Lett. **8**, 700 (2008)
179. D.A. Dikin, S. Stankovich, E.J. Zimney, R. Piner, G.H.B. Dommett, G. Evmenenko, S.T. Nguyen, R.S. Ruoff, Preparation and characterization of graphene oxide paper. Nature **448**, 457 (2007)
180. J. Wei, Y. Jia, Q. Shu, Z. Gu, K. Wang, D. Zhuang, G. Zhang, Z. Wang, J. Luo, A. Cao, D. Wu, Double-walled carbon nanotube solar cells. Nano Lett. **7**, 2317 (2007)
181. H. Ago, K. Petritsch, M.S.P. Shaffer, A.H. Windle, R.H. Friend, Composties of carbon nanotubes and conjugated polymers for photovoltaic devices. Adv. Mater. **11**, 1281 (1999)
182. X. Wang, L. Zhi, K. Mullen, Transparent, conductive graphene electrodes for dye-sensitized solar cells. Nano Lett. **8**, 323 (2008)

183. K.E.H. Gilbert, J.H. Lehman, A.C. Dillon, J.L. Blackburn, Toward rapid and inexpensive identification of bulk carbon nanotubes. Appl. Phys. Lett. **88**, 143122 (2006)
184. A. Nish, J.Y. Hwang, J. Doig, R.J. Nicholas, Highly selective dispersion of single-walled carbon nanotubes using aromatic polymers. Nat. Nanotechnol. **2**, 640 (2007)
185. P.G. Collins, M.S. Arnold, P. Avouris, Engineering carbon nanotubes and nanotube circuits using electrical breakdown. Science **292**, 706 (2001)
186. M.T. Martinez, M.A. Callejas, A.M. Benito, M. Cochet, T. Seeger, A. Anson, J. Schreiber, C. Gordon, C. Marhic, O. Chauvet, J.L.G. Fierro, W.K. Maser, Sensitivity of single wall carbon nanotubes to oxidative processing: structural modification, intercalation and functionalisation. Carbon **41**, 2247 (2003)
187. Q. Li, J. Zhang, H. Yan, M. He, Z. Liu, Thionine-mediated chemistry of carbon nanotubes. Carbon **42**, 287 (2004)
188. Y. Wang, Z. Iqbal, S.V. Malhotra, Functionalization of carbon nanotubes with amines and enzymes. Chem. Phys. Lett. **402**, 96 (2005)
189. J. Hu, J. Shi, S. Li, Y. Qin, Z. Guo, Y. Song, D. Zhu, Efficient method to functionalize carbon nanotubes with thiol groups and fabricate gold nanocomposites. Chem. Phys. Lett. **401**, 352 (2005)
190. R. Barthos, D. Méhn, A. Demorties, N. Pierard, Y. Morciaux, G. Demortier, A. Fonseca, J.B. Nagy, Functionalization of single-walled carbon nanotubes by using alkyl-halies. Carbon **43**, 321 (2005)
191. C.Y. Hong, Y.Z. You, C.Y. Pan, A new approach to functionalize multi-walled carbon nanotubes by the use of functional polymers. Polymer **47**, 4300 (2006)
192. L. Valentini, D. Puglia, I. Armentano, J.M. Kenny, Sidewall functionalization of single-walled carbon nanotubes through CF4 plasma treatment and subsequent reaction with aliphatic amines. Chem. Phys. Lett. **403**, 385 (2005)
193. N.O.V. Plank, R. Cheung, Functionalisation of carbon nanotubes for molecular electronics. Microelectron. Eng. **73**, 578 (2004)
194. A. Felten, C. Bittencourt, J.F. Colomer, G. Van Tendeloo, J.J. Pireaux, Nucleation of metal clusters on plasma treated multi wall carbon nanotubes. Carbon **45**, 110 (2007)
195. Y.H. Yan, M.B. Chan Park, Q. Zhou, C.M. Li, C.Y. Yue, Functionalization of carbon nanotubes by argon plasma-assisted ultraviolet grafting. Appl. Phys. Lett. **87**, 213101 (2005)
196. D. Yang, J. Rochette, E. Sacher, Controlled chemical functionalization of multiwalled carbon nanotubes by kiloelectronvolt argon ion treatment and air exposure. Langmuir **21**, 8539 (2005)
197. L. Brey, H.A. Fertig, Electronic states of graphene nanoribbons studied with the Dirac equation. Phys. Rev. B **73**, 235411 (2006)
198. K. Nakada, M. Fujita, G. Dresselhaus, M.S. Dresselhaus, Edge state in graphene ribbons: nanometer size effect and edge shape dependence. Phys. Rev. B **54**, 17954 (1996)
199. B. Trauzettel, D.V. Bulaev, D. Loss, G. Burkard, Spin qubits in graphene quantum dots. Nat. Phys. **3**, 192 (2007)
200. S.Y. Zhou, G.H. Gweon, A.V. Fedorov, P.N. First, W.A. de Heer, D.H. Lee, F. Guinea, A.H. Castro Neto, A. Lanzara, Substrate-induced bandgap opening in epitaxial graphene. Nat. Mater. **6**, 916 (2007)
201. P. Avouris, Z. Chen, V. Perebeinos, Carbon-based electronics. Nat. Nanotechnol. **2**, 605 (2007)
202. M.C. Lemme, T.J. Echtermeyer, M. Baus, H. Kurz, A graphene field-effect device. IEEE Electron Dev. Lett. **28**, 282 (2007)
203. Z. Chen, Y.M. Lin, M.J. Rooks, P. Avouris, Graphene nano-ribbon electronics. Phys. E **40**, 228 (2007)
204. J. Robertson, Growth of carbon nanotubes for electronics. Mater. Today **10**, 36 (2007)
205. A.P. Graham, G.S. Duesberg, R. Seidel, M. Liebau, E. Unger, F. Kreupl, W. Hönlein, Towards the integration of carbon nanotubes in microelectronics. Diam. Relat. Mater. **13**, 1296 (2004)

206. M. Nihei, A. Kawabata, D. Kondo, M. Horibe, S. Sato, Y. Awano, Electrical properties of carbon nanotube bundles for future via interconnects. Jpn. J. Appl. Phys. **44**, 1626 (2005)
207. M. Horibe, M. Nihei, D. Kondo, A. Kawabata, Y. Awano, Carbon nanotube growth technologies using tantalum barrier layer for future ULSIs with Cu/Low-k interconnect processes. Jpn. J. Appl. Phys. **44**, 5309 (2005)
208. G.F. Close, S. Yasuda, B. Paul, S. Fujita, H.S.P. Wong, A 1 GHz integrated circuit with carbon nanotube interconnects and silicon transistors. Nano Lett. **8**, 706 (2008)
209. S.J. Tans, A.R.M. Verschueren, C. Dekker, Room-temperature transistor based on a single carbon nanotube. Nature **393**, 49 (1998)
210. R.T. Weitz, U. Zschieschang, F. Effenberger, H. Klauk, M. Burghard, K. Kern, High-performance carbon nanotube field effect transistors with a thin gate dielectric based on a self-assembled monolayer. Nano Lett. **7**, 22 (2007)
211. Z. Chen, J. Appenzeller, Y.M. Lin, J. Sippel Oakley, A.G. Rinzler, J. Tang, S.J. Wind, P.M. Solomon, P. Avouris, An integrated logic circuit assembled on a single carbon nanotube. Science **311**, 1735 (2006)
212. A. Vijayaraghavan, S. Blatt, D. Weissenberger, M. Oron Carl, F. Hennrich, D. Gerthsen, H. Hahn, R. Krupke, Ultra-large-scale directed assembly of single-walled carbon nanotube devices. Nano Lett. **7**, 1556 (2007)
213. T. Rueckes, K. Kim, E. Joselevich, G.Y. Tseng, C.L. Cheung, C.M. Lieber, Carbon nanotube-based nonvolatile random access memory for molecular computing. Science **289**, 94 (2000)
214. J.B. Cui, R. Sordan, M. Burghard, K. Kern, Carbon nanotube memory devices of high charge storage stability. Appl. Phys. Lett. **81**, 3260 (2002)
215. J.P. Hollingsworth, P.R. Bandaru, Carbon nanotube based nonvolatile memory. Appl. Phys. Lett. **87**, 233115 (2005)
216. D. Gunlycke, D.A. Areshkin, J. Li, J.W. Mintmire, C.T. White, Graphene nanostrip digital memory device. Nano Lett. **7**, 3608 (2007)
217. D.N. Futaba, K. Hata, T. Yamada, T. Hiraoka, Y. Hayamizu, Y. Kakudate, O. Tanaike, H. Hatori, M. Yumura, S. Iijima, Shape-engineerable and highly densely packed single-walled carbon nanotubes and their application as super-capacitor electrodes. Nat. Mater. **5**, 987 (2006)
218. J.S. Ye, X. Liu, H.F. Cui, W.D. Zhang, F.S. Sheu, T.M. Lim, Electrochemical oxidation of multi-walled carbon nanotubes and its application to electrochemical double layer capacitors. Electrochem. Commun. **7**, 249 (2005)
219. F. Liu, M. Bao, H.J. Kim, K.L. Wang, C. Li, X. Liu, C. Zhou, Giant random telegraph signals in the carbon nanotubes as a single defect probe. Appl. Phys. Lett. **86**, 163102 (2005)
220. K. Jensen, J. Weldon, H. Garcia, A. Zettl, Nanotube radio. Nano Lett. **7**, 3508 (2007)
221. C. Rutherglen, P. Burke, Carbon nanotube radio. Nano Lett. **7**, 3296 (2007)
222. A. Volodin, M. Ahlskog, E. Seynaeve, C. Van Haesendonck, A. Fonseca, J.B. Nagy, Imaging the elastic properties of coiled carbon nanotubes with atomic force microscopy. Phys. Rev. Lett. **84**, 3342 (2000)
223. X. Chen, S. Zhang, D.A. Dikin, W. Ding, R.S. Ruoff, L. Pan, Y. Nakayama, Mechanics of a carbon nanocoil. Nano Lett. **3**, 1299 (2003)
224. A. Volodin, D. Buntinx, M. Ahlskog, A. Fonseca, J.B. Nagy, C. Van Haesendonck, Coiled carbon nanotubes as self-sensing mechanical resonators. Nano Lett. **4**, 1775 (2004)
225. V. Bajpai, L. Dai, T. Ohashi, Large-scale synthesis of perpendicularly aligned helical carbon nanotubes. J. Am. Chem. Soc. **126**, 5070 (2004)
226. W.I. Milne, K.B.K. Teo, M. Mann, I.Y.Y. Bu, G.A.J. Amaratunga, N. De Jonge, M. Allioux, J.T. Oostveen, P. Legagneux, E. Minoux, L. Gangloff, L. Hudanski, J.P. Schnell, L.D. Dieumegard, F. Peauger, T. Wells, M. El Gomati, Carbon nanotubes as electron sources. Physi. Status Solid A **203**, 1058 (2006)
227. R. Yabushita, K. Hata, H. Sato, Y. Saito, Development of compact field emission scanning electron microscope equipped with multiwalled carbon nanotube bundle cathode. J. Vac. Sci.Technol. B **25**, 640 (2007)

228. F.G. Zeng, C.C. Zhu, W. Liu, X. Liu, The fabrication and operation of fully printed carbon nanotube field emission displays. Microelectron. J. **37**, 495 (2006)
229. J.T.H. Tsai, H.C. Ko, Plasma illumination devices enhanced by carbon nanotubes. Appl. Phys. Lett. **88**, 013104 (2006)
230. M. Mauger, V.T. Binh, Vertically aligned carbon nanotube arrays for giant field emission displays. J. Vac. Scie. Technol. B **24**, 997 (2006)
231. K. Kawakita, K. Hata, H. Sato, Y. Saito, Development of microfocused x-ray source by using carbon nanotube field emitter. J. Vac. Sci. Technol. B **24**, 950 (2006)
232. O. Gröning, L.O. Nilsson, P. Gröning, L. Schlapbach, Properties and characterization of chemical vapor deposition diamond field emitters. Solid-State Electron. **45**, 929 (2001)
233. M.J. Fransen, Th.L. van Rooy, P. Kruit, Field emission energy distributions from individual multiwalled carbon nanotubes. Appl. Surf. Sci. **146**, 312 (1999)
234. J.M. Bonard, M. Croci, C. Klinke, R. Kurt, O. Noury, N. Weiss, Carbon nanotube films as electron field emitters. Carbon **40**, 1715 (2002)
235. H. Li, J. Li, C. Gu, Local field emission from individual vertical carbon nanofibres grown on tungsten filament. Carbon **43**, 849 (2005)
236. M.S. Wang, J.Y. Wang, L.M. Peng, Engineering the cap structure of individual carbon nanotubes and corresponding electron field emission characteristics. Appl. Phys. Lett. **88**, 243108 (2006)
237. L. Nilsson, O. Groening, C. Emmenegger, O. Kuettel, E. Schaller, L. Schlapbach, H. Kind, J.M. Bonard, K. Kern, Scanning field emission from patterned carbon nanotube films. Appl. Phys. Lett. **76**, 2071 (2000)
238. X.Q. Wang, M. Wang, H.L. Ge, Q. Chen, Y.B. Xu, Modeling and simulation for the field emission of carbon nanotubes array. Phys. E **30**, 101 (2005)
239. N. Sinha, J.Z. Ma, J.T.W. Yeow, Carbon nanotube-based sensors. J. Nanosci. Nanotechnol. **6**, 573 (2006)
240. F. Schedin, A.K. Geim, S.V. Morozov, E.W. Hill, P. Blake, M.I. Katsnelson, K. Novoselov, Detection of individual gas molecules adsorbed on graphene. Nat. Mater. **6**, 652 (2007)
241. I. Sayago, E. Terrado, M. Aleixandre, M.C. Horrillo, M.J. Fernandez, J. Lozano, E. Lafuente, W.K. Maser, A.M. Benito, M.T. Martinez, J. Gutierrez, E. Muñuz, Novel selective sensor based on carbon nanotube films for hydrogen detection. Sens. Actuators B Chem. **122**, 75 (2007)
242. L. Valentini, C. Cantalini, L. Lozzi, S. Picozzi, I. Armentano, J.M. Kenny, S. Santucci, Effects of oxygen annealing on cross sensitivity of carbon nanotubes thin films for gas sensing applications. Sens. Actuators B Chem. **100**, 33 (2004)
243. L. Valentini, C. Cantalini, L. Lozzi, I. Armentano, J.M. Kenny, S. Santucci, Highly sensitie and selective sensors based on carbon nanotubes thin films for molecular detection. Diam. Relat. Mater. **13**, 1301 (2004)
244. L.H. Nguyen, T.V. Phi, P.Q. Phan, H.N. Vu, C. Nguyen Duc, F. Fossard, Synthesis of multi-walled carbon nanotubes for NH3 gas detection. Phys. E **37**, 54 (2007)
245. M. Lucci, A. Reale, A. Di Carlo, S. Orlanducci, E. Tamburri, M.L. Terranova, I. Davoli, C. Di Natale, A. D'Amico, R. Paolese, Optimization of a NOx gas sensor based on single walled carbon nanotubes. Sens. Actuators B Chem. **118**, 226 (2006)
246. O.K. Varghese, P.D. Kichambre, D. Gong, K.G. Ong, E.C. Dickey, C.A. Grimes, Gas sensing characteristics of multi-wall carbon nanotubes. Sens. Actuators B Chem. **81**, 32 (2001)
247. H.Q. Nguyen, J.S. Huh, Behavior of single-walled carbon nanotube-based gas sensors at various temperatures of treatment and operation. Sens. Actuators B Chem. **117**, 426 (2006)
248. J.H. Lee, J. Kim, H.W. Seo, J.W. Song, E.S. Lee, M. Won, C.S. Han, Bias modulated highly sensitive NO2 gas detection using carbon nanotubes. Sens. Actuators B Chem. **129**, 628 (2008)
249. A.V. Desai, M.A. Haque, Mechanics of the interface for carbon nanotube-polymer composites. Thin-Walled Struct. **43**, 1787 (2005)

250. W. Ding, A. Eitan, F.T. Fisher, X. Chen, D.A. Dikin, R. Andrews, L.C. Brinson, L.S. Schadler, R.S. Ruoff, Direct observation of polymer sheathing in carbon nanotube-polycarbonate composites. Nano Lett. **3**, 1593 (2003)
251. S. Stankovich, D.A. Dikin, G.H.B. Dommett, K.M. Kohlhaas, E.J. Zimney, E.A. Stach, R.D. Piner, S.T. Nguyen, R.S. Ruoff, Graphene-based composite materials. Nature **442**, 282 (2006)
252. H.D. Wagner, R.A. Vaia, Nanocomposites: issues at the interface. Mater. Today **7**, 38 (2004)
253. Y. Hu, O.A. Shenderova, Z. Hu, C.W. Padgett, D.W. Brenner, Carbon nanostructures for advanced composites. Rep. Prog. Phys. **69**, 1847 (2006)
254. T. Ramanathan, A.A. Abdala, S. Stankovich, D.A. Dikin, M. Herrera Alonso, R.D. Piner, D.H. Adamson, H.C. Schniepp, X. Chen, R.S. Ruoff, S.T. Nguyen, I.A. Aksay, R.K. Prud'Homme, L.C. Brinson, Functionalized graphene sheets for polymer nanocomposites. Nat. Nanotechnol. **3**, 327 (2008)
255. M. Cadek, J.N. Coleman, V. Barron, K. Hedicke, W.J. Blau, Morphological and mechanical properties of carbon-nanotube-reinforced semicrystalline and amorphous polymer composites. Appl. Phys. Lett. **81**, 5123 (2002)
256. S.L. Ruan, P. Gao, X.G. Yang, T.X. Yu, Toughening high performance ultrahigh molecular weight polyethylene using multiwalled carbon nanotubes. Polymer **44**, 5643 (2003)
257. T.X. Liu, I.Y. Phang, L. Shen, S.Y. Chow, W.D. Zhang, Morphology and mechanical properties of multiwalled carbon nanotubes reinforced Nylon-6 composites. Macromolecules **37**, 7214 (2004)
258. J. Sandles, M.S.P. Shaffer, T. Prasse, W. Bauhofer, K. Schulte, A.H. Windle, Development of a dispersion process for carbon nanotubes in an epoxy matrix and the resulting electrical properties. Polymer **40**, 5967 (1999)
259. M.S.P. Shaffer, A.H. Windle, Fabrication and characterization of carbon nanotube/poly(vinyl alcohol) composites. Adv. Mater. **11**, 937 (1999)
260. H.D. Wagner, O. Lourie, Y. Feldman, R. Tenne, Stress-induced fragmentation of multiwall carbon nanotubes in a polymer matrix. Appl. Phys. Lett. **72**, 188 (1998)
261. Y.S. Song, J.R. Youn, Properties of epoxy nanocomposites filled with carbon nanomaterials. E-Polymers **1**, 80 (2004)
262. J.P. Salvetat, G.A.D. Briggs, J.M. Bonard, R.R. Bacsa, A.J. Kulik, T. Stockli, N.A. Burnham, L. Forro, Elastic and shear moduli of single-walled carbon nanotube ropes. Phys. Rev. Lett. **82**, 944 (1999)
263. L.Q. Lui, H.D. Wagner, Rubbery and glassy epoxy resins reinforced with carbon nanotubes. Composi. Sci. Technol. **65**, 1861 (2005)
264. F.H. Gojny, J. Nastalcyk, Z. Roslaniec, K. Schulte, Surface modified multi-walled carbon nanotubes in CNT/epoxy-composites. Chem. Phys. Lett. **370**, 820 (2003)
265. G.L. Hwang, K.C. Hwang, Carbon nanotube reinforced ceramics. J. Mater. Chem. **11**, 1722 (2001)
266. X. Wang, N.P. Padture, H. Tanaka, Contact-damage-resistant ceramic/single-wall carbon nanotubes and ceramic/graphite composites. Nat. Mater. **3**, 539 (2004)
267. B.S. Harrison, A. Atala, Carbon nanotube applications for tissue engineering. Biomaterials **28**, 344 (2007)
268. A. Bianco, K. Kostarelos, M. Prato, Applications of carbon nanotubes in drug delivery. Curr. Opin. Chem. Biol. **9**, 295 (2005)
269. T. Webster, M.C. Waid, J.L. McKenzie, R.L. Price, J.U. Ejiofor, Nano-biotehnology: carbon nanofibres as improved neural and orthopaedic implants. Nanotechnology **15**, 48 (2004)
270. C.W. Lam, J.T. James, R. McCluskey, S. Arepalli, R.L. Hunter, A review of carbon nanotube toxicity and assessment of potential occupational and environmental health risks. Crit. Rev. Toxicol. **36**, 189 (2006)

Index

S. Bellucci (ed.), *Physical Properties of Ceramic and Carbon Nanoscale Structures*,
Lecture Notes in Nanoscale Science and Technology 11,
DOI 10.1007/978-3-642-15778-3, © Springer-Verlag Berlin Heidelberg 2011